UNIVERSITY OF SOUTHAMPTON

FACULTY OF ENGINEERING AND THE ENVIRONMENT

Sustainable Energy Research Group

Performance Quantification of Marine Current Energy Converters in Constrained Flow Fields

by

Bradley Keogh

Thesis for the degree of Doctor of Philosophy

January 2016

UNIVERSITY OF SOUTHAMPTON

ABSTRACT

FACULTY OF ENGINEERING AND THE ENVIRONMENT
Sustainable Energy Research Group

Doctor of Philosophy

PERFORMANCE QUANTIFICATION OF MARINE CURRENT ENERGY CONVERTERS IN CONSTRAINED FLOW FIELDS

by Bradley Keogh

The Marine Current Energy Converter (MCEC) industry is currently at a stage where early farms are being designed. These farms will provide an indication of the commercial viability of the technology to future investors. Only limited full-scale device data is available in order to inform designers of performance, due to only small numbers of offshore deployments. Smaller-scale laboratory testing can provide greater understanding of device performance and loading. Understanding device performance and loading are important as they will impact on projects finances by affecting energy yield and allowing extreme loading to be designed for to avoid unplanned maintenance. The loading of MCEC devices in constrained flow fields is currently not well understood at either full or laboratory-scale.

The aim of this study is to investigate the influence of constrained flow fields on MCEC device loading and wake development. The results will inform: the limits of current analytical MCEC performance models, the calibration of empirical wake models, and the limits of existing computational fluid dynamic array models. The findings will therefore aid the development of design tools used in MCEC device modelling. This work presents the results from a series of small-scale laboratory static porous disk experiments in which the changes in loading and wake structure of a single device are characterised with variation in channel properties such as: area blockage ratio, Froude number and channel aspect ratio. Dual-array devices are also studied with the effects of device spacing and channel geometry upon wake formation and device loading characterised.

Thrust coefficient is shown to be a function of Froude number, area blockage ratio and channel aspect ratio; with each non-dimensional parameter contributing significantly to differences in loading. Despite differences in thrust coefficient with changes in channel aspect ratio it is shown that one-dimensional linear momentum actuator disk theory models are capable of accounting for these differences. Wake velocity profile, wake expansion, transition point from near to far wake and wake recovery are shown to be different in the vertical and horizontal planes in some channels geometries. Variation in channel geometry, i.e. the proximity of bounding surfaces, is shown to have an effect on these parameters indicating that it may be possible to calibrate semi-empirical wake models to predict wake development in either flows of constrained geometry or within array deployments. Device spacing in a dual-array is also shown to affect wake structure and device loading. The relationships between these two parameters are shown to be a function of device diameter/water depth ratio.

Contents

List of Figures

List of Tables

Declaration of Authorship

I, Bradley Keogh , declare that the thesis entitled *Performance Quantification of Marine Current Energy Converters in Constrained Flow Fields* and the work presented in the thesis are both my own, and have been generated by me as the result of my own original research. I confirm that:

- this work was done wholly or mainly while in candidature for a research degree at this University;
- where any part of this thesis has previously been submitted for a degree or any other qualification at this University or any other institution, this has been clearly stated;
- where I have consulted the published work of others, this is always clearly attributed;
- where I have quoted from the work of others, the source is always given. With the exception of such quotations, this thesis is entirely my own work;
- I have acknowledged all main sources of help;
- where the thesis is based on work done by myself jointly with others, I have made clear exactly what was done by others and what I have contributed myself;
- parts of this work have been published as described on the following page.

Signed:

Date: 17^{th} January 2016

Publications

- Some of the work in Chapter 8 was presented and published in the proceedings of the 9th European Wave and Tidal Energy Conference 2011 (Myers et al. 2011*b*) and the OCEANS 2011 conferences (Myers et al. 2011*a*).
- Some of the work in Chapter 6 was presented and published in the proceedings of the Grand Renewable Energy Congress Proceedings, 2014, (Keogh et al. 2014).
- The work in Chapter 5 has been submitted and is currently in review in the International Journal of Marine Energy.

Acknowledgements

Thanks to my supervisors Dr Luke Myers and Professor AbuBakr Bahaj for their support during this work. Thanks to the reviewers and examiners who have contributed greatly to the intellectual content of this work. Thanks to the EPSRC for funding this work and my development as a researcher. Thanks to Heather, Peter and Scott for always being there to listen and provide advice throughout my years of studying; without you I would not be who I am today. Thanks to all the many colleges who have co-inhabited B22 and B25 over the years; in particular: Tom Blackmore, Steve Haynes, Pascal Galloway, Natasha Carpenter, Will Nock, Jim Kerr, Sid Narayan, Khilan Shah, Caroline Stuiver, Danny Coles, Jon Coello and Pete Redshaw - people who were always there to discuss and help with work as well as to provide humorous relief and remind me to take much needed breaks. Thanks to all the inhabitants of 'K5': Rucha 'Team Leader' Amin, Dr Amelie 'House Führer' Heuer-Jungemann, Amy 'Top Ten' Gimson and Adam 'One Door' Johnson - who have made life much more enjoyable than it could otherwise have been during the writing process. Thanks to Professor Malcolm Munro for his advice surrounding the PhD process - which proved very useful. Thanks to Karl Scammell for his technical support at the magnificent University of Southampton hydraulics laboratories, and his flume-side banter - which lightened the mood massively at some very onerous times. Thanks to Caroline Powell who it is a delight to work for, and who has gone above and beyond what was required of her to support me at the final stages of this process. Lastly thanks to all those I have not listed but who have taken the time to ask the dreaded question "how is the PhD going?" over the last few years.

Notation

a	axial induction factor	
A	device area	m^2
B	blockage ratio	
C_d	discharge coefficient	
C_{drag}	drag coefficient	
C_p	power coefficient	
C_t	thrust coefficient	
d	device diameter	m
E	specific energy	m
E_k	kinetic energy	m
E_s	static energy	m
Fr	Froude number	
F_g	gravitational force	$kgms^{-2}$
F_I	inertial force	$kgms^{-2}$
F_ν	viscous force	$kgms^{-2}$
g	acceleration due to gravity	ms^{-2}
h	channel depth	m
h_c	critical depth	m
h_{we}	water surface height above weir	m
h_{1e}	Rebock formula height	m
I	turbulence intensity	%
k	resistance coefficient	
l	length	m
L	linear dimension	m
p	pressure	$kgm^{-1}s^{-2}$
P	power	kgm^2s^{-3}
q	volumetric flow rate	m^3s^{-1}
R	channel width/device width ratio	
Re	Reynolds number	
s	lag	s
S	device separation	D
t	timestep	s
T	thrust	$kgms^{-2}$
u	velocity	ms^{-1}
U_{def}	velocity deficit	
U_{ratio}	velocity ratio	
U_∞	upstream or freestream velocity	ms^{-1}
w	channel width	m
W	weir height above channel bed	m
X	axial force	$kgms^{-2}$
Z	autocorrelation function	
α_2	turbine flow induction factor	
α_4	wake flow induction factor	
β_4	bypass flow induction factor	
λ_l	integral lengthscale	m
λ_t	integral timescale	s

μ	dynamic viscosity	$kgm^{-1}s^{-1}$
ρ	fluid density	kgm^{-3}
τ	normalised shear tensor	
Γ	screen height	
Θ	geometric porosity	
Υ	source constant	
Ω	Aspect ratio	

Sub- and super-scripts

Φ'	fluctuation of Φ from the mean value
$\bar{\Phi}$	mean value of Φ
Φ_i	implies value Φ in any of the co-ordinate directions $i = x, y, z$
Φ_x	streamwise component
Φ_y	lateral (cross channel) component
Φ_z	vertical component
Φ_m	model parameter
Φ_p	prototype parameter
Φ_r	scaling ratio

Abbreviations

ADCP	Acoustic Doppler Current Profiler
ADV	Acoustic Doppler Velocimeter
B&W	Barnsley and Wellicome
CFD	Computational Fluid Dynamics
D	Device diameters
LMADT	Linear Momentum Actuator Disk Theory
MCEC	Marine Current Energy Converter
RANS	Reynolds Averaged Navier Stokes
TEL	Total Energy Line
TSR	Tip Speed Ratio

Chapter 1

Introduction

1.1 Renewable energy

Since the industrial revolution our society has become increasingly dependent on fossil fuels. These fuels include: oil, natural gas and coal. They are found below the Earth's surface and form as a result of the fossilised remains of plants being subject to high temperatures and pressures over millions of years within the Earth's crust. As an energy source fossil fuels remain attractive due to their high energy density, however they are in finite supply as our rate of consumption far outstrips the time scale of millions of years over which they require to form. As the global energy demand continues to increase it is clear that at some point new energy sources must be harnessed in order to satisfy the global demand for energy before fossil fuels are depleted.

There are other concerns which motivate this search for alternative sources of energy: global warming, climate change and energy prices. Global warming generally refers to the idea that the global consumption of fossil fuels as an energy source is leading to temperature increases within our atmosphere. This is due to the release of carbon dioxide and other gasses during the process of energy conversion which increasing in concentration in the Earth's atmosphere. The increase in these gas levels is hypothesised to lead to the increased trapping of the Sun's radiation within our atmosphere, contributing to the rising surface temperatures of the Earth. The rising of the Earth's temperature is linked to changes in the climate that we are currently experience on the planet and is suggested to contribute to the extreme weather events that have been observed more frequently in recent years. There is currently much disagreement as to whether the burning of fossil fuels is contributing to 'global warming' or 'climate change'. As Freeman Dyson stated "What I'm convinced of is that we don't understand climate...It will take a lot of very hard work before that question is settled" (Lin 2014).

What is certain however is that energy prices (currently dominated by fossil fuel cost) are, whilst subject to short term fluctuations, in the long term increasing. This driven

by an increasing demand and a reduction in the ease of procurement of fossil fuels. Due to the nature of fuel prices affecting the everyday lives of many people it this should be a significant contributor to the need for finding alternative sources of energy to supply our needs.

Whether it be the drive to combat global warming, the need for security of supply or the rise in energy prices governments are now pledging aid to develop non-carbon releasing sources of energy generation. In the UK possible sources include: nuclear, geothermal energy, hydroelectricity, solar energy, biomass, onshore wind energy, offshore wind energy, wave energy and tidal energy (MacKay 2009). Renewable energy sources are generally defined as energy sources which are replenished within a human time scale. Those listed above (apart from nuclear) are known as 'renewable energy' sources from which power may be generated. In order to meet targets of renewable energy generation the UK government is currently supporting mechanisms for the development and installation of: solar energy, biomass, onshore wind energy, offshore wind energy, wave energy, and tidal energy. This work focusses on Tidal Energy.

1.2 Tidal energy

The combination of the rotation of the Earth and positions of the Sun and Moon both contribute to the tides that we experience on Earth. The gravitational forces acting between these celestial bodies cause the oceans on the Earth's surface to be higher in some places than others. The rotation of the Earth means that an observer at a particular location on Earth will see changes in water height over the course of the Earth's 24 hour rotation period. This variation in ocean height is what we observe as tide. The tidal height will vary based on the relative positions of the Sun, Moon and Earth. When the Sun, Moon and Earth are in line (full moon and new moon) the gravitational forces acting on the oceans reinforce each other and cause greater water height differences. Bigger tides result, which are known as spring tides; occurring every two weeks. Neap tides occur at the intervening half moon periods. Here the gravitational forces partly cancel and hence the tides are smaller. The present description would result in an observer at the equator seeing two high and two low tides in a single lunar day (known as a semi-diurnal tides). However the presence of the continents on the Earth's surface means that this is not always the case. The presence of landmass prevents the oceans from freely moving across the Earth's surface as it rotates. Hence some locations on Earth, such as the Gulf of Mexico, only see a diurnal tide (only one high and low tide per day). Mixed semi-diurnal tides are also found, where the two high and low waters are different heights within the same lunar day.

The UK has semi-diurnal tides. The high and low tides embody changes in the potential energy of a substantial body of water which has the potential to be exploited. Tidal

energy has been utilised since as early as the Middle Ages in flour mills (an example of which given in Figure 1.1).

Figure 1.1: A tidal mill (reproduced from Darkoneko (2003)).

Most sources of renewable energy are intermittent and unpredictable. Whilst being intermittent (it is only possible to extract energy at certain times depending on tide state) tidal energy holds a significant advantage over other forms of renewable energy such as wind, wave and solar; namely its predictability. As the tides can be predicted accurately for hundreds of years it is possible to calculate when and where energy can be extracted. This predictability offers an opportunity when selling renewable electricity to electrical grids due to the fact it makes it easier to control the grid with limited energy storage capacity. Electricity supply has to meet the (largely predictable) instantaneous demand and so this ability to know exactly when energy will be generated increases its value. In the UK renewable generating capacity is increasingly replacing conventional power generation due to older power plants retiring from service and the 'Large Combustion Plants Directive' form the European Union (European Parliament 2001). As more intermittent and unpredictable sources, such as wind energy, account for larger proportions of the generating capacity predictable renewable energy sources such as tidal will become even more valuable. The tidal stream energy resource in UK and Irish waters is currently estimated to be $95TWh/yr$ (RenewableUK 2013*b*) of which $18TWh/yr$ (Black & Veatch Ltd 2005) is currently assessed as being economically recoverable with today's technologies. Putting these figures into perspective at present UK annual electricity demand is about $350TWh/yr$, meaning tidal energy could provide for $\approx 5\%$ of UK electricity demand. This indicates that tidal energy is also capable of supplying a significant proportion of UK demand.

Two fundamentally distinct types of tidal energy extraction are possible; namely tidal range and tidal stream. Tidal range type projects are usually referred to as barrage or lagoon projects (but also can include tidal mills, described earlier). These trap vast quantities of water at times of high tide and store them. When at low tide there will be a head difference between the stored water and the low tide state of the sea. Hence a potential difference is formed. Water is then released through turbines which convert

the potential energy to mechanical and electrical energy. An example is the La Rance barrage, located in France (seen left Figure 1.2). Tidal stream turbines by comparison are 'in-flow' mechanical devices which are placed in areas of high tidal flow speeds (an example seen right in Figure 1.2). These areas of high flow speed are created by the difference in water surface elevation combined with the bathymetry/landmasses found around the potential installation site. The considerable velocities found within theses flows allow the possibility of installing devices to convert the kinetic energy in the flow to mechanical energy, and then electrical energy for transmission. The work in this report focuses on the tidal stream variation exclusively.

Figure 1.2: Two distinct types of tidal energy extraction: (a) a tidal barrage (reproduced from Tswgb (2007)) and (b) a MCEC (reproduced from Atlantis Resources Ltd (2015)).

There are many types of tidal stream device concepts and prototypes currently undergoing testing. Examples include horizontal-axis, vertical-axis, oscillating hydrofoil and crossflow turbines. Horizontal-axis tidal turbines are the most common type being prototype tested at present (as seen in Table 1.1) and are potentially the most advanced device-type to date judging by the investment decisions being made in tidal farm developments. It is possible the reason for this is due to the investment and experience already available from the wind industry where horizontal-axis machines dominate the large scale commercial market. Therefore this work will focus primarily upon horizontal-axis devices. Most horizontal-axis tidal stream devices look and operate in a very similar manner to horizontal-axis wind turbines. Throughout this report tidal stream energy devices will be referred to as Marine Current Energy Converters (MCECs).

1.3 Tidal stream: state of play

The offshore renewable energy sector in the UK is currently growing (Department of Energy & Climate Change 2015). This must partly be a response to the recent legally binding targets and milestones introduced by the UK government which aim to reduce

carbon dioxide emissions. These themselves are due in part to EU climate change related targets increasing energy production from renewable sources by 2020 European Commission (2012) (the UK target is 15%), but also as a strategic move to reduce dependence on fossil fuel imports and hence increase UK energy security (Department of Trade and Industry (2007)). One mechanism by which the UK government is encouraging investment in new renewable generation is the use of Renewable Obligation Certificates (ROCs). As a result expansion of offshore wind generating capacity is increasing year on year; $5GW$ of capacity is currently operational with $12GW$ consented/approved. There are predictions of a 17% contribution by wind energy to the net UK electricity production by 2020 (RenewableUK (2013*a*)).

Tidal energy by comparison lags far behind the current state of offshore wind; this is partly due to the lack of understanding surrounding the new and unique environments into which tidal devices will be placed. The harsh offshore environment into which tidal stream devices will be installed is not currently well understood. High device thrust to area ratios (in comparison to wind turbines) and installation in areas of fast tidal currents each pose new challenges to device and array developers. All of these factors thus increase the potential risks for investors. Support is gathering for the sector however. In the long term the predictable nature of tidal energy generation as a renewable source will provide enhanced value in an increasingly diverse grid with a higher proportion of intermittent sources and limited energy storage. In the short term private investment is being further encouraged with the government promising stable prices for tidal energy through the Feed in Tariff Contract for Difference schemes. At the same time several device developers have demonstrated enough deployment experience to start providing devices for commercial projects. Hence it is an exciting time for the tidal stream energy industry with commercial tidal-arrays (schemes comprising of multiple devices) currently in the design, planning and pre-installation stages.

1.3.1 Commercial projects

MCEC prototype devices have been under development for many years. Some of the larger scale prototype devices that have been tested to date are listed in Table 1.1. Many of the companies listed are seen to have tested smaller (kW scale) devices offshore before developing and testing the current range of larger devices. The scale of these larger devices and the experience gained during their installation and operation now mean that some of the companies listed are in a position to offer devices for initial array developments. Table 1.2 shows some of the tidal stream array projects currently under development. As can be seen these first arrays are generally of the $\leq 10MW$ scale. However subsequent arrays of greater size are also being discussed by many of the companies involved in these early arrays, and in some cases licences to develop these have been already been obtained. Examples include the Meygen project in the

Pentland Firth (UK) (MeyGen 2015), which looks to install a $398MW$ capacity by the early 2020s. Along with the projects listed by OpenHydro (OpenHydro 2015) which amount to $600MW$ of capacity installed at three sites at: Antrim Coast - Northern Ireland, Orkney Islands (UK), and Alderney Islands (UK). These latter arrays should most likely be considered aspirational, with the success of the initial arrays currently under design likely to determine their subsequent development.

When considering Tables 1.1 and 1.2 it is clear that most large scale devices have been tested in the UK and are horizontal axis devices (Open centre (OC) devices are also seen in these tables. Strictly speaking these devices are horizontal axis, however the distinction is made here due to the generally employed generic description of a conventional bladed horizontal axis turbine - introduced in Chapter 2.1). Therefore this work will focus primarily on horizontal axis devices.

As well as the large scale prototype devices and array developments already discussed it is worth noting that smaller MCEC devices/arrays are currently being designed. For example Nova Innovation Ltd (Nova Innovation Ltd 2015) have installed a $30kW$ horizontal axis device offshore and plan to install five $100kW$ devices (three installations in 2015) at Shetland, UK. Sustainable Marine Energy Ltd (Sustainable Marine Energy Ltd 2015) are due to install five dual-rotor floating devices at the European Marine Energy Centre (EMEC) between 2015-2017. These devices will encompass Schottel Hydro SIT horizontal axis rotors which are small diameter devices rated to produce $50 - 70kW$ (Schottel Group 2015). The different scale of these devices give them a number of advantages over the larger devices discussed earlier. The advantages of smaller multiple generating units lie both in the reduced manufacturing costs (from not requiring large bespoke facilities) and reduced cost of offshore operational maintenance (from recovery being easier with smaller devices and from non-operational time being reduced). Both of these areas are currently a large part of the capital and running costs in tidal energy projects and so are important considerations at a time when long term funding for the tidal energy sector is not guaranteed. Some of the possible deployment options of smaller device being considered are shown in Figure 1.3.

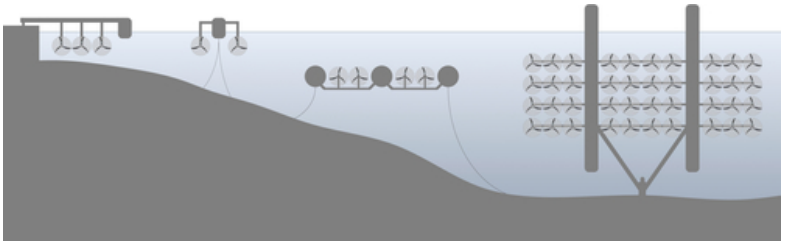

Figure 1.3: Possible deployment options of smaller-scale generating units (reproduced from Schottel Group (2015)).

Table 1.1: Large scale prototype MCEC installations. Device Type: HA - Horizontal axis, OH - Oscillating hydrofoil, OC - Open centre.

Device	Company	Location	Capacity	Device Type	Install Date
T100	Tocardo	Den Oever, Netherlands	100kW	HA	2008
Pulse-Stream 100	Pulse Tidal	Humber,UK	100kW	OH	2009
-	OpenHydro	EMEC,UK	250kW	OC	2006
SR250	Scotrenewables Tidal Power Ltd	EMEC,UK	250kW	HA	2012
Seaflow	Marine Current Turbines	Lynmouth,UK	300kW	HA	2003
HS300	ANDRITZ HYDRO Hammerfest	Finnmark,Norway	300kW	HA	2003
Deepgen	Alstrom	EMEC,UK	500kW	HA	2010
-	Alstrom	EMEC,UK	1MW	HA	2013
-	OpenHydro	Minas Passage,Nova Scotia	1MW	OC	2009
AR1000	Atlatis	EMEC,UK	1MW	HA	2011
HS1000	ANDRITZ HYDRO Hammerfest	EMEC,UK	1MW	HA	2011
HyTide	Voith Hydro	EMEC,UK	1MW	HA	2013
-	Kawasaki Heavy Industries	EMEC,UK	1MW	HA	2015
SeaGen	Marine Current Turbines	Strangford Lough,UK	1.2MW	HA	2008
-	OpenHydro	Paimpol,France	2.0MW	OC	2011

Table 1.2: Planned MCEC arrays currently started construction or in design phase.

Location	Company	Device	No. Devices	Capacity	Started	Completed
New York East River,USA	Verdant Power	KHPS(Gen4)	6	-	2006	2009
Paimpol-Brehat,France	EDF	OpenHydro	4	8MW	2012	-
Pentland Firth,UK	MEYGEN	Atlantis/Hammerfest	4	6MW	2015	2016
Eastern Scheldt, Netherlands	Tocardo	T2	5	1.2MW	2015	-
Islay,UK	ScottishPower Renewables	HS1000	10	10MW	-	-
Kyle Rhea,UK	RWE npower	SeaGen S	4 dual-rotor	8MW	-	-
Anglesey Skerries,UK	RWE npower	SeaGen S	5 dual-rotor	10MW	-	-
Pembrokeshire, UK	Tidal Energy Limited	DeltaStream	9 tri-rotor units	1MW	2017	-

1.4 Current challenges for developers

As outlined in Table 1.1 single devices have been installed at full scale test sites. Data has been acquired during operational experience by the developers, however this is limited. Some basic wake measurements such as wake transects behind an operating device have been measured (Royal Haskoning 2011) in order to determine how far downstream wakes are likely to propagate. Other measurements from the device itself can give indications of performance, such as power production, of a developer's MCEC device (Fraenkel 2010). The latter may also be used for the validation of performance models for loading and power production, such as Blade Element Momentum (BEM) codes. The prediction of forces a MCEC will experience is vitally important to ensure a suitable and robust design. Inadequate predictions and the subsequent design have led to problems of blade loss after deployment (CBC News 2010), and even loss of entire MCECs. These problems could affect investor-developer relationships, with investors less likely to fund projects, due to the potential risks they perceive to their investment. One of the possible contributing causes of device failures is that of the lack of fundamental understanding of energy extraction through MCECs from bounded flows. Placing turbines into a flow field which is bounded, as tidal flows are (by a free surface, channel bed and possibly channel walls), can increase loading and energy extraction beyond that which would be expected if placed in an unbounded environment, such as that which wind turbines experience. At present there is limited experience from full scale turbine deployments to fully characterise this phenomenon and quantify its effects. In order to develop robust MCEC devices developers require guidance on these effects. This will allow corrections to account for the effects of constrained flow in models using BEM codes, and thus enhance performance prediction allowing more accurate loading predictions.

Details of the MCEC arrays currently being planned are highlighted in Table 1.2. These early deployments are to be the first tidal-arrays in history and hence there is no deployment data or clear guidance for developers to follow in how to plan such farms. Decisions need to be made regarding device spacing within these MCEC farms by the developers themselves. These decisions will take into account many factors such as: shipping restrictions, cable-routing, deployment procedure as well as power performance and device interactions. With regard to the power performance and device interaction considerations, some lessons can be learned from the wind industry; here full scale studies have shown devices operating behind others can have reduced power production and increased fatigue loading. This is a consequence of operating in the 'wake' of another device; the wake being mainly made up of the fluid which has passed through the upstream rotor which propagates downstream behind a device. In tidal arrays the characteristics of MCEC wakes will be similarly important in determining the power production and loading of subsequent downstream MCECs.

Early arrays are likely to be designed based on ambient site flow measurements coupled with local, site-specific, numerical Computational Fluid Dynamics (CFD) model predictions (Crammond et al. 2011). Site flow measurements conducted to date will no doubt be useful in revealing site conditions for initial validation of CFD models and basic resource estimates, however the introduction of MCECs to these models moves them away from being validated in the absence of full-scale data. Less complex performance tools are also available to developers, such as the commercial TidalFarmer software (Garrad Hassan and Partners Ltd. 2015), however these simplified models suffer from the same uncertainty as those mentioned above. Validation of turbine performance within these models is not possible in the absence of full scale data (which does not currently exist in detail for individual devices or at all in the case of multiple device arrays). Even after the installation and operation of these first arrays limitations due to the acoustic devices used in offshore flow measurement will not allow detailed analysis of the flow field around MCECs.

At present then it is clear that developers must use idealised smaller-scale laboratory studies in order to inform the development of performance prediction tools for full-scale deployments. Laboratory studies offer the opportunity to provide high-resolution spatial and temporal flow measurements which are not possible at full-scale testing sites (due to both cost and limitations surrounding the acoustic devices used in offshore flow measurement). To date laboratory studies of MCEC devices have been completed which show changes in wake characteristics can occur when operating in bounded flow fields. However these studies have been fairly limited in number and as such have not fully characterised and understood the mechanisms governing MCEC wake changes with changes in channel geometry. The limitations of smaller-scale model testing also needs to be understood if the findings are to be applied to full-scale performance models accurately.

In a similar manner to the early wind industry additional laboratory testing, although expensive in its own right (but comparatively cheap in comparison to full-scale offshore data collection), can provide detailed and targeted information which can help support the industry at this critical time when there is a lack of understanding due to limited offshore deployments. This can help prevent costly mistakes, such as device failure and sub-optimal power performance, in full-scale MCEC deployments; costly both in terms of the possible physical maintenance required on deployed MCECs and the impact on potential future investors if initial arrays are perceived to have been monetarily unsuccessful. The work in this thesis focusses on understanding the fluid dynamics considerations when deploying MCECs at full-scale, through a series of small-scale experimental model testing.

1.5 Aims and Objectives

The aim of this study is to investigate the influence of constrained flow fields on MCEC device loading and wake development. The results will inform: the limits of current analytical MCEC performance models, the calibration of empirical wake models, and the limits of CFD array models. The findings will therefore aid the development of design tools used in MCEC device modelling.

The investigation will be split into four main objectives:

1. Investigate the accuracy of existing analytical methods of predicting the thrust coefficient of a porous model based on porosity. Examine in detail the differences in the near and far wakes of a rotating MCEC model and smaller-scale porous disk model. Show the limitations of scale models and their use in informing full-scale design models.

2. Study the effects on device loading of the non-dimensional parameters: Froude number, area blockage ratio and channel aspect ratio. Validate or understand the limits of existing analytical models for blockage and performance prediction.

3. Investigate the/any changes in wake structure with variation in channel geometry, i.e. the proximity of bounding surfaces.

4. Examine the effects of channel geometry and device spacing in a dual-device array on device loading and wake structure/dissipation.

Chapter 2

Literature Review

2.1 Turbine wakes and porous disk models

2.1.1 Fluid flow around and through a turbine

In this section a physical picture of the flow field around a generic horizontal axis turbine is discussed. Firstly the classic aerodynamic description of turbine operation, as outlined for example by Burton et al. (2001), is presented. This generalised description of the energy extraction process around a turbine is known as the actuator disk, from the work originally belonging to Betz (1920). The basic model presumes an idealised flow (inviscid) in an infinite domain (no bounding effects) of a generic turbine (no inclination to any particular design). Operation in air or water is immaterial at this stage as the aerodynamic/hydrodynamic principals remain the same.

Figure 2.1 shows the variation in fluid velocity and pressure within the streamtube of an energy extracting turbine. Fluid approaching a turbine experiences a reduction in velocity even before it reaches the rotor plane. This is due to the expansion of the streamtube encompassing the turbine and corresponds with an increase in static pressure, to account for the reduced kinetic energy, as no work has yet been done. As the fluid passes though the rotor plane it experiences a sudden decrease in pressure and it will then encounter a region of flow behind the turbine which is propagating downstream at a lower velocity than the bypass flow passing around the rotor. This slower moving region is referred to as the wake. The force experienced on the rotor plane as a combination of the increased upstream and reduced downstream static pressures is a function of the energy extracted and is often presented as a non-dimensional thrust coefficient. Larger thrust coefficients will be associated with an increased pressure difference, greater straining of the streamtube encasing the rotor and higher velocity deficits in the wake. The near wake region immediately downstream of the turbine contains the bulk of the slowest moving fluid throughout the whole turbine wake, which has lost kinetic energy across

the turbine rotor plane, due to the energy extraction process. As the fluid continues to move downstream the surrounding streamtube continues to expand in order to return to ambient pressure conditions, this leading to further reduction in the magnitude of the fluid velocity in this region. At a distance far downstream of the turbine rotor plane the fluid will have fully recovered pressure to that of the ambient flow but will have reduced kinetic energy. This is a very simplistic explanation for the flow around a turbine based upon the conservation of momentum within the control volume and continuity of mass flow.

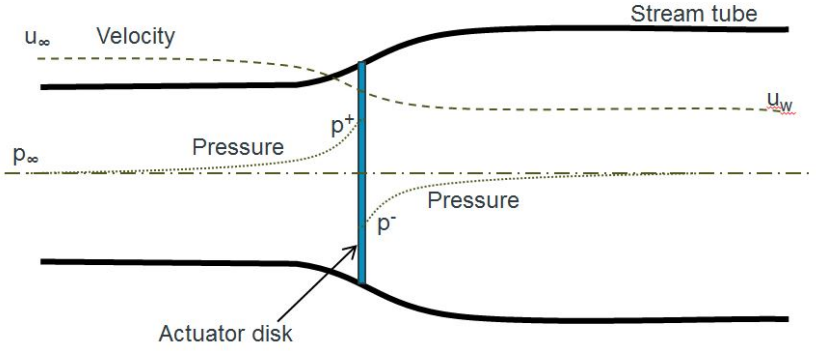

Figure 2.1: An energy extracting actuator disk and its streamtube.

In reality the flow is not inviscid with turbulent structures characterising various regions of the flow and also contributing to the rate at which the downstream wake dissipates. This more realistic wake structure is further described by Crespo et al. (1999). Pressure and velocity fields in the near wake region are non-uniform with an azimuthal velocity component present within the flow due to the blade rotation. Vortex sheets are shed from the trailing edges of the rotor blades and the blade tips generate tip vortices. These vortices are carried downstream and, upon merging, form a ring-shaped shear layer which bounds the bulk of the slower moving wake fluid from that of the faster bypass flow as it progresses downstream (vortices are of course present at this interface regardless, due to the disparity in fluid velocity between the wake and bypass flow causing shear layer instability). The thickness of this shear layer ring increases with downstream distance due to turbulent diffusion. The shear layer will eventually reach the turbine centreline axis (found to occur between two and five diameters downstream in wind applications) and this point is commonly defined as the transition from near to far wake region. Strictly speaking this is not a point; there is a short region where the transition occurs. Identification can be made visually from velocity profiles where the shear layer reaches the wake centreline and the cross wake velocity profile becomes Gaussian in nature. The near wake is heavily influenced by the change in momentum across the rotor plane (a function of thrust coefficient) (Ainslie 1988), the physical structure of the turbine (Myers & Bahaj 2009), the rotor speed - which will induce rotational motion in the wake (Ainslie 1988) and the nature of the turbulent flow into which the device is placed

(discussed later in this section). As the development of the near wake will determine the transition point each of these factors will also influence its downstream location.

The far wake is fully-developed and hypothetically, in the absence of ambient shear flow, the time averaged velocity deficit and turbulence intensity profiles will be axisymmetric, showing self-similar distributions in the cross-section of the wake (Vermeer et al. 2003). It is in the far wake region the shear layer becomes one of the more dominant mechanisms responsible for wake recovery, aiding the mixing of momentum within the wake region. The fluid continuing downstream within the far wake region will begin to see an increase in magnitude of its velocity as a result of turbulent momentum transfer; this occurring between the low-momentum fluid within the slower moving wake and the faster high-momentum bypass flow surrounding it. Although the mixing contributed by the shear layer may become one of the dominating drivers for wake recovery in this region it should be noted by the reader that the ambient turbulent conditions will also play a significant role in the speed of global wake recovery. Higher ambient turbulence will aid the wake recovery by helping to augment the momentum transfer between the wake and freestream flow further. This is the basis of the semi-empirical wind turbine wake model developed by Ainslie (1988). Maganga et al. (2010) showed experimentally that a tidal turbine model operating in flow with high turbulence intensity level will exhibit a much shorter wake in comparison to the same device operating in an ambient flow of lower turbulence intensity level. Other experimental work (Blackmore et al. 2014) has shown the significance of ambient flow integral lengthscale and turbulence intensity value on the thrust force acting upon a disk.

All the mechanisms described above contribute to the wake recovery which, at distances far enough downstream, will result in homogeneous velocity and pressure fields behind the turbine. Figure 2.2 and Table 2.1 surmise the various regions highlighted within this section.

Tedds et al. (2013) investigated changes in rotating tidal turbine wake experimentally in a water channel. In this case swirl, defined here as an azimuthal component within the wake, was still apparent up to 5 diameters(D) downstream within the wake. Flow statistics of standard deviation and turbulent kinetic energy (TKE) presented by Tedds et al. (2013) show the shear layer close behind (1.5D downstream) the device at the wake edges. The shear layer is seen to diffuse and hence values of standard deviation and TKE become more uniform across the wake flow with downstream distance. The shear layer appears to reach the axis centreline at around 5D downstream, indicating that tidal turbine wake appear to operate in a fundamentally similar manner to that of wind turbines. The diffusion/mixing of the shear layer to the turbine centreline appears to correspond with the reduction in swirl, indicating that swirl is most significant in the near wake of rotating tidal turbine device. This is also consistent with observations of rotating wind turbine devices Aubrun et al. (2013). Morris et al. (2015) showed with a numerical model that for most turbine designs the swirl of a MCEC device cannot

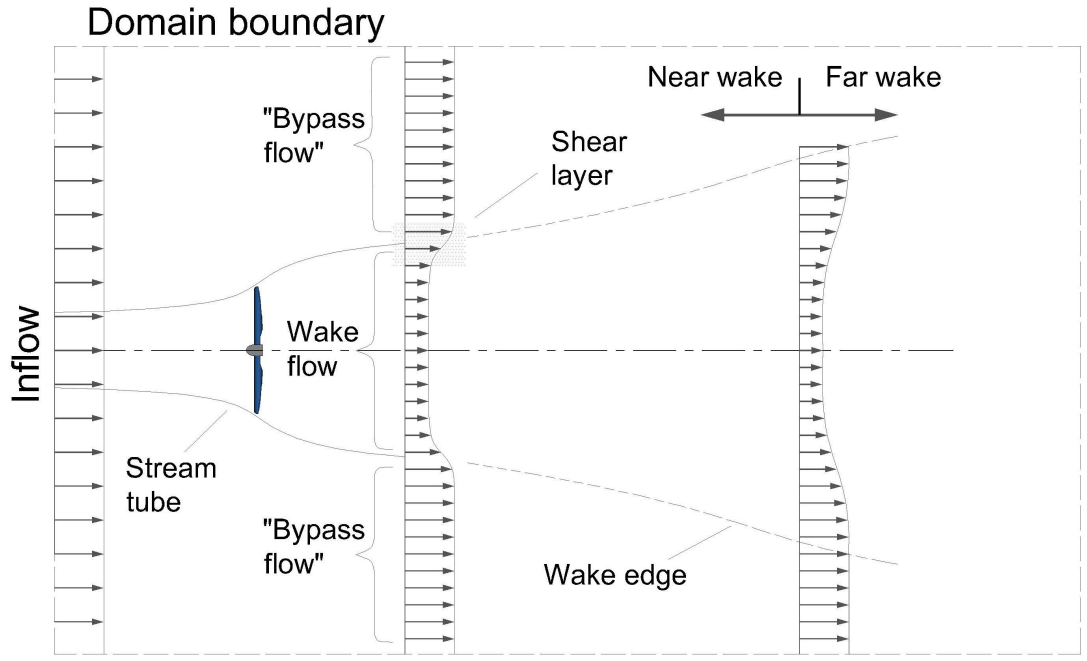

Figure 2.2: Wake and bypass flows through and around an energy extracting turbine.

be used to predict wake recovery. For some designs of turbine, such as four bladed devices, swirl is shown to become more significant. Morris et al. (2015) suggest that wake recovery may be linked to swirl in these cases.

Both Aubrun et al. (2013) and Maganga et al. (2010) show that the transition to the far wake can occur at differing downstream distances depending on flow conditions. The former work experimentally investigates a rotating wind turbine model and porous disk model in a wind tunnel in differing flow conditions. Both devices show transition to the far wake region before 3D downstream in one flow condition (atmospheric boundary layer conditions) and under different conditions (decaying isotropic turbulence conditions, generated behind a grid) show the transition to occur at $> 3D$ downstream. Maganga et al. (2010) provides wake data from an experimental MCEC model operating at the same facility with differing flow conditions. Transition is seen by 5D downstream in one flow case and by 2D in another case (where ambient turbulence intensity levels are higher). This provides evidence that MCEC wakes develop in a similar manner to that of wind turbines wakes and that the ambient flow conditions can have an important impact on wake development.

Table 2.1: Summary of near and far wake properties.

Near wake	• High velocity deficit • Initial reduction in velocity driven by amount of energy extracted • Azimuthal velocity component • Expanding streamtube as a result of mass continuity • Strong shear layer formed at blade tips • Thin, spatially periodic, shear layer • Turbulent structures shed at blade tips and sheet vortices shed from blades
Far wake	• Velocity deficit continues to reduce with downstream distance • Gaussian profiles of velocity and turbulence intensity • Shear layer has reached centreline of wake • Turbulent momentum transfer from bypass flow • Expanding wake edge as a result of momentum mixing • Thicker and diffusing homogenous shear layer

2.1.2 Ambient turbulence

As well as turbulent structures present in a flow due to the installation of a turbine (previously discussed) and its supporting structure, most ambient flows (and certainly natural flows) will be turbulent to some degree. All relevant flows (natural or laboratory) discussed in this thesis will have a sufficiently high Reynolds number to contain turbulent structures as a result of shear profiles induced by the flow boundaries. The nature of these structures themselves may vary depending on aspects such as surface roughness (of the wall itself in a laboratory, or a natural channel bed having debris of varying size present), channel geometry or bathymetry, and flow speed. Thomson et al. (2012) describes how naturally occurring flows, into which full scale tidal devices may be installed, may also contain larger structures shed from local headlands and shows how characteristics of particular sites can vary considerably. Laboratory flows on the other hand can contain turbulent structures which are developed as a result of their design and flow propulsion.

The ambient turbulence of a flow is an important consideration as it can affect the device loading, power production and wake development of a MCEC device. Maganga et al. (2010) are one of the few authors to investigate experimentally a tidal turbine operating in two flows of varying ambient turbulence levels. Three-dimensional turbulence intensity values of 25% and 8% were investigated within the same laboratory facility. Power coefficient and thrust coefficient values for the turbine were observed to be almost 10% lower in the flow of higher turbulence. Whilst in the lower turbulence intensity case the wake is seen to develop and continue to decay beyond 10D (10 turbine diameters) downstream, the higher turbulence case shows complete wake dissipation back to ambient flow levels (in terms of both velocity deficit and turbulence intensity) by 8D downstream. When considering velocity deficit a gaussian profile (associated with the far wake region) is first seen to develop at 5D and 3D downstream in the low and high turbulence cases respectively. These observations indicate that both near wake and far wake regions are decaying more quickly with greater ambient turbulence levels. The lower ambient turbulence case shows greatest values of turbulence intensity up to 40% in a distinct region around the shear layer at the edge of the rotor plane. By comparison the higher ambient turbulence case displays no clear shear layer regions and the highest turbulence intensity values are found spread laterally across the near wake region.

The findings above possibly indicate that the shear layer plays a smaller role in wake recovery in this case due to the more intense structures present in the ambient flow. The results may also imply that the ambient turbulent structures incident to the rotor plane are able to pass through the rotor plane in some form, and are present in the near wake. If so structures will be capable of aiding in the mixing of the wake and bypass flows and hence will aid wake recovery. This is acknowledged by Vermeer et al. (2003) with regard to wake recovery in wind turbines: "shear in the external atmospheric flow also plays an important role, at least in the redistribution of the generated turbulence." Generally speaking it is possible for turbulence to aid MCEC wake recovery due to its ability to mix flows. In helping to augment the momentum transfer between the wake and bypass flow the velocity of the fluid within the wake is increased. Hence the wake will be able to recover to values of the ambient flow more quickly with the presence of ambient turbulence. As highlighted above there can be a contribution to this momentum mixing from both device generated turbulence and ambient turbulent structures contained within a ambient flow. As to which of the turbulent structures will be most dominant in the wake recovery of a tidal stream turbine it is currently difficult to say; a fully comprehensive study which definitively investigates turbines in a water channel environment has not been completed to date.

As discussed above Maganga et al. (2010) showed experimentally that wake recovery can be altered due to the presence of different ambient turbulence levels, however does not discuss in detail the nature of the ambient turbulence structures present (i.e. only three dimensional turbulence intensity values are presented, no lengthscale information

is provided) or the relative importance of these with respect to the device generated structures. Although no experimental turbine studies have been completed investigating these more detailed characteristics of ambient flow Blackmore (2013) used porous disk models in a water flume to investigate the changes in thrust experienced under different ambient flow integral lengthscale and turbulence intensity values. Normalised thrust coefficient was observed to be a function of both of these parameters. As integral lengthscale values correspond with the larger scales within a flow, this result implies that it is the larger turbulent scales within a flow which affect turbine performance. In the same work Blackmore (2013) showed through numerical simulation that wakes behind semi-porous disks would decay at different rates and the decay was a function of the same two ambient flow parameters.

These sections have provided an overview of MCEC turbine wake structure and some of the parameters which are known to affect wake development/behaviour. Introducing the theory behind turbine wakes has provided a basis for the discussion of the use of small scale non-rotating experimental models to inform future full scale deployments. The current usage of these models in now discussed.

2.1.3 Porous disk models

Experimental rotor testing can be costly both in time and expense. Model development and the need for large hydraulics facilities (required to fit a larger device within) both contribute to the overall cost. In order to reduce costs smaller rotors may be used. However operational problems can arise when scaling turbine models. Hydrodynamic problems will occur which can result in severe modifications to blade geometry and could lead to unrepresentative power extraction. One method outlining the possible modifications for smaller scale turbine models are discussed by Whelan & Stallard (2011) in relation to the testing of 1/70th-scale rotors ($0.27m$ diameter) in a circulating flume facility by Stallard et al. (2011). These experiments and those 1/20th-scale ($0.8m$ diameter) rotor tests described by Myers & Bahaj (2009) were large enough to enable use of standard industry blade profiles. More aggressive twist along blade length was required (in comparison to full scale devices) in order to account for the increase in rotational speed. Whilst an increased chord length and thickness was also used in the latter case to help prevent the onset of stall around the root section. These modifications may lead to unrealistic/unrepresentative power extraction and wake development. There is currently no detailed literature which addresses this issue. Downscaling of turbine models can produce other practical problems not associated with the hydrodynamic performance issues already described; blade flexing, higher relative drive train resistance and disproportionate component size can impact upon the model design.

One form of experimental model which offers a reduction in the size of facility, the operational complexity and cost of the model required, is the use of porous disks. A static

non-rotating porous plate (porous disk) is substituted in place of a rotating turbine model. Sforza et al. (1981) and Builtjes (1978) used porous disk models in both horizontal and vertical axis wind turbine testing respectively. These devices simulate energy extraction from a flow by dissipating energy through small scale turbulence, rather than extracting energy as mechanical work. Builtjes (1978) used up to 100 of these models to investigate turbine spacing effects within a wind farm and by measuring the thrust force acting upon each device, was able to suggest an optimal spacing to obtain a maximum energy output of the array. Porous disks are still being used experimentally in wind turbine wake analysis; España et al. (2012) used porous disk models to investigate wake meandering effects as a function of ambient turbulence.

Due to the similar behaviour of MCECs during energy conversion several authors have completed experimental studies using porous disks in the investigation of MCEC operation as opposed to wind turbine operation. One of the first uses in marine application was completed by Bahaj, Myers, Thomson & Jorge (2007). In this work small scale experimental results (device diameter $0.1m$) were presented in order to characterise the wake of a MCEC. Sun et al. (2008) also published some wake measurements taken behind a porous disk in a larger scale experiment ($0.25m$ diameter). Whelan et al. (2009) completed work utilising porous disks, this work focused on the thrust observed with varying porous models porosity and geometry within a circulating water flume. Myers & Bahaj (2010*b*) disseminated some effects of bed roughness and rotor height placement of devices within the water column. Subsequent studies have quantified interaction effects between devices operating within small arrays (Myers & Bahaj (2012),Bahaj & Myers (2013),Xiao et al. (2013)). Some boundary interaction effects on wake response have been investigated by Giles et al. (2011) and the effect of array placement within split tidal channels has been investigated by Daly et al. (2011) using porous fences (rectangular porous sheets as opposed to circular disks) as a representation of multiple-device arrays.

Upon reviewing the literature there appears to be some disagreement between authors as to whether the use of porous disk models are acceptable in the small scale investigation of MCECs. Tedds et al. (2013) present experimental wake results from a rotating MCEC turbine model and show disagreement with wake measurements presented by Harrison et al. (2010) behind a porous disk. A large discrepancy is seen between the two types of devices. The porous disk velocity deficit values are greater than those measured for the turbine at all downstream points; the same is observed for the turbulent kinetic energy measurements. Tedds et al. (2013) attribute these changes to the addition of swirl within the turbine wake and states that porous disks are not a good representation of a turbine. Other differences are however present between the two experiment types compared: blockage ratio, channel aspect ratio, ambient turbulence levels, turbulence structure, Froude number (≈ 0.29 versus ≈ 0.17) and turbine/disk support structure are all different in the cases compared. Hence the differences in results cannot be attributed

solely to the lack of swirl present in the disk case, or indeed to the difference in device type. Authors investigating MCEC operation with porous disks (such as Harrison et al. (2010) and Myers & Bahaj (2010*b*)) discuss the differences expected in each type of device wake and justify that the use of such models is plausible due to the differences in structure being associated with phenomena within the near wake only. These arguments are the same originally given by Sforza et al. (1981), for justification of wind tunnel studies of small scale porous disk models, who argue that although a porous disk model does not accurately replicate all aspects of a rotating device model it can be used to "reveal important features of the flow pertinent to practical situations." Clearly these statements do not fully justify the use of porous disks as MCEC models and further information/investigation is required in order to ascertain the effects of these differences in model type on the results of experimental studies. This information would allow better interpretation of experimental results when using this method.

More detailed studies in wind energy research have compared the wake of a rotating model with that of a porous disk model. Builtjes (1978) showed that centreline (directly downstream from the device hub) velocity deficit within each device wake decayed at a similar rate. More recent work by Aubrun et al. (2013) investigated similar parameters looking at more detailed velocity deficit and turbulent flow characteristics within the wakes. The wake velocity deficit and turbulence intensity values presented for various lateral and downstream positions showed that differences were present close to the device (at 0.5 diameters (D) downstream) but agreed very closely by 3D downstream. Velocity deficit values were almost identical at this distance downstream at all lateral positions. Aubrun et al. (2013) showed that the rotational momentum and tip vortices generated by the spinning rotor were not detectable at a distance of 3D downstream. Aubrun et al. (2013) also postulates that wake diffusion is dependent on the boundary layer conditions and hence conducts two experimental investigations under different conditions to test this hypothesis (both conditions, however, show similar rates of diffusion). Presumably a similar study is required in a MCEC environment in order to ascertain if the the boundary layer interaction or constrained nature of tidal flows will affect the replication of MCEC wakes with porous disks. Other than the study discussed previously (Tedds et al. 2013) to date Bahaj & Myers (2013) are the only authors to have completed a basic comparison between a rotating MCEC and porous disk. Bahaj & Myers (2013) compares the turbine model described by Myers & Bahaj (2009) with a porous disk operating in a smaller facility with scaled channel dimensions and Froude number similitude. Some wake measurements and thrust values were compared between the two device types. Velocity deficit values directly behind the hub (at various downstream distances) and at varying lateral positions (at 7D and 10D downstream) are compared. Results show some values of similar magnitude when comparing the two device types. Greater discrepancies are observed when comparing closer behind each of the devices however wake velocity deficit values are seen to agree more closely with increasing downstream distance. With

a lack of more detailed wake data (and no comparison of the ambient turbulence characteristics of each facility) it is difficult to comment in detail on the differences between each model type and the suitability of porous disks for the replication of larger scale MCEC devices/models.

Clearly porous disks offer a desirable form of testing due to the simplicity of method and the reduction in facility size required. However there currently appears to be confusion over the suitability of the method and the conditions in which porous disks may be used to investigate practical situations with confidence. Further work is required in order to ascertain the suitability of the method for representing MCEC devices. There is a current lack of information surrounding some keys points:

- Understanding if wake profiles and wake expansion behind porous disk models are similar to those of rotating model MCEC devices operating in water channels.
- Understanding if differences in turbulence properties within the wake of each model type are similar, and what effect any differences may have on the far-wake development.
- Understanding the difference the lack of wake rotation will have on wake development.
- Understanding the differences in wake characteristics between different scales of rotating model turbines, and porous disk models.

Understanding the differences in these parameters will allow assessment of the limitations of porous disk models and their use in small-scale MCEC laboratory testing. It will allow the wider research community to be able to interpret and use data from such experiments to inform full scale MCEC design more clearly.

2.1.4 Summary

This section has provided a review of the current literature surrounding the wake structure of MCEC devices and smaller scale MCEC laboratory models. A summary of findings are presented here:

- The detailed wake structures of horizontal wind turbines and MCEC devices are outlined.
- Turbulence levels (turbulence intensity and lengthscale) in the ambient flow field into which a MCEC device is placed have been shown to have significant impact on the device performance and wake structure and dissipation.

- Porous disk models have been used in small-scale laboratory studies in both wind and MCEC applications. In MCEC applications they have been used to investigate the changes in wake propagation due to: device positioning within channels, the effects of bed roughness, the effect of array placement in split channels, interaction with vertical flow constraints and device spacing within multiple device arrays.
- The wakes of porous disks are known to be different to that of rotating turbine models. The differences are thought to be mainly contained within the near wake region. However to date no detailed comparative studies between the two model types has been conducted for MCEC applications.

2.2 Blockage

2.2.1 Introduction

Blockage is a term commonly used to refer to the effect of interaction between an object and the boundaries of the flow into which it is placed. Glauert (1947) observed that propeller thrust could increase in wind tunnel flows when this effect was increased; namely in flows where the ratio of device cross-sectional area to total flow domain cross-sectional area was greater. Maskell (1965) similarly observed that bluff bodies operating in wind tunnels could see a drag coefficient increase based on this area ratio. These increases in thrust or drag are caused by the constraint placed on the flow by solid boundaries. As fluid approaches a turbine device/airscrew the presence of boundaries does not allow diversion of the fluid around the object as freely as in an unbounded situation. A greater amount of fluid is therefore forced through the device, causing larger thrust or drag values (and normalised thrust or drag values). MCECs will observe similar effects as outlined by Vennell (2013). MCECs will be constrained by the presence of solid channel floor and walls as well as a free surface (or pressure) boundary. In an experimental study of a model MCEC device by Bahaj, Molland, Chaplin & Batten (2007) similar increases were observed in measured device performance (thrust and power coefficients); in this case a correction was applied to the experimental data in order show equivalent data expected if the device operated in an 'unblocked' case. Other authors such as Buckland et al. (2013) have applied different corrections based on work by Whelan et al. (2009). There seems to be no universally accepted method in the use of blockage corrections at present.

In this work area blockage ratio will refer to the ratio of device area to channel area, defined as:

$$B = \frac{A}{hw}. \tag{2.1}$$

Where A is device area, h is channel depth and w is channel width. A is taken to be $\pi d^2/4$ or $h_f w_f$ in the case of a circular device or fence respectively, where d is device diameter, h_f is fence height and w_f is fence width. Figure 2.3 illustrates the two cases.

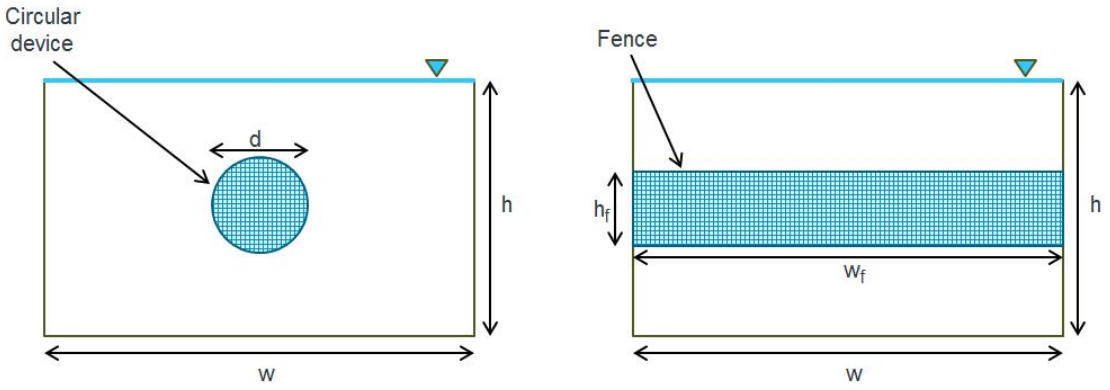

Figure 2.3: Channel blockage case of a circular device and a fence.

2.2.2 Correction of measured thrust and power

The main motivation for the blockage correction of thrust and power coefficient is to normalise experimental data so that comparisons can be made between experiments (and devices). However, it would be also be useful if such a model could be used to predict a thrust expected when a device is placed within a known flow geometry. If the correction used is a simple algebraic model such as those currently available (based on Linear Momentum Actuator Disk Theory) this could be combined with Blade Element Momemtum (BEM) code in order to incorporate flow boundary effects on MCEC loading and performance predictions. This would represent a model of low computational cost but of great use to the MCEC industry. Such a model could be used to inform initial MCEC deployments of expected loading and performance. Further guidance could also be given in array design in a similar manner to simple analytical models such as those described by Nishino & Willden (2012*b*) (introduced in Section 2.4).

Glauert (1947) presented an analytical treatment which allows the correction of thrust and power of an airscrew operating in an enclosed tunnel. This treatment supposes that an increase in fluid velocity incident to a device is seen when operating in a bounded tunnel case (by comparison to an unbounded case). The ratio of increased tunnel speed to free airspeed relates to the extent of the correction applied. In all 'high blockage' scenarios larger increases in tunnel speed are expected than at lower values of area blockage ratio.

Two distinct blockage corrections have been posed to correct MCEC model tests, those of Barnsley & Wellicome (1990) (who used a correction for wind tunnel tests, which has since been applied to a MCEC device by Bahaj, Molland, Chaplin & Batten (2007)) and Whelan et al. (2009). Both these methods are similar in nature to that proposed

by Glauert (1947) in that they apply continuity, momentum and Bernoulli equations to develop a correction. Authors of the MCEC corrections both agree that the corrections by Glauert (1947) are not suitable when considering negative thrust devices and hence changes are made to apply to a negative thrust machine (an energy extracting turbine as opposed to an airscrew). The correction used by Barnsley & Wellicome (1990) (referred to as B&W herein) assumes the presence of solid tunnel walls and no free surface (which would not be the case when operating in an open channel). In contrast the correction according to Whelan et al. (2009) allows for deformation of the free surface. These models are discussed in more detail in Chapter 3.

Some limitations of these corrections include:

- Generic assumptions associated with Linear Momentum Actuator Disk Theory, such as uniform flow across rotor plane and channel, and inviscid flow assumption.
- The B&W correction is unable to take into account kinematic changes within the channel (i.e. changes in Froude number).
- The B&W correction does not take into account surface deformation, which may be an important parameter in MCEC performance prediction and corrections.
- Both blockage corrections are one-dimensional, i.e. it is assumed that the bounding effect is equal around each side of the device. Therefore the corrections cannot take into account changes in channel geometry. There is currently no guidance in applying these models to cases where channel width and depth are unequal.

One of the main limitations of these corrections is the nature of them being only one-dimensional. Due to this the use of corrections in cases where the channel depth and width are unequal is currently uncertain. There is confusion of how to apply and when to apply the corrections. Table 2.2 summarises some of the experimental MCEC work that has been completed to date and indicates which correction has been applied to the results, if any. As can be seen there is confusion as to when (at what level of area blockage ratio) and which model may be applied in any given scenario. Galloway et al. (2014) suggest that a suitable model does not currently exist and hence chooses not to apply a correction to experimental or Blade Element Momentum Theory (BEMT) model.

Neither of the corrections have been validated with experimental rigour for use in MCEC applications. The model by Whelan et al. (2009) was partly validated (seen left Figure 2.4), however only for a single Froude number and with only limited data points (which are observed to contain significant scatter). The changes in surface height of the free surface boundary due to the presence of energy extraction within the flow are also predicted by the model. To date no comparisons have been made experimentally to this parameter. Shives (2011) notes this lack of experimental data with regard to wishing to

Table 2.2: Single device experimental studies: facility types, correction applied and blockage ratios.

Author	Facility	Correction?	B
McTavish et al. (2013)	Tow tank	B&W	0.25
Bahaj, Molland, Chaplin & Batten (2007)	Cavitation tunnel	B&W	0.17
Buckland et al. (2013)	Cavitation tunnel	Whelan	0.17
Tedds et al. (2013)	Open channel	-	0.16
Galloway et al. (2011)	Towing tank	B&W	0.075
Galloway et al. (2014)	Towing tank	-	0.075
Bahaj, Molland, Chaplin & Batten (2007)	Towing tank	B&W	0.075
Myers & Bahaj (2009)	Open channel	-	0.063
McTavish et al. (2013)	Tow tank	-	0.06
Doman et al. (2015)	Tow tank	-	0.045
Walker et al. (2014)	Tow tank	B&W	0.035
Maganga et al. (2010)	Open channel	-	0.035
Bahaj, Myers, Thomson & Jorge (2007)	Open channel	-	0.02

validate a numerical model. McTavish et al. (2013) are the only authors to date who have published experimental data at a variety of area blockage ratio values in order to ascertain if the B&W correction is suitable for MCEC applications. Results (seen right Figure 2.4) show corrected C_t values reduce, but do not return to the same value as would be expected in a successful correction. McTavish et al. (2013) conducted their work towing MCEC devices in an open channel, and although free surface disturbance was observed to be minimal this may have some impact on the performance values (which cannot taken into account by the B&W correction).

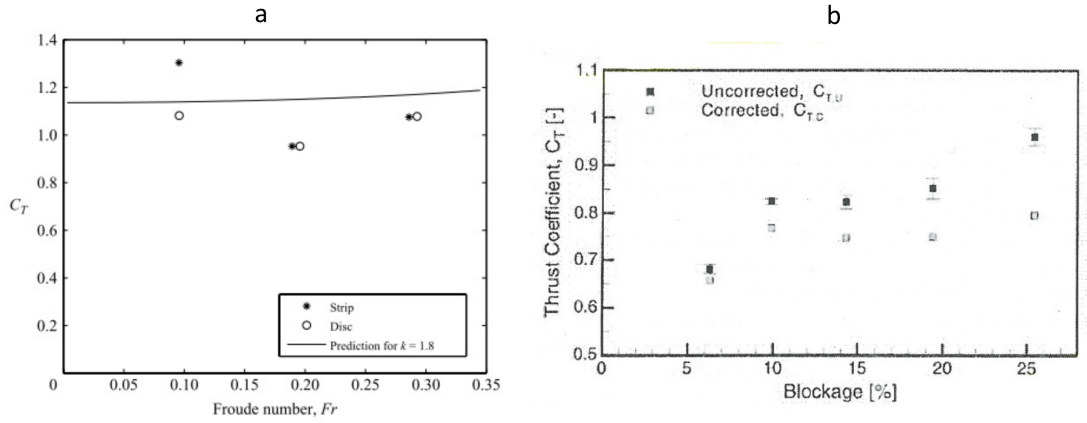

Figure 2.4: Existing experimental validations: (a) comparison of C_t measured experimentally to prediction in model presented by Whelan et al. (2009) and (b) comparison of C_t measured experimentally for varying area blockage ratio values with B&W correction applied (McTavish et al. 2013).

It is clear that more work is required to understand the current blockage models and how accurate they are able to correct/predict MCEC performance. Work is also needed to understand the accuracy of such models when applied to cases where channel depth and

width are not equal. Understanding these limits will aid MCEC experimental testing analysis and allow developers to more accurately predict device performance and loading in constrained marine environments.

2.2.3 Channel aspect ratio

Channel aspect ratio may be used to refer to the non-dimensional channel property of channel width to channel depth ratio. In this report all instances of aspect ratio will be reported by:

$$\Omega = \frac{w}{h}. \tag{2.2}$$

Where Ω is channel aspect ratio, w is channel width and h is channel depth. No experimental study of the effect of channel aspect ratio on the performance of a MCEC device has been completed to date. Nishino & Willden (2012*a*) used a Reynolds Averaged Navier Stokes (RANS) Computation Fluid Dynamics (CFD) model to investigate the effects of channel aspect ratio on turbine performance. The numerical model is highly idealised: no wall boundary layers are present, no free surface is modelled and varying levels of turbulence model are applied. The model is therefore validated against a 1-D Linear Momentum Actuator Disk Theory (LMADT) model (Garrett & Cummins 2007). Results which do not include a turbulent source at the device itself match closely with the LMADT model. The discrepancies between the models are put down to the effect of turbulent mixing within the numerical model (which cannot be accounted for in the LMADT model), which acts to increase thrust coefficient and power coefficient within the numerical model. Results show that increases in channel aspect ratio can alter the turbine performance (both thrust and power); for a constant axial induction factor increases in both thrust coefficient and power coefficient of $\approx 5\%$ are shown to occur at a fixed area blockage ratio when a device operates in channels which have $\Omega = 1$ and $\Omega = 0.25$; the larger values are observed in the latter case. The authors link these changes in performance to the anisotropic wakes observed downstream of the device when operating in a channel of $\Omega \neq 1$. The work concludes that the power coefficient and thrust coefficient values do not vary significantly with changes in channel aspect ratio.

Currently the area blockage ratio corrections previously discussed are applied without taking into account aspect ratio values associated with the domain; this is in conflict with the study of Nishino & Willden (2012*a*) discussed above. A detailed parametric study is required that fixes B and investigates changes in aspect ratio in a domain which has a deforming free surface. This will help ascertain the relationship between device performance and channel aspect ratio. Furthermore a study which incorporates a flow domain with a vertical velocity gradient and channel free surface will be able to give

further insight in MCEC operation as this will represent more realistic flow conditions into which full scale MCEC devices will be placed.

2.2.4 Variation in thrust with channel Froude number

At proposed full-scale MCEC installation sites a variation in flow speed and possibly channel depth will be expected over the duration of a tidal cycle. A MCEC device will therefore see changes in flow speed incident to its rotor and could operate in a variety of water depths.

Blackmore et al. (2014) shows experimentally in a circulating water channel that a circular porous disk has little change in normalised thrust coefficient over a range of Reynolds numbers. This is for for a 'low blockage' case where $B = 0.015$. Whelan et al. (2009) on the other hand presents an analytical model which shows that variation in channel flow velocity (Froude number changes at a fixed depth) will affect thrust coefficient and energy extraction from an open channel. The model also predicts increases in thrust coefficient and energy extraction values with increasing area blockage ratio values (i.e. reducing channel depth). As previously discussed and shown in Figure 2.4 the analytical model is compared with only six experimental (porous fence/disk) data points for validation and the experimental/analytical trends do not agree closely. An increase in thrust coefficient with channel velocity is predicted by the model, whereas the trend from the experimental work is unclear.

Figure 2.5 presents data from the studies currently introduced as well as data from McAdam et al. (2013) who conducted experimental testing of a cross-flow turbine. Each data set investigates changes in channel velocity (or Froude number) with fixed area blockage ratio for rotor and porous disk experiments. It shows that that higher blockage ratios generally lead to greater thrust coefficients (as would be expected). It also demonstrates that no experimental data set is currently available which clearly shows that increases in channel Froude number result in changes in thrust coefficient. Clarification is needed through further experimental work to ascertain if changes in channel Froude number effect device loading and energy extraction within an open channel flow. This could aid device developers in understanding how the performance of a device may be likely to vary over the duration of a tidal cycle at an offshore site. This will also allow comparison to the Whelan analytical model presented to ascertain if it behaves in a realistic manner.

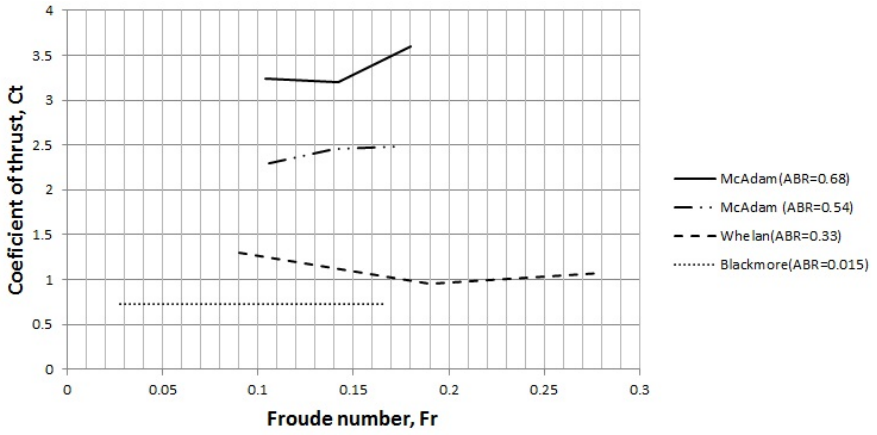

Figure 2.5: Change in thrust coefficient with variation in Froude number for fixed area blockage ratio.

2.2.5 Analytical models for performance prediction

Betz (1920) originally presented an analytical analysis of a wind turbine operating in an unbounded flow. The analysis combines energy, continuity and momentum equations to produce traditional 1-Dimensional Linear Momentum Actuator Disk Theory (LMADT). Garrett & Cummins (2007) furthered the analysis by investigating a turbine operating in confined flow (solid walls) but including analysis of the bypass flow region (flow that passes between the device and flow boundaries). This alters the performance prediction for devices that operate in bounded conditions, with possible greater thrust coefficient and power coefficient values obtained in these cases of greater blockage. Whelan et al. (2009) also completed a 1-Dimensional LMADT analysis which included effects of changes in free surface (in response to energy extraction from an open channel) and Froude number on MCEC performance. This model is the basis of the blockage correction discussed in Section 2.2.2. Each of these models are examined in more detail in Chapter 3.

These models provide a prediction of device performance in constrained flows which can be incorporated into Blade Element Momentum (BEM) codes. These models can be used for detailed loading calculations and cavitation prediction as presented by Galloway et al. (2014) and Buckland et al. (2013). Such models offer significant benefits in terms of reduced computational resource, for MCEC performance prediction in confined flows, when compared with 3D CFD models.

There are a number of limitations of these LMADT models, which include:

- 1-Dimensional, hence no channel aspect ratio consideration or able to account for turbine-boundary proximity.
- Inviscid flow assumption (although energy loss due to wake mixing is accounted for).

- No energy loss due to channel friction.
- Betz's analysis was limited to not being applicable to higher axial induction factors. The limits of the solid walled, and free-surface deforming models are not presented in the literature.
- Uniform flow over rotor disk and channel (i.e. no velocity profile).

Nishino & Willden (2012*a*) compared the LMADT suggested by Garrett & Cummins (2007) to a RANS CFD numerical model. A good comparison was found where turbulence was not present, however with increased ambient turbulence or additional turbulence added at the rotor plane deviation from the LMADT was found.

Work needs to be completed to ascertain how capable these models are of MCEC performance prediction in realistic environments into which MCECs will be placed. This will allow discussion of their suitability for use as a first estimate of turbine performance. Much work has been published utilising simple LMADT to estimate and predict array performance/optimal array spacings. Examples including: Vennell (2010), Nishino & Willden (2012*b*), Nishino & Willden (2013) and Draper & Nishino (2013). The work proposed above will allow also the limitations of such models to be ascertained.

2.2.6 Summary

This section has provided a review of the current literature surrounding the performance and loading of MCEC devices operating in bounded flows. Key deficiencies were identified in present understanding.

- Current blockage correction models have not been validated and may be inadequate in the correction (or prediction) of MCEC device loading.
- Channel aspect ratio is a variable which can alter device performance. Data/current understanding of the affects and relative importance of this variable on device performance is not available.
- It is apparent that changes in channel Froude number (at fixed water depth) may affect MCEC device loading and performance when operating in bounded channel flows. Little data is currently available supporting this hypothesis.
- Analytical models for the prediction of device and array performance are currently available. However no comprehensive work has been completed in understanding the accuracy of the use of such models.

2.3 Turbine wakes and their propagation

2.3.1 Wake recovery and importance

The development and structures associated with a MCEC wake were described in detail in Section 2.1 for a generic turbine operating in unconfined flow. The 'recovery' of a turbine wake implies a return to original conditions; as such the recovery of a turbine wake could refer to the pressure, density (if there were any changes) and velocity recovery towards that of the ambient conditions (such that were present before a device was placed in the flow). In MCEC applications the working fluid is incompressible and hence no changes in density will occur. Pressure and velocity on the other hand will vary across the wake flow of a MCEC and in the fluid of the bypass flow surrounding it. It is most common to measure velocity values to ascertain the details of flow structure around MCEC devices. In recording velocity data it makes possible statistical analysis, which allows further understanding of the flow around MCEC devices.

In most cases in this document the description of 'wake recovery' will refer to the return of mean streamwise velocity values, towards that of ambient flow conditions (unless otherwise stated). In spite of this it is useful to note that other statistical measures of flows, such as turbulence intensity and shear stress, may also be presented in order to understand the flow characteristics at hand.

Knowing the downstream distance a turbine wake will take to recover allows decisions to be made regarding the placement of downstream devices, without said devices encountering the wake produced by the upstream placements. The interaction of devices in this way is referred to as 'shadowing' in wind farms. González-Longatt et al. (2012) cite the main effects of shadowing as:

- a reduction in wind speed which in turn reduces the energy production of the wind farm,
- an increase in the turbulence of the wind, potentially increasing the dynamic mechanical loading on downwind turbines.

Mycek et al. (2011) has confirmed through experimental investigation that MCEC devices operating in the shadow of others see reduced power production. A rotating turbine model was placed directly downstream of another similar model MCEC at a distance of 4 device diameters (D). Measurements showed significantly lower power production (a reduction of $\approx 75\%$ than that of the upstream device) in the downstream device, with recovery of power production as the device was spaced at larger distances downstream. At a distance of 10D downstream the downstream device maximum power coefficient had returned to 80% of the upstream device. Wake measurements taken in the same work show that the turbulence intensity values into which the downstream device is placed

are greater than ambient, suggesting that increased dynamic mechanical loading will be present in the downstream turbine model. It hence appears that similar conclusions about device shadowing are applicable to MCECs as well as wind turbines.

Contrary to wind turbines MCECs will operate in bounded flows, there are hence other parameters which may affect wake development which are unique to MCEC operation. The literature review has already highlighted that each of the parameters below can have some effect on MCEC loading and performance. It stands to reason that wake propagation and a wake rate of recovery of MCEC devices may also vary depending on these parameters:

- ambient turbulence,
- channel geometry (e.g. channel cross section),
- boundary proximity (e.g. position of a MCEC within a channel),
- channel flow properties (e.g. Froude number).

The effects of ambient turbulence on wake development and propagation has been detailed in Section 2.1 previously. The latter three parameters are now discussed.

2.3.2 Channel geometry effects

Giles et al. (2011) has suggested changes in water depth can alter the wake development of a MCEC. Porous disks were used to represent a MCEC device and investigate wake changes experimentally with changes in water depth. Using a fixed device diameter, flow depth was reduced to produce device diameter/channel depth ratios within the range $0.05 - 0.66$. Channel width was $\geq 13D$ and so it is argued that no horizontal boundary interaction was present in these experiments. Froude number was kept constant in the experiments. Centreline velocity deficit values (those downstream of the device centre) are presented with a shortest downstream wake length (faster wake recovery) found at a device diameter/depth ratio of 0.25. The authors indicate this is an optimum rotor diameter/flow depth ratio for a marine devices to operate within in order to minimise the spacing required for devices within an array.

It is suggested that slower wake recovery in very deep cases is a result of limited local flow acceleration reducing wake mixing and hence wake recovery rate. Conversely slower wake recovery in very shallow cases is a result of vertical blockage preventing flow acceleration vertically around the disk, and hence wake/bypass flow mixing in the vertical plane. Hence it is suggested an optimum ratio is therefore present where fluid is sufficiently accelerated in the vertical plane to enhance mixing between the bypass and wake flows. This is shown within the experimental results to result in a faster rate of

wake recovery with downstream distance. It is possible that mixing between wake and bypass flows can occur at different rates in the vertical and horizontal planes, due to the presence of channel flow boundaries. This is something that has not been investigated experimentally in current literature to date.

Similar observations have been made numerically, however, by Nishino & Willden (2012*a*). Numerical RANS CFD model results have shown wakes to be symmetrical in cases where flow boundaries (induced by symmetry plane method) are equidistant in vertical and horizontal planes from an energy extracting device. This is in contrast to cases where distances between device and flow boundaries are not equal in vertical and horizontal planes (i.e. cases if channel aspect ratio $\neq 1$). Here asymmetric velocity profiles were observed within the wake in the vertical and horizontal planes. Flow acceleration between device and boundary (i.e. in the bypass region) and turbulent kinetic energy values in the wake were observed to be different in channels of different aspect ratio. Nishino & Willden (2012*a*) do not provide any more detailed explanation surrounding these differences.

An in depth experimental study has not been completed to date to investigate the wake development of MCEC devices in channels of varying depth and width. Such a study will develop overall understanding of wake development for individual devices in constrained flows and will aid in the understanding of how devices will behave in multiple device arrays. The results will aid MCEC array developers in the interpretation of the limited offshore measurement data obtained from prototype offshore installations more clearly and help advise developers how to space devices in order to avoid negative interaction between devices within a MCEC array.

2.3.3 Boundary proximity effects

Myers & Bahaj (2010*b*) present results from an experimental porous disk study, in which device proximity to the water surface and channel bed were investigated at a fixed water depth. It was shown that downstream wake propagation could change based on changes in the vertical positioning of the device in the water column. It is postulated in the study that varying proximity to boundaries introduced differences in the mass flow rate above and below the the rotor causing the wake to persist much further downstream than would occur when the device was placed at mid depth. In towing tank experiments thrust and power values have also been observed to change with vertical positioning of a rotating model turbine device by Bahaj, Molland, Chaplin & Batten (2007). Reductions in thrust and power coefficients were observed to be around 5% and $10 - 15\%$ respectively when the devices were moved, from being positioned in the centre of the channel cross section, towards the free surface. These studies indicate that turbine performance and wake development are likely to alter with vertical positioning. This will be to be considered when planning experimental work.

2.3.4 Channel flow properties

Flow velocity will inevitably vary in most tidal channels during flood and ebb tides. It is therefore useful to understand will see so it is important to understand how wakes will likely vary within a range of flow velocities. In the experimental porous disk study by Bahaj, Myers, Thomson & Jorge (2007) inflow velocity was varied to the same device showing that, once normalised to the upstream inflow velocity, wake recovery on the centreline (downstream behind the device hub) was independent of Froude number (at least within the range $Fr = 0.14 - 0.19$ investigated in the study). Results are seen in Figure 2.6.

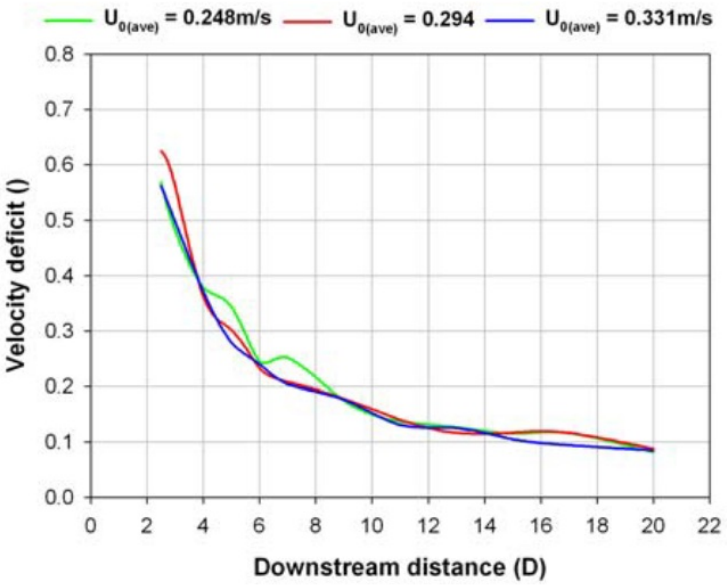

Figure 2.6: Change in downstream wake behind the centre of a porous disk with variation in Froude number for fixed depth and area blockage ratio (reproduced from: Bahaj, Myers, Thomson & Jorge (2007)).

The experiment was completed in a domain where area blockage ratio was equal to 0.019%. This represents a 'low blockage' case in which, as outlined in Section 2.2.4, the energy extracting device will see little change in thrust coefficient over a range of Froude numbers. It appears from these results that little changes are expected in the device wake either. However, as Section 2.2.4 highlighted, at greater area blockage ratio values changes in Froude number may affect thrust coefficient values (Section 2.2.4). Changes in thrust coefficient are likely to correspond with changes in the wake. No work currently exists to show this.

2.3.5 Wake edge measurement

Velocity data is often presented from downstream measurement points in order to characterise the wake recovery of MCEC devices. Data is often presented on the 'centreline'

(i.e. downstream of the hub/centre axis of a horizontal axis device) and also in a horizontal or vertical series of points at various downstream distances. These can give some indication of the rate of recovery of a device wake and the rate at which wake spreading is occurring (or width of the wake). Another useful method of presenting wake data is to characterise the wake edge. This can give a clearer indication of the vertical or horizontal rate of wake expansion. This is a useful presentation for two reasons: firstly it is an indication of the rate of wake expansion and can give an idea of how fast the wake is recovering, secondly the position of the wake edge is useful in guiding where subsequent devices may be placed in order to not experience adverse effects within an array.

Myers & Bahaj (2010*a*) discuss possible methods for defining the wake edge of a MCEC. Each method relies on calculating the distance from the device centreline to a defined limit of recovery to ambient flow conditions which marks the 'wake edge'. This is similar to defining the edge of a fluid boundary layer, where the edge is taken to be the distance where the mean flow velocity has reached 99% of the free-stream mean flow velocity. Myers & Bahaj (2010*a*) suggested it may be of use to relax the limit to that of 95% of the free-stream mean value, due to the nature of variability in the measurement of wake velocity.

In this work changes in the wake edge will be a useful parameter in characterising wake development and recovery during experimental investigation. Hence the above methods will be used in the presentation of wake data where appropriate. The quantification of the extents of the wakes, and how they change, will be useful when considering parameters used in wake models.

2.3.6 Semi-empirical wake models

Simple kinematic wake models, such as that presented by Jensen (1983), have often been used for modelling wakes in wind farm arrays. Such models are heavily simplified and treat the resulting wake behind a turbine as a turbulent wake or negative jet. An initial momentum deficit is assumed behind the device along with an angle of wake expansion. The areal spread of momentum can then be calculated as a function of downstream distance within the expanding wake. The corresponding velocity field can then also be calculated. Jensen (1983) showed that with calibration of the model to experimental field data it is possible to predict the centreline velocity deficit of a device accurately between 6-16D downstream. Palm et al. (2010) applied the model of Jensen to a MCEC device and compared results to RANS CFD model simulations, of a device operating within a closed channel, for validation. Palm et al. (2010) compared other single wake models, but concluded that the Jensen model was the most accurate. Although not disclosed similar calibration constants to those in wind applications were observed by Palm et al. (2010).

Another simple wake model used to calculate the velocity and turbulence field behind a wind energy device was originally proposed by Ainslie (1988). This model is based on a simplified eddy-viscosity model. It is assumed that beyond the first few diameters downstream the gradients of mean quantities in the axial direction are much smaller than those in the radial direction. This allows the Navier-Stokes equations to be replaced with the equivalent thin shear layer approximations. An eddy-viscosity term is introduced which combines the effects of ambient turbulence levels and the turbulence contained within the shear layer of the wake. Such models have been used extensively in the modelling of device power outputs within wind farms (Garrad Hassan and Partners Ltd. 2009). Myers et al. (2008) used the same model for a MCEC application, applying the model to experimental results from a porous disk.

The models described above are computationally simple and so offer the potential to model the flow field of a wind or MCEC device, in a simplified manner, at reduced computational cost. As previously discussed little experimental work has been conduced to date looking at the detailed effects of blockage on the wake development of MCEC devices in constrained flow fields. Such investigations could also inform the empirical assumptions/constants behind such wake models described here and hence allow them to be applied to MCEC devices operating in bounded flows more accurately.

2.3.7 Summary

Review of the present literature surrounding MCEC wake development and dissipation has found:

- Understanding and predicting wake development and dissipation is important due to the impact of reduced performance and increased loading possible when operating MCECs in arrays.
- Channel geometry into which MCEC devices are placed has the potential to significantly alter wake development and dissipation. Some studies have been completed observing these effects but full understanding of the channel geometry and the mechanisms that result in these changes are still not fully understood.
- Placement of a MCEC at different locations within a channel cross section can lead to variations in wake development.
- After the normalisation of data, wake changes have not been observed to occur with changes in channel flow speed (for low blockage cases). However no data is currently available characterising this phenomena in higher blockage cases.
- It appears, due to the similar parameters discussed in this section and the previous Section 2.2 that changes in device performance/loading are closely linked with

that of wake development and dissipation. Understanding these links could be of importance in order to inform MCEC array developers of the possible impacts of array layout decisions.

- Semi-empirical wake models require calibrated values for accurate wake modelling. Whilst such values have been studied extensively for wind energy applications, only limited studies have been published for tidal energy applications. The effects of bounded flows on the calibration parameters of such models is currently unknown.

2.4 Arrays and device interaction

2.4.1 Importance of study

In order to generate useful amounts of energy (relative to the electricity needs of the UK) devices will be installed in multiples in a similar manner to wind farms/arrays. MCEC arrays are currently in the planning and design stages, as outlined in Section 1.3.1. When under design decisions need to be made as to the spacing of MCEC devices within these arrays. The effect of shadowing on wind turbine performance within an array of devices was described earlier in Section 2.3. It was shown that MCEC devices suffer similar effects of reduced performance when operating within the wake of upstream devices. It is therefore crucial to understand how the spacing of devices can impact on wake development and wake dissipation of MCEC devices in order to determine the downstream spacing within an array. Furthermore the performance of MCEC models operating at the same downstream position relative to the oncoming flow (i.e. alongside each other) has also been shown to vary based on device lateral separation (Myers & Bahaj 2012). With both of these factors contributing to the overall performance of a MCEC array it is crucial that a holistic study of device separation is completed in order to better advise developers in the best strategy for maximum power output and reduced structural loading in array installations.

Barthelmie et al. (2010) presents data from existing offshore wind farms which shows the reduction in performance due to shadowing within arrays. For two offshore wind farms measurements showed power reduction in the second row of devices of more than 37% in some cases (for downstream row spacings of 7D and 10.5D). The power loss was also observed to reduce with changes in wind direction. In contrary to current wind energy practices there is a new opportunity during MCEC device installation to ensure minimal negative device interaction within arrays at some sites. This due to the predictability in the direction of tidal flows, in contrast to that of the multi-directionality of the wind resource available to wind farms. For any given tidal site it is possible to measure and predict the expected flow speeds and direction of a flow for years in advance. Therefore

if the device interaction is fully understood then it may be possible plan MCEC arrays with minimal device interaction.

The recently published EquiMar protocols for the testing and evaluation of marine energy extraction devices (Ingram et al. 2011) give very basic guidance to array developers deployment of multi-megawatt device arrays . Figure 2.7 shows how the protocols suggest 'first-generation' arrays may be spaced. It shows a potential future array which highlights the potential for negative device interaction. The protocols suggest in a first generation array it is likely that turbines would only be placed in either a single or dual row arrangement separated by distances 'A', or both 'A' and 'B' respectively. It is suggested both of these geometries need to be carefully planned if the devices downstream at 'B' are to avoid interaction with the highly turbulent wakes of the upstream MCEC devices. It is further suggested that second generation arrays are likely to include additional rows, which are likely to find it unavoidable to operate in the wake flow emanating from upstream devices. This argument is based on the fact distance 'C' will be small in comparison to the distance taken for the upstream wakes to re-energise toward that of the ambient flow conditions. No information is given for the likely spacing required in any of these cases whilst this is one of the leading documents currently in existence to advise developers. Clearly more detailed and quantitative information is required in order to aid in providing guidance to MCEC developers. Some studies concerning MCEC device interaction (in terms of performance and wake development) have been completed and are now discussed.

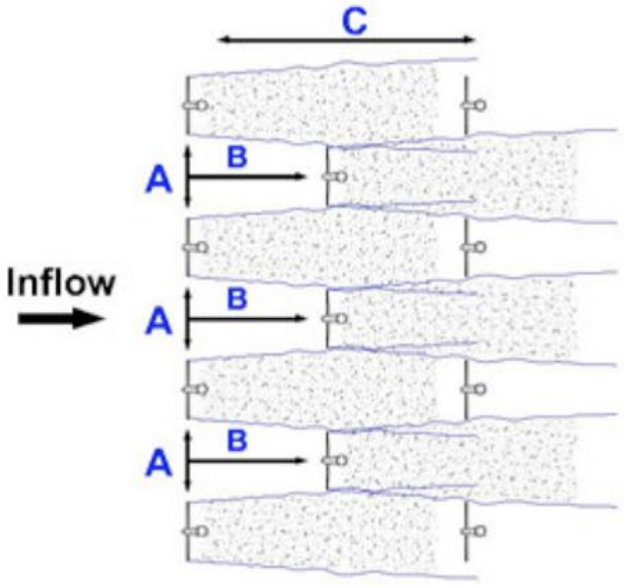

Figure 2.7: Suggested spacing of MCEC devices in EquiMar protocols. Reproduced from Ingram et al. (2011).

2.4.2 Experimental study

Myers & Bahaj (2012) investigated experimentally the changes in downstream wake propagation with device spacing using non-rotating porous disks. Disks were placed at separations (measured from the disk edges) of 0.5D, 1.0D and 1.5D. The smallest of these separations reflect that of the deployed Seagen device. Changes in thrust coefficient were observed only at the smallest spacing. In this case thrust coefficient was equal to 1.08, representing an increase from values of around 0.91 observed of a single disk and the wider separations investigated. Figure 2.8 shows the wake changes observed as a result of these lateral spacing changes. Reduced wake intensities are seen at larger separations, with closer separations yielding higher velocity deficit values which persist for longer distances downstream. Myers & Bahaj (2012) propose that this is due to the merging of the two device wakes which acts to slow the mixing between the wake and bypass flow regions and hence increase the downstream distance taken for recovery.

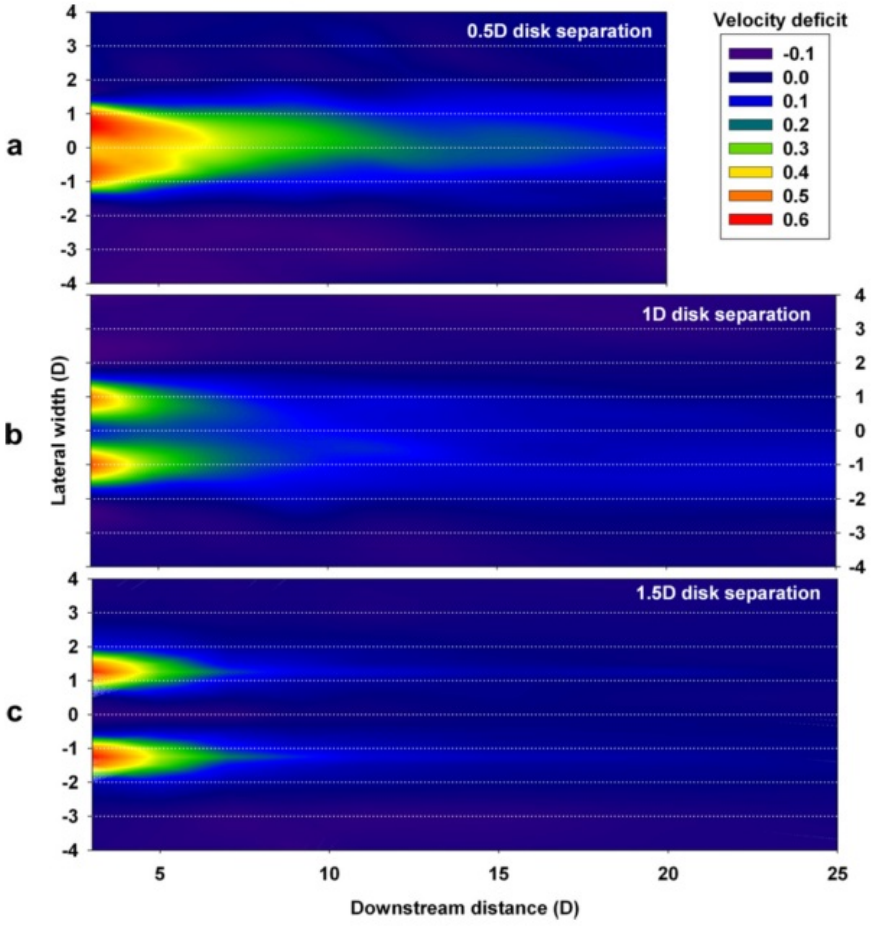

Figure 2.8: Experimental results showing changes in downstream wake propagation with changes in the lateral spacing of two MCEC porous disk model devices. Reproduced from Myers & Bahaj (2012)

Stallard et al. (2013) presents results from an experimental study of small-scale rotating MCEC models. Multiple devices were placed into a circulating water flume at separations 0.5D, 1.0D and 2.0D (measured from the device edges). Results were compared to a single similar device operating in isolation. Wake profiles presented show that device wakes again appear to behave in a similar manner to isolated device wakes at larger lateral spacings (in this case at around 2D of lateral separation). Wakes were also similarly observed to merge further downstream when placed at closer lateral separations (1.5D) in a similar manner to the observations of Myers & Bahaj (2012). No loading values are presented in this study and so it is not possible to compare the differences in loading as a function of device spacing.

When comparing the results of each study some discrepancies are present. Myers & Bahaj (2012) show that for 0.5D lateral separation the flow merges at less than 4D downstream whilst beyond 4D downstream the two wakes have merged into one Gaussian lateral profile. For similar lateral separations Stallard et al. (2013) shows again that at $< 4D$ downstream some wake merging is observed between the devices, however in contrast at 4D the wakes have not yet merged to become Gaussian (as in the previous study). At lateral separations of 1D Myers & Bahaj (2012) shows that the fluid directly between the two devices between 3-5D downstream to have a velocity deficit of around $12-18\%$. In similar setup and measurements Stallard et al. (2013) shows at distances of 2D and 4D downstream fluid velocity deficits of -10% and 0% respectively (indicating a flow acceleration between the disks at distances of $< 4D$ downstream. Similar disparity is found between the experiments at larger separations, with flow acceleration between the devices found to last upto 10D downstream in by Myers & Bahaj (2012) (1.5D separation) and not to last beyond 4D by Stallard et al. (2013) (2.0D separation).

Possible reasons for these differences include the difference in device type or differences in ambient flow turbulence. Small scale model turbine and porous disk wakes may develop in different ways due to differences in the near wake mixing in each case. It is currently not clear how this is likely to affect device wake interaction, as discussed in Section 2.1 (differences in the effects of ambient turbulent flow are also discussed in the same section). Another factor which may cause these differences is the value of device diameter/water depth ratio (Myers & Bahaj (2012) = 0.33, Stallard et al. (2013) = 0.6). Earlier sections have outlined how device thrust (Section 2.2) and wake behaviour (Section 2.3) can vary with changes in this parameter. At present with the differences in data presentation of the two studies it is difficult to isolate the possible changes (and causes) in device behaviour due to this parameter.

Myers & Bahaj (2012) discusses the possibility of exploiting the accelerated fluid between two laterally separated devices in order to generate more power within an array (i.e. a positive interaction effect). The positioning of a third device downstream in the region of accelerated fluid is proposed. It is proposed the increased kinetic energy in this accelerated flow region will lead to an increased energy extraction in the downstream

device (above its power extraction when operating in isolation). The setup is investigated experimentally with porous disks however thrust coefficient values are not presented, due to the difficulty in the normalisation requiring velocity values. Investigation of the flow field behind the three-disk array revealed increased velocity deficits which propagated to greater distances downstream. The reasons for this observation are put down to the lack of ambient flow entering the array, and hence the reduction in bypass flow and wake mixing.

Some effects of device spacing on wake development and device loading have been characterised in experimental studies to date. However the detailed changes in wake structure that occur with device proximity (such as: position of transition region, wake edge, differences in lateral and vertical wake planes and rate of wake recovery) has not been characterised as yet. Furthermore the significance of device spacing in varying degrees of bounded flow has yet to be investigated experimentally. Further experimental study, as well as providing useful insight in the understanding of the wake development in bounded flows, could be of importance in the use of semi-empirical wake models.

2.4.3 Semi-empirical farm wake models

Both of the models described in section 2.3.6 have been used for device performance modelling within wind farm models. The commercial WindFarmer software for example can implement either the Jensen or eddy-viscosity wake models (Garrad Hassan and Partners Ltd. 2009). Other existing wind farm software have used either of the wake models to implement wind farm performance calculations. Examples include, but not limited to, those described by Cleve et al. (2009) and Barthelmie et al. (2007). Similar models are of interest in MCEC applications due to the reduced computational cost in comparison to three-dimensional CFD simulations. Similar models have therefore been developed which incorporate these simple wake models into MCEC array design tools (Thomson et al. 2011).

As well as the empirical values discussed in Section 2.3.6 assumptions/methods must also be chosen around how the wakes interact within the farm, i.e. how expanding wakes are summated downstream to set the inflow parameters for downstream devices. Palm et al. (2011) applies a range of wake interaction methods for the Jenson model and compares wake results to those obtained from numerical and experimental investigations of multiple MCECs. The velocity field, on the centreline directly behind the device hub, is shown to be predicted to within 10% of the CFD validation cases however Palm et al. (2011) acknowledges that the CFD reference data are not fully validated.

Section 2.4.2 introduced the MCEC array experimental studies completed to date. As discussed in the section the experimental data sets that exist for MCEC arrays are limited and are not capable of providing detailed understanding of the wake changes

that occur with differing device spacing under varying bounded flow conditions. Further experimental investigation is needed in order to provide empirical data to inform the assumptions made in the farm wake models discussed above.

2.4.4 Analytical models

Nishino & Willden (2012*b*) present an adaptation of an existing LMADT model (Garrett & Cummins 2007) which estimates the performance predictions of MCEC arrays operating within an enclosed channel (as opposed to just a single device). The model allows parameters to be set which take into account arrays that block only part of a channel. A solution is obtained from the original model equations applied to both the array-scale and device-scale problems. The nature of these different scales are highlighted in the schematic in Figure 2.9. The two solutions are related by the simple realisation that the thrust acting on each individual device can be summed to give equal the total thrust acting on the array. As a result the equations can then be solved simultaneously to give individual and array performance values. The variables within the model include the individual device spacing and the overall array blockage within a channel. The model can therefore be used as a basic array design tool, informing a potential developer of the optimal spacings required for maximum power production from an array, given limitations on array size and bounding channel dimensions.

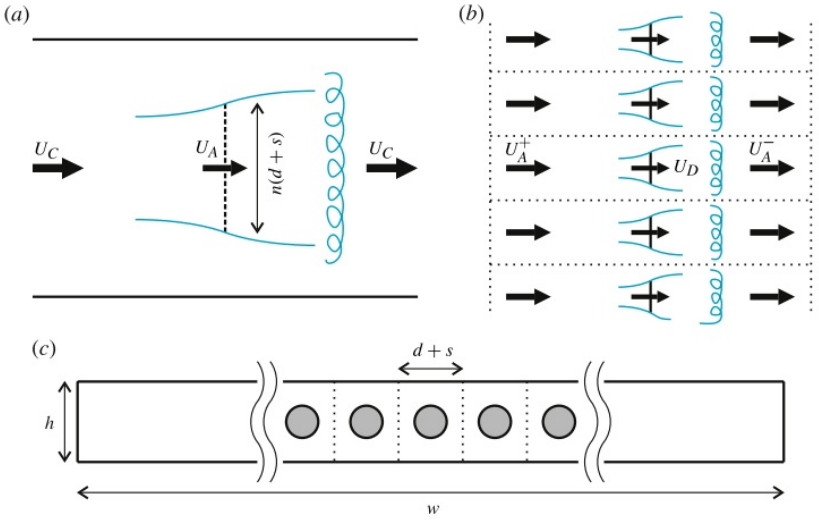

Figure 2.9: Schematic of the turbine array model presented by Nishino & Willden (2012*b*): (a) array-scale expansion and mixing, (b) device-scale flow expansion and mixing, (c) a cross-sectional view of the channel.

The models described here use the same assumptions as those detailed in Section 2.2.5. Therefore the same questions of suitability and accuracy of performance prediction are present in the use of these array models. A further assumption is that the array is large enough that the effect of any difference in individual device performance at the array

edges are insignificant. The optimisation of overall array performance in these models involves the spacing of both the devices within an array and the size of the array within a channel. Due to the one-dimensional nature of the model the aspect ratio of the channel in which individual devices within the array operate cannot be taken into account (aspect ratio has been discussed as a possible parameter which may alter device performance in Section 2.2.3). Similar assumptions are present within the model at the array-scale as well as device-scale and hence the accuracy of the array performance prediction will be similarly limited. Draper & Nishino (2013) have used similar LMADT models to model multiple rows and staggered row arrays of MCEC devices within a channel. Again similar limitations are expected to apply.

The investigation and validation of the single device LMADT models (described in Section 2.2.5) will allow the models presented here to be validated to some degree. This will highlight if these can be used to predict array performance and optimal device spacing with accuracy.

2.4.5 Summary

This section has presented a review of the current literature surrounding the deployment of MCEC arrays. The key findings are:

- Little information is currently available to advise developers on the deployment of multiple devices in arrays. Due to the predictability in direction of flow at potential tidal sites it may be possible to design arrays to both minimise negative interaction effects and increase power production through positive interaction.
- Performance, loading and wake development can be influenced by the lateral spacing of MCECs in arrays. The studies to date do not fully agree and are not detailed enough to provide a holistic understanding of the performance and wake development of MCECs operating in different flow geometries (such as different water depth).
- Current analytical models for array performance utilise the same LMADT, which is limited as described in the previous Section 2.2. The accuracy of array performance prediction and optimisation using these models is therefore limited in similar ways to LMADT applied to a single device.
- Semi-empirical wake models require empirical calibration for use within farm models. Experimental data to inform such calibration is currently limited for MCEC devices operating in confined flow domains. Further experimental data sets are required to further understand the relationship between device spacing within farms and flow boundary interaction.

Chapter 3

Theory

3.1 Scaling

3.1.1 Scale models

It is common in the field of fluid study to investigate problems at smaller scale in order to inform the development of larger projects. Such testing usually involves the use of smaller models which are inherently cheaper to develop. Although there is an additional cost in developing and using such models the knowledge gained often outweighs the additional cost, and in some cases can save costly choices in the design of the full scale prototype.

A full-scale prototype and smaller-scale model are two similar systems of different sizes. Models cannot give a complete solution to the problem at hand, but can be used in the investigation of certain parameters to help understand complex natural behaviour and inform full-scale design decisions. Three types of similarity are required in order to ensure a model accurately represents a prototype and its behaviour. These three main similarities are: geometric, kinematic and dynamic.

Geometric similarity refers to the shape of a model in comparison to its prototype. All linear dimensions will scale by a fixed factor known as scale ratio, L_r:

$$L_r = \frac{L_m}{L_p}. \tag{3.1}$$

Here L_m and L_p are linear dimensions of the model and prototype respectively. For example a $1/70^{th}$ scale model ship will therefore have a length 70 times smaller than its prototype.

Kinematic similarity refers to the similarity of motion between a prototype and model. It requires that the shape of the steamlines for any two corresponding physical points,

and at any time, are the same in both the model and the prototype systems. If kinematic similarity is found between a model and a prototype then geometric similarity is assured.

Dynamic similarity refers to the similarity of forces between two kinematically similar systems, the two systems will therefore be geometrically similar. As forces are responsible for the acceleration, deceleration or maintaining of fluid velocity within a flow the overall action of the forces in the model must be the same as the prototype. As such two different types of forces will have the same ratio in each of the dynamically similar systems (prototype and model). As such the force ratio,

$$F_r = \frac{(F_I)_m}{(F_I)_p} = \frac{(F_g)_m}{(F_g)_p} = \frac{(F_\nu)_m}{(F_\nu)_p} = const, \tag{3.2}$$

where F_I, F_g and F_ν are inertial, gravitational and viscous forces respectively.

Models are subject to different forces according to the system being investigated. In the case of open channel flows gravity forces dominate. Other forces such as viscous forces and surface tension also exist in some such systems but their effect is quite minimal (Cruise et al. 2007). Dynamic similarity is possible by ensuring that the ratio of inertial and gravity forces are equal in prototype and model cases. A dimensionless parameter derived from the ratio of inertial to gravitational forces is Froude number:

$$Fr = \frac{u}{\sqrt{gh}}, \tag{3.3}$$

where u is fluid velocity, g is acceleration due to gravity and h is depth of channel.

Flow around submerged bodies is dominated by viscous forces. The ratio of inertial to viscous forces is given by the dimensionless parameter Reynolds number:

$$Re = \frac{\rho u L}{\mu}, \tag{3.4}$$

where ρ is fluid density, L is a characteristic length within the flow being studied and μ is dynamic viscosity.

In this work submerged bodies operating in open channel flows will be investigated, hence both the viscous and gravitational forces are important. For dynamic similarity between each sets of forces both Reynolds and Froude numbers must be equal at each experimental scale. Assuming the same working fluid at each experimental scale it is not possible to match both Reynolds and Froude number unless the models are of equal size. Hence in this work Froude number will be conserved between model scales with a resultant disparity in Reynolds number.

3.1.2 Rotor scaling and the use of porous disk models

As outlined above model testing inevitably involves some form of geometric, kinematic and dynamic scaling in order for replication in a laboratory setting. Froude scaling (a kinematic property) of a channel is imperative in order to prevent non-realistic free surface behaviour. However, scaling with Froude number similitude will always result in Reynolds number (dynamic) disparity between model and prototype. As a result of this operational problems can arise when scaling turbines down from prototype to model. Increased blade drag and reduction in lift at model scale result in a lower rotor torque and hence un-representative thrust and power coefficient. Inflow angles are altered along the blade length due to the changes in rotational speed, hence more aggressive twist along blade length is usually required in an effort to counteract this. This allows extension of the operational Tip Speed Ratio (TSR) region over which the turbine can operate without encountering stall. Increased chord length and thickness can also help prevent the onset of stall around the root section. Downscaling of turbine models can produce other practical problems un-associated with the hydrodynamic performance issues already described; blade flexing, higher relative drive train resistance and disproportionate component size can impact upon the model design.

The 1/20th-scale ($0.8m$ diameter) rotor tests described by Myers & Bahaj (2009) were large enough to enable use of standard industry blade profiles whilst maintaining representative C_t and C_p values (when compared to full-scale devices). However, further downscaling of model size can lead to similar problems as those mentioned above. Some of these are discussed by Whelan & Stallard (2011) in relation to the testing of 1/70th-scale rotors ($0.27m$ diameter) in a circulating flume facility by Stallard et al. (2011). Extensive modification of blade profile and geometry is likely to be needed at scales smaller than this in order to provide realistic thrust coefficient variation over a larger range of operational speeds. For the correct scaling of tip speeds an increase in rotational speed is required, thus significantly affecting the flow field produced. Sforza et al. (1981) suggest the effect of increased speed can introduce significant radial pressure gradients in the wake which prevents the development of an accurately scaled wake. Power coefficient values are seen to be reduced in smaller model testing when compared with the full-scale devices being modelled.

The use of porous disks in small-scale MCEC laboratory testing was introduced in Section 2.1.3. It is clear that the use of porous disks will not fully replicate all the features of a rotational turbine wake. Beside the absence of the azimuthal velocity component presently discussed, the temporal variations of vorticity within the turbine wake, such as those associated with the blade shed vortex sheets and tip vortices, will also not be present. The turbulent wake generated by a porous disk is likely to comprise of two main features. Larger vortices will be shed from the disk edges in the shear layer, whilst comparatively smaller structures associated with the orifices present will

be generated over the whole disk. Both of these features (although turbulent and hence intermittent) do not have a temporal and spatial periodicity as in the case of a turbine with a discrete number of rotating blades (described by Vermeer et al. (2003)).

The reader will distinguish from Section 2.1 that these differences in wake structure are solely associated with the near wake of a turbine. Although the initial wake clearly has some part to play in overall wake evolution, it has been suggested by Sforza et al. (1981) that these areas in which replication differ in the near wake are not necessarily the fundamental drivers responsible for wake formation and recovery in the far wake. Furthermore as it is expected that the downstream spacing of MCECs deployed within an array will place devices in the far wake region, where the inflow to a device is similar to that for upstream MCECs (Mortimer 2010), the replication of near wake conditions may not be of primary concern when modelling MCEC arrays at small-scale. Studies do not currently exist which compare in detail the far wake regions of rotating model MCECS with those of porous disk models.

The lack of rotation within a model wake (or indeed the increased rotational speed of small turbine models) may lead to a difference in measured thrust coefficient compared to that of full-scale MCEC devices. An increase in azimuthal momentum associated with wake swirl will lead to a corresponding increase in momentum change over the device (and hence a drop in pressure over the rotor/disk), resulting in differences in thrust coefficient between model scales. Sforza et al. (1981) suggest that correct scaling of tip speeds (in rotating model devices) require an increase in rotor rotational speed in smaller models. It is suggested that the effect of this increase can introduce significant radial pressure gradients in the wake which prevents the development of an accurately scaled wake. Further study is required in order to ascertain the effects of differences in both the scale of rotating model and the type of model (i.e. rotating model or porous disk) on wake structure.

3.1.3 Design of porous disk models

Myers & Bahaj (2010*b*) showed the increase in porous disk model thrust coefficient (by varying porosity) results in a wake velocity reduction close behind the disk. This follows expected turbine behaviour as a larger pressure drop (and hence disk thrust) would cause a larger rate of change of momentum across the disk and hence lower flow velocity through the disk. Disks of varying porosity may therefore be used to simulate different parts of MCEC operational states. An example MCEC device performance over a range of TSR values is given in Figure 3.1. By choosing correct disk porosity values small-scale porous disks may be used to simulate a turbine operating at any TSR.

It may be possible to predict analytically the porosity required to give certain C_t values in order to plan experiments. Whelan et al. (2009) has suggested an analytical method

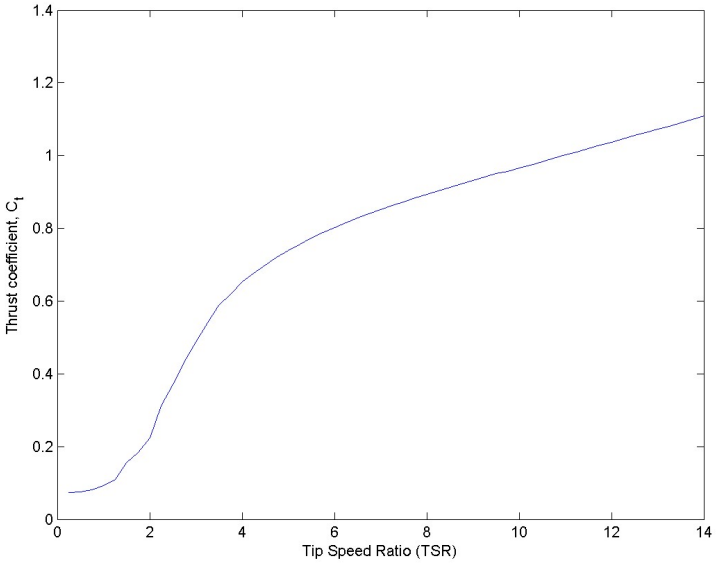

Figure 3.1: A typical TSR curve for a MCEC device taken from numerical BEM code for performance prediction.

for this based on work by Taylor (1963). The thrust coefficient of a porous plate was found by Taylor to be related by:

$$C_t = \frac{k}{(1 + \frac{1}{4}k)^2}, \tag{3.5}$$

where k, resistance coefficient, can be experimentally determined. Koo & James (1973) suggested a new model for the relationship:

$$C_t = \frac{k}{(1 + \frac{1}{2}\Upsilon k)^2}, \tag{3.6}$$

where Υ is a source constant; which can be determined from the equation:

$$k = \frac{2\Upsilon k + (\Upsilon k)^2}{(1 + \Upsilon k)^2}(1 + \frac{\Upsilon k}{2}(1 + \Gamma))^2, \tag{3.7}$$

where Γ is the height of a screen as a proportion of the open channel depth. In this work Γ is assumed to be zero as analysis is confined to an unbounded flow. Figure 3.2 shows the thrust coefficient variation over a range of resistance coefficient values for both of the models. The model by Taylor (1963) shows a reduction in thrust coefficient at values of $k > 4$, which is not to be expected in physical models (indeed Taylor states that his model is only valid at low values of k). Koo & James (1973) have shown Equation 3.6 has a good fit with experimental data of Taylor (1963).

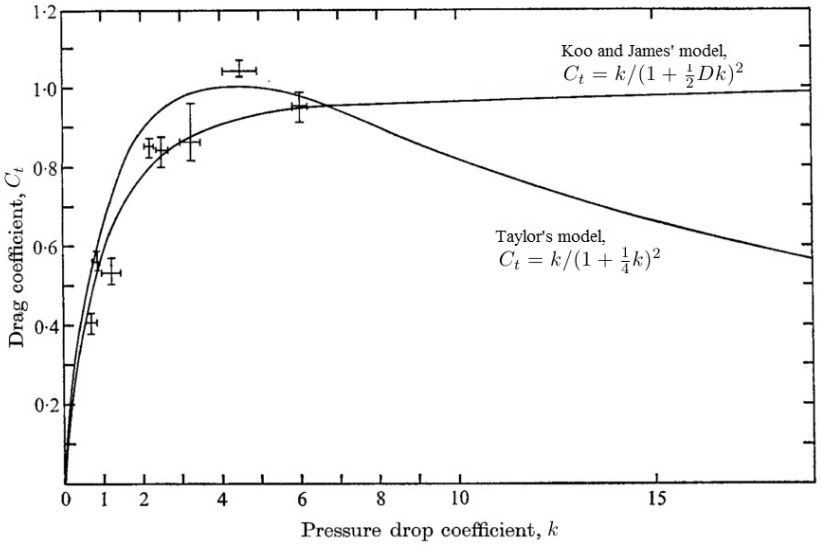

Figure 3.2: Predictions of thrust coefficient, from the models of Taylor (1963) and Koo & James (1973), over a range of resistance coefficient values (adapted from Koo & James (1973).

In order to relate the models above to physical porous disks it is convenient to use a relationship between k and geometric porosity, Θ. Geometric porosity is defined as the ratio of open area and total area of a disk or plate. The relationship between Θ and k is dependent on the nature of the holes or pores that the disk is made up of Roberts (1980), for example sharp edged or smooth edged pores. Whelan et al. (2009) uses the relationship proposed by Taylor (1963):

$$\Theta = \sqrt{\frac{1}{1+k}}, \tag{3.8}$$

in small-scale MCEC porous fence experiments. Roberts (1980) also used the relationship:

$$\Theta = \sqrt{\frac{0.58}{1+k}}, \tag{3.9}$$

when investigating the drag on circular porous disks. It should be noted that these methods are only applicable in the prediction of thrust coefficient values for porous plates in unbounded flows. Further work is required in order to adapt this method for use in predicting thrust in open channels or other bounded flows.

3.2 Energy extraction from an open channel

Cruise et al. (2007) states that open channels are characterised by the presence of a free surface and, as such, are not completely enclosed by solid boundaries. It is only possible therefore for open channels to transfer fluid from one location to another under gravity

forces. For this reason open channel flow is also referred to as free-surface flow or gravity flow, due to the lack of need for an external force or head with which to drive the flow (as can be the case in enclosed pipe flows). Open channels must therefore ultimately move fluid down a gradient or slope or across a horizontal plane.

A steady uniform flow in an open channel is a result of dynamic equilibrium. Figure 3.3 depicts this. The water depth is constant throughout the channel length indicating that the hydrostatic forces are equal and opposite; the gravitational forces acting to move the fluid downhill are exactly countered by the resistance forces which act to slow down the flow. In this case the energy lost through the resistive forces are exactly equal to those gained through the change in vertical height (down the slope) through which the fluid moves. The specific energy of the channel therefore remains constant and so the bed slope, water surface and Total Energy Line (TEL) are all parallel to each other. In this case the channel depth is constant and known as the normal depth.

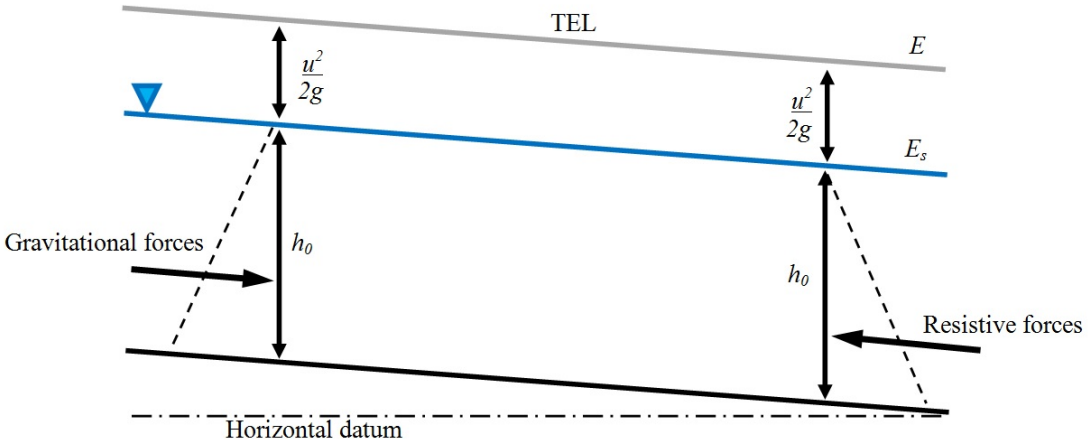

Figure 3.3: Steady, uniform flow in an open channel.

A steady non-uniform flow is a result of the non-equilibrium between gravitational and resistive forces acting on fluid within a channel. Figure 3.4 shows an example of this case. The disparity in force-equilibrium results in the acceleration of the fluid and hence a shallower flow within the channel (the resistive forces are now smaller than the gravitational forces acting on the fluid). Similarly if the resistive forces became larger than the gravitational forces (if the bed slope reduced) a deceleration of the fluid would occur and flow depth would increase. In these cases of non-uniform flow the slope of the channel bed, water surface and TEL line gradients are not the same. The above situations are referred to as gradually varied flow as the assumption is made that changes are small in comparison to the length over which the change occurs.

When analysing channel flows it is common practice for the measurement of energy to be expressed in head. Total energy is energy measured from a fixed datum height (for example, at or below bed level) and incorporates the kinetic energy and the potential

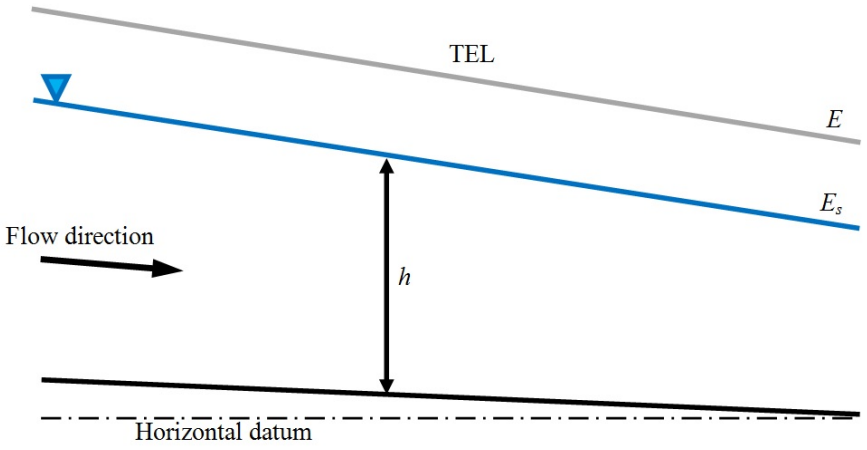

Figure 3.4: Steady, gradually varied flow in an open channel.

energy of the flow. The potential energy is made up of the depth of water within a channel and the vertical distance to the datum. Specific energy, E, may be used to represent the total energy in a channel flow however this uses the channel bed as the datum, hence E (measured in head) is made up of the kinetic energy and the water depth. The equation:

$$E = E_k + E_s = \frac{u^2}{2g} + h, \tag{3.10}$$

shows that specific energy is made up of the static energy, E_s, and kinetic energy E_k; where u is fluid velocity within the channel, g is acceleration due to gravity and h is the channel depth. Specific energy diagrams can be used to represent graphically the changes in specific energy with depth of a channel flow. A generic example is given in Figure 3.5. Static energy is seen to vary linearly with the depth of flow however kinetic energy varies non-linearly with flow depth. As depth reduces the kinetic energy increases. This is consistent with the continuity relationship; if a flow depth reduces (with no change in channel geometry or slope) flow velocity will increase resulting in a higher kinetic energy in the flow. As the sum of static and kinetic energies is equal to the specific energy the sum of the horizontal values of the two dotted lines in the graph are used to give the specific energy curve.

It can be seen from the graph that for a given specific energy, e.g. E_1, there are two alternate depth of flow possible. Small depths such as h_1 are associated with shallow high velocity flows, whilst larger depths such as h_2 are associated with deeper, slower flows. These types of flow are known as supercritical and subcritical respectively. The flow regimes are separated at a point at which the channel has the lowest specific energy at a depth known as critical depth, h_C. The Froude number, Fr, of the channel was given in Equation 3.3 and can be used to determine what type of flow is present in a channel. Table 3.1 highlights the typical flow states associated with channel Froude number. The flows encountered by MCEC devices are expected to be in the sub-critical range. For

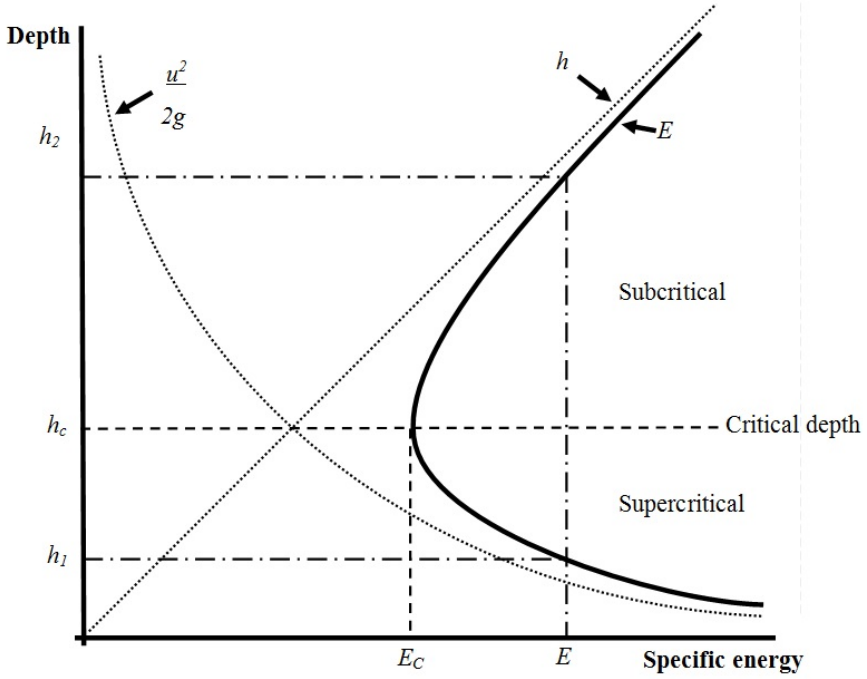

Figure 3.5: Generalised specific energy curve.

example velocity measurements at the offshore MCEC development site in the Sound of Islay, UK, (reported by Milne et al. (2013)) equate to a corresponding Froude number of 0.11. Some man made channels, such as that at the Den Oever test site, Netherlands, report maximum flows (Tidal Testing Centre 2013) with a corresponding Froude number of 0.7.

Table 3.1: Types of flow associated with channel flow Froude numbers.

Froude number value		Flow characteristics
$Fr < 1$	Subcritical	Slower, deeper flow
$Fr = 1$	Critical	-
$Fr > 1$	Supercritical	Faster, shallower flow

It should be noted that only some of the current MCEC sites, such as the man-made Den Oever testing site are akin to the gravity-driven flows discussed so far in this section. Most offshore MCEC sites are more complex, with varying bathymetry, and with flows driven by ever-varying water height differences over the course of a tidal cycle. However the theory introduced in this section will be useful in the planning of experiments to ensure that the scaled channels used are realistic, and exhibit realistic behaviour, during the testing of MCEC models. The simplified discussion is also relevant in informing the behaviour of channels in the presence of MCEC devices.

Figure 3.6 highlights the differences between an open channel and the same channel with a tidal turbine operating in it. In the simple open channel case (top) the flow depth is assumed to be normal depth; this implies that the frictional and gravitational forces

are equal and opposite, hence flow depth and specific energy remain constant down the channel length, l, with respect to the channel bed. Froude number is less than one, meaning that flow is in the subcritical region (as expected in natural tidal flows).

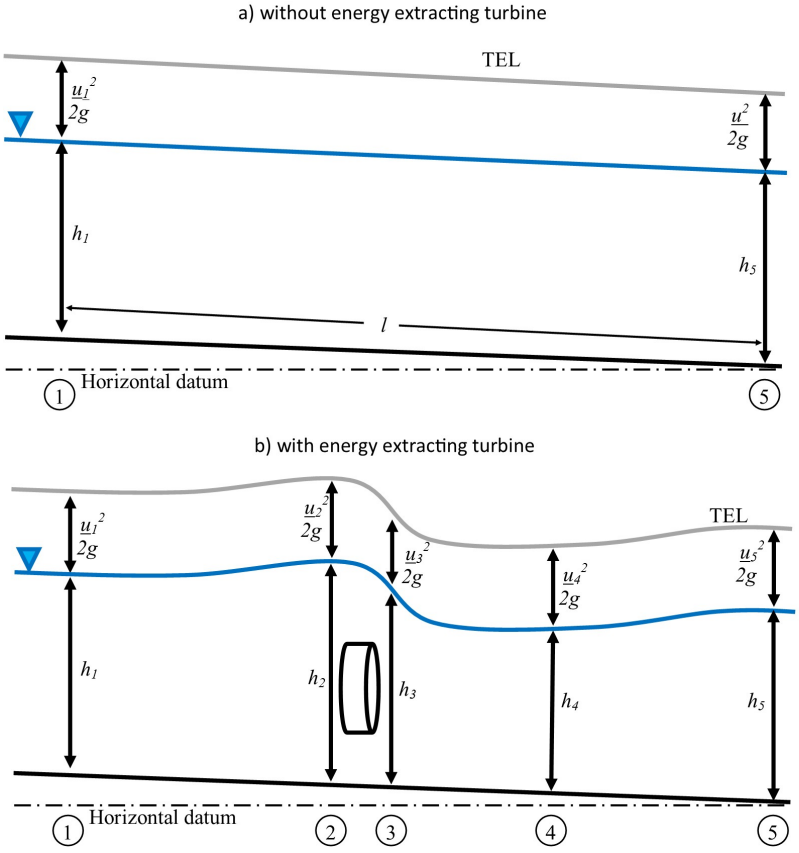

Figure 3.6: Channel energy in a channel with steady, uniform flow: (a) without and (b) with an energy extracting turbine.

In the energy extracting turbine case (bottom) changes in both flow depth and specific energy can be seen over the channel length. At station 1 (far upstream) and station 5 (far downstream) flow depth and specific energy are equal (and assumed to be correspond to normal depth as in the prior empty channel case); as fluid passes between these points, however, differences are seen. Around station 2 the turbine introduction leads to an initial imbalance in forces (as the resistive forces now comprise of bed friction as well as the force exerted on the fluid by the turbine). Non-steady flow (flow variant with time) is encountered initially as the channel flow decelerates locally and leads to an increase in depth and specific energy. This simple change in flow was highlighted earlier in Figure 3.5 where and increase in depth is observed in the subcritical region. Once the depth has increased sufficiently the problem has returned to steady state (at a higher specific energy); the resistive forces are now once again equal and opposite to the gravitational forces. As the flow continues through to station 3 energy is extracted by the turbine itself and so leads to a reduction in channel specific energy. Downstream of station 3 the resistance the turbine had exerted on the flow is removed and so the channel depth

reduces back to that of normal depth as it approaches station 5. At station 4 a reduction in depth can be observed which recovers back to that of original channel flow depth by station 5. This is a result of the lower pressure found in the wake of a turbine due to the energy extraction from the flow and the reduction in pressure of the bypass flow (flow which does not pass through the turbine) due to its acceleration around the device.

It is expected that turbines which are extracting greater levels of power will cause greater changes in depth (and total energy) within a channel as larger forces will be exerted on the channel fluid by such devices. Generally speaking larger area blockage ratios may lead to greater forces and hence energy extraction (as discussed in Section 2). This would result in larger disturbances in water surface occurring. As highlighted in the literature review section no detailed experimental work has been completed to date measuring the forces and water surface elevation changes of an energy extracting device operating within open channel flows.

3.3 Analytical modelling of an energy extracting turbine

The literature review highlighted that the existing LMADT analytical models for MCEC performance prediction have not been validated. The existing models are now introduced in order for comparison to experimental results. Three models are relevant to our present study (original authors in brackets):

- Traditional LMADT (Betz 1920),
- LMADT applied to a single device operating in a solid walled channel (Garrett & Cummins 2007),
- LMADT applied to open channel flow (Whelan et al. 2009).

Each model is summarised by Houlsby et al. (2008) with the same notation used for each case. This is now presented.

3.3.1 Linear Momentum Actuator Disk Theory (LMADT)

It is possible, even without a specific design, to begin a basic analysis of the aerodynamic/hydrodynamic behaviour of a turbine operating in a medium of infinite extent. The analysis presented here is based on the original work belonging to Betz (1920) however is in large reproduced from Houlsby et al. (2008). Figure 3.7 shows such a turbine and four stations are identified: (1) far upstream of the turbine, (2) immediately upstream of the turbine, (3) immediately downstream of the turbine and (4) sufficiently far downstream

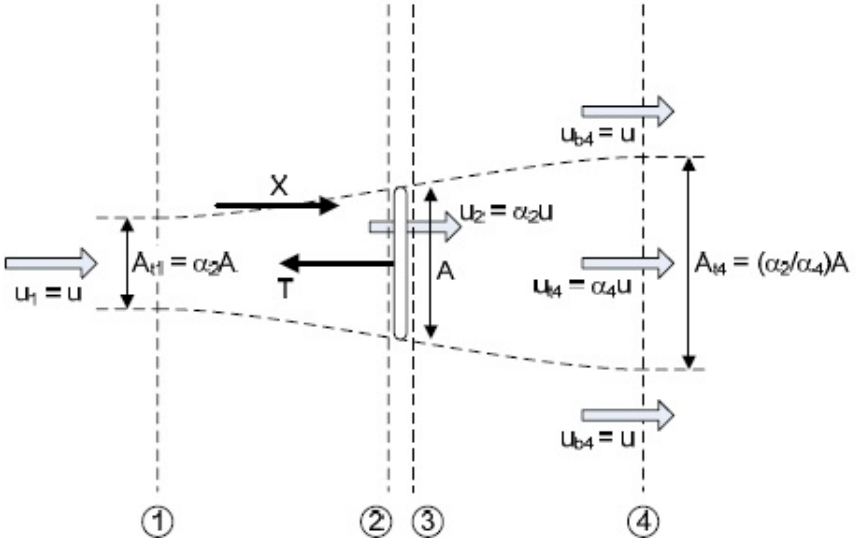

Figure 3.7: An energy extracting actuator disk operating in an infinite flow field(reproduced from Houlsby et al. (2008)).

Table 3.2: Continuity relationships for an energy extracting actuator disk operating in an infinite flow field(reproduced from Houlsby et al. (2008)).

Region		Station 1	Station 2	Station 3	Station 4
Turbine	Area	$A_{1t} = A\alpha_2$	$A_{2t} = A_{3t} = A$		$A_{4t} = A\frac{\alpha_2}{\alpha_4}$
	Velocity	$u_{1t} = u$	$u_{2t} = u_{3t} = u\alpha_2$		$u_{4t} = u\alpha_4$
	Volumetric flow	$q_{1t} = q_t = uA\alpha_2$	$q_{2t} = q_{3t} = uA\alpha_2$		$q_{4t} = uA\alpha_2$
	Pressure	$p_{1t} = p$	p_{2t}	p_{3t}	$p_{4t} = p$
By-pass	Velocity	$u_{1b} = u$			$u_{4b} = u$
	Pressure	$p_{1b} = p$			$p_{4b} = p$

from the turbine that the pressure can be treated as uniform (velocity is not). Numbered subscripts are used to distinguish between variables at each of these downstream locations whilst the subscripts t and b are used to distinguish between the flow passing through the turbine itself and the bypass flow respectively. The analysis is confined to the flow passing through the turbine in this case. The continuity relations for this case is presented in Table 3.2. Note: flow induction factors are denoted as α for both stations 2 and 4.

At station 1 the pressure and velocity are uniform so that $p_{1t} = p_{1b} = p$ and $u_{1t} = u_{1b} = u$. At the turbine the velocity has been reduced to $u_{2t} = u_{3t} = u\alpha_2$, whilst due to the expansion of the streamtube this slows further to $u_{4t} = u\alpha_4$. It is assumed at station 4 that pressure is once again homogeneous across the flow, hence $p_{4t} = p_{4b} = p$, whilst velcoity is not. Pressure is assumed to be p throughout the bypass region.

Applying Bernoulli from stations 1 to 2 and between stations 3 and 4 within the the turbine flow gives:

$$p + \frac{1}{2}\rho u^2 = p_{2t} + \frac{1}{2}\rho u^2 \alpha_2^2, \tag{3.11}$$

$$p_{3t} + \frac{1}{2}\rho u^2 \alpha_2^2 = p + \frac{1}{2}\rho u^2 \alpha_4^2, \tag{3.12}$$

where p is pressure, α_2 and α_2 are flow induction factor at stations 2 and 4 respectively.

Equilibrium across the turbine gives:

$$p_{2t} - p_{3t} = \frac{T}{A}, \tag{3.13}$$

where T is thrust acting on the device and A is device area. Upon combining the three above equations we obtain:

$$\frac{1}{2}\rho u^2 \left(1 - \alpha_4^2\right) = \frac{T}{A}. \tag{3.14}$$

The volumetric flow rate through the turbine is $q_t = vA\alpha_2$. Now considering the momentum equation between stations 1 and 4, if the net axial force on the surface of the streamtube is X above the ambient pressure then we obtain:

$$X - T = \rho q_t \left(u_{4t} - u_{1t}\right) = \rho v^2 A \alpha_2 \left(\alpha_4 - 1\right). \tag{3.15}$$

Assuming no net change of momentum in the bypass flow we may deduce that $X = 0$. Strictly this is untrue however the assumption is justifiable. We therefore obtain:

$$\frac{T}{A} = \rho u^2 \alpha_2 \left(1 - \alpha_4\right). \tag{3.16}$$

Equating 3.14 and 3.16 obtains $\alpha_2 = \left(1 + \alpha_4\right)/2$, which allows the flow to be expressed solely as a function of α_4. Writing an expression for the power absorbed by the turbine:

$$P = T\alpha_2 u = \frac{1}{2}\rho u^3 A \alpha_2 \left(1 - \alpha_4^2\right) = \frac{1}{2}\rho u^3 A 4 \alpha_2^2 \left(1 - \alpha_2\right) = \frac{1}{2}\rho u^3 A C_p, \tag{3.17}$$

where C_p is coefficient of power.

It is usual in this analysis to utilise a term a, axial induction factor, where α_2 = 1 - a. Hence from Equation 3.17:

$$C_p = 4\alpha_2^2 \left(1 - \alpha_2\right) = 4a \left(1 - a\right)^2. \tag{3.18}$$

A similar expression can be obtained for thrust on the turbine:

$$T = \frac{1}{2}\rho u^2 A\left(1-\alpha_4^2\right) = \frac{1}{2}\rho u^2 A 4\alpha_2\left(1-\alpha_2\right) = \frac{1}{2}\rho u^2 A C_t, \tag{3.19}$$

where C_t is coefficient of thrust. This can be re-arranged as below. Note that $a = (1-\alpha_2)$, where a is axial induction factor as used in common derivations of actuator disk theory such as Burton et al. (2001).

$$C_t = 4\alpha_2\left(1-\alpha_2\right) = 4a\left(1-a\right). \tag{3.20}$$

The non-dimensional parameters derived in Equations 3.18 and 3.20 are plotted with respect to axial induction factor in Figure 3.8. Differentiation of Equation 3.17 shows C_p is maximum when $\alpha_2 = 2/3$ ($a = 1/3$). Here $C_p = 16/27$, which is the Betz limit - the theoretical limit of power extraction efficiency.

It should be noted that beyond station 4 (far downstream) the wake will eventually mix with the bypass flow (engendering an additional energy loss), however this is not accounted for in the analysis. Limitations of this original Betz analysis include the assumption that only axial velocity components are significant -radial and azimuthal (swirl) velocity components are ignored. The infinite domain assumes that the velocity and pressure far downstream will be equal to that far upstream - and hence implying no energy has been extracted. This is of course not possible, however this issue can only be resolved upon considering a finite flow (considered in the following section).

In practice modification of the rotor thrust predicted by the momentum theory presented is required (it is counter intuitive when considering Figure 3.8 that C_t should reduce in more heavily loaded rotors where a ≥ 0.5). Although no doubt the theory presented overlooks an increased pressure difference due to rotational velocity components imparted to the flow (an increase in velocity can only be acompanied by pressure reduction), it is acknowledged by Burton et al. (2001) that this could only result in a small pressure change - and hence variation in thrust. Instead the modification of thrust is due to the flow separation at the edge of the disk (Burton et al. 2001). An empirical correction is usually applied to the turbine C_t in order to match experimental observations taken with wind turbine rotors. Burton et al. (2001) offers an empirical correction proposed by Glauert in which a value is chosen for $a = 1$, with a line fitted between this point and the theorectical curve (an example is given in Figure 3.9). Other authors such as Buhl (2005) have offered similar empirical corrections.

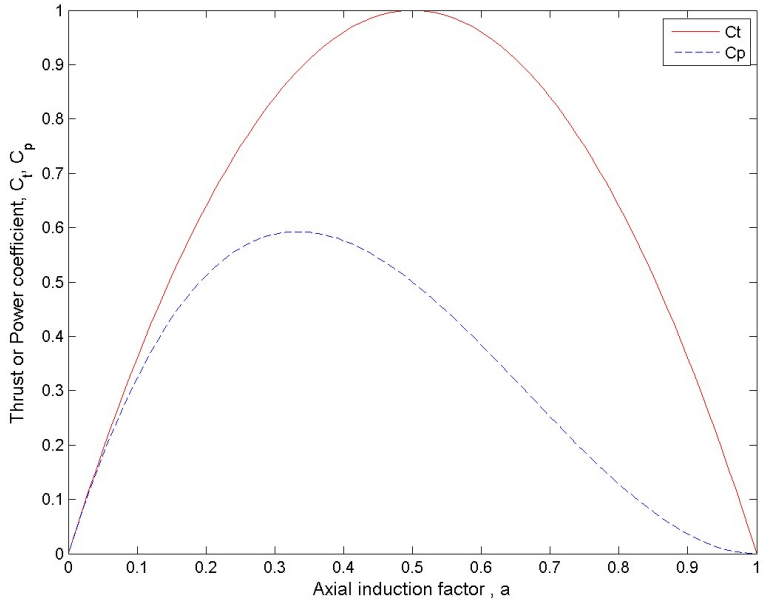

Figure 3.8: Variation in theoretical C_p and C_t with axial induction factor for a turbine operating in unbounded flow.

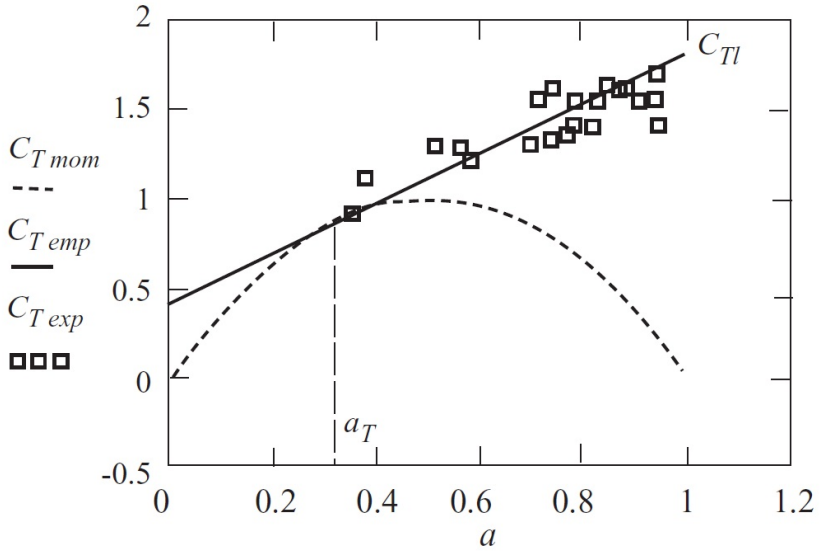

Figure 3.9: Typical corrections to C_t values for a turbine operating in unbounded flow (Burton et al. 2001).

3.3.2 LMADT applied to solid wall cases

Garrett & Cummins (2007) analysed analytically the case of an actuator disk operating in a solid walled tube. Figure 3.10 shows this case. Comparing with the previous analysis presented for an actuator disk operating in an infinite flow we now see that a fifth station is introduced downstream. This station is sufficiently far downstream that mixing has occurred and the flow is of uniform velocity (uniform pressure is still observed at station

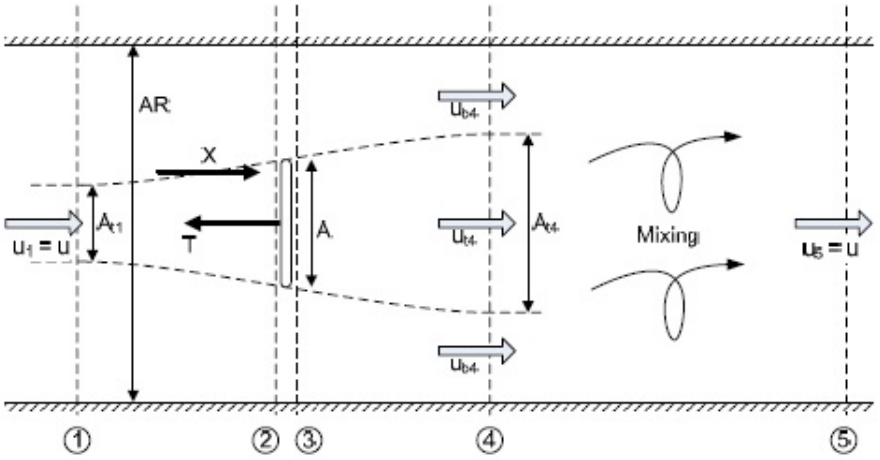

Figure 3.10: An energy extracting actuator disk operating in a solid walled tube(reproduced from Houlsby et al. (2008)).

Table 3.3: Continuity relationships for an energy extracting actuator disk operating in an solid wall tube(reproduced from Houlsby et al. (2008)).

Region		Station 1	Station 2	Station 3	Station 4	Station 5
Turbine	Area	$A_{1t} = A\alpha_2$	$A_{2t} = A_{3t} = A$		$A_{4t} = A\frac{\alpha_2}{\alpha_4}$	
	Velocity	$u_{1t} = u$	$u_{2t} = u_{3t} = u\alpha_2$		$u_{4t} = u\alpha_4$	
	Volumetric flow	$q_{1t} = q_t = uA\alpha_2$	$q_{2t} = q_{3t} = uA\alpha_2$		$q_{4t} = uA\alpha_2$	
	Pressure	$p_{1t} = p$	p_{2t}	p_{3t}	$p_{4t} = p_4$	
By-pass	Area	$A_{1b} = A(R-\alpha_2)$			$A_{4b} = A\left(R-\frac{\alpha_2}{\alpha_4}\right)$	
	Velocity	$u_{1b} = u$			$u_{4b} = u\frac{(R-\alpha_2)}{(R-\alpha_2/\alpha_4)}$	
	Volumetric flow	$q_{1b} = q_b = uA(R-\alpha_2)$			$q_{4b} = uA(R-\alpha_2)$	
	Pressure	$p_{1b} = p$			$p_{4b} = p_4$	
Total	Area	$A_1 = AR$			$A_4 = AR$	$A_5 = AR$
	Velocity	$u_1 = u$	Varies		Varies	$u_5 = u$
	Volumetric flow	$q_1 = q = uAR$			$q_4 = uAR$	$q_5 = uAR$
	Pressure	$p_1 = p$	Varies	Varies	p_4	$p_5 = p - \frac{T}{AR} = p - \Delta p$

4). The bypass flow is no longer at constant velocity and so it can be deduced that $u_{4b} = u\frac{(R-\alpha_2)}{(R-\alpha_2/\alpha_4)} = u\beta_4$, where β_4 is the bypass flow induction factor at station 4.

The continuity relations for this case are seen in Table 3.3.

It follows that Bernoulli in the bypass flow gives:

$$p_4 - p = \frac{1}{2}\rho u^2(1-\beta_4^2) = \frac{1}{2}\rho u^2(1-\frac{(R-\alpha_2)^2}{(R-\alpha_2/\alpha_4)^2}), \tag{3.21}$$

where R is the channel width divided by device width.

Equations 3.11 and 3.13 are unchanged, however 3.12 becomes

$$p_{3t} + \frac{1}{2}\rho u^2 \alpha_2^2 = p_4 + \frac{1}{2}\rho u^2 \alpha_4^2. \tag{3.22}$$

Combining Equations 3.11, 3.13, 3.21 and 3.22 gives:

$$\frac{1}{2}\rho u^2(\beta_4^2 - \alpha_4^2 = \frac{1}{2}\rho u^2(\frac{(R-\alpha_2)^2}{(R-\alpha_2/\alpha_4)^2} - \alpha_4^2) = \frac{T}{A}. \tag{3.23}$$

The momentum equation for the entire flow between stations one and four is:

$$pAR - p_4 AR - T = u^2 A\rho\alpha_2(\alpha_4 - 1) + u^2 A\rho(R-\alpha_2)(\frac{(R-\alpha_2)}{(R-\alpha_2/\alpha_4} - 1), \tag{3.24}$$

which may be simplified to

$$p - p_4 = \frac{T}{RA} + \rho u^2 \frac{\alpha_2}{\alpha_4}(\frac{(1-\alpha_4)^2}{(R-\alpha_2/\alpha_4}). \tag{3.25}$$

Combining Equations 3.25, 3.21 and 3.23 gives:

$$-\frac{1}{2}\rho u^2(1-\beta_4^2) = \frac{1}{2}\rho u^2 \frac{(\beta_4^2 - \alpha_4^2)}{R} + \rho u^2 \frac{\alpha_2}{\alpha_4}\frac{(1-\alpha_4)^2}{(R-\alpha_2/\alpha_4)}, \tag{3.26}$$

which simplifies to

$$R\alpha_4^2(2\alpha_2 - 1 - \alpha_4) + \alpha_2(2\alpha_4^2 + \alpha_2 - 3\alpha_4\alpha_2) = 0. \tag{3.27}$$

Solving the quadratic

$$(1-3\alpha_4)\alpha_2^2 + 2(R+1)\alpha_4^2\alpha_2 - R\alpha_4^2(1-\alpha_4) = 0, \tag{3.28}$$

gives the solution in most convenient form:

$$\alpha_2 = \frac{(1+\alpha_4)}{(1+B) + \sqrt{(1-B)^2 + B(1-1/\alpha_4)^2}}, \tag{3.29}$$

where B is blockage ratio ($B = 1/R$). The power is given by:

$$P = Tu_{2t} = Tu\alpha_2 = \frac{1}{2}\rho A u^3 \alpha_2(\frac{(R-\alpha_2)^2}{(R-\alpha_2/\alpha_4)^2} - \alpha_4^2) \tag{3.30}$$

$$= \frac{1}{2}\rho A u^3 \alpha_2(1-\alpha_4)(\frac{(1+\alpha_4) - 2B\alpha_2}{(1-B\alpha_2/\alpha_4)^2}) = \frac{1}{2}\rho A u^3 C_p. \tag{3.31}$$

The thrust is given by:

$$T = \frac{1}{2}\rho u^2 A(1-\alpha_4)(\frac{(1+\alpha_4)-2B\alpha_2}{(1-B\alpha_2/\alpha_4)^2}) = \frac{1}{2}\rho u^2 A C_t. \tag{3.32}$$

Equation 3.32 reduces to:

$$C_t = ((\frac{1-B\alpha_2}{1-B\alpha_2/\alpha_4})^2 - \alpha_4^2), \tag{3.33}$$

whilst C_t is related to C_p by:

$$C_p = \alpha_2 C_t, \tag{3.34}$$

The solutions can be solved numerically to produce predictions of C_t and C_p with axial induction factor and varying blockage of a channel. Figure 3.11 shows the results. Increases in thrust and power are predicted for increasing blockage ratios.

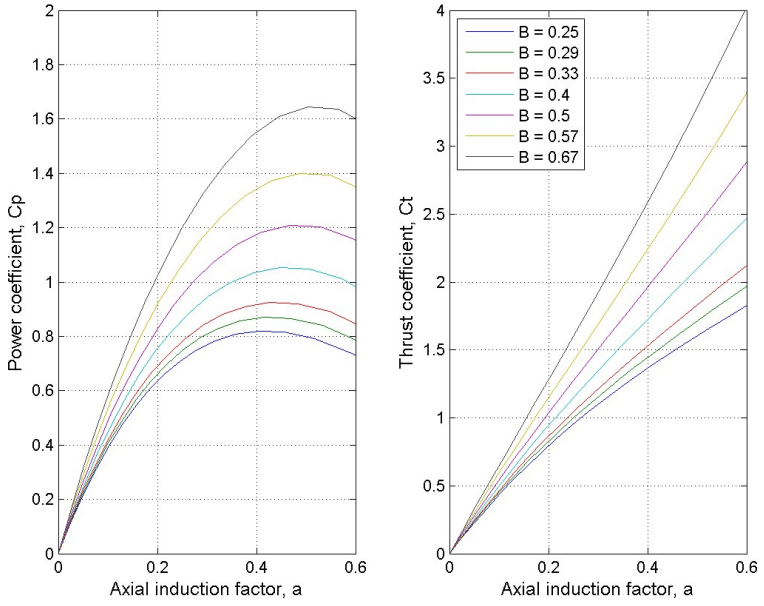

Figure 3.11: Coefficient of power and thrust for varying axial induction factor and blockage.

3.3.3 LMADT applied to open channels

Whelan et al. (2009) analysed analytically an actuator disk operating in an open channel, allowing for deformation of the free surface. Figure 3.12 shows an actuator disk operating within this scenario. The calculations proceed in a similar manner to the previous analysis, however total head is now employed in the Bernoulli calculation. We assume that at stations one, four and five the pressure can be treated as hydrostatic.

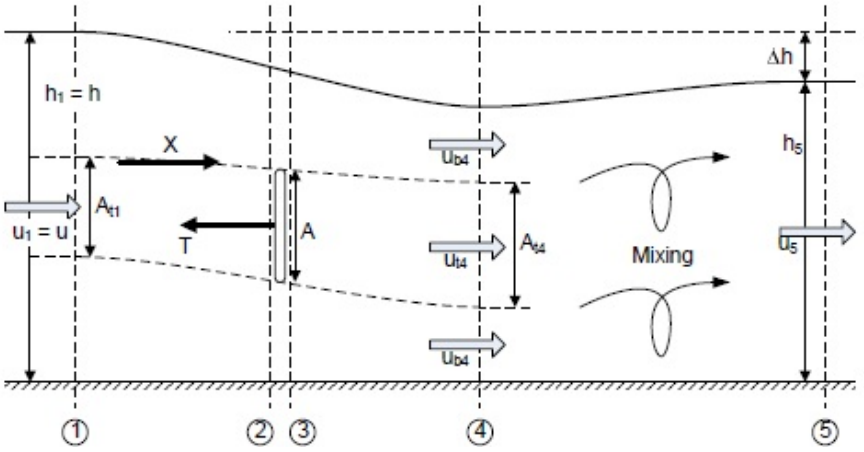

Figure 3.12: An energy extracting actuator disk operating in an open channel(reproduced from Houlsby et al. (2008)).

Table 3.4: Continuity relationships for an energy extracting actuator disk operating in an open channel(reproduced from Houlsby et al. (2008)).

Region		Station 1	Station 2	Station 3	Station 4	Station 5
Turbine	Area	$A_{1t} = whB\alpha_2$	$A_{2t} = A_{3t} = whB$		$A_{4t} = whB\frac{\alpha_2}{\alpha_4}$	
	Velocity	$u_{1t} = u$	$u_{2t} = u_{3t} = u\alpha_2$		$u_{4t} = u\alpha_4$	
	Volumetric flow	$q_{1t} = q_t = uwhB\alpha_2$	$q_{2t} = q_{3t} = u\,w\,hB\alpha_2$		$q_{4t} = u\,w\,hB\alpha_2$	
	Elevation head	$h_{1t} = h$	h_{2t}	h_{3t}	$h_{4t} = h_4$	
By-pass	Area	$A_{1b} = wh(1-B\alpha_2)$			$A_{4b} = wh\frac{(1-B\alpha_2)}{\beta_4}$	
	Velocity	$u_{1b} = u$			$u_{4b} = u\beta_4$	
	Volumetric flow	$q_{1b} = q_b = uhw(1-B\alpha_2)$			$q_{4b} = uhw(1-B\alpha_2)$	
	Elevation head	$h_{1b} = h$			$h_{4b} = h_4$	
Total	Depth	$h_1 = h$			h_4	$h_5 = h - \Delta h$
	Velocity	$u_1 = u$	Varies		Varies	$u_5 = \frac{uh}{(h-\Delta h)}$
	Volumetric flow	$q_1 = q = uwh$			$q_4 = uwh$	$q_5 = uwh$
	Pressure force	$p_1 = \frac{1}{2}\rho g h^2$	Varies	Varies	$p_4 = \frac{1}{2}\rho g h_4^2$	$p_5 = \frac{1}{2}\rho g(h-\Delta h)^2$

The downstream dimensions of the flow are not fixed, but there are relationships between dimension and velocity and between dimension and pressure force. The continuity relations for this case are shown in Table 3.4.

Now in the bypass flow:

$$h + \frac{u^2}{2g} = h_4 + \frac{u^2\beta_4^2}{2g}, \tag{3.35}$$

where h is channel depth. Bernoulli in the turbine flow upstream and downstream of the turbine gives:

$$h + \frac{u^2}{2g} = h_{2t} + \frac{u^2\alpha_2^2}{2g}, \tag{3.36}$$

$$h_{3t} + \frac{u^2\alpha_2^2}{2g} = h_4 + \frac{u^2\alpha_4^2}{2g}. \tag{3.37}$$

Equilibrium of the turbine yields:

$$\rho g(h_{2t} - h_{3t})Bwh = T. \tag{3.38}$$

Combining Equations 3.35, 3.36, 3.37 and 3.38 gives:

$$h_{2t} - h_{3t} = \frac{T}{\rho g B w h} = \frac{u^2}{2g}(\beta_4^2 - \alpha_4^2), \tag{3.39}$$

$$T = \frac{\rho u^2 B w h}{2}(\beta_4^2 - \alpha_4^2). \tag{3.40}$$

Considering the momentum equation between stations one and four gives:

$$\frac{1}{2}\rho g w(h^2 - h_4^2) - T = \rho u^2 w h B\alpha_2(\alpha_4 - 1) + \rho u^2 h w(1 - B\alpha_2)(\beta_4 - 1). \tag{3.41}$$

Equating 3.40 and 3.41 gives:

$$\frac{1}{2}g(h^2 - h_4^2) - Bh\frac{u^2}{2}(\beta_4^2 - \alpha_4^2) = u^2 h B\alpha_2(\alpha_4 - 1) + u^2 h(1 - B\alpha_2)(\beta_4 - 1). \tag{3.42}$$

The continuity relationship

$$h_4 = Bh\frac{\alpha_2}{\alpha_4} + h\frac{(1 - B\alpha_2)}{\beta_4}, \tag{3.43}$$

is of use.

As are the following:

$$\beta_4 = h(1 - B\alpha_2)/(h_4 - Bh\alpha_2/\alpha_4), \tag{3.44}$$

$$\alpha_2 = \frac{\alpha_4}{Bh}\frac{(h(1 - \beta_4) + \beta_4(h - h_4))}{(\alpha_4 - \beta_4)}. \tag{3.45}$$

Combining Equations 3.35, 3.42 and 3.43 leaves a relationship between α_2 and α_4:

$$(1-(\frac{B\alpha_2}{\alpha_4}+\frac{(1-B\alpha_2)}{\beta_4}))=\frac{u^2}{2gh}(\beta_4^2-1) \tag{3.46}$$

and

$$(1-(\frac{B\alpha_2}{\alpha_4}+\frac{(1-B\alpha_2)}{\beta_4}))=\frac{u^2}{gh}(2B\alpha_2(\alpha_4-\beta_4)+2(\beta_4-1)+B(\beta_4^2-\alpha_4^2)). \tag{3.47}$$

Combining Equations 3.46 and 3.47 eventually leads to the solution:

$$\alpha_2=\frac{2(\beta_4+\alpha_4)-\frac{(\beta_4-1)^3}{B\beta_4(\beta_4-\alpha_4)}}{4+\frac{(\beta_4^2-1)}{\alpha_4\beta_4}}. \tag{3.48}$$

Manipulating Equation 3.46 and dividing by Equation 3.48 after some manipulations gives:

$$\frac{Fr^2}{2}\beta_4^4+2\alpha_4Fr^2\beta_4^3-(2-2B+Fr^2)\beta_4^2-(4\alpha_4+2\alpha_4Fr^2-4)\beta_4+(\frac{Fr^2}{2}+4\alpha_4-2B\alpha_4^2-2)=0, \tag{3.49}$$

which is a quartic in β_4.

The downstream head drop, where Δh is the reduction in channel depth from upstream depth, can be calculated from overall momentum:

$$\frac{1}{2}\rho gw(h^2-(h-\Delta h)^2)-T=\rho bhu(\frac{uh}{h-\Delta h}-u), \tag{3.50}$$

$$\frac{1}{2}(2\frac{\Delta h}{h}-(\frac{\Delta h}{h})^2)-\frac{T}{\rho wgh^2}=Fr^2(\frac{\Delta h/h}{1-\Delta h/h}). \tag{3.51}$$

Where $C_t=\frac{T}{\frac{1}{2}\rho Bwhv^2}$, so that $\frac{T}{\rho wgh^2}=\frac{C_tBFr^2}{2}$, Equation 3.51 is a cubic:

$$\frac{1}{2}(\frac{\Delta h}{h})^3-\frac{3}{2}(\frac{\Delta h}{h})^2+(1-Fr^2+\frac{C_tBFr^2}{2})\frac{\Delta h}{h}-\frac{C_tBFr^2}{2}=0. \tag{3.52}$$

The relationships for thrust and power are:

$$C_t=(\beta_4^2-\alpha_4^2), \tag{3.53}$$

$$C_p=\alpha_2C_t. \tag{3.54}$$

Solving the Equation 3.49 numerically and with the use of 3.48, 3.53 and 3.54 relationships can be found between C_t, C_p with varying blockage and Fr. Finding the solution to Equation 3.52 provides the prediction of depth change within the channel due to

energy extraction. The model can solved for a range of Fr and blockage values. Model results for one set of channel parameters ($Fr = 0.17$, $B = 0.33$) are shown in Figure 3.13. Increases in axial induction factor correspond with increases in C_t and change in surface height. Figure 3.13 shows similar results but for lower channel Fr number ($Fr = 0.11$, $B = 0.33$). Little variation is seen in thrust and power coefficient, however a reduction in half of the water surface change is predicted. This shows some sensitivity of the model to changes in channel flow velocity.

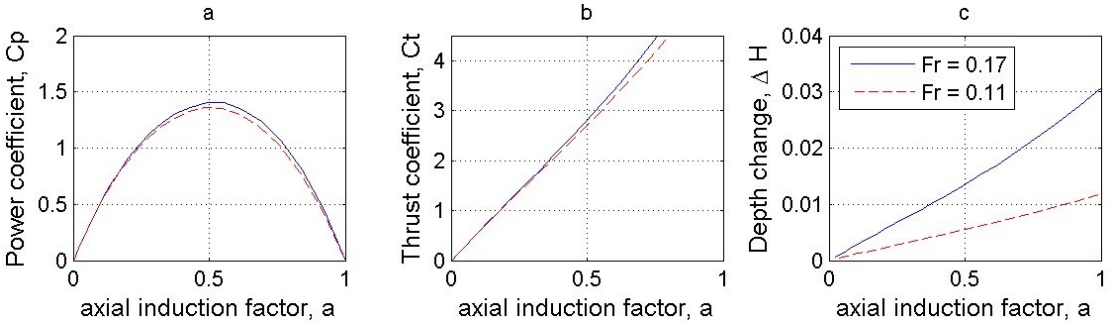

Figure 3.13: Predicted changes in (a) coefficient of power, (b) coefficient of thrust and (c) change in surface height, for varying axial induction factor. Results for channels of Fr = 0.17 and Fr = 0.11, B = 0.33.

The analytical models presented above provide a 1D analysis of an actuator disk operating within an: unbounded flow, solid walled channel and open channel respectively. As highlighted in the literature review none of the models have been validated with experimental data (some, limited, experimental thrust data was presented by Whelan et al. (2009) for the surface deforming analytical case, however this data only looked at cases with little predicted surface deformation, and surface deformation was not measured in these cases), either for device performance (thrust and power) or for prediction of channel surface change within the channel. The applicability of the models are also in question due to their nature being only 1D. Whelan et al. (2009) suggests that the model may be used in the analysis of an array of infinite width, however this constitutes a greatly idealised model (device performance has been shown to vary with lateral spacing between devices (Myers & Bahaj 2012)). It is unclear if this is a useful approximation for the performance prediction of tidal arrays which contain a discrete number of devices.

3.4 Turbulence

One statistical measure of the turbulence present within a flow is turbulence intensity, I_{3D}. This is defined as the root-mean-square of the velocity fluctuations with respect to the mean velocity and is calculated by:

$$I_{3D} = 100 \times \sqrt{\frac{\frac{1}{3}(u_x'^2 + u_y'^2 + u_z'^2)}{\bar{u}_x^2 + \bar{u}_y^2 + \bar{u}_z^2}}. \tag{3.55}$$

Here $\bar{u}_i$ denotes the mean velocity and u_i' the fluctuating velocity component ($u_i = u_i' + \bar{u}_i$) for $i = x, y, z$ (longitudinal, lateral and vertical components respectively). In this work longitudinal turbulence intensity, I_x, is also sometimes presented:

$$I_x = 100 \times \sqrt{\frac{(u_x'^2)}{\bar{u}_{(x)}^2}}. \tag{3.56}$$

Turbulence intensity can give an idea of the level of turbulence present in a flow, hence it is a useful indicator which can be used to understand the processes occurring within a flow domain. However whilst it is a useful quantity for understanding turbulence within a flow it also does not provide a holistic picture. For example two different flows may present similar I_{3D} values at some spatial position, but have different flow mixing properties.

Within a turbulent flow rotation will be present due to shear within the flow. These rotational structures are often referred to as eddies or vortices. Many scales will be present within a flow: possibly including macro scales corresponding to the flow geometry (e.g. channel depth or width), scales corresponding to objects within a flow (such as a MCEC rotor), and those down at the molecular level. Energy is transferred in a turbulent flow from the largest scales down to the smallest, with dissipation of the energy through viscous forces at the smaller scales. This is known as the 'energy cascade' (Pope 2000). The size of the spatial and temporal scales within a turbulent flow are often referred to as length scales and time scales respectively. Integral length scales are the largest spatial scales within a flow and hence contain most of the turbulent energy.

It is possible to calculate length scales of a flow with a time series from a single point within a flow. The approximation of spatial correlations by temporal correlations is known as Taylors hypothesis (Pope 2000). The autocorrelation function can be calculated from a time series using the following:

$$Z(s) = \sum \frac{< u_i'(t) u_i'(t+s) >}{< u_i'^2(t) >}, \tag{3.57}$$

where t is time step and s is lag within the time series. Integrating this quantity with respect to time between the limits $s = 0$ and the first instance of $Z = 0$ yields the integral time scale of the flow, λ_t. This quantity is related to integral length scale, λ_l by the equation:

$$\lambda_l = \lambda_t \bar{u}_i. \tag{3.58}$$

Milne et al. (2011) used a similar method for analysis of data at a site that is planned for tidal stream array development. The data was collected with acoustic flow measurement instruments, similar to those utilised in this work.

The Reynolds shear tensor can also be used to investigate and characterise different regions within a flow. A normalised shear stress tensor, τ_{ij}, can be defined as:

$$\tau_{ij} = \frac{\overline{u_i' u_j'}}{\bar{u}_i^2}. \tag{3.59}$$

A component in the longitudinal direction can be defined as:

$$\tau_{xx} = \frac{\overline{u_x' u_x'}}{\bar{u}_x^2}, \tag{3.60}$$

which is a normalised normal stress.

Turbulence intensity values presented within this work will be based on calculations made in all three-dimensions unless otherwise stated. Length scale and normalised shear tensor calculations have been confined to the streamwise or longitudinal (x) direction only. The statistical measures presented here will be used within the presentation of results in order to characterise areas of different flow in MCEC model experiments.

Chapter 4

Equipment and methods

4.1 Facilities

4.1.1 Large circulating water flume

The Chilworth circulating flume, located at the University of Southampton, can be seen in Figure 4.1. The working channel section is $21m$ in length and $1.37m$ in width, with flow depths of up to $0.5m$. The large width of the working section allows experiments to take place with limited interaction between the test pieces and the side walls. The majority of results presented within this report were conducted at this facility. The schematic view of the flume can be seen in Figure 4.2.

There are no flow straightening devices present within the flume and hence the turbulence generated at the inlet (water is passed down two pipes and dumped into the overspilling inlet) along with that of the walls and bed of the channel, will both act to create the turbulence field at $14m$ downstream. All experiments at the Chilworth facility presented within this work were conducted at $14m$ downstream of the inlet. The wakes of the devices tested were observed to dissipate by around $2m$ downstream, hence when placed at this downstream position the outlet of the channel was far enough downstream to not effect the wake development of any of the devices testing.

Figure 4.1: Chilworth $21m$ circulating flume.

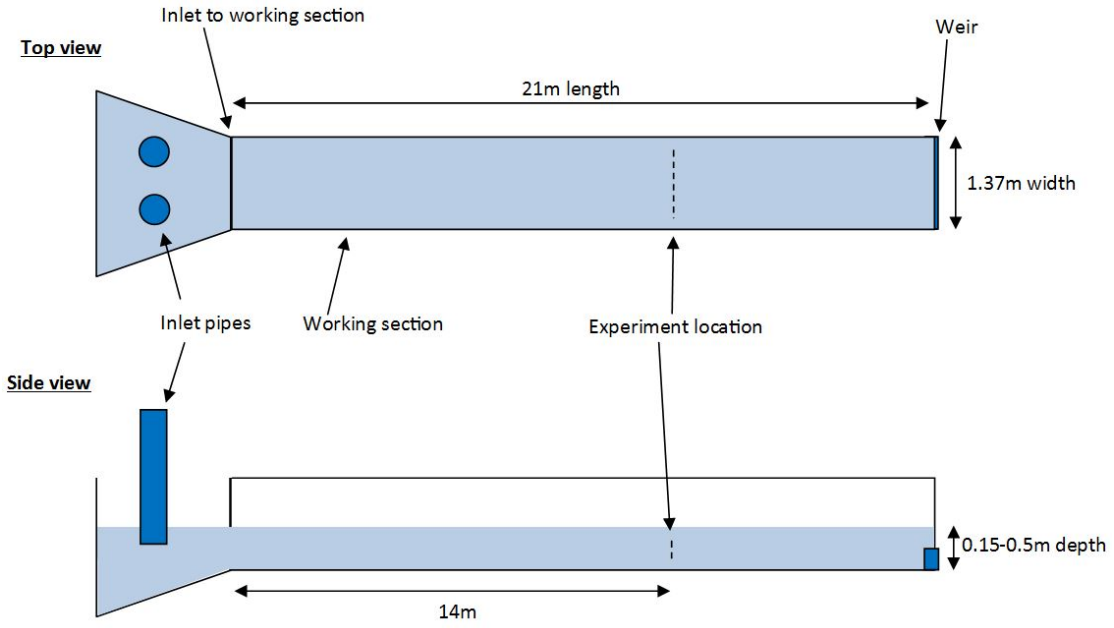

Figure 4.2: Chilworth $21m$ circulating flume schematic view.

4.1.2 Small circulating water flume

The Plint flume, located at the University of Southampton, has a working section $11m$ long and width of $0.3m$, with flow depths of up to $0.35m$. The small cross sectional area of this facility does not allow work without the local presence of boundaries to any test piece, however will provide testing of simplified one-dimensional cases. A schematic view of the flume can be seen in Figure 4.4. Turbulence levels in this flume are lower than the previous due to the nature of the inlet design. Again no flow straightening devices are present.

Figure 4.3: Plint $11m$ circulating flume.

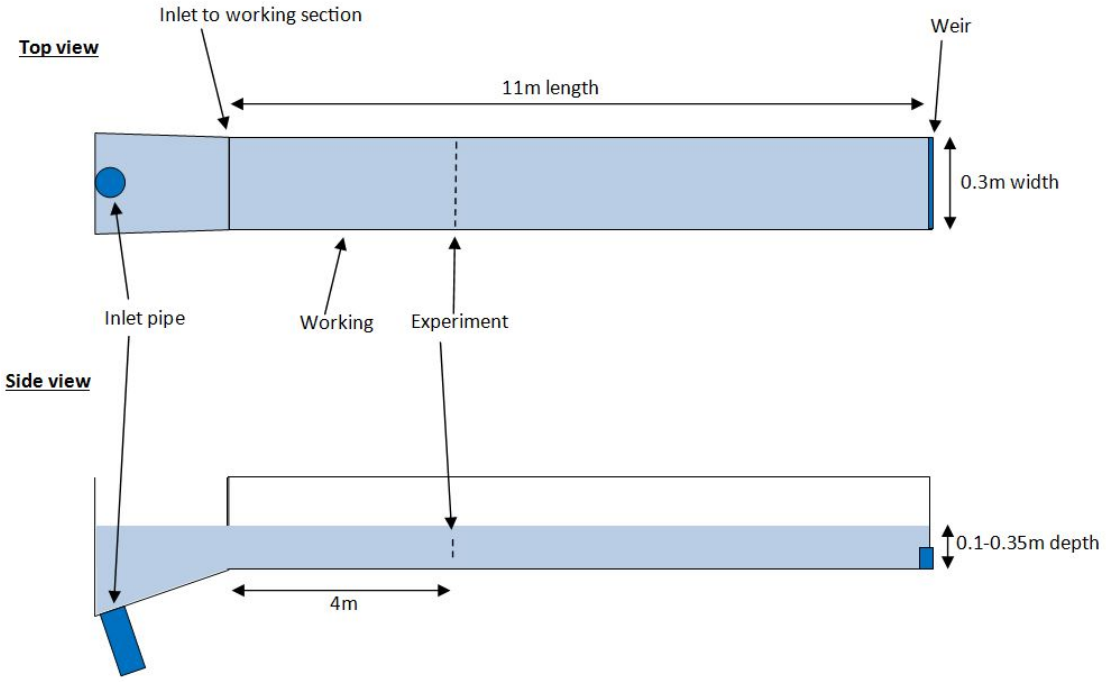

Figure 4.4: Plint $11m$ circulating flume schematic view.

4.1.3 Large current circulation tank

The IFREMER facility is located Boulogne-sur-Mer, France. It has a working section of $5m$ width and up to $2m$ depth. This facility was utilised to test the 1/20th scale rotating turbine model described in the following section. Existing data has been analysed from

this facility in order for comparison with scaled porous disk experiments conducted in the large circulating water flume described earlier.

4.2 Equipment

4.2.1 Turbine model

The rotating turbine 1/20th scale model can be seen in Figure 4.5 and is a three-bladed horizontal-axis device, details of which are described by Myers & Bahaj (2009). The blade profiles used were industry standard (N.A.C.A 48XX) with variable twist angle along the blade length and increased chord length around the root section to prevent stall and allow operation over a greater range of tip speed ratios (TSR). In the turbine model tests thrust was measured directly at the hub using a custom built dynamometer. The turbine is load limited and and controlled by a variable resistance bank, which is altered in order to change the operational TSR value.

Figure 4.5: Rotating turbine model, 1/20th scale, at the Ifremer flume.

4.2.2 Porous disk models

The porous disks used were CNC machined from PVC sheet of $5mm$ thickness. Various disks were used with varying porosity values (ratio of open to closed area). The machined disks were rigid enough to provide no deflection during testing. Although changes in

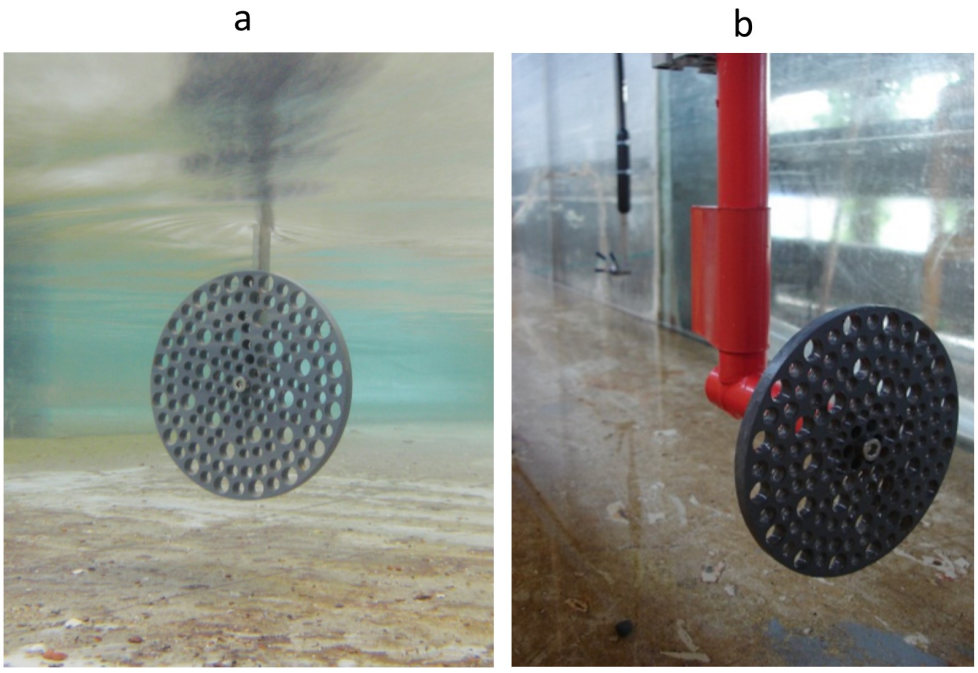

Figure 4.6: Porous disk: (a) on stem and (b) with scaled support structure.

disk porosity will dominate the measured thrust coefficient (discussed in Section 3.1.2), other aspects of disk design will result in smaller variations in thrust coefficient and the nature of the turbulent wake produced. Differences in hole size, disk thickness as well as sharp edged orifices versus chamfered or rounded edges will all have an effect on these. Results presented throughout this study investigate only changes of porosity (no chamfers or rounded edges) and focus on showing the validity of porous disks (and also utilising them).

Initial testing indicated that repeatable thrust measurements were possible at disk sizes of $0.1m$ and greater, whilst smaller disk sizes could also result in problems with spatial measurement accuracy during wake studies. In most experimental cases the disks were mounted on thin stainless steel bar of $3mm$ width. This minimised the additional drag and disturbance to the flow, and thus allowed experimental investigation of device performance without considering the effect of support structures (which are device specific). An appropriate deduction was made in these cases for the additional drag contribution of the support bar; this was important when comparing thrust values at different flow depths, where different lengths of the supporting bar would be present in the flow. In some experiments (such as experiment 1B, Chapter 5) scaling of a specific support structure was required and in this case an exact scale replica was produced. These support structures can be seen in Figure 4.6.

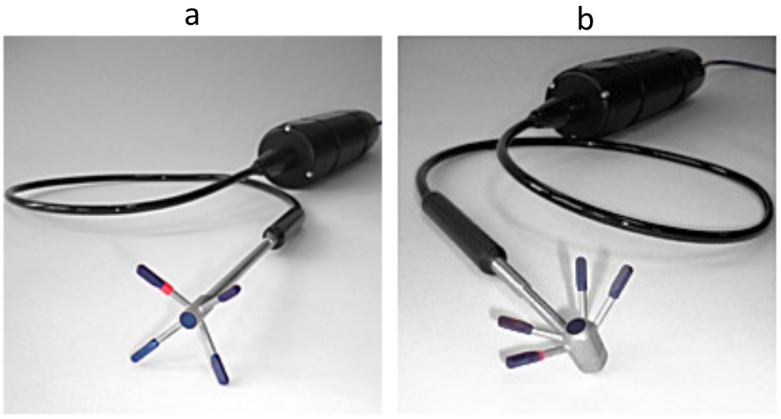

Figure 4.7: ADV flow measuring devices: (a) downward looking ADV head and (b) side looking ADV (reproduced from Nortek AS (2014)).

4.2.3 Flow measurement

Flow measurements are taken using multiple Acoustic Doppler Velocimeters (ADVs). These devices are capable of non-intrusive flow velocity measurement in three-dimensions. The velocimeter operates by transmitting a pulse from a central transducer. A Doppler shift is introduced by reflections from particles travelling through the sampling volume and the resulting signal is picked up by the four receiver arms (seen in Figure 4.7). Up to three Nortek Vectrino ADVs have been used whilst conducting studies during this work. Nortek PolySync software was used to collect data simultaneously whilst using multiple probes. Two different heads are available for Nortek ADVs: a downward looking head (seen in left Figure 4.7) and a side looking head (seen right in Figure 4.7). Both devices operate in a similar manner however each is oriented differently within the flow in accordance with their names. The side looking probe is capable of measuring flow samples much closer to the free surface and to channel walls due to its geometry. Differences can occur in some of the quantities calculated when using velocity time-series collected with each head-type. This is due to the change in orientation of the sample volume and receiver arm angles and is discussed in Section 4.4.

4.2.4 Thrust measurement

Thrust measurements were taken using a force rig designed for use in the Chilworth flume. This is seen in Figure 4.8. A pivoted load arm transfers the force experienced from the fluid to a calibrated load cell. The force experienced by the disk can then be deduced using a simple moment calculation. Thrust data was collected using a National Instruments USB Data Acquisition device, controlled with National Instruments LabVIEW software.

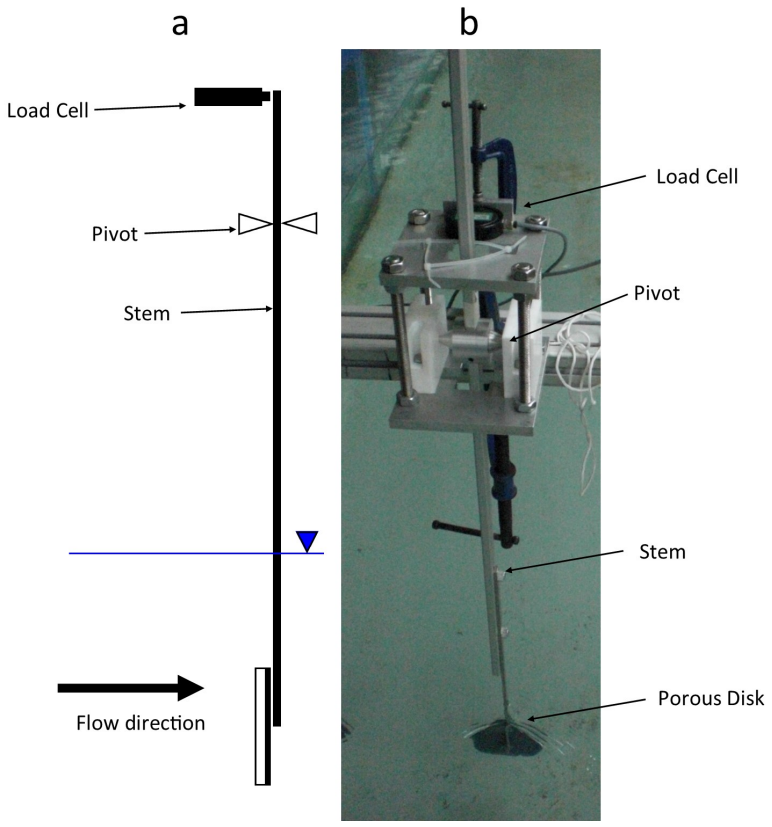

Figure 4.8: Load rig: (a) schematic and (b) operating in the Chilworth laboratory.

4.2.5 Surface height measurement

In order to measure surface height with greater accuracy and precision Senix ToughSonic distance sensors were used. These devices use ultrasonic sound to measure the distance from the probe to either solid or liquid boundaries. Ultrasonic sound is emitted from the probe, this is reflected from the water surface and detected again by the probe in order to calculate the distance travelled by the ultrasonic sound wave. These devices offer many advantages over simple drop depth gauges, such as the ability to take measurements over several minutes in order to average out small fluctuations in surface height. Sub-millimetre precision is also possible, which is not possible with drop depth gauges. The devices therefore allow the measurement of very small changes in surface height. Multiple probes were positioned up and downstream of energy extracting models in order to characterise changes in surface height. Surface height data was similarly collected (as thrust data) using a National Instruments USB Data Acquisition device, controlled with National Instruments LabVIEW software.

Most of the equipment described in this section is shown in Figure 4.9 during testing at the Chilworth facility.

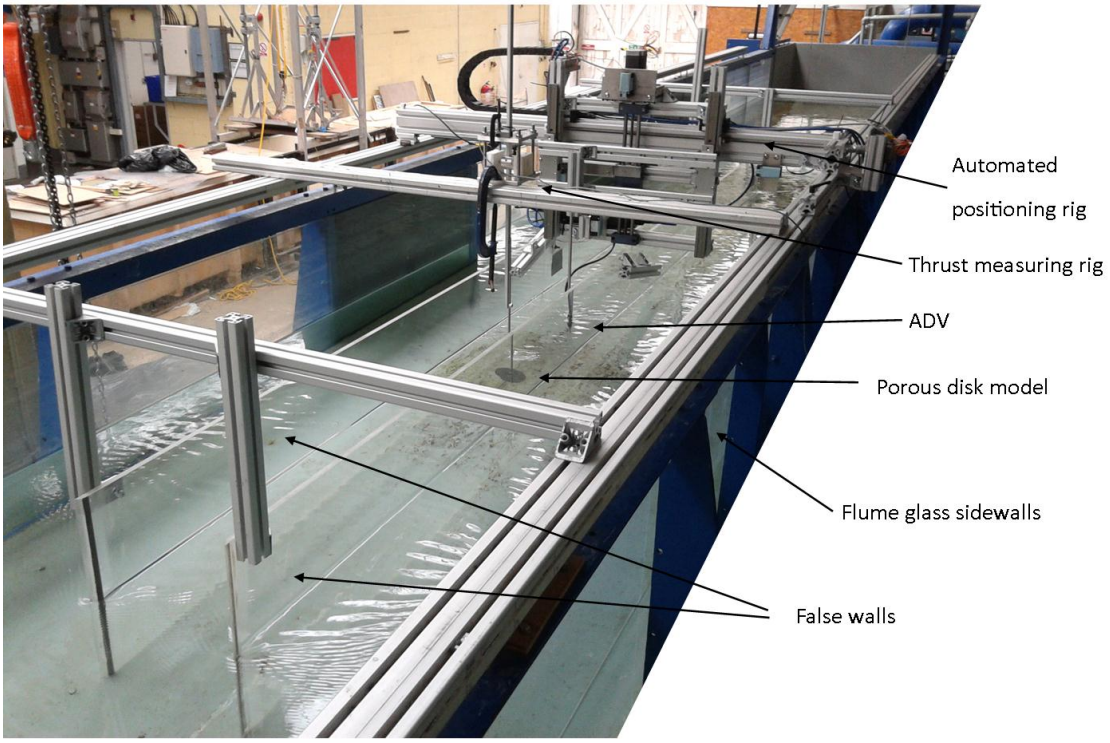

Figure 4.9: Equipment within the Chilworth flume.

4.3 Equipment development

4.3.1 Thrust measurement

In order to increase the positioning accuracy of the porous disks within the Chilworth flume the pivot rigs and disk stems were re-designed. A larger pivot and stem was introduced which ensured no movement of the disks laterally (due to the support arm deflecting) between the setup and running of the flume. The original thinner stems were incorporated into the new design as part of the pivot arm in contact with the water; this ensured minimal flow disturbance as a result of the support structure. These changes can be seen in Figure 4.10.

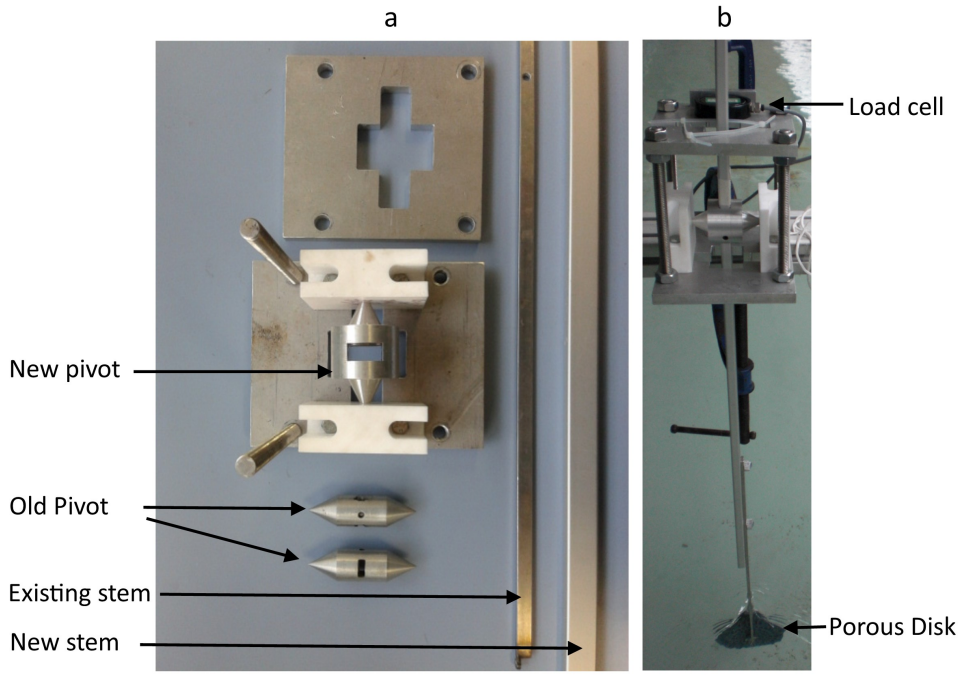

Figure 4.10: (a) Old and new pivot/stem design and (b) new force rig in operation in Chilworth flume.

4.3.2 False walls

In order to constrain the flow field moveable false walls were inserted into the Chilworth flume (see Figure 4.9). The addition of these allowed channels of varying width to be created, which upon combining various flow depths, allowed investigation of channels of varying aspect ratio and area blockage ratio. A smooth radius was placed on the front edge of these sheets in order to minimise flow disturbance due to their presence. Initial testing showed considerable cross-channel velocity gradients could occur in smaller channels when only one false wall was utilised, due to the large boundary layer attached to the permanent glass side wall in comparison to the false one inserted. Hence two such false walls were utilised, placed equidistant from the middle of the flume. The walls were $4m$ in length and experiments were conducted $1.5m$ downstream from the front of the false walls, which allowed a stable boundary layer to have formed.

4.3.3 Automated positioning rig

In order to aid data collection an automatic positioning rig was designed, built and commissioned for use in the Chilworth flume (see Figure 4.11). The rig allows positioning of multiple ADV probes (to within $1mm$ precision) anywhere within the working section of the flume. It also allows queued-batch runs of multiple point measurements within the 2D (vertical-lateral) planes across the full working width at any distance downstream

of the inlet. This device increased the data collection speed and accuracy of wake measurements in this work.

Figure 4.11: Automated ADV positiong rig: (a) PC, drivers and controller, in Chilworth flume working section (b).

4.4 Methods

4.4.1 Flow measurement

Sampling duration

As described earlier most flow characterisation will be carried out using ADVs. Depending on the turbulent flow characteristics different sample lengths at each spatial measurement may be needed to produce accurate velocity measurements. For example, in a highly turbulent flow with larger turbulent time scales a longer duration of sampling will be needed to produce a more repeatable velocity value upon averaging. A sensitivity study was conducted at the Chilworth circulating flume which showed that a 90 second sample duration generally can ascertain mean flow speed to within $\pm 1\%$ in the free stream. Figures 4.12a and 4.13a show both ambient and wake flow cumulative mean velocity values tend to a steady value after 90 seconds have elapsed. Greater variation in velocity values for the wake case is observed. Higher order quantities such as turbulence intensity can take greater sample durations to attain a steady cumulative mean value, such as those found in wake flows. Figure 4.12b and 4.13b show the cumulative mean value of streamwise turbulence intensity values for the same ambient and wake flow velocity time-series. The cumulative mean is seen to converge within 50 seconds in the ambient flow case. Longer sample duration is needed in order for the wake flow running average to become steady, however this occurs within 180 seconds. As a result of this analysis measurements conducted during this work use a sample duration of at least 180 seconds.

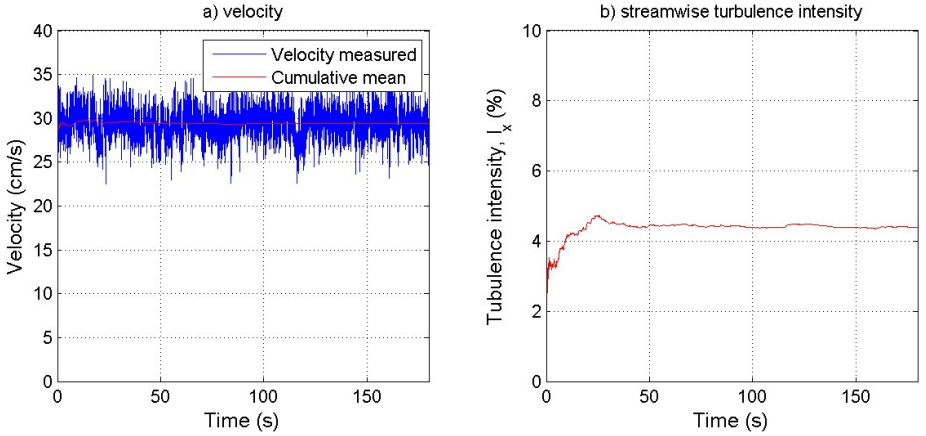

Figure 4.12: Three minute velocity readings with cumulative mean in ambient flow.

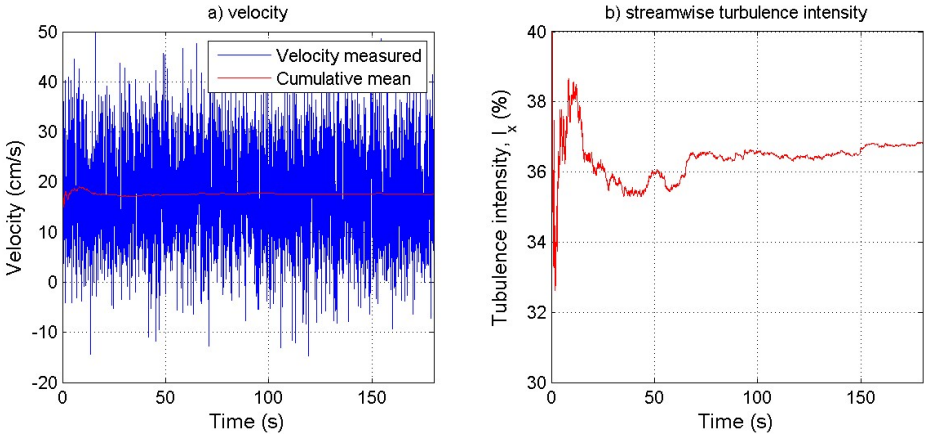

Figure 4.13: Three minute velocity readings with cumulative mean in a wake flow.

A sampling frequency of $50Hz$ meant that each 180 second sample set consisted of 9000 individual readings. The ADVs were capable of sampling up to $200Hz$ however a $50Hz$ sampling frequency was chosen as this value is just above the noise floor of the instrument (Rusello et al. 2006). It therefore allowed characterisation of the turbulence present within the flow without the inclusion of excessive instrument noise within the sample.

Measurement quality

ADV sampling volume and duration can be varied to tailor measurements to particular fluid particle content and flow regimes. A flow with high particle content will indicate a highly 'seeded' flow. Highly seeded flows or slow moving water flows will only require a small sampling volume in order to yield a high strength signal. The water at each facility used in this work was artificially 'seeded' with neutrally buoyant particles in order improve the signal strength and provide fewer anomalous velocity samples within

readings. This allowed high signal strengths to be maintained even when using the smallest possible sample volume heights (set to $3.1mm$).

Even with additional seeding present within the flow some anomalous velocity samples are still recorded. In order to remove these all results data presented within this report has been passed through a velocity correlation filter based on the method outlined by Cea et al. (2007). In this filter the only basis for deciding if a measurement is valid is its relation to the entire sample. The method was used iteratively until less than 1% of the total population size was removed with each pass. The method was chosen as it removes only the outliers of the sample, whereas filtering ADV data based on other methods has been shown to not remove all anomalous spikes and can also remove, what may be, good quality data points (Cea et al. 2007). This leads to a reduction in the sample size used in an analysis (Myers & Bahaj 2010*b*). Removed points were replaced with interpolated values using a cubic interpolation method outlined by Cea et al. (2007). Interpolated values were observed to have a minimal effect on the overall mean velocity, however can become important if data is to be analysed in the frequency domain.

The differences in a typical data set before and after filtering are highlighted in Figure 4.14. As can be seen erroneous spikes have been removed. When applying the filter to some data samples the filter would iteratively remove all points from the sample. These samples were unusable and so were removed from the data analysis.

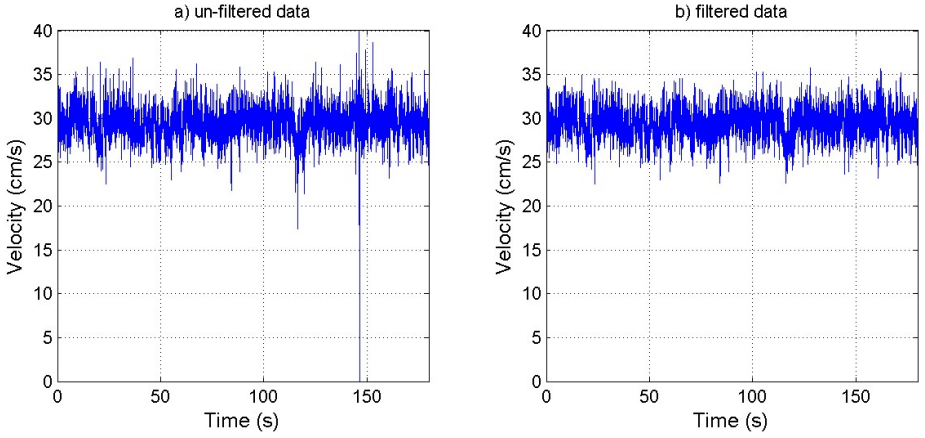

Figure 4.14: Typical velocity data set (a) before and (b) after filtering.

Some experiments within this work were repeated in order to ascertain that the equipment and methods used allow accurate and reproducible results and trends. Figure 4.15a and Figure 4.15b show results from the same experiment which was set up and conducted on separate occasions. The results show very similar trends and values.

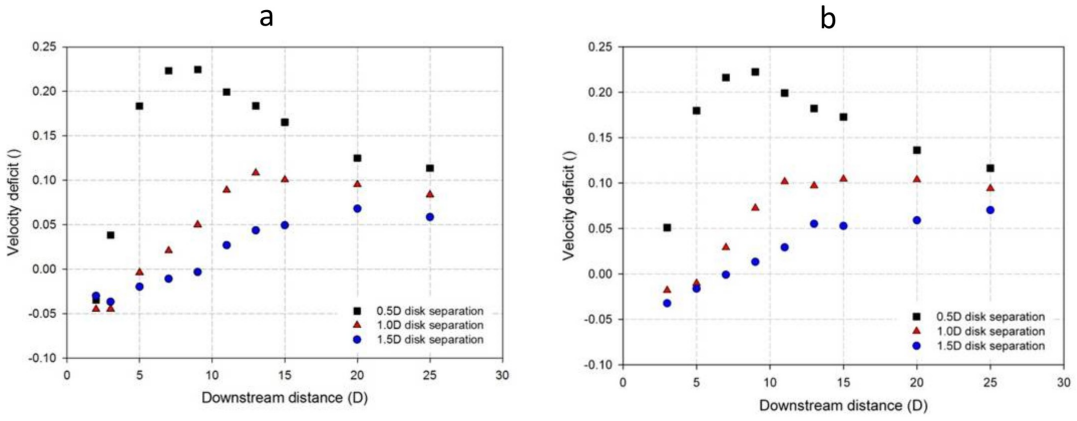

Figure 4.15: Wake results measured from the same experimental setup completed on two separate occasions: (a) experiment run 1 and (b) experiment run 2.

Weir flow measurements

In order to obtain overall channel volumetric flow rate, and infer channel velocity values, in the circulating Plint flume ADVs were not used. Instead flow rate measurements were taken at the sharp crested weir based on the method outlined in BS ISO (2008). The Rehbock formula is suitable for suppressed weirs and was used to calculate volumetric flow rate:

$$q = C_d \frac{2}{3} \sqrt{2g} w h_{1e}^{3/2}, \tag{4.1}$$

in which: q is volumetric flow rate, coefficient of discharge $C_d = 0.602 + 0.083 \frac{h_{we}}{W}$, $h_{1e} = h_{we} + 0.0012$, w is channel width, W is weir height above channel bed and h_{we} is water surface height above weir. Once volumetric flow rate has been ascertained it is possible to calculate an average channel velocity based on the flume depth and width.

ADV probe orientation

Two ADV probe head types were introduced in Section 4.2.3. Both of these probes were used in flow measurement within this work. The head type will effect the orientation of the sample volume in which velocity readings are measured. It is therefore important that any variation in measurement of the different flow properties for each of the head types is quantified. Sets of flow readings, each 10 minutes in length, were recorded at four separate positions in the Chilworth flume. Both ADV head types were used to record a measurement at the same spatial position, one after the other. Table 4.1 shows the calculated flow statistics for each measurement. It is observed that each

probe type records close values for streamwise quantities (I_x and τ_x) however non-streamwise quantities (I_y, I_z, τ_y, τ_z) are observed to have systematic bias. Therefore the only parameters that are compared when both the down and side-looking probes are used in flow mapping in this work are the streamwise parameters: I_x and τ_x. Average streamwise flow velocity, $\bar{u}_x$, is observed to be slightly lower in each of the side looking probe measurements. Hence when velocity measurements are normalised only values recorded upstream using the same probe type are used.

Table 4.1: Comparison of flow statistics measured from down and side looking ADV probes.

measurement number	head type	$\bar{u}_x$	I_{3D}	I_x	I_y	I_z	τ_x	τ_y	τ_z
1	down	30.9	3.72	4.94	581	81.2	0.00244	0.00139	0.00033
	side	30.7	3.62	4.93	280	64.0	0.00243	0.00059	0.00092
2	down	31.1	3.66	4.72	708	80.7	0.00223	0.00147	0.00031
	side	30.9	3.51	4.72	276	63.2	0.00223	0.00057	0.00091
3	down	31.1	3.70	4.73	802	86.6	0.00224	0.00152	0.00035
	side	30.7	3.16	4.54	183	47.8	0.00206	0.00038	0.00057
4	down	30.7	3.85	4.98	906	87.6	0.00248	0.00160	0.00037
	side	30.1	3.48	4.93	279	55.6	0.00243	0.00050	0.00071

4.4.2 Thrust measurement

Non-dimensional thrust coefficient

Device thrust measurements in this work are reported non-dimensionally as a thrust coefficient, given by:

$$C_t = \frac{T}{\frac{1}{2}\rho \bar{u}_x^2 A}, \tag{4.2}$$

where T is measured thrust, A disk area normal to flow and $\bar{u}_x$ is mean stream wise velocity. Errors when calculating C_t will be present in both the thrust and velocity measurements, with the potential of greater error contributed by the velocity due to it's power relationship in the Equation 4.2. In order to reduce error from the velocity measurements the velocity was measured at a distance of $5D$ upstream and at nine separate points across the disk plane (spaced equally as a grid). Velocity measurements were taken immediately after thrust measurements in order to reduce the effect of any longer time-scale variations in flume flow speed. The measurement at nine separate points across the disk plane was especially important when investigating varying channel geometry as the device sometimes was operating in a flow with varying degrees of lateral and vertical velocity profile. This method accounted for any change in velocity profile which may be encountered between experiments with differing flow geometry (such as

changes in channel depth or width) and hence provided a more representable inflow to the disk.

Voltage measurement samples were taken at $200Hz$ for durations of 240 seconds. A mean value was calculated from the samples. Figure 4.16 shows a typical voltage reading for a duration of 240 seconds. The cumulative mean of the sample is also shown, which indicates that convergence to within 1% of sample mean value occurs within a sampling duration 180 seconds.

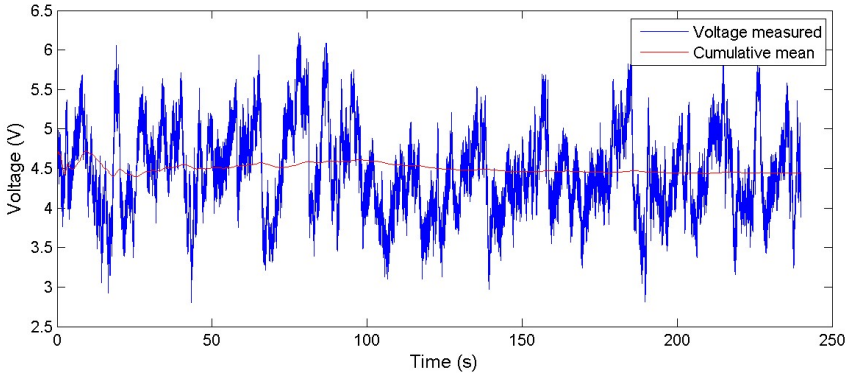

Figure 4.16: Typical measured load cell thrust voltage and running mean convergence.

Voltage recordings were converted to force measurements through calibration measurements. Load cell calibration can change with temperature variation of the system. The load cells were therefore switched on and left for 30 minutes prior to experimental tests. This allowed the equipment to warm up and so account for any change in calibration due to a temperature change with the equipment powered on. Calibration was done, after this initial 30 minute period, by removing the load cell from the thrust measuring rig and inverting the load cell. Known masses were added and voltage readings taken for each load. Calibration was also completed at the end of each test day in order to ascertain any changes in to this calibration data. C_t values were calculated using the most recent calibration coefficients.

Deduction of support strut drag

As experiments will be carried out at varying depth during this work it is possible that the drag on the supporting stem of the disk will contribute differently to moment calculations in different cases. In order to determine if the drag from the supporting stem is significant, and hence C_t values need to be corrected, estimations of the moment contributed by the stem and disk are made. Figure 4.17 shows a free body diagram of the moment balance used in the deduction of support drag.

The moment balance around the pivot in Figure 4.17 gives:

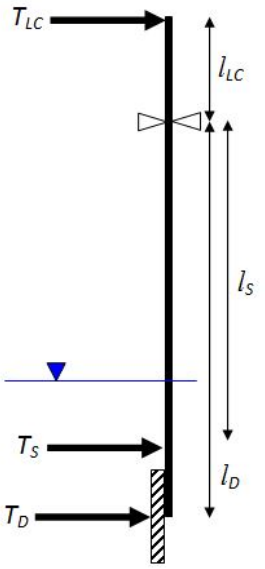

Figure 4.17: Free body diagram of load cell arrangement.

$$T_{LC} l_{LC} = T_S l_S + T_D l_D, \tag{4.3}$$

where T_{LC}, T_S and T_D denote the thrust forces acting on the load cell, stem and disk respectively; whilst l_{LC}, l_S and l_D denote the pivot lengths for the load cell, stem and disk respectively. It is observed that the moment at the load cell, $T_{LC} l_{LC}$, is made up of the moments at the stem and disk ($T_S l_S$ and $T_D l_D$) respectively. The values T_S and T_D were calculated using the re-arranged, modified Equation 4.2:

$$T = \frac{1}{2} \rho u_x^2 A C_{drag}, \tag{4.4}$$

for a range of flow depths (where C_{drag} is drag coefficient). Velocity values were calculated for each depth based on a fixed Froude number of 0.2. In the calculation of T_D a C_{drag} value of 0.8 is assumed. Munson et al. (1998) provides drag coefficient data for a flat bar which shows a C_{drag} value 0.03 at the relevant Reynolds number range. The calculation of T_S assumes a thrust force acting along the entire length of the submerged bar. The moment arm, l_s, is assumed to act between the pivot and the mid-distance between water surface and disk hub height. Relative contribution of each of the forces and moments was calculated as $100 \times T_S/T_D$ and $100 \times T_S l_S / T_D l_D$ respectively. Figure 4.18 shows the estimated relative contribution of the forces and moments (as a percentage of the stem and disk contributions), in the Chilworth experimental setup, over a range of flow depths. A difference in relative moment contribution of 0.64% and a maximum change of 2% is observed over the range of depths studied. This indicates

that the change is not significant enough to warrant a correction to the calculated C_t values presented in experimental results. This is considered a conservative estimate as greater forces on the disk are to be expected in more confined flow cases (which is not taken into account with a fixed value of $C_{drag} = 0.8$ used in the calculation of T_D).

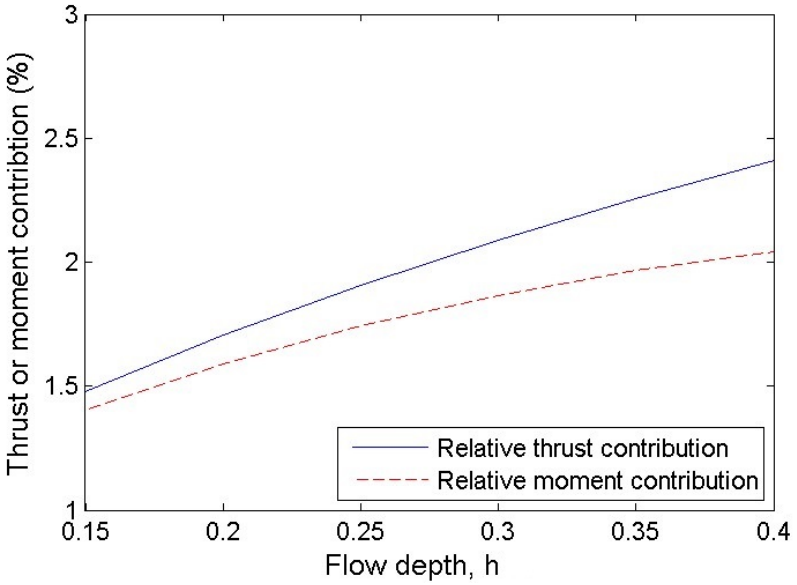

Figure 4.18: Estimated relative contribution of the thrust and moment of stem and disk, operating in the Chilworth flume, over a range of flow depths.

4.4.3 Depth measurement

Change in free surface height was measured using ultrasonic distance probes as outlined in the earlier equipment section. These devices require calibration in a similar manner to the load cells discussed above. The calibration of these devices is also dependent on their temperature, hence the devices were similarly switched on and left for 30 minutes prior to experimental tests. Calibration was done after this initial 30 minute period in order to convert the voltage reading to useful distance values. Calibration was done by removing the distance sensor from the thrust measuring rig and mounting to a calibration table. A screen was placed at known distances and voltage readings taken. Calibration was also completed at the end of each test day in order to ascertain any changes to the calibration constants. Where significant differences in calibration coefficients were observed surface height values were calculated using the calibration coefficients taken at a time closest to that of each experiment.

Due to such small changes in surface elevation occurring with the extraction of energy from small channels a method was devised that would reduce the dependency on the calibration coefficients. Figure 4.19 shows a schematic of expected changes in channel depth, h, with the addition of a MCEC model. Absolute measurements of water depth

will incur measurement errors, however, measurements taken only of the difference in water surface height with and without the presence of the energy extracting device ensure that the errors associated with measuring absolute depth will not be present. This method also accounts for any natural difference in surface height between upstream and downstream distance sensors (providing there is no significant change in flow rate within the channel with the addition of the MCEC) due to the channel not being set up to operate at the channel normal depth.

At 20D distance downstream the wake of the MCEC device models has been observed to have almost fully dissipated and so the presence of the device will no longer affect the channel properties. Therefore the downstream sensor was placed at this distance as it was expected that the effects of the device on the channel surface height would be minimal. It is expected that a turbine device will cause changes in pressure upstream of it (Burton et al. 2001) and so the upstream sensor was placed at a distance of 2D upstream in order that it was more likely to measure the upstream surface height change without the local effect of the MCEC device model.

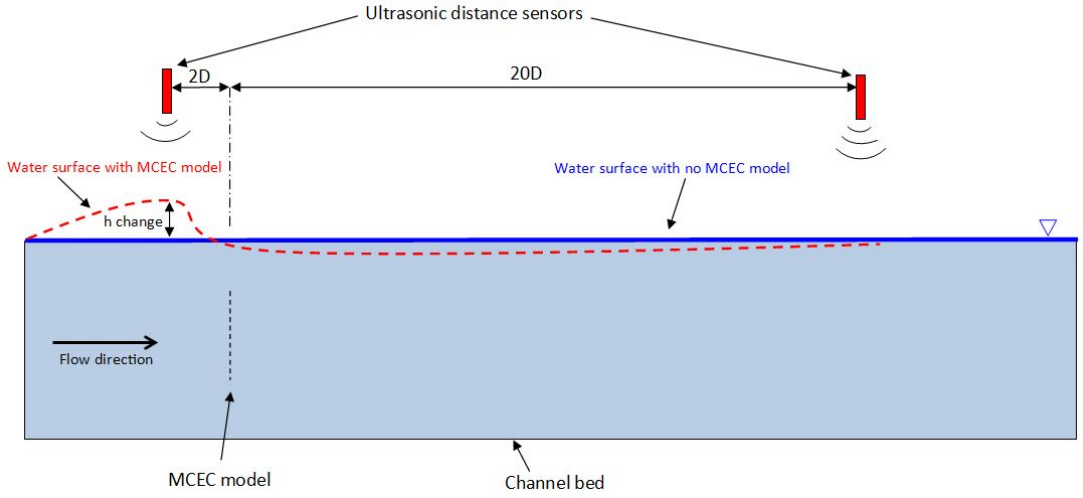

Figure 4.19: Schematic of experimental depth measurement using ultrasonic distance sensors.

4.5 Data presentation

4.5.1 Regions of flow mapping

In order for clarity in the presentation of results, regions of flow mapping that will be commonly referred to are now explained. Figure 4.20 shows what is referred to as 'centreline' measurements; measurements made in the wake directly behind the device hub. The co-ordinates: x (streamwise), y (horizontal) and z (vertical) are shown in the figure. Throughout this work the origin is taken to be at the centre of the device. Figure

4.21 shows measurements in the 'vertical plane' (measurements taken at $y = 0$ with varying downstream and vertical distances) and the 'horizontal plane' (measurements taken at $z = 0$ with varying downstream and horizontal distances). Distances in x, y and z directions will be reported normalised by device diameters (measured in units of: D).

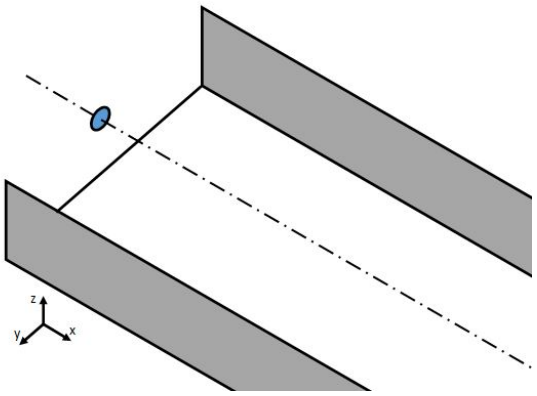

Figure 4.20: Schematic of centreline flow measurement behind a MCEC device model in a flume.

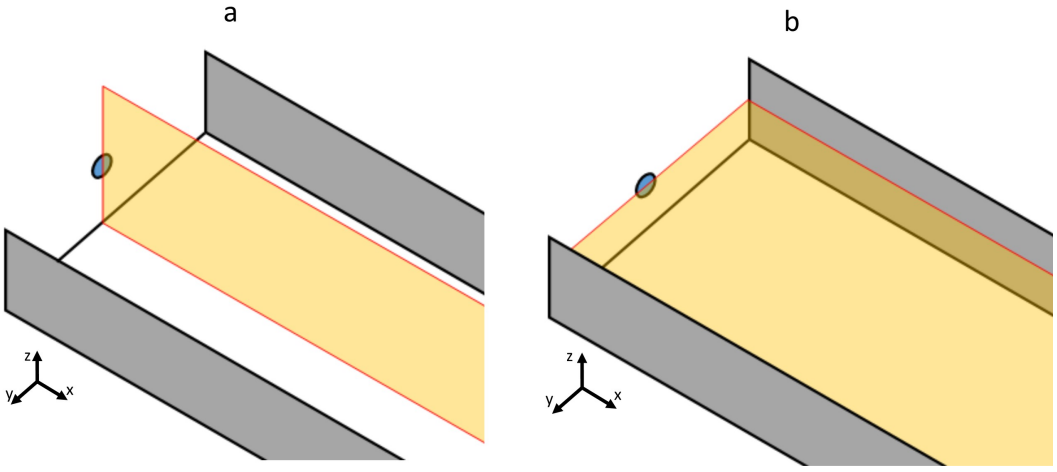

Figure 4.21: Schematic of (a) vertical plane and (b) horizontal plane measurement behind a MCEC device model in a flume.

4.5.2 Normalisation of data

All velocity measurements downstream of the investigated devices have been normalised against measurements recorded five diameters upstream of the rotor plane. These values are expressed by a dimensionless parameter:

$$U_{def} = 1 - \frac{\bar{u}_x}{U_\infty}. \tag{4.5}$$

Here U_{def} is the velocity deficit and U_∞ is the upstream mean flow. Velocity measurements were taken upstream with curves fitted (horizontally and vertically) across the channel in order to determine the velocity profiles present. The fitted curves were used to calculate the upstream mean flow values (U_∞) used when normalising downstream velocity measurements. This method was used instead of individual upstream point measurements in order to reduce the effect of random error associated with single measurements. This method also reduced overall time required to sample the free stream flow as not every wake measurement required a corresponding upstream ambient flow measurement. Figure 4.22 shows a typical lateral and vertical velocity flow fitting in a channel of $3D$ depth and $13.7D$ width. In some channels with smaller width a velocity profile was observed due to the boundary layers present at the channel walls. In these cases a polynomial was fitted.

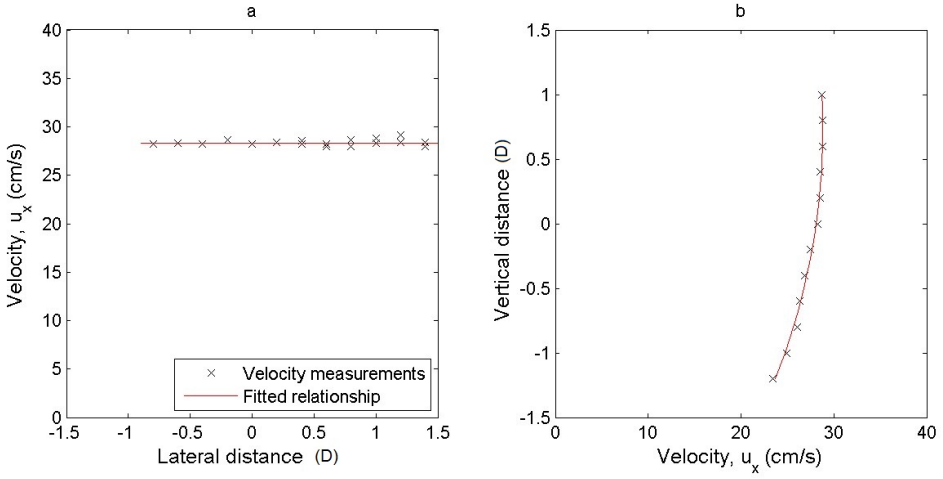

Figure 4.22: Example upstream velocity measurements and curve fitting in (a) horizontal plane and (b) vertical plane.

The velocity ratio, U_{ratio} is also used to present normalised ambient flow measurements:

$$U_{ratio} = \frac{\bar{u}_x}{\bar{U}_\infty}, \tag{4.6}$$

where $\bar{U}_\infty$ is the mean upstream streamwise velocity calculated from each of the mean upstream velocity measurements.

4.6 Experiment design and list

4.6.1 Experiment plan

Table 4.2 details the experiments which were conducted. Experiment numbers ('Expt' column in table) 1,2,3 and 4 will contribute respectively to the numbered objectives in Section 1.5. The alphabetic indicator gives a reference to each individual experiment

carried out. The column labelled 'Motivation' gives the relevant section number within the Literature Review and Theory Chapters that introduce why the particular investigation is of importance. The subsequent sections within this chapter provide the detailed experimental set up for each of the experiments.

4.6.2 Investigation 1

Experiment 1A

Porous disk models of varying porosity were tested at the Chilworth flume at a fixed flow and channel geometry. The channel properties are shown in Table 4.3. Thrust coefficient values were recorded for each of the porosity values: 0.32, 0.36, 0.48, 0.54, 0.6.

Experiment 1B

Two experimental studies were completed at different scale. The 1/20th-scale model turbine (introduced in Section 4.2) was tested at the Ifremer circulating water facility in Boulogne-sur-mer, France. This is a closed-loop facility with two variable speed axial drive impellers circulating the flow around in a similar manner to a wind tunnel. The model turbine was large enough to enable the use of standard industry blade profiles (N.A.C.A 48XX) and produce power coefficient (Cp) and thrust coefficient (Ct) performance similar to full scale devices across a range of TSRs. Blade element model predictions and experimental performance of the rotor are presented by Galloway et al. (2011). Comparable experiments were also completed at 1/160th-scale with an equivalent device represented by a porous disk and geometrically scaled support structure (shown in Figure 4.6b) at the Chilworth Laboratory in Southampton, UK. The comparative scale of these devices and the channel properties in which they operated are outlined in Table 4.4. Both sets of experiments employed identical geometric scaling as shown in Figure 4.23.

It was essential to ensure that the channel size was scaled geometrically. False sidewalls were used to narrow the working section of the Chilworth facility such that the aspect ratio of the channel (equal to two) was identical to that of the larger facility. The area blockage ratio in each of the channels was equal to 0.063. In order to allow a comparison of the turbulent structures behind the porous disk models in varying ambient flow a grid was placed at the front of the false channel to alter the ambient turbulent properties. The properties of the ambient turbulence in each case are presented in the corresponding results section.

Rotor thrust was measured on both devices. In the turbine model experiments thrust was measured directly at the hub using a custom built dynamometer. In the porous disk

Table 4.2: List of experiments and the parameters investigated in each along with corresponding sections outlining the motivation for study and the presentation of results.

Expt	Motivation	Description	Fixed	Varying	Results
1A	3.1.3	Effect of porosity on thrust coefficient	B, Ω, Fr	Θ	5.1
1B	2.1	Turbine and porous disk comparison	A, Ω, Fr	Device type,Θ	5.2
2A	2.2.4	Idealised 1D energy extraction from a channel	B	Fr	6.1,6.2
2B	2.2.4		Fr	B	6.3
2C	2.2.2	The loading of a single disk in square channel	Ω, Fr	B	6.3
2D	2.2.3	The effect of channel aspect ratio on loading	Fr	Ω, B	6.4
3A	2.3	Wake changes of a single disk in various constrained flows	Fr	B, Ω	7
4A	2.4	The effects of dual-disk spacing on loading and wake formation	B, Ω, Fr	S	8.1
4B	2.4	...with variation in flow depth	Fr	S, h	8.2

Table 4.3: Experiment 1A channel properties.

Property	Value
Width, w	13.7D
Depth, h	4D
Area blockage ratio, B	0.014
Fr no., Fr	0.2

Table 4.4: Absolute dimensions of test facilities/devices.

	Ifremer (Turbine)	Chilworth (Disc)
Turbine Diameter (m)	0.8	0.1
Channel Width (m)	4	0.5
Channel Depth (m)	2	0.25
Channel Length (m)	18	4
Approx Flow Speed (m/s)	0.82	0.31
Fr no.	0.19	0.20
Re no.	6.6×10^5	3.1×10^4

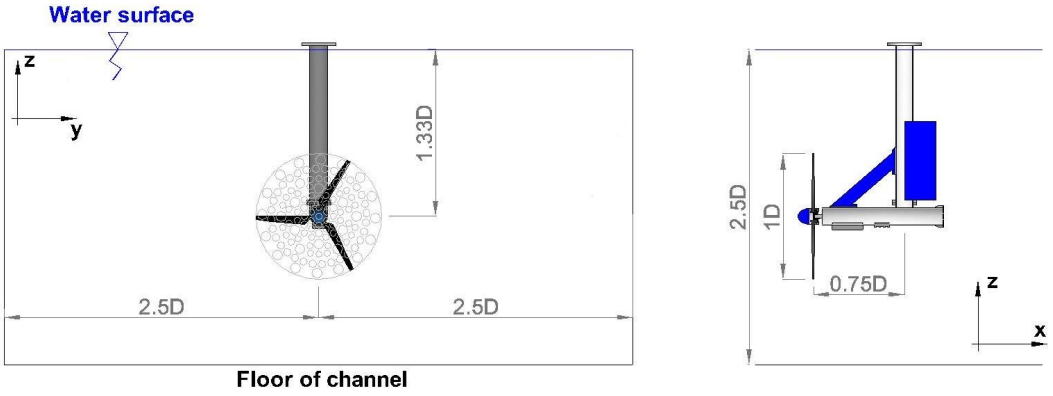

Figure 4.23: Normalised dimensions for 1/20th and 1/160th scale experiments using a rotating turbine and porous disk respectively.

experiment focus was placed on two separate disk models with porosity values (ratio of open to closed area) of 0.32 and 0.48. Load measurement was made using the apparatus described in Section 4.2.4. During loading measurements the scaled support structure was held rigidly in place behind the device in order that the scaled support model did not contribute to the thrust calculations.

4.6.3 Investigation 2

Experiment 2A,2B

An investigation was completed using the small circulating water flume at the University of Southampton. This comprised of a 1D scenario designed to mimic that of the method

proposed by Whelan et al. (2009) to model an infinite row of MCEC devices. Figure 4.24 presents a schematic view of the experiment, where w is fixed as the flume width (0.3m). A porous fence of dimensions: $w_f = 0.3$m and $h_f = 0.1$m, is utilised in order to simulate an array of turbines supposed to be of infinite length; in this case spanning the full width of the channel. The fence porosity, Θ, was 0.4. Area blockage ratio, B, and Froude number, Fr, will be varied in the experiments by running the flume at different depths (varying h) and flow-speeds (varying u). For the experimental setup described it was possible to operate over the range of Froude numbers: 0.04-0.2, at the area blockage ratios 0.33, 0.5 and 0.66. Absolute values of flow rate will be measured using a sharp crested weir tailgate. Weir surface height will be measured using drop depth gauges. Thrust values will be measured using the load cell arrangement introduced in Section 4.2.4. Surface height changes will be measured using ultrasonic distance measuring devices (introduced in Section 4.2.5.

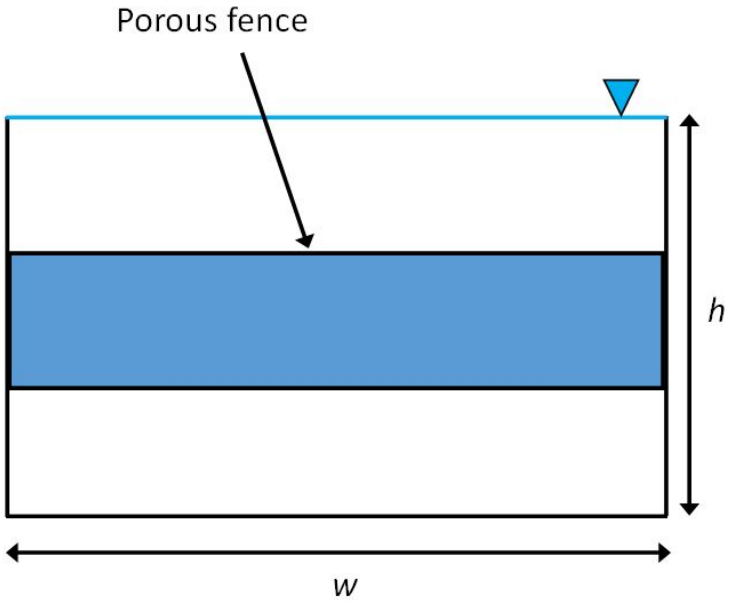

Figure 4.24: Schematic of channel cross sectional geometry and porous fence at the Plint flume, University of Southampton.

Experiment 2C, 2D

The large circulating flume at Chilworth hydraulics laboratory, University of Southampton, was used to investigate the changes in thrust coefficient on a single porous disk (of diameter 0.1m) with variation in channel area blockage ratio and channel aspect ratio. Figure 4.25 shows a schematic of the channel cross section used in each of the experiments. Water depth was varied by changing the outlet weir height of the flume and altering the flow rate of the flume pumps. Channel width was altered by using the false walls described in Section 4.3.2. In each experiment the disk was situated in the geometric centre of the channel, i.e. the disk hub was located at mid-depth and mid-width

in each case. Channel velocity was reduced in smaller channels to ensure a constant Froude number for each experiment. In experiment 2C channel aspect ratio was fixed at a value of one in order to investigate changes in thrust coefficient as a function of area blockage ratio only. In experiment 2D area blockage ratio was fixed at at values of 0.05 and 0.08 in order to investigate changes in thrust coefficient as a function of aspect ratio. Table 4.5 shows the properties of each of the channels investigated.

Table 4.5: Experiment 2C and 2D channel properties.

Experiment	2C	2D
Aspect ratio, Ω	1	1 - 7
Area blockage ratio, B	0.05-0.35	0.05, 0.08
Fr no., Fr	0.17	0.2

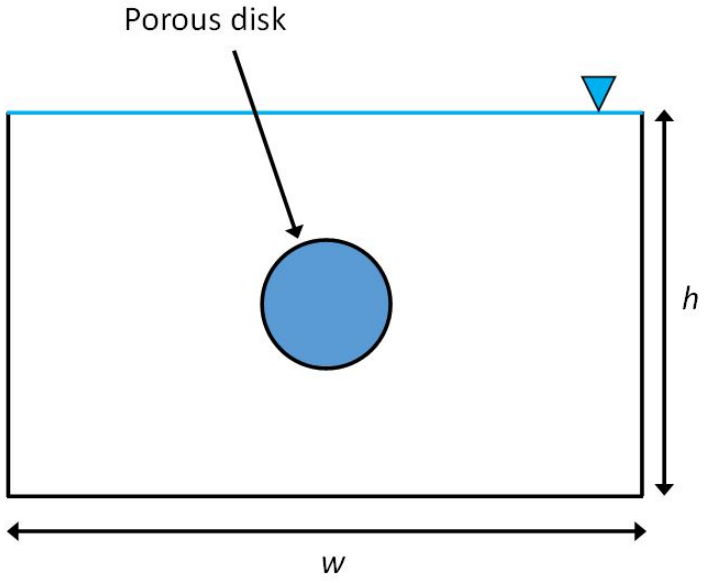

Figure 4.25: Schematic of channel geometry and porous disk at the Chilworth flume.

4.6.4 Investigation 3

Experiment 3A

The experimental set-up for this investigation is similar to Investigation 2C and 2D. A single porous disk will be placed in channels of varying geometry. Channel width and depth will be varied with the use of false walls and changes in weir height respectively. Three separate area blockage ratio channels, with aspect ratio equal to one, will be investigated (depths of 4D, 3D and 1.75D). Subsequent changes in channel aspect ratio and area blockage ratio will also be investigated. Wake measurements are the focus of the study in contrast to Investigation 2; vertical-downstream and lateral-downstream plane

measurements will be recorded at a range of downstream distances in order to characterise vertical and lateral wake expansion for each channel geometry. Significant detail will be recorded in areas of high shear within the wakes (generally located downstream of the device edges) in order to accurately characterise the wake expansion in each case. The experiment will highlight the differences in lateral and vertical wake expansion in channels of $\Omega \neq 1$ as well as varying area blockage ratio, B. A summary of the channel properties investigated are found in Table 4.6.

Table 4.6: Experiment 3A channel properties.

w (D)	h (D)	B	Ω	Fr
4	4	0.05	1	0.17
3	3	0.09	1	0.17
1.75	1.75	0.26	1	0.18
13.7	3	0.02	4.6	0.17
13.7	1.75	0.03	7.8	0.16

4.6.5 Investigation 4

Experiment 4A

Experiments 4A was conducted at the large circulating water flume at the University of Southampton. Two porous disks, of diameter 0.1m, were placed in the full-width open channel (w =13.7m) at the same downstream distance and at mid-depth. Figure 4.26 shows a schematic of the setup. Wake and thrust measurements were taken with the devices at varying degrees of lateral separation, S. Lateral separation of the devices was varied from 0.5 - 2.2 disk diameters (D). This lateral disk separation is measured from the closest disk edges as illustrated in Figure 4.26. The origin used in these experiments, and in the presentation of results, is located at hub height at the mid point between the two disk. The two device array was positioned equidistant from each of the flume walls. The device diameter/water depth ratio, d/h, was set at 0.33 (a corresponding channel depth of 3D). Wake measurements were taken on the lateral plane behind the devices. Results are presented on the centreline between the two devices, which was located directly downstream of the origin. Some data is also presented on the 'centreline offset', which was located parallel to the centreline, on the horizontal plane, but at a lateral position of half a disk diameter from the centreline. This corresponds with the edge of a possible third downstream disk. Figure 4.27 shows both of the centrelines discussed.

Experiment 4B

Similar experiments were conducted to those in experiment 4A with variation in the device diameter/water depth ratio, d/h (at a fixed device diameter). This was investigated

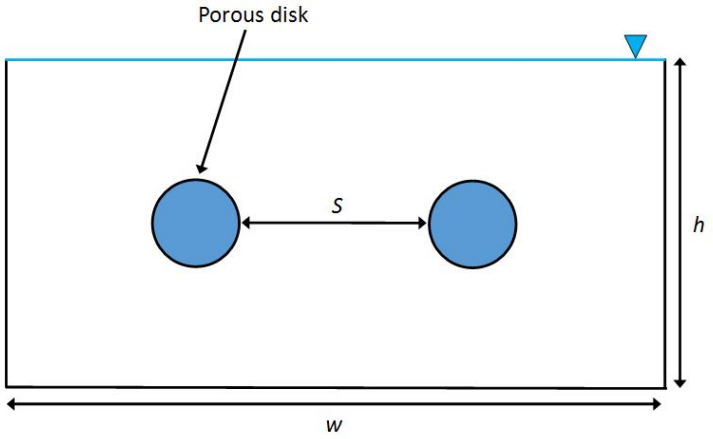

Figure 4.26: Schematic of channel geometry and porous disk spacing at the Chilworth flume (cross sectional view).

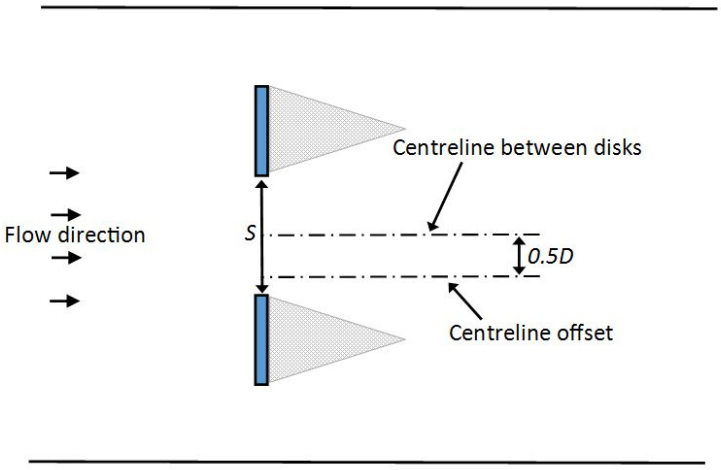

Figure 4.27: Schematic of channel geometry and porous disk spacing at the Chilworth flume (plan view).

at three values for comparison: 0.33, 0.225, 0.175.

Chapter 5

The use of porous disks in small scale testing of marine current energy converters

As outlined in Section 2.1.3 porous disks have been used as small scale device models in laboratory studies of wind and MCEC devices. The validity of porous disk models however has not been studied in detail for MCEC applications and so there are still some uncertainties as to whether they are suitable for use in the small scale testing of MCECs. Although the differences in wake structure of such models have been discussed and investigated, no detailed discussion is yet present which highlights how results from different scale laboratory experiments should be used in the validation of larger scale MCEC performance modelling. There are also some uncertainties surrounding the design of porous disk models which need to be addressed in order to make smaller-scale experiment design easier.

Results presented in this Chapter aim to address these issues which are outlined in Objective 1 in Section 1.5. The detailed method of the experiments conducted in this chapter can be found in Section 4.6.

5.1 The relationship between thrust coefficient and disk porosity

Often the thrust coefficient of a MCEC device model is matched across experimental model scales in order to ensure realistic scaled testing data (discussed in detail in Section 3.1.2). It is important to be able to predict the thrust coefficient of a porous disk in order to plan small-scale experimental studies. Some of the possible methods of calculation for a porous disk model were highlighted in Section 3.1.3 although only one method has

been utilised in MCEC experimental model design. As there is uncertainty of the effects of blockage on thrust coefficient of a device operating in constrained marine flows it is only possible to evaluate these for (relatively) unconstrained flows.

Figure 5.1 presents a number of experimentally measured thrust coefficient values for porous disks of varying porosity in a low area blockage ratio (0.014) flow. The same points are presented with different calculations of resistance coefficient, k, from disk porosity, Θ, based on the relationships outlined by Taylor (1963) and Roberts (1980) (found respectively in Equations 3.8 and 3.9). Also presented in the figure are the correlations between resistance coefficient, k, and coefficient of thrust, C_t, presented by Taylor (1963) and Koo & James (1973) (found respectively in Equations 3.5 and 3.6).

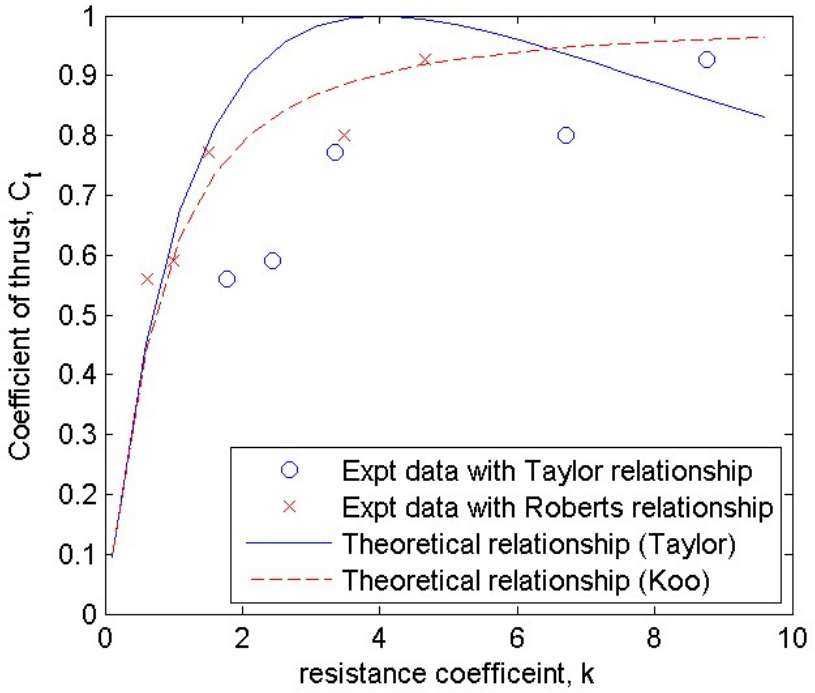

Figure 5.1: Comparison of analytical relationship between Ct and resistance coefficient compared to experimental data.

For the designs of disks used in this work it appears that the use of the relationships proposed by Roberts (1980) and Koo & James (1973) allow a more accurate prediction of thrust coefficient from porosity than that of the relationships posed by Taylor (1963) (used in MCEC laboratory testing work by Whelan et al. (2009)). Variation in porous disk design, such as thickness or sharp/smooth edged pores (discussed by Roberts (1980)), could lead to differences in thrust coefficient of disks with the same porosity value. Hence the relationships presented here may only be valid in experiments where the design of porous disks (described in Section 4.2.2) are similar. The relationships highlighted in this work will only be valid for low area blockage ratio cases, however, the relationships used in this work will be useful in providing guidance to an experiment designer.

5.2 Wake replication using porous disks

This section compares the wakes of a rotating turbine model with that of a porous disk model in facilities with corresponding area blockage ratio (0.063), channel aspect ratio (2) and Froude number (0.19-0.2). The detailed experimental methods employed in this section can be found in Section 4.6.2. Emphasis is placed on understanding the differences in each turbine device wake and how models interact with ambient flow turbulent structures.

5.2.1 Facility ambient flow

Consideration of the ambient flow conditions at each facility are essential in order to understand and fully interpret results obtained when testing each model. Velocity profiles and turbulent structures in the ambient flow can affect turbine performance along with downstream wake formation and dissipation. Flow straightening elements were present in the Chilworth channel but these were removed in some cases in order to test the porous disks under two separate ambient flow conditions. Chilworth A refers to the ambient flow with elements present whilst B refers to the channel with these removed. Table 5.1 compares the ambient flow at each facility. With the flow straightening elements present, in Chilworth A, smaller lengthscales and slightly higher turbulence intensity values are present than in the Ifremer channel. Chilworth B on the other hand shows higher turbulence intensity and lengthscale values. The disparity in turbulence is most likely a result of the nature of the differing inlets at each facility. The turbulence produced by the circulating pumps at the Ifremer facility is reduced with flow straightening structures, whereas at the Chilworth facility the incoming flow is deposited downwards into an overtopping sump which directly feeds the inlet to the channel. Hence in case B the only conditioning of the turbulent structures within the flow is the natural development as the flow propagates downstream within the channel. Fluctuations in both facilities were larger in the streamwise direction than either the lateral or vertical directions; a phenomenon that has been characterised with ADV data at potential tidal sites with channel characteristics (Milne et al. 2013). *Unless otherwise stated the disk results presented within this work will be under Chilworth A conditions.*

Table 5.1: Comparison of ambient flow conditions at the rotor plane in the Ifremer and Chilworth facilities.

	Ifremer	Chilworth A	Chilworth B
Turbulence Intensity, I_{3D} (%)	4.5	5.9	6.3
I ratio ($I_x : I_y : I_z$)	1:0.5:0.2	1:0.9:0.7	1:0.8:0.2
lengthscale, λ_l (m)	0.97	0.02	0.42
normalised lengthscale, λ_l/d	1.21	0.2	4.2

Figures 5.2 show a comparison of the lateral variation in streamwise channel velocity (normalised to the facility average) and turbulence intensity at each facility. The velocity profile at the Chilworth facility is seen to show greater variation across the rotor plane (between the lateral positions of -0.5D and 0.5D). The lateral velocity profile in the larger Ifremer channel showed smaller variation, however these differences are small enough to have little effect on the wake produced once the data has been normalised as is observed later in the lateral wake profile data. 3D turbulence intensity values were greater in the Chilworth facility; point measurements were generally higher than 6% with little variation laterally across the channel width. By comparison the larger channel had measured values between 3-5% with a greater lateral variability.

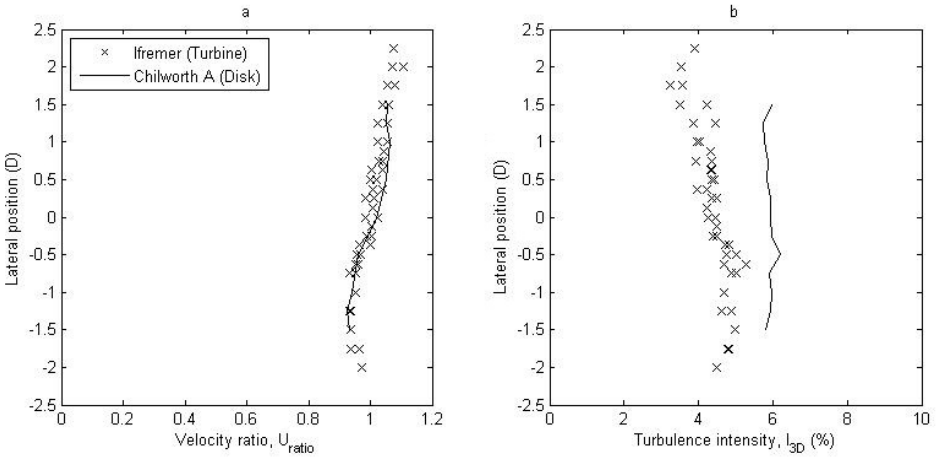

Figure 5.2: Lateral variation of (a) streamwise velocity and (b) three-dimensional turbulence intensity at each facility at hub height.

Figure 5.3 shows the vertical ambient flow profile with no devices present at each facility. The Chilworth facility is seen to have some variation due to the slower moving fluid towards the flume bed, which appears to form a boundary layer. The slower moving fluid in the boundary layer is observed below the rotor plane (i.e. vertical position -0.5D − 0.5D) and so is suspected to have minimal impact on the flow of the device.

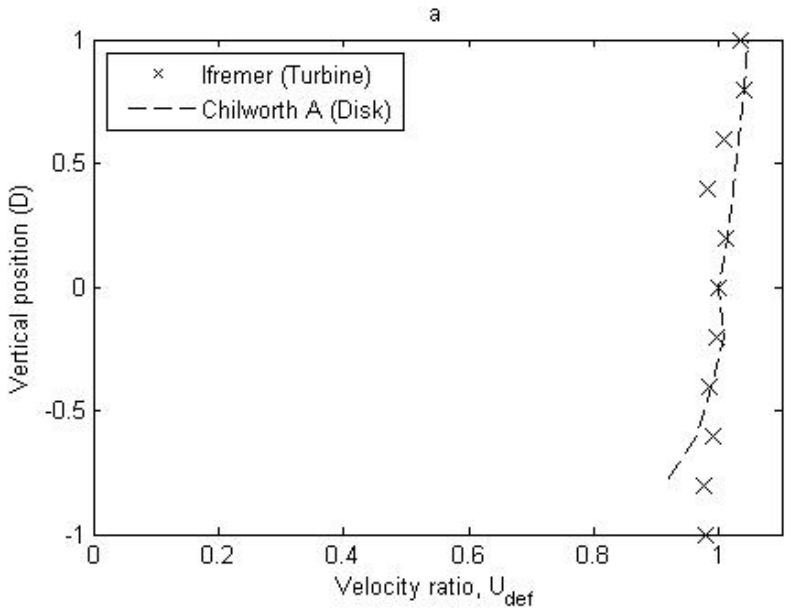

Figure 5.3: Vertical velocity profiles in each facility with no devices present. Measurements taken at the centre of the flume, i.e. 2.5D from channel side walls.

5.2.2 Wake velocity field replication

Figure 5.4 presents values of velocity deficit on the centreline behind each of the devices tested. Values are observed to be of greater magnitude at closer downstream distances to the devices and decay with increased downstream distance, which appears to indicate that the wakes form and recover in a broadly similar manner. Porous disk velocity deficit values are observed to be higher than the rotor model at distances close behind the disk such as 3 disk diameters (D) downstream indicating that slower moving fluid can be present in porous disk models close behind the device. Values are observed to be of similar magnitude between 4-9D downstream. At 10D downstream it appears that the rotating model wake is recovering at a faster rate than either of the porous disk devices. This may be due to the differences in ambient turbulence levels, the difference in model type or differences in vertical migration of the wake due to vertical shear flows. Table 5.2 presents the mean values of velocity deficit deviation. In the near wake, far wake and as a whole the disk of lower Ct produces values which match more closely that of the rotating model.

Table 5.2: Mean difference in centreline velocity deficit of porous disk wakes compared to turbine wake values.

	Ct = 1.07	Ct = 0.82
3-10D	0.034	0.019
3-5D	0.059	0.024
5-10D	0.019	0.016

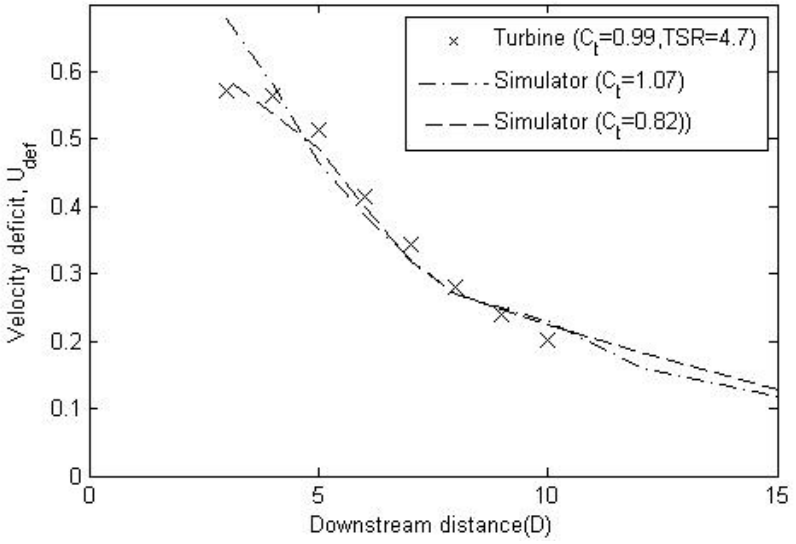

Figure 5.4: Experimental velocity deficit measurements on the centreline behind turbine and porous disks (Chilworth A conditions).

Figure 5.5 presents velocity deficit values laterally at hub depth in the wake of each device. Lateral measurements are presented at 3, 5 and 10D downstream in order to characterise the lateral velocity profiles of each model in areas of the near wake, transition region and far wake respectively. The transition region, defined earlier in Section 2.1, was determined visually from inspecting the velocity profiles and was judged to have occurred on the device centrelines by 5D downstream in each of the devices investigated in this study. The velocity deficit profiles were also inspected for self-similarity at each downstream distance in each case and results showed agreement on the centreline at similar distances of approximately 5D downstream.

Figure 5.5b shows measurements in the wakes on each side of the centreline. The results indicate the wakes are generally symmetrical about the centreline in each facility and so it is acceptable to take measurements only on one side of the wake in order to reduce data acquisition time. Profiles in the near wake, at 3D downstream, show that the porous disk models are capable of producing lateral velocity profiles of similar shape to that of a rotating turbine model. When comparing the two porous disk models greater velocity deficit values are seen in the near wake of the porous disk with larger Ct which, corresponds with greater changes in fluid momentum expected for this device, and has been highlighted by Vermeer et al. (2003). When comparing the porous disk model, Ct = 1.07, to the rotating model of similar Ct, velocity deficit values are observed to be greater in the porous disk model near wake. Velocity profiles in the near wake, when comparing the disk of Ct = 0.82, are observed to have greater similarity to the rotating turbine model. The velocity deficits of both porous disks appear to have decayed at a faster rate than the rotating model at 5D (confirmed in Figure 5.4). Between 5 and 10D downstream the turbine wake appears to recover at a faster rate than either of the

porous disks. At a downstream distance of 10D the lateral velocity profiles of each device wake show the greatest level of agreement. Table 5.3 presents the mean velocity deficit deviation in the wakes of the porous disk models, with respect to those measured in the turbine wake, at 3D, 5D and 10D downstream. Values highlight the greater velocity field similarity of the lower porosity disk to the turbine model. At a distance of 10D downstream small difference is seen in the velocity field of the porous disk wakes.

Table 5.3: Mean difference in lateral velocity deficit values of porous disk wakes compared to turbine model wake.

	Ct = 1.07	Ct = 0.82
3D	0.085	0.064
5D	0.026	0.020
10D	0.015	0.014

The expansion of each wake edge laterally, defined here as the recovery of velocity deficit to 99% of the free stream, is shown in Figure 5.6. Expansion of the wake for each device is observed to occur between 3 and 10D downstream. Although the velocity deficit values previously shown appear to be generally similar between the two disks, differences are observed in the way in which the wakes expand; the Ct = 1.07 disk wake expands laterally at a faster rate in the near wake section, most likely due to the greater reduction in momentum across the disk. By comparison the porous disk of lower Ct and the turbine wake are both observed to expand laterally at a greater rate between 5 and 10D downstream.

Figure 5.7 shows the velocity deficit values at varying depth at 5D downstream in the wake of the turbine model (note differences in turbine operating point: Ct = 0.84, TSR = 3.5) and the porous disk of Ct = 0.82. Similar vertical velocity profiles are observed in each case (shown in Figure 5.7). The peak value of velocity deficit is observed to be higher in the turbine case; however the difference seen would be reduced between the two cases if a greater number of measurement points were taken around the area of maximum velocity deficit in the porous disk wake. The figure is useful in showing that in cases where vertical and lateral blockage ratios are identical (and device Ct and ambient turbulence intensity are similar) that broadly similar vertical velocity profiles are developed when using porous disk or rotating models. As well as the difference in model type (i.e. porous disk or rotating turbine), some differences in wake replication may also be present due to the differences in ambient vertical velocity profile (see Figure 5.3) within the channels studied. One useful point to note is the movement of the turbine model wake in the vertical plane. This has resulted in the maximum velocity deficit occurring above the device centrelines which will affect the apparent rate of wake recovery when viewing Figures 5.4 and 5.5. As a result greater velocity deficit values than those recorded at hub height may be found in either device wake. This could affect the velocity deficit values presented on the centreline or horizontal plane.

The results presented in this section show that porous disks can be used to produce a reasonable replication of the velocity field of a rotating turbine model. The largest differences in velocity field are observed within and towards the end of the near wake region, 3-5D downstream, with larger values of velocity deficit observed close behind the porous disks around the centreline. These differences are likely due to the different wake structures associated with each device type (discussed in detail in Section 2.1). Some differences in lateral wake expansion are observed between disks of different porosity between 3-10D downstream. By 10D downstream velocity deficit values in the wake of the porous disks and the rotating turbine model are observed to be most similar. Beyond this downstream distance wake dissipation is thought to be mainly driven by ambient turbulence levels. The velocity field results indicate that, when placing devices directly downstream of one another in porous disk studies, the minimum downstream separation should be between 5-10D downstream.

The studies presented in this work were conducted in facilities with differing ambient turbulence levels which are known to change the loading and wake dissipation of porous disks and turbine models (as discussed in Section 2.1). If ambient turbulence levels and vertical velocity profile were the same in each of the facilities used in this study then the velocity deficit values may be different from those reported. Therefore the minimum spacing guideline suggested above should be taken as a preliminary value. It may therefore be possible to place devices at closer downstream distances or, on the other hand, greater downstream spacing may be required. Further work is required, controlling the ambient flow conditions in order to clarify this point. It will also be possible to alter the initial wake formation of porous disks by the radial variation of disk porosity. Turbine energy extraction differs radially along the blade length in rotating models and so these changes could allow the initial velocity profiles and wake expansion to be more closely replicated when using porous disks. This approach has been used in small-scale wind tunnel porous disk testing by Aubrun et al. (2013) and has been shown to reproduce the near wake velocity field of a rotating model extremely closely. If specific device wake replication is not the aim of the study then it is suggested that this is not an important consideration in porous disk testing. The current disks (with no significant radial change in porosity) can be utilised in generic studies. These could involve boundary proximity investigations and device spacing studies within multiple device arrays.

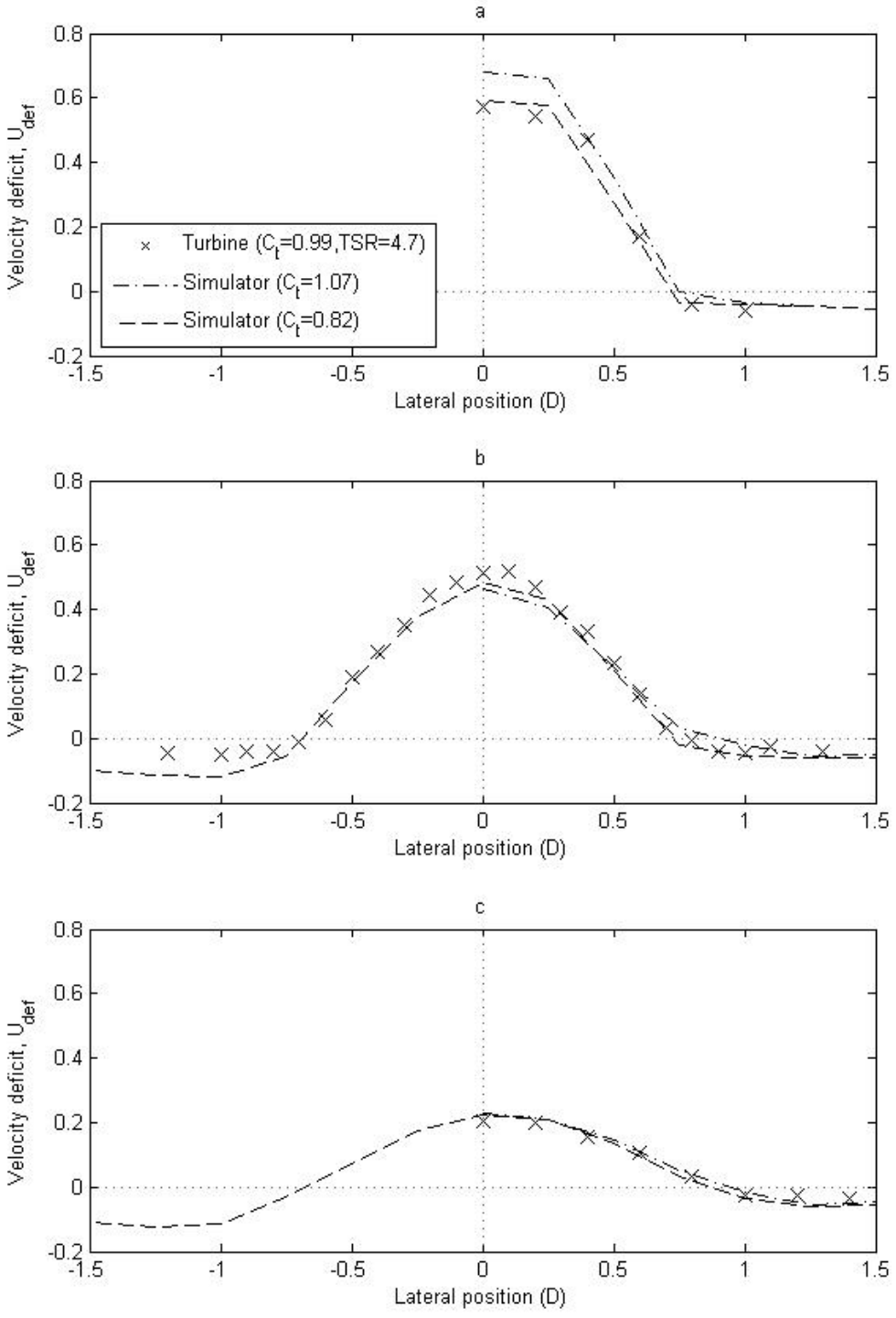

Figure 5.5: Lateral velocity deficit comparisons between turbine and porous disk data: (a) 3D downstream, (b) 5D downstream and (c) 10D downstream. All measurements taken at hub height; 1.33D from the water surface.

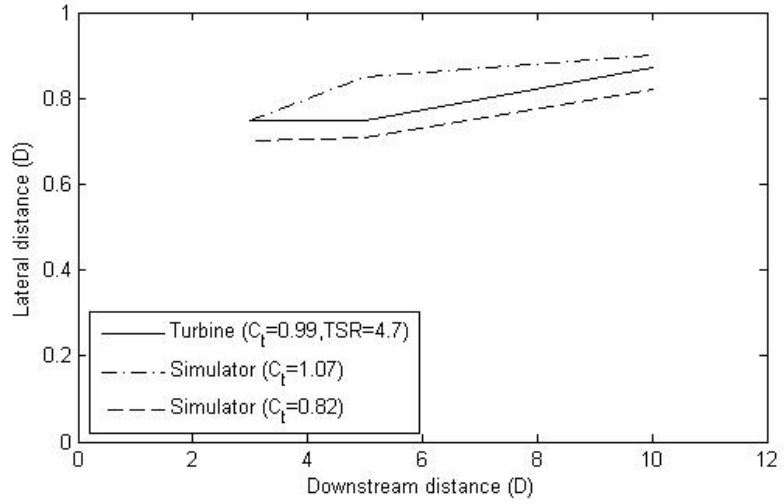

Figure 5.6: Change in lateral wake edge at hub depth with downstream distance. Wake edge is defined as 99% of free-stream values.

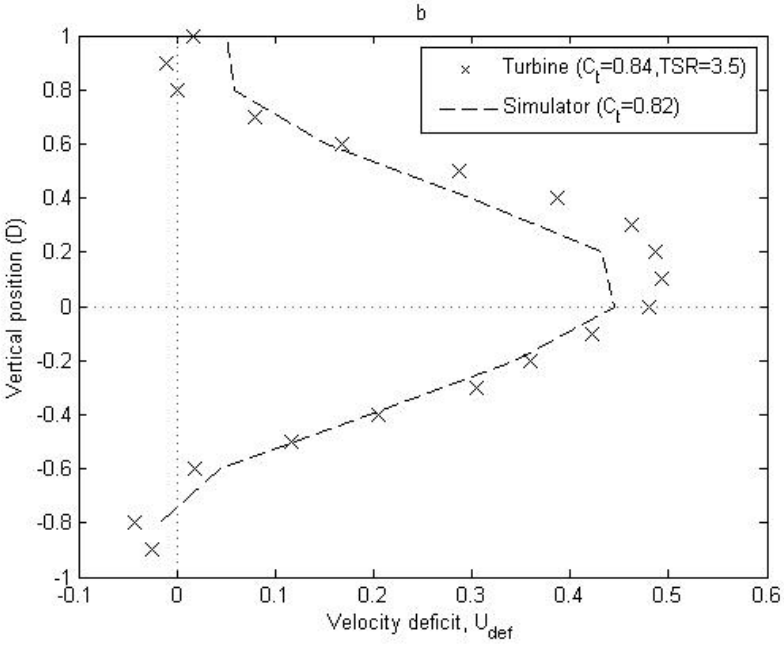

Figure 5.7: Vertical velocity profiles in the wake of each device at 5D downstream (note different turbine TSR). Measurements taken at the centre of the flume, i.e. 2.5D from channel side walls.

5.2.3 Wake turbulence field replication

The differences in wake structure between rotating models and porous disks were highlighted in Section 2.1. The influence of these differences in wake structure on wake development and dissipation are not fully understood. This section investigates the differences in the turbulence structure in order to understand this further.

Figure 5.8 shows 3D-turbulence intensity measurements at hub-height laterally in the near wake, transition region and far wake behind each of the devices previously introduced. Greatest discrepancies between rotating turbine and porous disk models are seen at 3D downstream in the near wake. At the end of the near wake region, 5D downstream, turbulence intensity values for each device at any lateral position agree to within 5 percentage points. In the far wake region at 10D downstream values appear to agree to within 1-2 percentage points. At 3D downstream at a lateral position of 0.2D the value of turbulence intensity is observed to be lower than those around it. This appears to be an anomaly which continues downstream. It is unclear if this is a feature of the flow or a source of experimental error.

Upon viewing the centreline in Figure 5.9 it is seen that values of three-dimensional turbulence intensity are greater in the turbine wake between 5-10D downstream. The porous disk and turbine values appear to converge around 10D downstream, in agreement with the data presented in Figure 5.8c.

Figure 5.10 highlights the nature of the anisotropy of the turbulence on the centreline in the wake of each device. Similar values of turbulence intensity are seen in the x-direction for each device type between 5-10D diameters downstream, however elevated values in y and z directions are observed in the rotating model wake. This could be a result of turbulent structures generated from the swirl in the rotating model case (which are not present in the wakes of the porous disk models) or the differences in the turbulent structures shed directly from each device.

Differences in the turbulent structure of the ambient flow are known to affect device wake formation and recovery. The porous disk devices under consideration were also tested within the Chilworth facility with the flow conditioning elements removed in order to compare results in different ambient flow conditions with the rotating turbine model. Table 5.1 presented a comparison of the ambient turbulent conditions of each flow. Figure 5.11 shows comparison of 3D-turbulence intensity values on the centreline behind the rotating model in the Ifremer flume and the porous disk devices in the Chilworth B ambient flow. With the changes in ambient flow some differences are seen in the near wake turbulence intensity values however the values in the far wake region (5-15D downstream) show little change. This may be due to the relatively small difference in turbulence intensity values measured in each ambient flow. In both ambient flow cases

differences in turbulence intensity value are seen to converge to within 2 percentage points by 8D downstream.

Figure 5.12 shows integral lengthscale values (normalised by device diameter) on the centreline behind the porous disks in the Chilworth A conditions and the rotating model turbine at Ifremer facility. When operating in the same ambient flow the integral lengthscale values observed in the disk wakes appear to be similar in spite of the differences in disk porosity. This may indicate that the changes in wake lengthscale value are relatively small for the range of disk porosities investigated in this study.

Mean streamwise lengthscale values behind the porous disks (average taken from measurements behind each porous disk) are shown for both Chilworth ambient flow conditions in Figure 5.13, and compared to those measured in the rotating model wake. The integral lengthscale behind the porous disk models appears to change based on the ambient flow characteristics. A larger ambient flow turbulent lengthscale value appears to lead to larger lengthscale observations in the device wakes. In the Chilworth A case of the porous disks the maximum integral lengthscale observed in the wake was seen to stabilise around 6D downstream, whereas in the Chilworth B and rotating model wake the values were observed to continue increasing until 10-15D downstream. The relative size of lengthscales further downstream behind each device correspond roughly with those found in the ambient flows; this indicates the possibility that that ambient turbulent lengthscales may pass through both porous disk and rotating turbine model devices in similar manners. It is clear from the results that the ambient flow structures can pass through the porous disk models, which indicates that such models may be suitable for experimental studies looking to characterise the effects of changes in ambient turbulence. Further work will be required in order to characterise these changes in more detail.

Differences in turbulence intensity, turbulence isotropy and lengthscale were found in the wake of the rotating turbine model and porous disk models. These differences are attributed to both the disparity in model type and ambient flow characteristics under which they were tested. In spite of these differences the discrepancies in the velocity field behind the devices were found to be relatively small when considering areas further downstream of the near wake region. This may indicate that the differences in the swirl and turbulent structures in the wake of each device type do not cause significant changes in wake development and downstream dissipation beyond the near wake region. As the near wake turbulence characteristics are not replicated precisely with porous disks, placing devices in any near wake region during array testing would be erroneous. Turbulence field results indicate in array studies it may be pertinent to ensure downstream device spacing of up to 8D downstream or greater, where the wake turbulence characteristics are expected to be most similar to that of a rotating model device. This may be a conservative estimate as it may be reduced if the turbulent

characteristics of the ambient flows in this work were identical. As previously indicated, at the end of Section 5.2.2, further work will be required in order to clarify this.

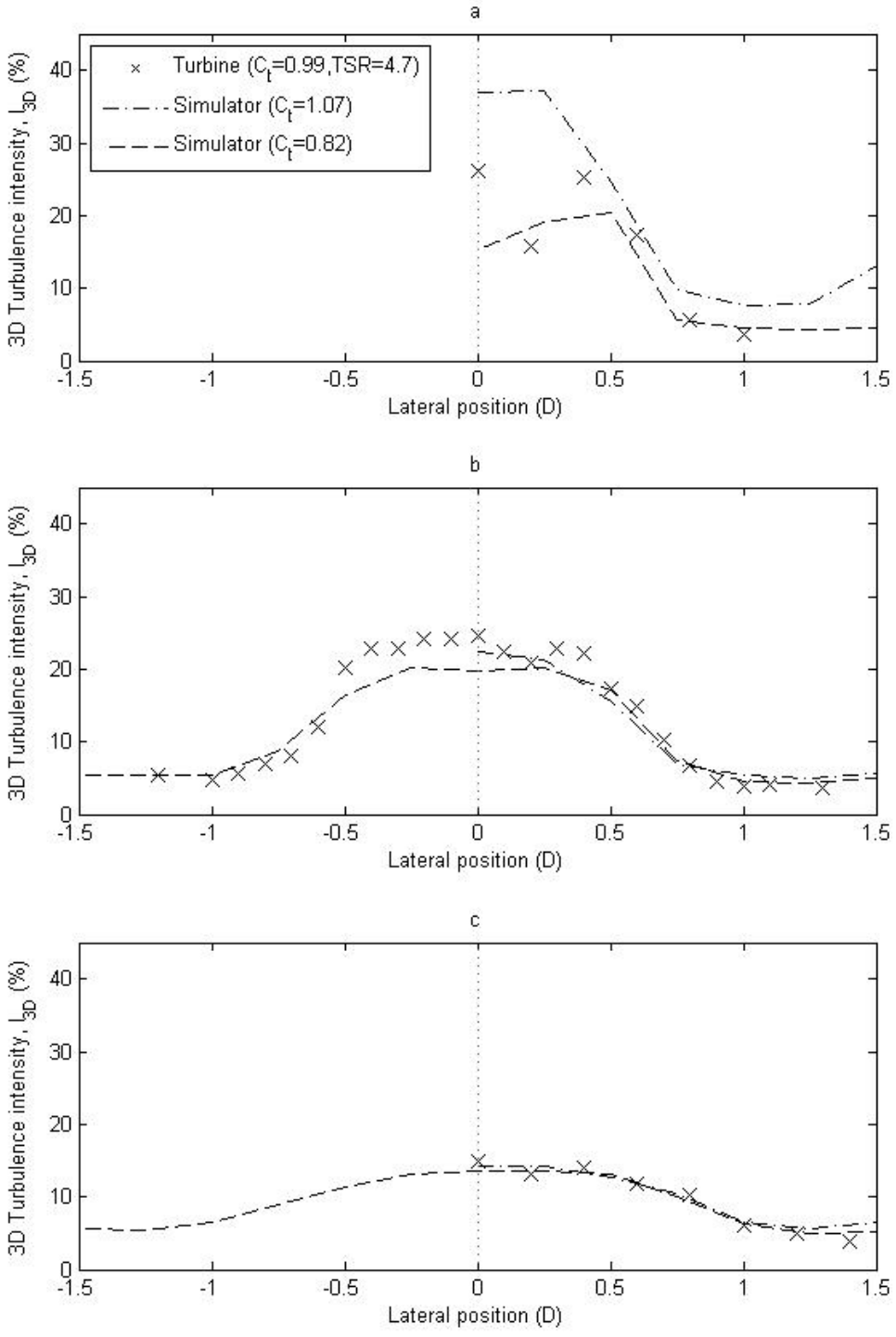

Figure 5.8: Lateral turbulence intensity comparisons between rotating turbine and porous disk data: (a) 3D downstream, (b) 5D downstream and (c) 10D downstream.

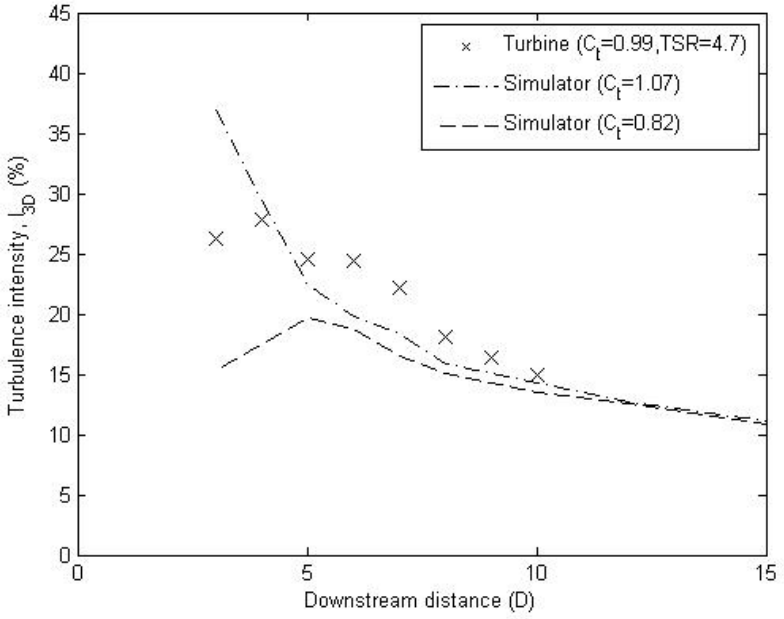

Figure 5.9: Three-dimensional turbulence intensity on the centreline behind each model.

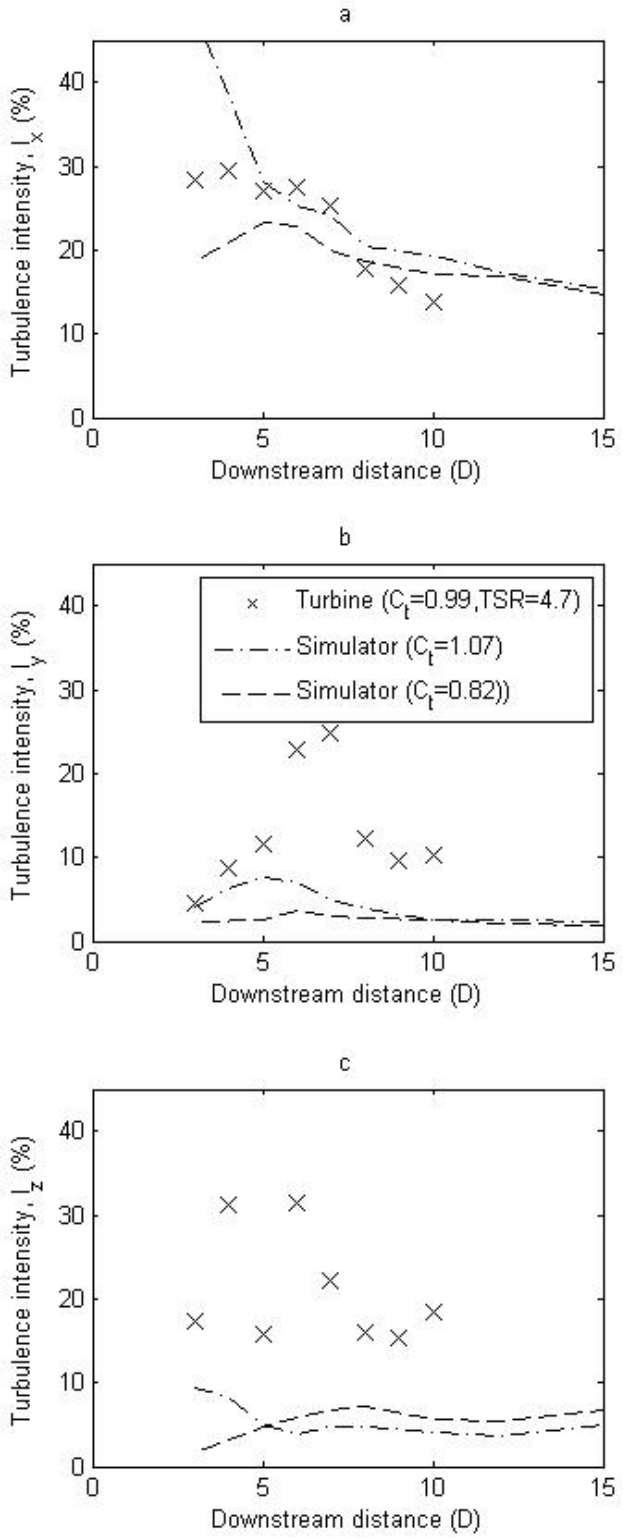

Figure 5.10: Turbulence intensity components in x,y & z direction on centreline in the wake of each device.

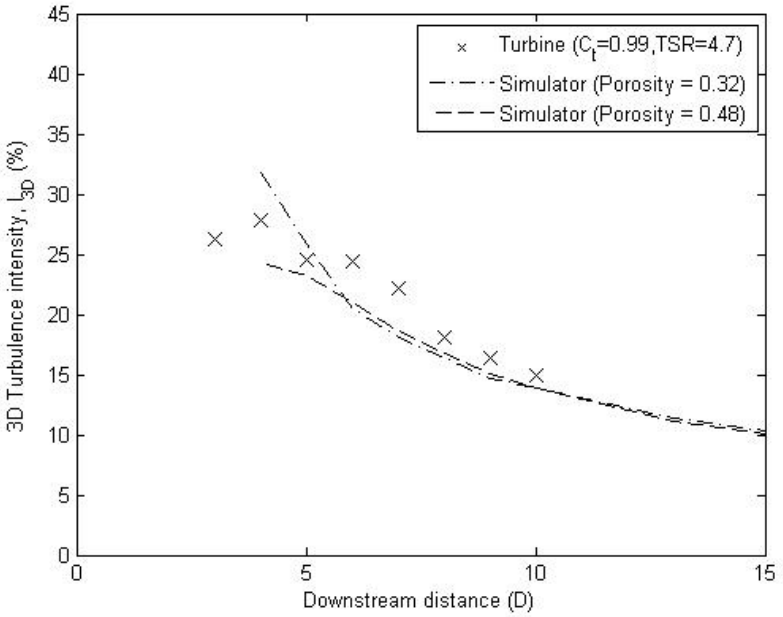

Figure 5.11: Three-dimensional turbulence intensity on the centreline behind each model for Chilworth ambient flow case B.

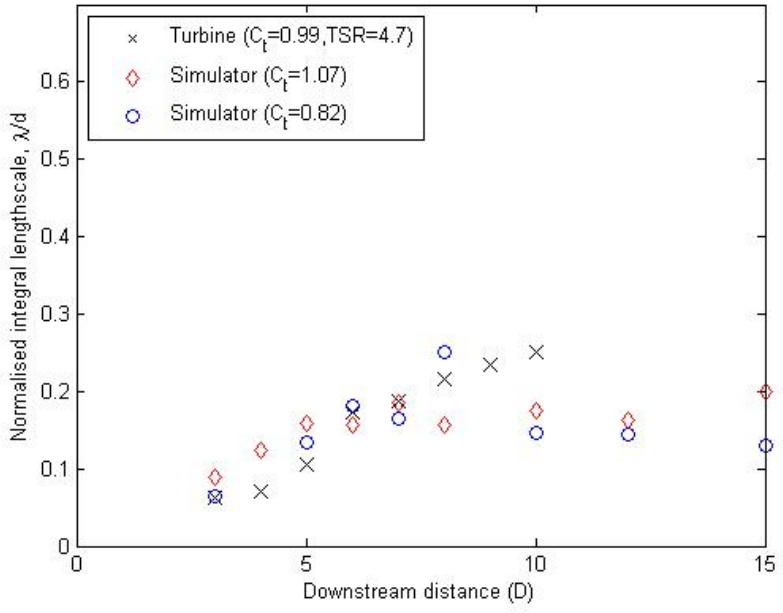

Figure 5.12: Normalised integral lengthscale values on centrelines behind: porous disks in Chilworth A conditions and rotating model turbine at Ifremer facility.

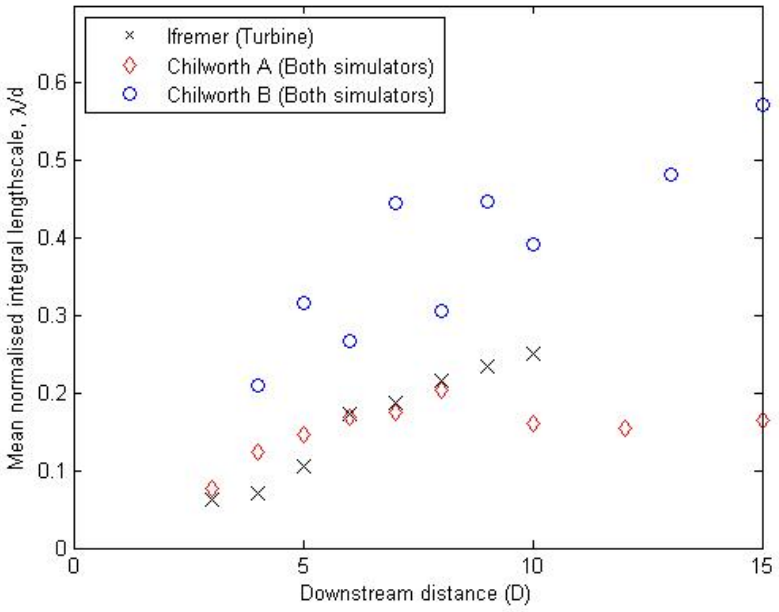

Figure 5.13: Mean normalised integral streamwise lengthscale measurement on centreline behind porous disks, under varying ambient flow conditions in Chilworth facility, and rotating model at Ifremer flume.

5.3 The effects of model scale on the structures within a wake

Figure 5.14 offers a summary of the differences in energy extraction arising in different types of models at various scales; it should be noted that the values depicted in the figure are qualitative estimates only. The method of matching Ct values at different model scales is typically enacted in order to ensure the scaled rate of change of momentum is the same in each case. An attempt to scale Cp is made where possible in order to ensure that a similar proportion of energy is extracted mechanically at each scale. However, even with model Ct and Cp values matched to that of a full scale device, as in a typical 1/20th scale model, it is seen that the distribution of energy in the wake will be different; the difference in this case will be associated with the levels of conversion of streamwise kinetic energy to swirl and turbulence generation in the wake. Greater swirl will be imparted to the flow in the smaller model due to the increased rotational speed of the rotor upon matching TSR. This will be accompanied by a reduction in the turbulence generation across the rotor/blades due to the overall scaled energy extraction being the same at each scale.

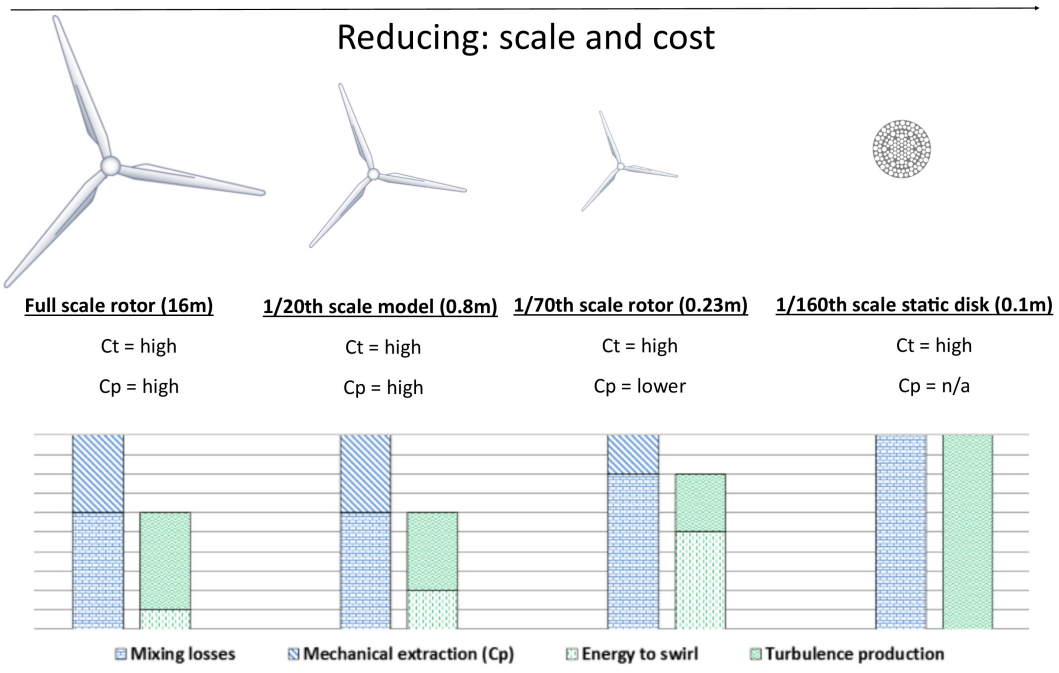

Figure 5.14: Typical energy extraction changes with reducing model size and type, where thrust coefficient is matched across device scales.

Further reduction in rotating model scale, as in a typical 1/70th scale model, will again result in increased levels of swirl within the wake; a higher proportion of the kinetic energy extracted from the ambient flow will have been converted to swirl. Lower Cp values when compared to full scale will also be observed. Hence at this scale the energy typically contained within the device wake is less representative of the full scale device,

as is highlighted in Figure 5.14. Further reductions in the scale of rotating models are difficult as other practical problems un-associated with the hydrodynamic performance issues already described can occur; blade flexing, higher relative drive train resistance and disproportionate component size can impact upon the model design. As such smaller scale models are usually in the form of porous disks. Again if disk Ct is matched these devices also extract the same proportion of energy from the ambient flow as a full scale device; however all of the energy is dissipated through turbulence generation in the absence of any mechanical extraction (i.e. where Cp = 0).

Differences in the proportion/distribution of energy containing structures of each device size/type will lead to variation in the formation and dissipation of a device wake. This will need to be accounted for when attempting to synthesise results from different scales of laboratory testing to inform full-scale prototype device design. For example smaller scale models (regardless of device type) will produce near wake velocity and turbulence fields which should not be expected to match that of larger devices, even when presented non-dimensionally. This realisation marks a change in current thinking, which has been that the type of model is the marker of valid wake replication rather than the scale of model. Although differences are present in the near wake the results presented in Section 5.2 suggest that the far wake velocity and turbulence fields are comparable between porous disk models and rotating turbine models (which match Cp and Ct to that of full-scale devices). The same may be true of small-scale rotating models, however no data currently exists to confirm this. In light of the present discussion MCEC developers attempting to match full-scale CFD site simulations to smaller scale laboratory data should not attempt to match near wake characteristics of models (which do not match the performance values expected in full-scale devices, i.e. Cp and Ct). They should however attempt to replicate device performance values and attempt matches with far wake velocity and turbulence fields. In laboratory studies where performance values of the model are matched to that expected at full-scale, there may still be some difference in the near wake characteristics encountered at each scale.

5.4 The limitations of small-scale models

Laboratory testing can provide valuable insight into the operation of MCECs, in a similar manner previously experienced in the wind industry, which would otherwise not be possible or very expensive to complete offshore. The use of porous disks as in place of rotor models reduces the cost of laboratory testing dramatically and allows the possibility of suitable array testing (minimising blockage ratios) within affordable facilities.

Results show it is possible to replicate the far wake axial velocity flow field behind a rotor when utilising porous disks, both in the vertical and lateral planes, when matching thrust coefficient values. Greater agreement between the velocity field measurements

were found beyond the near wake region (distances greater than 5D downstream) when comparing results from equivalent thrust coefficient porous disk and turbine models. Mean deviation of the velocity deficit on the centreline in the near wake was observed to be within 0.059, for similar thrust coefficient device, and no more than 0.019 in the far wake. At the end of the near wake region (5D) and in the far wake region (10D) mean velocity deficit deviation in the lateral plane was observed to be no greater than 0.026 and 0.015 respectively.

As well as ensuring the far velocity field is accurately replicated when using models it is important to understand the nature of the turbulence field behind each device type in order to understand if porous disk models are capable of suitable wake replication. Differences in the centreline turbulence intensity were found within the wakes of the rotating model and porous disk devices, however values were seen to converge to within 1-2 percentage points in the lateral profiles at 10D downstream. Differences in the turbulence intensity an-isotropy were observed in the rotating model and porous disk wakes which are attributed to the differences in swirl and turbulent structures shed from the devices. No significant differences in 3D turbulence intensity or lengthscale were measured in the far wake of the porous disk models with the changes in disk porosity investigated in this study. Differences in ambient turbulent lengthscale were observed to alter the lengthscale values measured in the porous disk wakes, which indicates such models may be suitable for use in experimental studies looking to characterise the effects of changes in ambient turbulence.

Results show despite the differences in the near wake region the flow field produced by the porous disks, especially in regions of interest for inter-device spacing studies (i.e. the far wake), are representative of a rotating energy extracting turbine. When considering multiple device arrays this study suggests that porous disk models should be placed at a downstream distance of at least 8D in order to ensure that downstream devices encounter realistic incoming flow fields (both velocity and turbulence fields). In light of the differences in ambient flow of the experiments within this work, and the ability to alter porous disk geometry to more closely mimic the extraction of energy from a specific MCEC device, this is thought to be a conservative constraint. When investigating array layouts it is possible at closer spacings that wakes interact and merge within the near wake region. Although in the case of an isolated device the difference in near-wake turbulent structure appears to have limited impact on the far-wake it is less certain that this will also occur in arrays where multiple device wakes have merged. Here the differences in turbulent structures (due to model type or scale), which end up interacting could affect the wake development and dissipation in a different manner to devices of larger scale. This uncertainty could be expected for any small-scale model device, regardless of device type (i.e. either a small-scale rotating model or porous disk).

It is important that device modellers using results from different laboratory testing scale are aware of the differences in wake structures highlighted in this work. It would

be sensible in full-scale device numerical models to only replicate the far wake velocity field characteristics of smaller scale laboratory results if they wish to calibrate/validate full-scale models. Comparative studies, similar to the one presented here, are needed for smaller-scale rotating models in order to ascertain the differences in wake structure and velocity field replication when compared to full-scale devices. This will allow further discussion of how to infer laboratory scale results to larger scale models and hence will further aid in the accuracy of full scale device performance prediction.

Whilst porous disk models may be limited in the validation of full-scale performance models in this way, their use does mark a significant increase in the range of conditions in which current numerical models may be validated with the current lack of full-scale/offshore MCEC data. Porous disk laboratory models allow experimental testing of much reduced complexity, with lower working cost, at a wider range of flumes due to lower blockage ratios. The method provides the opportunity to investigate some of the fundamental parameters affecting device performance and wake development, along with complex arrangements of devices likely to be deployed in the future, which would not otherwise be possible with larger facilities and models.

5.5 Summary and further work

- An alternative method of relating disk porosity to expected thrust coefficient is shown to give better relationship than previous methods used (Whelan et al. 2009).
- A detailed comparison of the velocity and turbulence field behind turbine and smaller-scale porous disk experiments shows comparable wakes in the far wake region. The results indicate the minimum downstream spacing porous disk devices should be placed in order to allow valid experimental conclusions to be drawn from porous disk laboratory testing should be at least 8D. This may be a cautious value due to the differences in ambient flow turbulence, which is likely to affect far wake dissipation.
- The integral lengthscale values behind porous disk models are shown to be sensitive to the turbulence levels present in the ambient flow. Which indicates porous disk models may be suitable in studies investigating effects of ambient turbulence on MCEC device wakes.
- As well as the type of model (i.e. porous disk or rotating turbine) the scale of a model will also have a bearing on the wake replication. Developers should only attempt to match the near wake flow field in numerical models in cases where Cp and Ct are accurately scaled.
- Further work is needed comparing smaller-scale rotating model and porous disk devices at the same scaled ambient turbulence conditions in order to more precisely

inform the downstream distances at which models may be placed in order that they operate in flow fields realistic to those that would be encountered within a full-scale offshore array. Work is also required to understand the differences in merged downstream wakes of small scale-devices which do not have near wake structures representative to those of full-scale devices.

Chapter 6

Energy extraction from open channel flow

Results presented in this Chapter aim to answer Objective 2 outlined in Section 1.5 and are the result of the Investigation 2 experiments outlined in Section 4.6.

6.1 Changes in free surface height as a result of energy extraction from an open channel

Many studies have neglected the change in surface height that is accompanied with energy extraction from an open channel flow, e.g. Turnock et al. (2011), Nishino & Willden (2012*b*), Schluntz & Willden (2013), Hunter et al. (2013), Schluntz et al. (2014). However little is understood about at which blockage ratios significant changes in free surface elevation will occur, and hence under what conditions this assumption is valid. It was highlighted in the literature review that little experimental work has been completed to understand the changes in free surface elevation as a result of energy extraction from an open channel. The effect of Froude number on energy extraction and device loading similarly needs to be experimentally studied in order to better understand the relationships between these parameters. This section investigates changes in free surface height with varying energy energy extraction using porous fence models at a range of Froude numbers. The experimental methods used are outlined in Section 4.6.

6.1.1 Experimental observations

Figures 6.1a and 6.1b show the changes in free surface height that occur with the presence of a fixed porosity fence operating at the same area blockage ratio (0.66) within an open channel. The channel free surface upstream and downstream is highlighted in red. The

difference in Froude number in each case highlights that differences in the open channel behaviour can occur with variation of this non-dimensional parameter.

The lower velocity case, Froude number = 0.11 (Figure 6.1a), shows minimal surface deformation over the fence itself and a relatively small reduction in channel depth, measured as $\approx 3.5mm$, when comparing depths upstream and downstream of the fence. In the higher velocity case, Froude number = 0.22, both greater variation in surface height directly behind the fence and greater difference in channel flow depth when comparing upstream and downstream of the fence ($\approx 16mm$) were observed. These observations respectively indicate a greater local Froude number within the bypass flow, and greater overall energy extraction from the channel is present in the channel of greater velocity (or Froude number). This shows that free surface height changes are dependent on channel Froude number. The percentage change in free surface height for the two cases of different channel Froude number were $\approx 2.3\%$ and $\approx 10.7\%$ respectively.

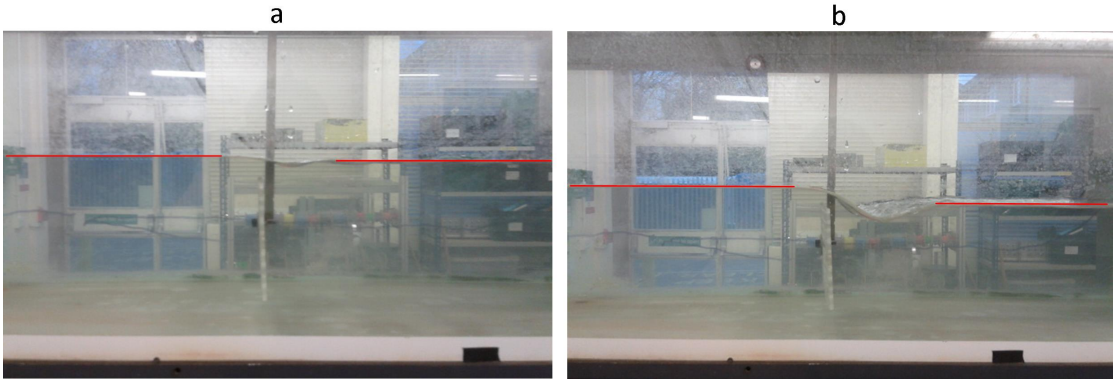

Figure 6.1: Surface deformation behind porous fence operating at $B = 0.66$ in a channel with: (a) $Fr = 0.11$ and (b) $Fr = 0.22$.

6.1.2 Loading and free surface elevation measurements

Figures 6.2a and 6.2b show the fence thrust coefficient and channel depth change with variation in channel Froude number for three different area blockage ratios (0.33, 0.5, 0.66). Figure 6.2a indicates that for a fixed area blockage ratio fence thrust coefficient is a function of Froude number. Increases in Froude number from values of 0.05 to 0.15, see an increase in thrust coefficient value of around 25% for the 0.33 blockage case. Greater increases are observed in the higher blockage cases for the same Froude number range; increases in thrust coefficient of 40% are observed when area blockage ratio is equal to 0.66. This indicates a greater variation in thrust coefficient with channel Froude number in cases where area blockage ratio are higher and proves that thrust coefficient is a function of area blockage ratio and channel Froude number. It is also noted that the increases in thrust coefficient do not correspond directly with the square of the change in velocity (as would be expected based on the analysis presented in Section 3.3.1, for an

unbounded flow). For example, in the area blockage ratio equal to 0.33 case discussed above the increase in Froude number (0.05-0.15) seen would correspond with an increase in velocity by three times. The expected increase in thrust coefficient in an unbounded environment would therefore be nine times the value, however only 25% increase is observed. The reason for this disparity is that the relationships for unbounded LMADT are no longer valid in the bounded case. Further discussion of bounded LMADT, with regard to these experimental results is included in Section 6.2.

As detailed in Section 3.2 changes in water surface show velocity head which subsequently "recovers" downstream. The difference in upstream and downstream channel depth indicates the level of energy dissipated from the open channel. Figure 6.2b shows larger changes in channel depth with increasing Froude number. Therefore, for a fixed area blockage ratio, greater levels of energy extraction will occur in channels with greater Froude number. The results also show that higher levels of area blockage ratio are also associated with greater levels of energy extraction. Changes in channel depth are observed to be greatest at the highest Froude number and blockage ratio. At an area blockage ratio of 0.66 and Froude number of ≈ 0.2 an 8.5% reduction in channel depth was observed over the fence.

Energy extraction from the channel is seen to continue increasing with increasing Froude number over the range investigated. Thrust coefficient however does not continue increasing over the same Froude range. Changes in momentum over the disk plane will correspond to increases in thrust. Hence the further energy loss must be occurring downstream of the disk within the channel. This may indicate that more energy is being lost due to wake mixing in higher Froude number flows.

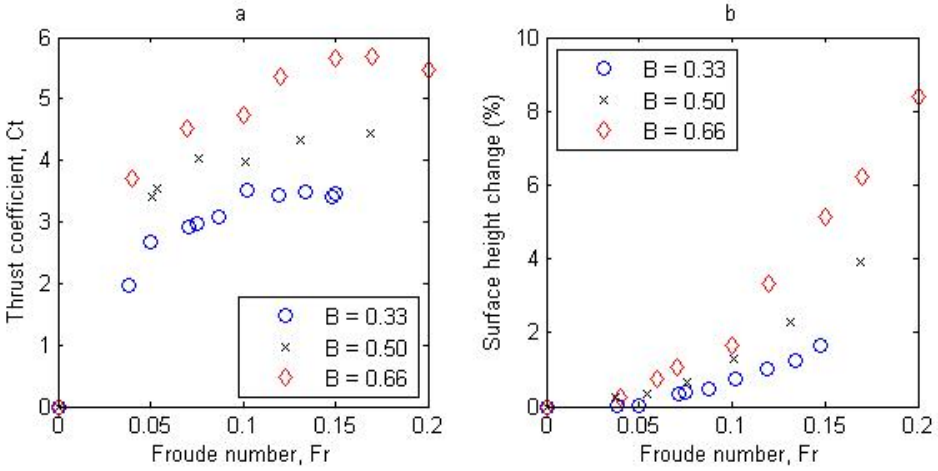

Figure 6.2: (a) Changes in fence thrust coefficient with Froude number and area blockage ratio and (b) Variation in fence thrust coefficient and channel depth with variation in channel Froude number and fence area blockage ratio.

Section 1.3.1 discussed the different device deployment options currently being considered for full-scale deployments. It is possible that the experimental results detailed here

may be applied directly with some of these deployment scenarios (e.g. the development at Eastern Scheldt, Netherlands, by Tocardo). The results may be used directly to inform these cases of possible levels of surface deformation and increased device loading with different area blockage ratio and variation in channel Froude number deployments.

The results are also useful in relation to understanding the validity of some numerical studies such as that of Schluntz & Willden (2013) and Hunter et al. (2013). The numerical models in these studies do not model the free surface and are known as 'rigid lid' models. Area blockage ratio values of 0.35 (the full domain) and 0.26 (locally within the array) are investigated in these studies. At the Froude numbers expected in tidal flows (see Section 3.2), around 0.11 or greater, significant variation in coefficient of thrust and surface deformation is observed at corresponding blockage ratios (0.33). The experimental results presented here clearly show an increase in device loading in open channels is associated with an increase in surface deformation. Hence it may be possible at such high area blockage ratio values investigated in the studies above that the assumption of a 'rigid lid' does not allow accurate performance modelling of the devices.

The experimental results presented have shown that device loading is a function of both channel Froude number and area blockage ratio. The changes in Froude number are shown to have significant differences on normalised device loading. One-dimensional analytical models which are unable to take into account Froude number, such as that presented by Garrett & Cummins (2007) will therefore be unable to accurately predict device performance and loading. The error in these models will be expected to increase with increasing blockage and channel Froude values due to greater changes in channel surface height. One-dimensional models which use the same principles but apply to tidal fence array arrangements, such as Nishino & Willden (2012*b*) and Nishino & Willden (2013), will suffer from the same limitations.

6.2 Validation of analytical model with deforming free surface

Whelan (2010) uses the equation 6.1, in conjunction with the free surface model introduced in Section 3.3.3, to compare the predicted performance values with porous disk/plate experiments. The same methodology was used to compare the results presented in the previous section to that of the free surface model. The comparison is shown in Figure 6.3.

$$k = \frac{C_T}{(1-a)^2}. \tag{6.1}$$

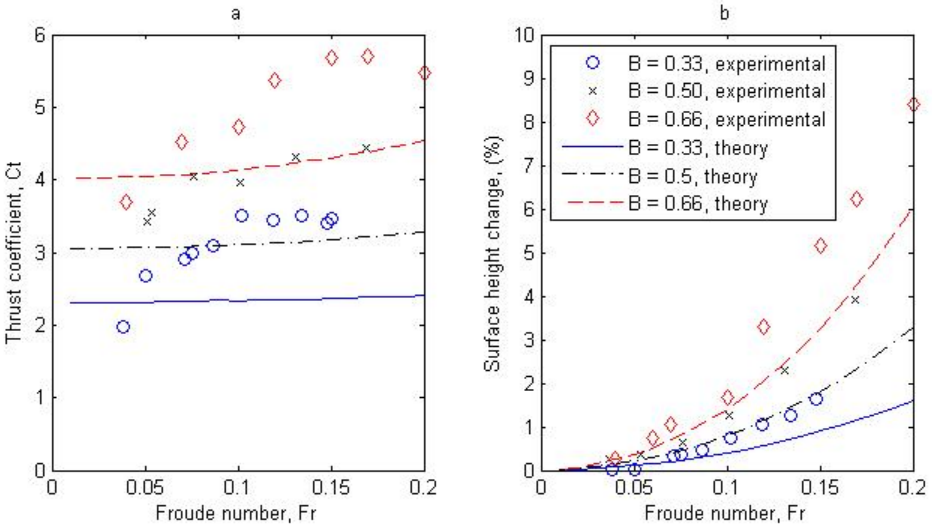

Figure 6.3: Comparison of experimentally measured Ct and free surface height change with analytical free surface model prediction.

For each of the area blockage ratio cases investigated the free surface model is seen to underestimate the device loading and change in free surface height. These differences are observed to be as large as 30% in some cases. These results show greater differences between predicted loading and experimental measurements than those presented by Whelan (2010) when using a similar validation method. In the validation study by Whelan (2010) the free surface model is observed to over-predict the loading which is in disparity to the study presented in this work. Differences could arise from experimental error or variation in fence design, leading to the use of incorrect values of resistance coefficient, k, being used to evaluate the model. Experimental error in the results presented in this work is ruled out as no source of systematic error large enough is considered to be present within the experimental method. Variation in porous fence model design could have had some effect on the energy extraction and hence the thrust coefficient and changes in surface height. However sensitivity analysis performed on the model by utilising differing values of resistance coefficient value showed that only (unrealistic) resistance coefficient values ($k > 12$) would come close to predicting the levels of energy extraction observed in the experiments.

As outlined in Section 3.3.1 classic one-dimensional LMADT requires a correction at high axial induction factor values in order for accurate thrust prediction. When applying the free surface model within a BEM model Whelan (2010) shows at higher tip-speed ratios thrust and power coefficients were under predicted when compared to rotor experimental results. The known limitations of LMADT models, namely that a reversed flow state will occur at higher axial induction factor values, appear to explain the lack of agreement between experimental and theoretical model in this case.

The results presented in the present work represent low porosity porous fence experiments (i.e. a high resistance coefficient) which in unbounded flow would correspond

with higher axial induction factor values. In flows of greater area blockage ratio axial induction factor values are seen to be reduced for the same porosity (or resistance coefficient) due to the presence of channel walls (which would also be expected in the case of a rotating device). The under prediction of the energy extraction and thrust coefficient shown in these results indicate that under blocked conditions the range of axial induction factors that the LMADT model is valid are reduced. Figure 6.4 illustrates the experimental cases investigated (along with the known limitations of unblocked LMADT) in relation to area blockage ratio and Froude number. If the experiments conducted in the present work are assumed to be cases where the model is not valid the plot gives an understanding of the range of valid axial induction factor values where the free-surface LMADT model can be used in varying area blockage ratio and Froude number cases. It is clear the original LMADT valid region of a < 0.5 no longer applies in blocked cases, as values are not predicted accurately at axial induction factor values below this limit in some cases. It is also clear from the results that the limit of validity will be dependent on the resistance coefficient of the device. Beyond the valid region indicated empirical corrections will be required to allow accurate performance prediction of thrust and power coefficients.

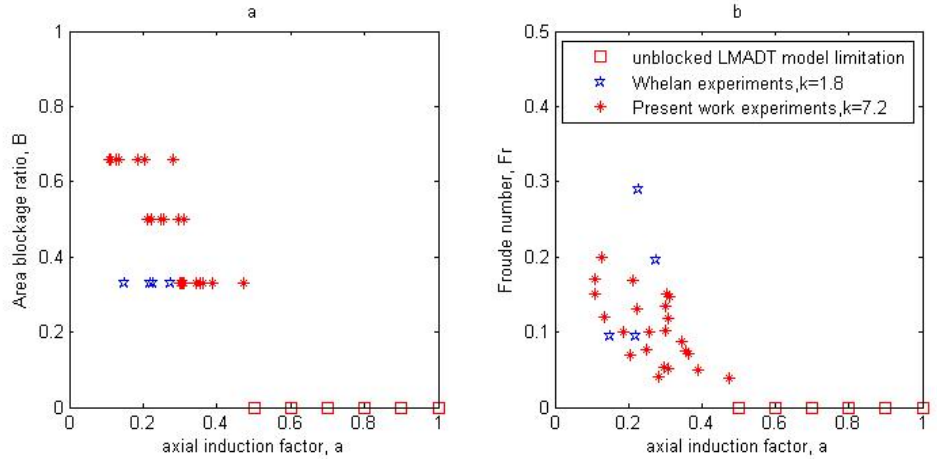

Figure 6.4: Experimental variation in axial induction factor with (a) blockage (b) Froude number.

It is important to make the distinction surrounding the valid limits of the LMADT model as some CFD studies (Turnock et al. 2011) have concluded that the free surface does not need to be modelled based on calculations using the one-dimensional free surface model under discussion presently. As the LMADT model is shown to under predict energy extraction and hence surface height changes it is important to understand the limits of the model validity in order to ensure that invalid assumptions underpinning CFD modelling are not made.

6.3 Validation of blockage corrections

Experiments were also carried out on circular porous disk models operating in channels of square cross section, the methodology of which is included in Section 4.6. Figure 6.5 shows the variation of thrust coefficient of a single porous disk operating in channels of varying area blockage ratio with channel of aspect ratio equal to one. An increase in thrust coefficient is observed with increases in channel area blockage ratio as expected. An increase in Ct of 83% is observed when comparing the least (area blockage ratio equal to 0.05) and most heavily blocked cases (area blockage ratio equal to 0.35) investigated. Area blockage ratio values towards the larger magnitude are only likely to be encountered in some deployment scenarios. Conventional horizontal axis machines are likely to operate within the region of area blockage ratio equal to 0.2 or lower (corresponding roughly to a gap between rotors of one diameter or greater). In the figure thrust coefficient values are observed to be 28% greater at an area blockage ratio of 0.2 rather than 0.05, indicating that the effects of blockage could be a significant source of increased loading for horizontal axis MCECs operating at area blockage ratio values of less than 0.2.

As outlined in the literature section blockage corrections have been applied to MCEC devices to remove the effect of blockage from thrust values and provide thrust measurements equivalent to operating in free stream flow. Both the method proposed by Whelan (2010) and Bahaj, Molland, Chaplin & Batten (2007) are applied to the experimental data in Figure 6.5. A reduction of thrust coefficient is observed in both cases. Both methods show a similar trend of corrected values with Ct increasing with increasing blockage. With a successful correction one would expect all area blockage ratio cases to reduce to the same value of Ct. Increases of 24% and 22% (Whelan (2010) and Bahaj, Molland, Chaplin & Batten (2007) methods respectively) were observed when comparing to the smallest value obtained in each correction case. This magnitude of difference indicates that the correction methods are limited in their accuracy of device thrust prediction.

Channel Froude number did change across the cases investigated. A small variation in Froude number was observed (ranging between 0.14-0.18) from the lowest to highest area blockage ratio case. The change in Froude number was accounted for in the Whelan correction, however as shown in Figure 6.5 the correction does not account for this change. Changes in the relative size of the boundary layer will also have affected the thrust coefficient values calculated, however this was accounted for by taking the average of nine upstream velocity measurement points across the disk area in order to calculate the thrust coefficient values.

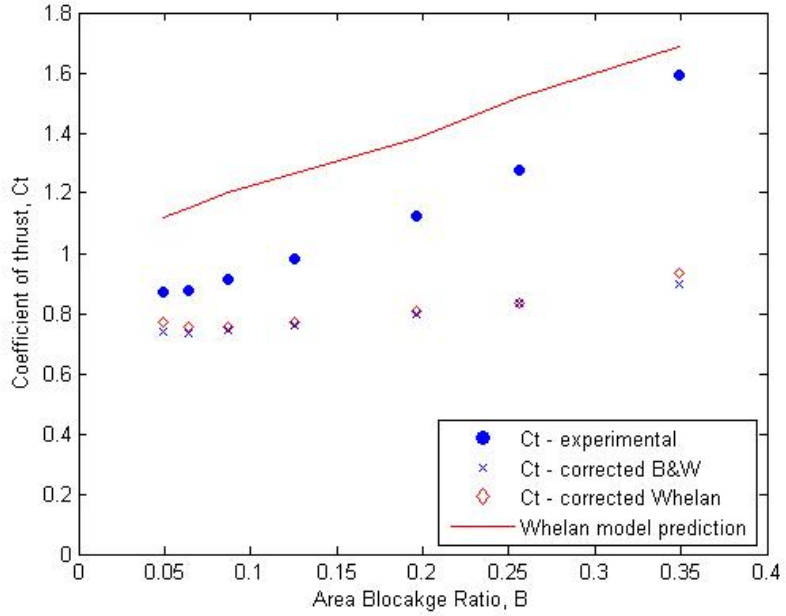

Figure 6.5: Coefficient of thrust variation in channels of varying area blockage ratio and aspect ratio = 1.

6.4 Aspect ratio: a new non-dimensional parameter

Experiments were also conducted on a single device operating in channels with non-square cross section i.e. varying aspect ratio. Here channel Froude number was fixed. Figure 6.6 shows the relationship of measured thrust coefficient with changes in channel aspect ratio at two different area blockage ratio values (0.08 and 0.05). In each blockage case significant variation is seen in thrust coefficient values with increases of upto 29% from values recorded where channel aspect ratio is equal to one. In both blockage cases increases in channel aspect ratio result in an increase in thrust coefficient value until a peak value is reached, after which further increases in channel aspect ratio lead to a reduction in thrust coefficient. Peak thrust coefficient values are recorded at different values of channel aspect ratio in channels of differing area blockage ratio but appear to show similar magnitude of increase in thrust coefficient value.

Figure 6.7 gives an indication of the possible reason for these changes in thrust coefficient in the case where the area blockage ratio is equal to 0.08. The figure depicts the differences in the bypass flow region with changes in channel aspect ratio. The red arrows indicate qualitatively the size of the flow acceleration expected in the bypass flow in each case. For the channel where aspect ratio is equal to one the bypass region flow acceleration in the vertical and lateral planes is similar due to the symmetry of the channel depth and width. In the case where channel aspect ratio is equal to 2.25 the depth reduction leads to a greater 'blockage effect' in (only) the vertical plane; here the presence of the free surface and the channel bed are in closer proximity to the disk resulting

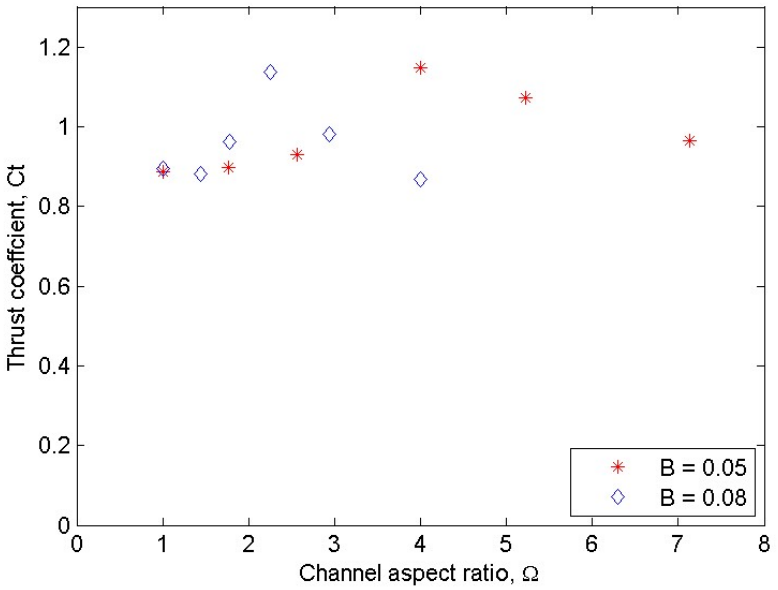

Figure 6.6: Variation in thrust coefficient with channel aspect ratio at fixed area blockage ratio values of 0.08 and 0.05.

in greater flow acceleration in the bypass flow region in the vertical plane. The increased flow rate in this region corresponds with an increase in the fluid flow rate through the disk, increasing disk thrust coefficient. The lateral plane does not see an increase in the fluid velocity in the bypass flow region due to the reduced 'lateral blockage' in this plane (the channel side walls are at greater distances from the disk in comparison to the earlier case). With further increases in channel aspect ratio (e.g. channel aspect ratio equal to four) a reduction in flow in the vertical plane is observed due to the increasing 'vertical blockage', the fluid in the channel can pass more easily around the disk in the lateral plane due to the increased distance between sidewalls and disk. This reduced 'lateral blockage' results in only a small increase in the bypass flow region fluid velocity. Differences in flow around individual devices in the vertical and lateral planes may also lead to additional cyclic loading of individual blades in rotating devices. Further work will be needed to ascertain if this could be a significant source of increased individual blade loading.

In order to simplify the problem it is possible to plot thrust coefficient against the product of the two non-dimensional channel parameters: area blockage ratio and aspect ratio. This maintains the non-dimensional axis, the result of which is shown in Figure 6.8. It is clear the results show broadly identical behaviour with each fixed area blockage ratio series sitting closely together. This similarity is an important phenomenon and in this case gives indication that all of the important non-dimensional parameters of the problem have been considered. Upon considering this the equation:

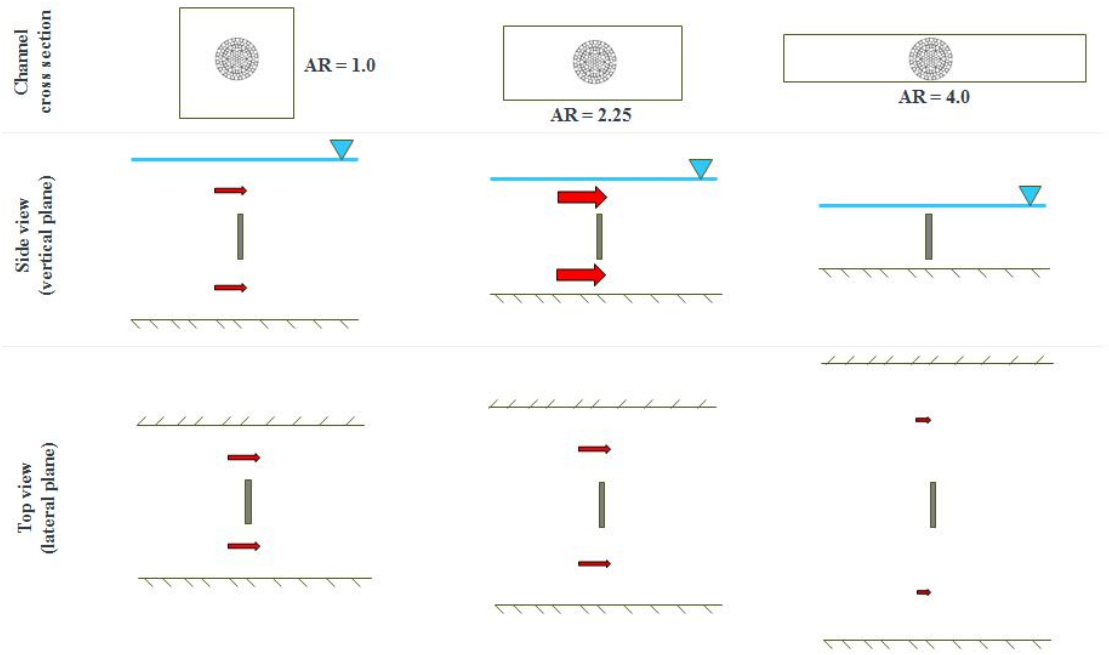

Figure 6.7: Changes in flow acceleration in the lateral and vertical planes around a single disk within a channel of varying aspect ratio.

$$C_t = f(\Omega, B) = f(\frac{w}{h}, \frac{\pi d^2}{4hw}), \tag{6.2}$$

can be further simplified to

$$C_t = f(\Omega B) = f(\frac{w}{h}\frac{\pi d^2}{4hw}) = f(\frac{\pi w d^2}{4h^2 w}) = \frac{\pi}{4} f(\frac{d}{h}). \tag{6.3}$$

The resulting equation 6.3 implies that for a circular device operating in a channel of any rectangular cross section (at a fixed Froude number) the thrust coefficient of the device will be a function of only the device diameter to water depth ratio (d/h). Therefore the LMADT models of Whelan et al. (2009) and Garrett & Cummins (2007), although being inherently one-dimensional, can be utilised in two-dimensional applications as they are capable of accounting for changes in thrust coefficient due to differences in aspect ratio. When using such models the overall area blockage ratio as defined in Equation 2.1 should be used. It should be noted that all of the experimental data collected in this section were collected at a Froude number of 0.2. It is likely in light of the results presented in Section 6.1 that differences in the trends found here may be observed if operating the same experiments at a different Froude number. Peak thrust coefficient values in Figure 6.8 are observed where the product of channel aspect ratio and area blockage ratio is equal to a value of 0.2, which corresponds with the Froude value. Further work is required in order to ascertain if this is the case for any value of Froude.

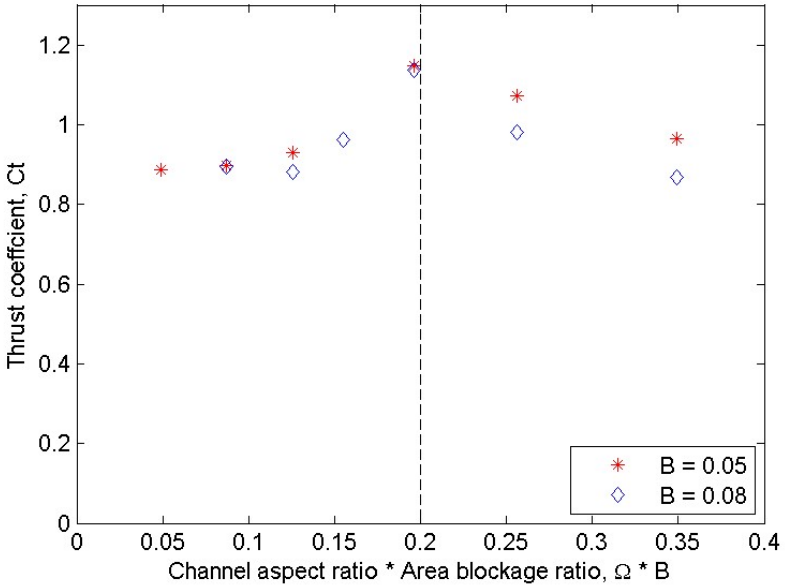

Figure 6.8: Variation in thrust coefficient with the product of channel aspect ratio and area blockage ratio, $\Omega \times B$.

The above section describes the results of a single device operating within a channel. However the results can possibly also be applied to multiple devices operating within an array when spaced in longitudinal arrangement (i.e. on the same inflow plane). This may be assumed due to the symmetry plane methods commonly invoked in numerical fluid dynamic simulations. The importance of single device results on that of multiple device arrays is highlighted in Figure 6.9. It should be noted that this assumption will only be valid in large MCEC arrays where the devices are far from the end of the array. The results in this section therefore have significance when considering the validity of one-dimensional LMADT array models, such as those presented by Nishino & Willden (2012*b*) and Nishino & Willden (2013). The results presented here imply that such models are capable of accounting for differences in channel cross section.

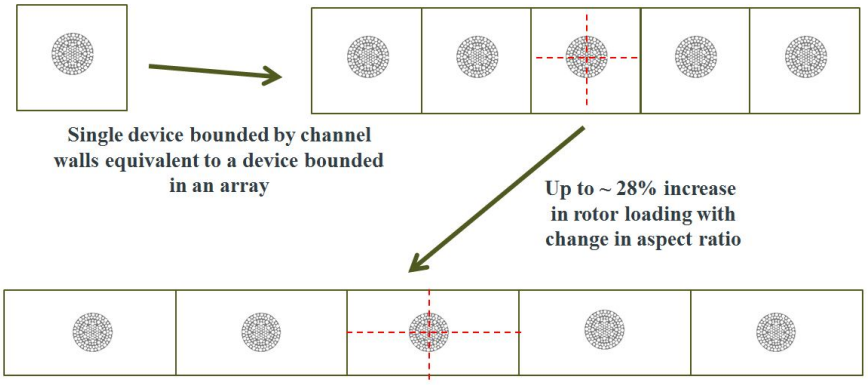

Figure 6.9: Significance of single device results in MCEC arrays.

6.5 Summary and further work

- This work is the first experimental study which clearly indicates that turbine operation in environments with greater area blockage ratio will incur variation of normalised device loading which is dependent on channel Froude number. The values of the channel area blockage ratio and Froude number are shown to affect normalised device loading significantly; increases are observed at greater blockage ratios and greater Froude numbers. The variation in free surface height change over an energy extracting device is shown to be dependent on the Froude number and area blockage ratio.

- The one-dimensional analytical model, which incorporates free surface deformation given by Whelan et al. (2009) is shown to not predict device thrust accurately at a particular level of energy extraction. The results demonstrate that the known limit of validity of original LMADT (i.e. $a < 0.5$) is not suitable in bounded flow cases. The range of axial induction factor values over which the model is valid is observed to reduce with increasing area blockage ratio. Further work is required to ascertain how the limits change with device flow resistance.

- Current one dimensional blockage models are capable of aiding somewhat in the normalisation of results between experiments conducted under varying blockage conditions, in channels of square cross section only. However the models cannot be used to make reliable estimates of device loading. Results show the area blockage ratio corrected values could show a difference of up to 22%.

- A new non-dimensional channel parameter is examined and defined: aspect ratio. Experiments presented show that thrust coefficient is a function of both the channel aspect ratio and area blockage ratio. Differences in loading due to channel aspect ratio are shown to be independent of area blockage ratio and capable of contributing to differences in loading of 28%.

- It is shown that the thrust coefficient of a circular device, operating in an open channel of any cross-section (at a fixed Froude number), is dependent only on device diameter to water depth ratio (d/h). This implies that one-dimensional LMADT models, such as those of Whelan et al. (2009) and Garrett & Cummins (2007), are capable of accounting for changes in device thrust coefficient due to changes in channel aspect ratio. Further investigation increasing the range of data presented in this work is required in order to understand further the effect and relationships on thrust coefficient between the three governing parameters: Froude number, area blockage ratio and channel aspect ratio. Similar experiments to those presented are required but at different channel Froude number values in order to investigate further simplification of the relationships between these parameters.

Chapter 7

Wake changes within constrained flow fields

Results presented in this Chapter aim to answer Objective 3 outlined in Section 1.5 and are the result of the Investigation 3 experiments outlined in Section 4.6.

7.1 Asymmetrical wakes in confined flows

Figures 7.1 and 7.2 show wake measurements, of velocity deficit and normal stress, behind the same porous disk models operating in channels of different geometry. Figure 7.1 shows results from a channel of 4D width and 4D depth whilst Figure 7.2 shows results from a channel of 13.7D width and 3D depth. When considering the vertical velocity profiles (Figures 7.1a and 7.2a) differences are observed in both the near and far wakes. For example in the 4D square cross section channel case greater flow acceleration is observed around the disk in the bypass flow between 1-5D downstream. This is indicated by velocity deficit values less than zero both above and below the disk, which is not the case in the rectangular channel under consideration. At around 5D downstream the wake appears to have spread at a quicker rate in the rectangular case (confirmed in Figure 7.3(c and e). By 13D downstream in the far wake region some symmetry can still be seen in the square channel case. This is in contradiction to the rectangular channel case where the vertical velocity profile appears to be more closely resembling a open channel velocity profile. When comparing the velocity deficit in the horizontal plane (Figures 7.1c and 7.2c) in each case only slight differences in the wake velocity profile shape can be seen.

Figures 7.3(c and e) show the wake edges in the vertical and horizontal planes. In this figure 95% velocity deficit recovery (compared to that of the inflow) was used to calculate the wake edges. A 95% limit was chosen (based on the work of Myers & Bahaj

(2010*a*)) as this allowed a greater number of wake edge data points by comparison to a 99% value. The measurement of the wake edge gives an indication of the extent of the wake and it's spread with downstream distance. This can inform the placement of subsequent MCEC devices within an array. It is observed that minimal wake expansion is seen in the square channel case (7.3c). Little difference is seen between the expansion in the top and bottom vertical plane wake edges in this case, however the wake width in the horizontal plane is seen to be greater than that in the vertical. By comparison the rectangular channel under consideration (7.3e) shows wake expansion in both the horizontal and vertical planes. Initial wake width in the vertical plane is greater in this case and continues to expand with downstream distance. Initial wake width in the horizontal plane is smaller than in the square channel case but has expanded to be greater than that of the square channel case by 15D downstream. The disk coefficient of thrust recorded in each of the cases were similar (within 1%, 0.89 and 0.9). Therefore results show that both initial wake width and wake expansion appear to be related to the channel geometry in which the disk is operating.

The near to far wake transition point, where the velocity and normal stress profiles became Gaussian, were ascertained from the wake measurements of each channel. In each geometry case transition was observed to occur in the vertical plane at roughly the same downstream distance at 3D and 4D for velocity deficit and normal stress profiles respectively. However, the transition point was observed to be different when comparing the lateral planes of the two different channel geometries. In the square cross section channel transition was observed to occur at 3D and 5D for velocity deficit and normal stress respectively. In the 13.7D width and 3D depth channel transition was seen to occur at 2D and 4D downstream. This indicates that the wake transition point can differ depending on the channel geometry. A change in wake transition point will lead to differences in wake recovery rate, which is important when considering downstream spacing of subsequent MCEC devices within an array.

When considering the vertical normal stress values in Figure 7.1b two peak values are observed closer to the disk (1D and 3D downstream). These correspond with the disk edges and are a result of the larger velocity gradients between wake and bypass flows. The normal stress profile behind the disk is observed to decay towards being Gaussian at greater distances downstream. When comparing wake normal stresses in the vertical plane (Figures 7.1b and 7.2b) do not show any significant differences. However differences in and around the near wake (1-5D downstream) are observed (Figures 7.1b and 7.2b) in the horizontal plane. Greater values of normal stress are observed in the rectangular channel case where almost double the maximum value is observed at 1D downstream. These increases in normal stress values local to the horizontal plane could be linked with the closer downstream transition point discussed earlier. Differences in normal stress value in the horizontal and vertical planes are likely to result in different rates of mixing and lead to the development of wakes which are dissimilar in each plane.

These results highlight that wakes can be asymmetrical in the horizontal and vertical planes. The results also highlight that when the same device operates in a channel of different cross sectional geometry differences in wake width, wake transition point and normal stress production can be evident. Changes in each of these parameters will lead to differences in wake recovery rate, which is important when considering the downstream spacing of subsequent MCEC devices within an array. The differences are likely to occur because of the disk interaction with both the vertical channel boundary layer as well as the channel boundaries. Part of the interaction with the lateral channel boundaries will be due to the presence of a boundary layer associated with the presence of the solid walls. In some cases the interaction will be greater than others with changes in lateral boundary position. For example in the 4D square channel introduced above the disk will be subject to three boundary layers; two from the lateral walls and one from the channel bed. By comparison the rectangular case will operate in proximity to only the channel bed boundary layer, due to the extreme distance between the device and channel walls. The next section looks at effects of channel boundary proximity in more detail.

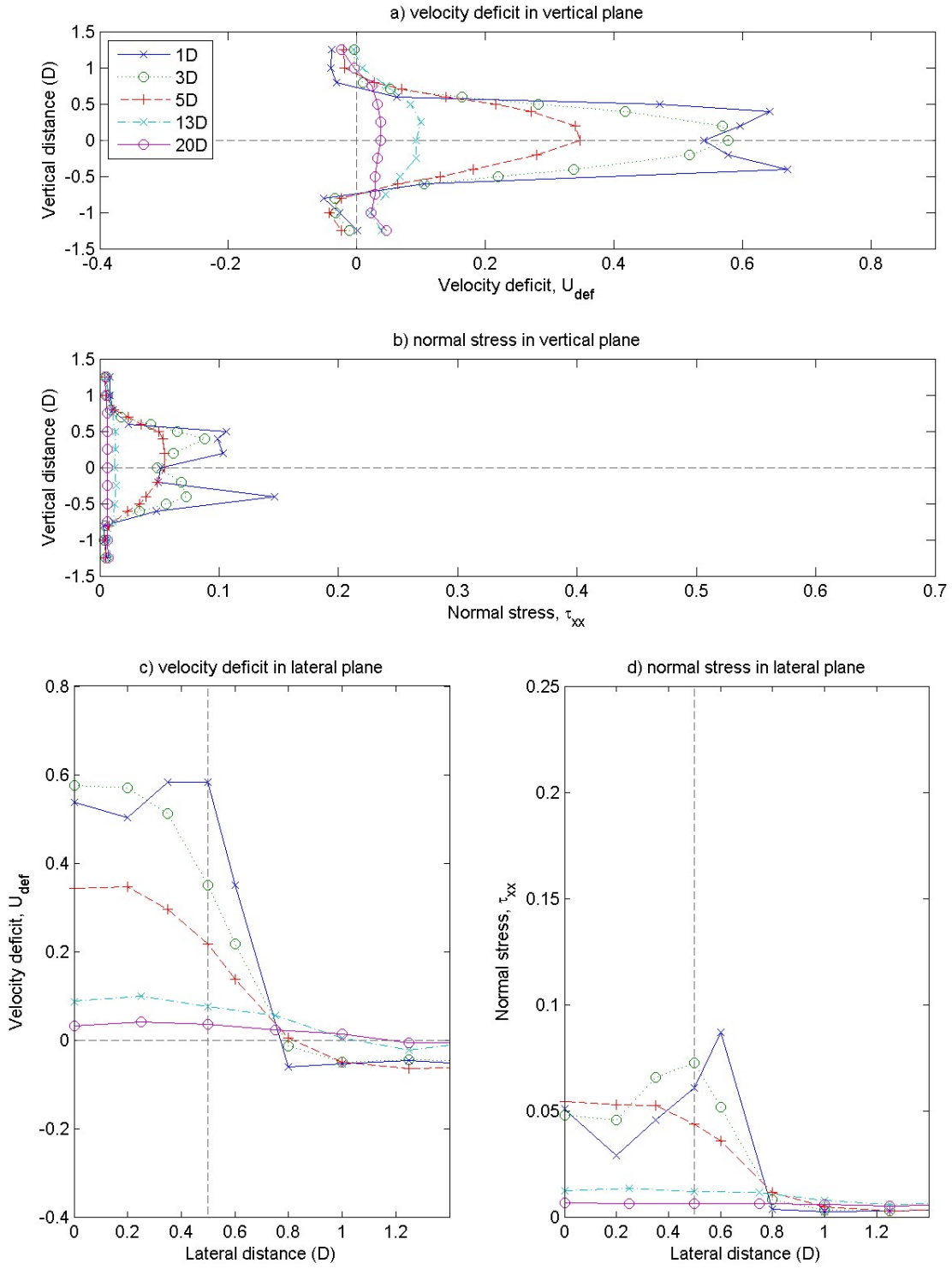

Figure 7.1: Flow measurements behind a single porous disk operating in a channel of 4D width and 4D depth (Froude number = 0.17, Ct = 0.9).

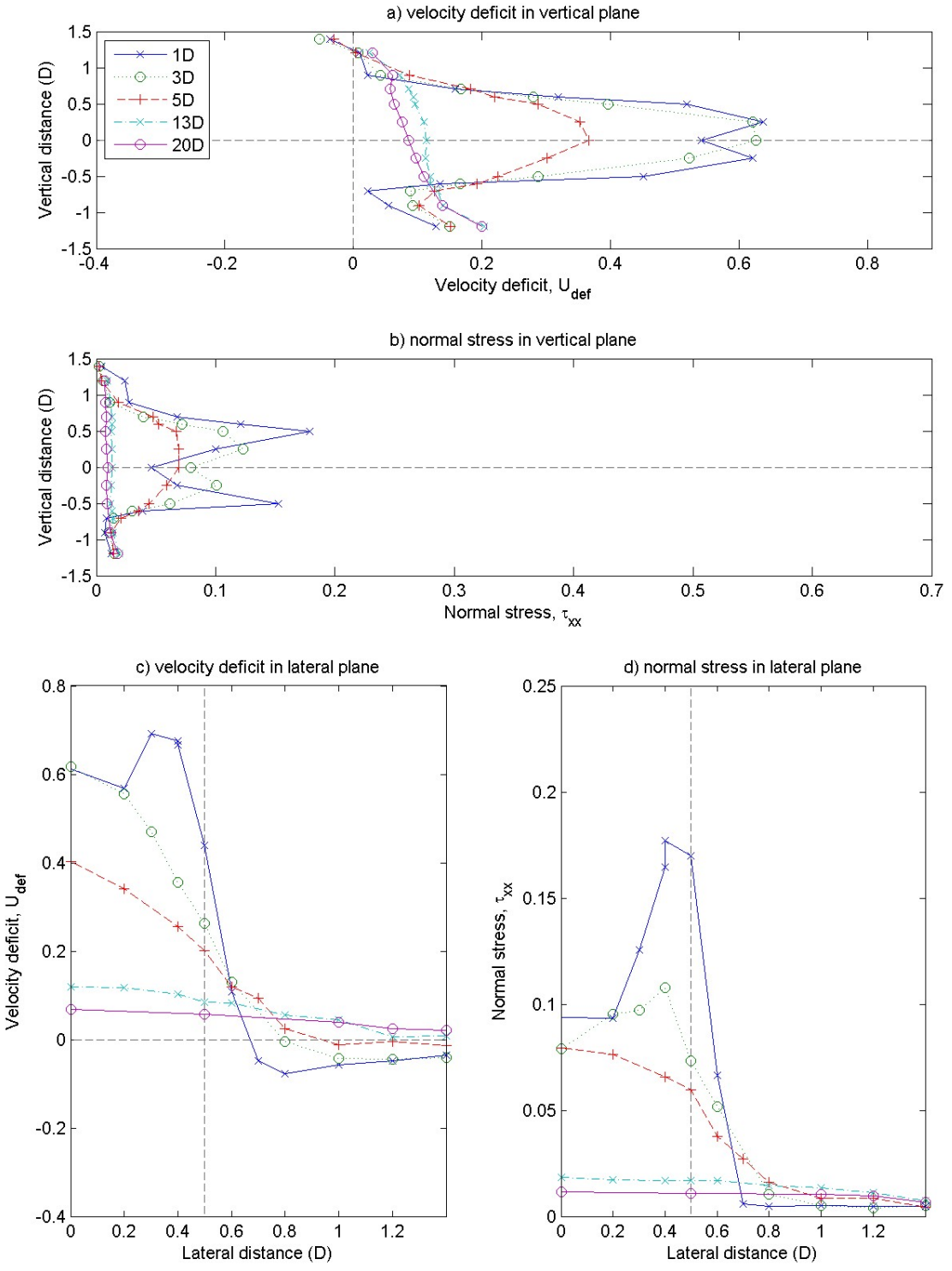

Figure 7.2: Flow measurements behind a single porous disk operating in a channel of 13.7D width and 3D depth (Froude number = 0.17, Ct = 0.89).

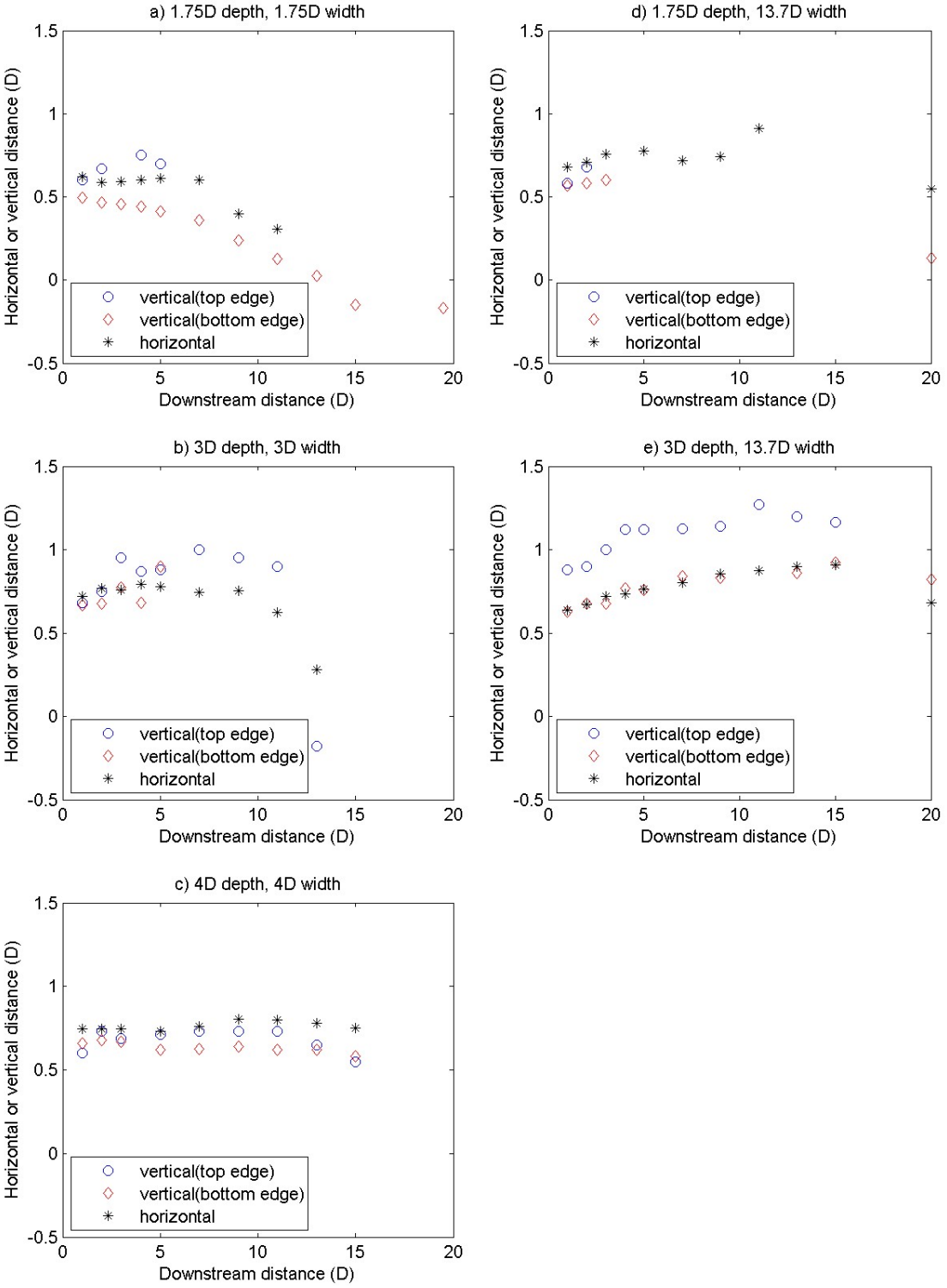

Figure 7.3: Wake edge calculations, showing 95% velocity recovery to ambient, for channels of various cross sectional geometries (note that bottom edge distance values have been made positive in order for easier comparison).

7.2 Wake changes with boundary proximity

Figure 7.4 shows wake measurements in a channel of 3D width and 3D depth. Comparing with Figure 7.2 allows comparison of the same device operating at the same depth and hence the same vertical velocity profile. Therefore any changes in wake are the result of differences in the placement of the channel wall and are not attributed to differences in the vertical free-stream boundary layer position within the channel. Comparing Figures 7.4a and 7.2a it is seen that greater velocity deficit values are present in the vertical plane in the near wake of the 3D square channel case. Greater levels of flow acceleration in the bypass region are also observed for this case, both above and below the disk. Comparing Figures 7.4b and 7.2b it is observed that larger normal stress values are present around the disk near wake in the square channel case, which persist further downstream until 5D. These increased normal stress values may be a result of the interaction between the greater flow velocity observed in the bypass region, and the slower velocity values seen in the disk wake. The two peaks in normal stress value observed close behind the disk indicate the mixing regions between bypass and wake flows behind each disk edge. Greater and more persistent values downstream may indicate greater intensity and more prolonged mixing. Greater normal stress values are also observed in the horizontal plane in Figure 7.4d in the 3D square cross section channel. Figures 7.3b and 7.3e show the wake edge for the two channel geometries discussed. The rectangular channel case 7.3e shows wake edges expanding with downstream distance. However the more constrained square channel geometry case shows initial wake edge expansion only to around 5-7D downstream, followed by what seems to be a contraction in the wake.

These results imply that changes in channel geometry in the lateral plane (i.e. changing channel width) can also affect the wake development and mixing in the vertical plane. It is possible that by reducing channel width greater flow acceleration in the bypass region is caused due to the constraint of the flow between disk edge and boundary. As well as this occurring in the in the horizontal plane more fluid is forced above and below the disk, causing flow acceleration in the bypass flow of the vertical plane.

Figure 7.5 shows results obtained with the same device operating in a channel of 13.7D width and 1.75D depth. The effects of reduction in channel depth on wake development can be considered when comparing these results with those in Figure 7.2. Figures 7.5a and 7.2a show similar velocity deficit values on the vertical plane 1-3D downstream. However at 5D downstream, where both wakes appear to have transitioned to the far wake, higher velocity deficit values are observed in the shallower channel. This is also observed further downstream at 13D however by 20D downstream the velocity deficit values in each case are similar. A similar trend is noticed in the lateral plane when considering Figures 7.2c and 7.5c. Differences are also seen in normal stress values at 1D downstream of the disk when considering Figures 7.5(b and d) and Figures 7.2(b and d). Smaller values are observed in the vertical plane above the disk and in the horizontal

plane. The smaller normal stress values observed may explain the more persistent higher velocity deficit values observed in the shallower case. Lower levels of mixing in the near wake shear layer could lead to slower wake recovery with downstream distance.

Figures 7.3(d and e) highlight the differences in wake edge position in each of the channels under consideration. The overall wake width (the sum of the vertical top edge and vertical bottom edge distances) is seen to be much greater ($\approx 25\%$) at initial distances downstream in the deeper channel case. This shows that the presence of channel bed and free surface can result in the constraint of wake expansion. Smaller vertical wake width is observed in the shallower channel and no wake edge data is observed beyond 3D downstream in the vertical plane. This is due to the quick dissipation in the regions of accelerated bypass flow above and below the disk, which results in no data points beyond 3D downstream where the flow velocity is above 95% of the inflow value. The disk wake in the vertical plane hence has hence merged with the channel boundary layer and no longer has distinct bypass and wake flow regions.

It should be noted that the differences in wake dissipation observed above cannot be solely attributed to the changes in boundary proximity. Changes in the vertical channel boundary layer, and the extent to which the disk operates within the boundary layer in each case, will be different and will play some part in wake development. Further work will be needed to decouple the effects of boundary layer and boundary proximity on wake development and dissipation.

Figure 7.6 shows wake measurements in a channel of 1.75D width and 1.75D depth. The results can be compared with that of Figure 7.5, where the same device operates in the same flow depth, in a 13.7D width and 1.75D depth channel. Upon considering Figures 7.5(a and c) and 7.6(a and c) the reduction in channel width is seen to correspond with an increase in the flow speed in the bypass flow, in both the vertical and horizontal planes. Significant differences in vertical plane bypass flow are observed, indicating that changes in lateral boundary position can result in differences in the flow though and around a disk in any plane. It is possible that the increased flow constraint in the lateral plane results in a greater volume of fluid being forced above and below the disk. When comparing this to the rectangular channel case in Figure 7.5 fluid is not forced above and below the disk to the same extent due to the lack of lateral boundary presence.

Only small changes in normal stress are observed between the two cases in the horizontal plane (Figures 7.5d and 7.6d). However there are increases seen in the near wake at 1D downstream above the disk (comparing Figures 7.5b and 7.6b)as a result of reducing channel width. This indicates that there is a greater intensity of mixing in this region, most likely due to the increased difference in bypass and wake fluid velocities. More significantly there is a large increase in normal stress at 5D downstream in Figure 7.6b, which is uncharacteristic of other channels investigated. This may be due to the high

area blockage ratio of the channel in comparison to the other cases investigated. Figure 7.6a shows greater flow acceleration in the vertical direction above and below the porous disk, when compared with the other cases investigated, as far downstream as 5D. The increased values of normal stress at 5D downstream will most likely be a result of the large velocity gradient, between wake and bypass flows, which persists to this downstream distance.

When considering Figure 7.3a it is observed that in the square channel of 1.75D width no wake expansion is present in either the horizontal or vertical plane. Wake width (in the vertical plane wake width is the sum of top edge and bottom edge distances) is seen to be constant until 4-5D downstream, after which contraction in the wake width in both planes is seen to occur. The close presence of boundaries preventing the wake expanding in this channel may prevent initial wake recovery, which is observed at 5D downstream in Figure 7.6a. Much higher velocity deficit values are observed, at this distance downstream, than in any other channel geometry investigated in this study.

The results presented in this section show that differences in wake transition, wake normal stress development, wake width and wake expansion occur with changes in channel geometry. Changes in boundary proximity in either the vertical or horizontal planes can result in wake changes in both planes, which indicates that channel aspect ratio and area blockage ratio are both important parameters in determining wake development and dissipation. These findings highlight that wake models such as those introduced in Section 2.3.6 will need to be implemented carefully if they are to be utilised for accurate modelling of turbine wakes operating in constrained flows.

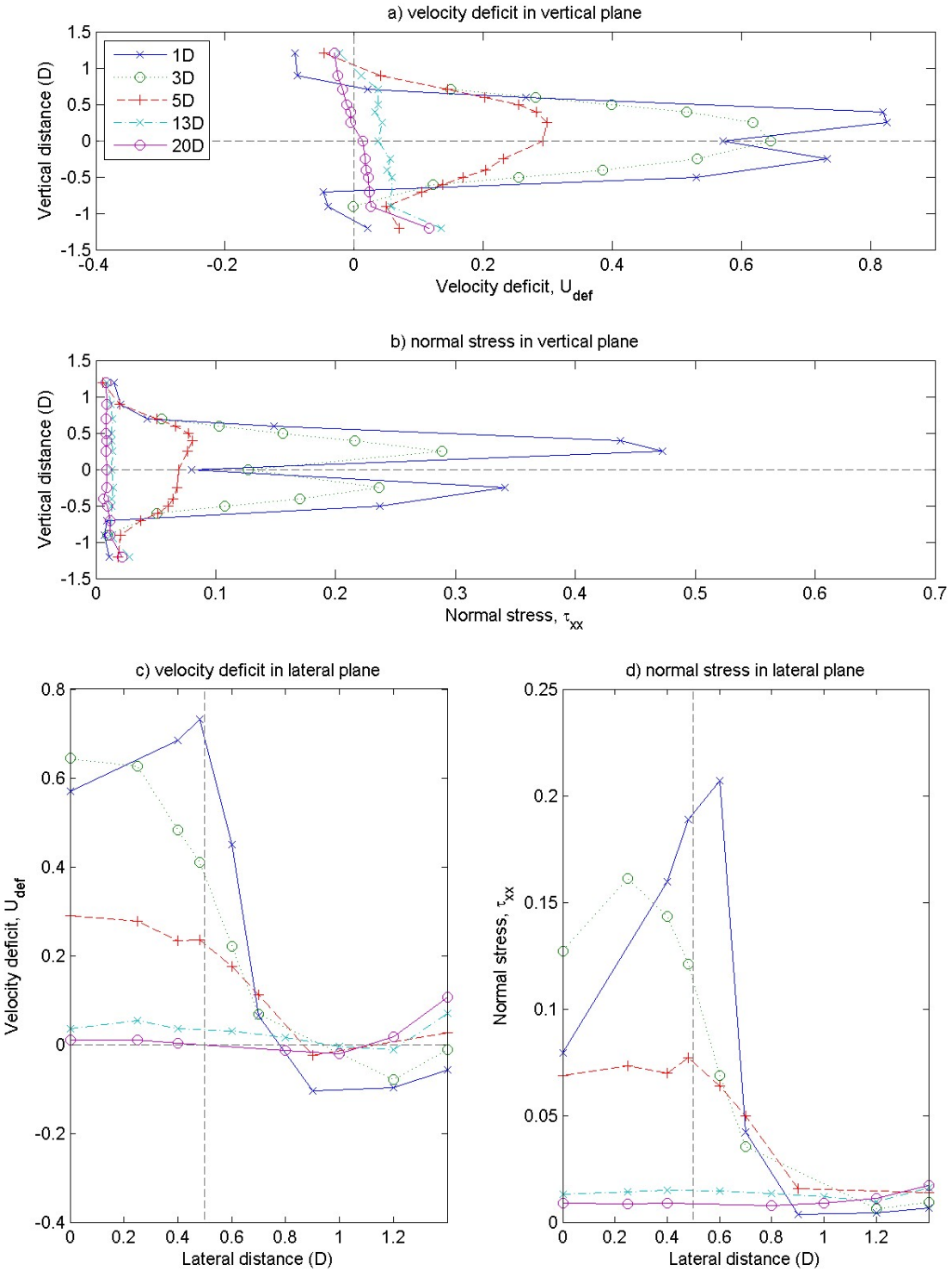

Figure 7.4: Flow measurements behind a single porous disk operating in a channel of 3D width and 3D depth (Froude number = 0.17).

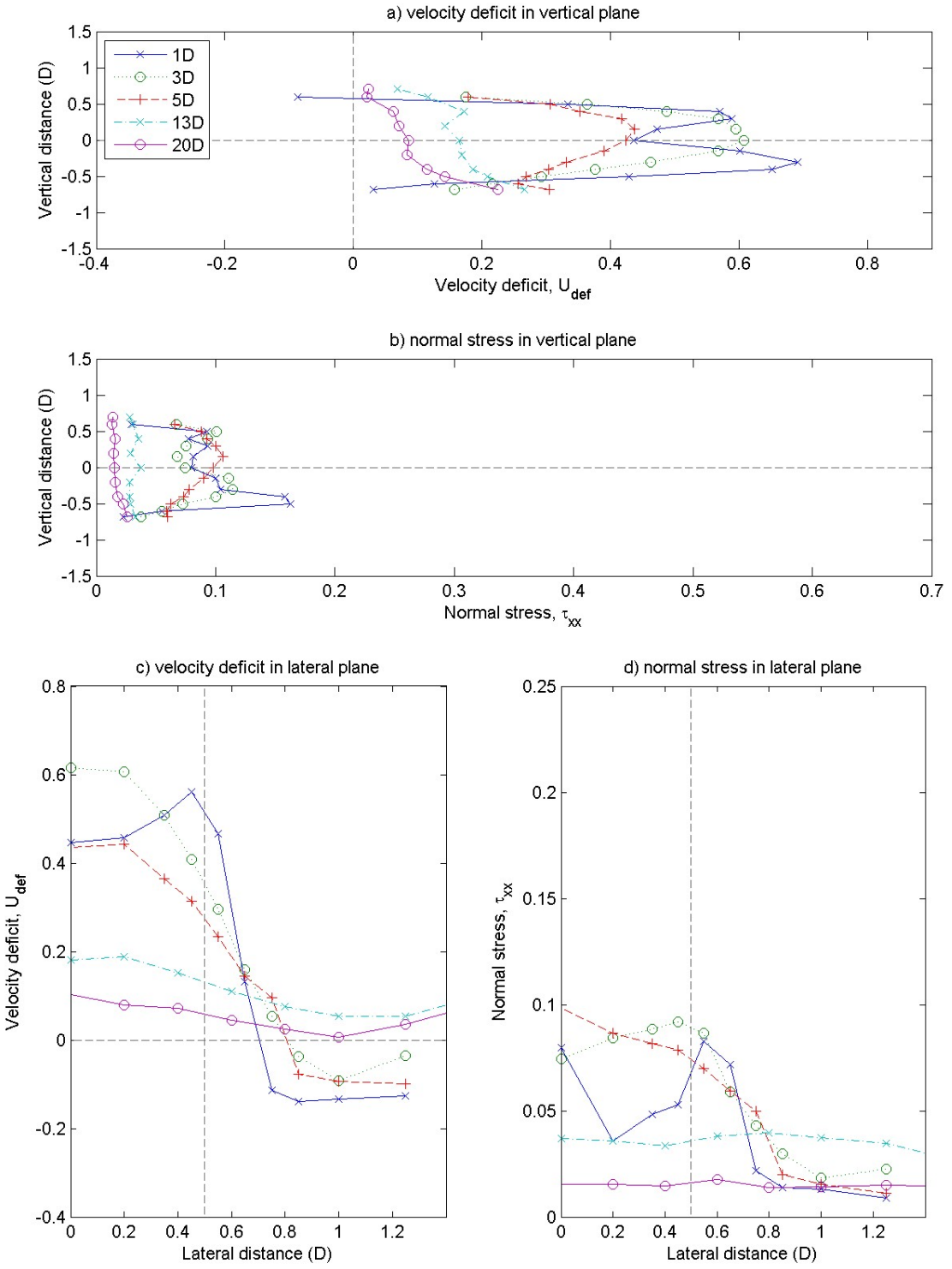

Figure 7.5: Flow measurements behind a single porous disk operating in a channel of 13.7D width and 1.75D depth (Froude number = 0.16).

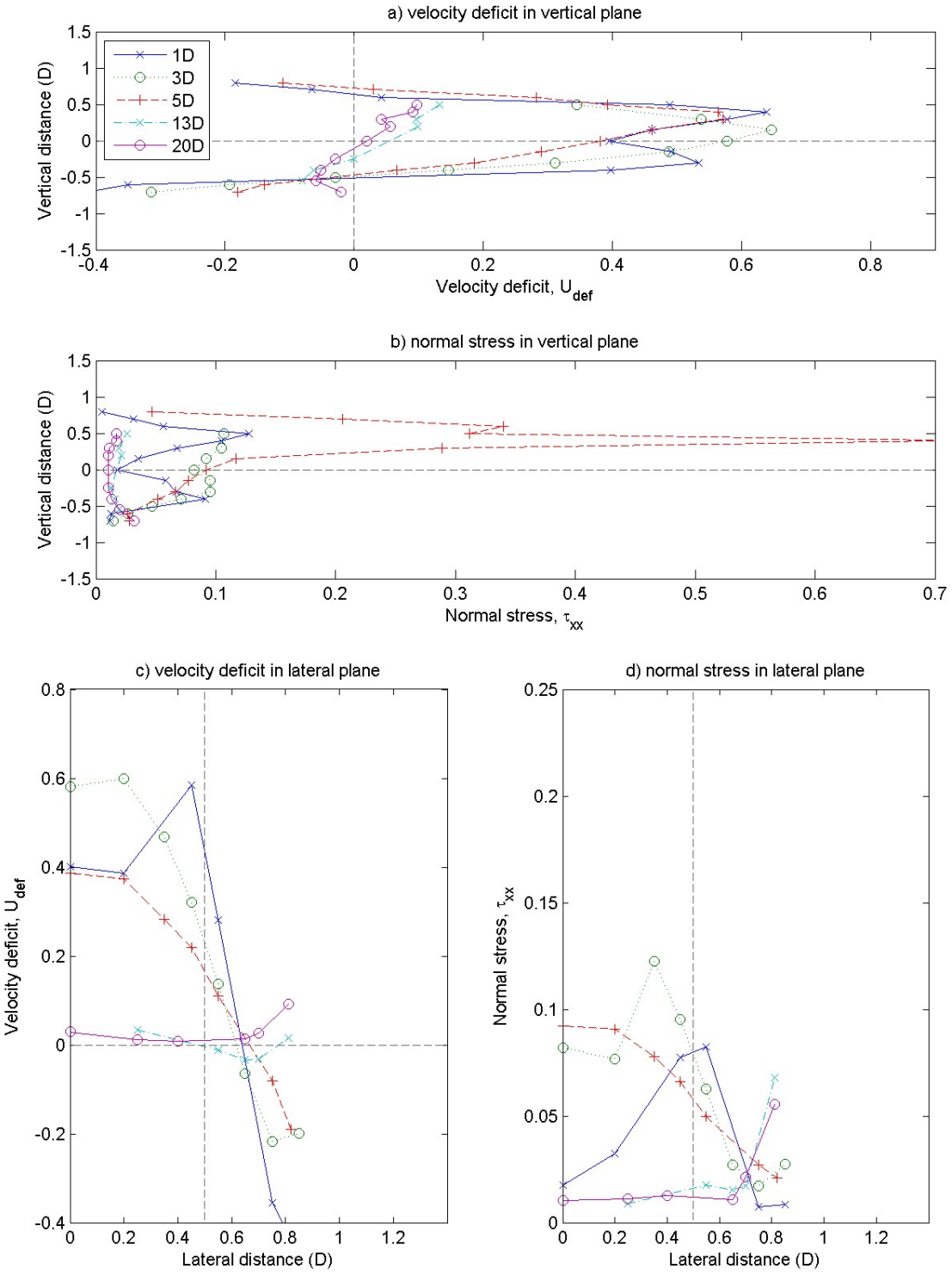

Figure 7.6: Flow measurements behind a single porous disk operating in a channel of 1.75D width and 1.75D depth (Froude number = 0.18).

7.3 Vertical wake migration in channel

The results presented in this chapter show that the wake of the same device operating in confined flows of different geometry can be asymmetric. A lack of rotational symmetry about the disk centreline was observed when comparing the wake in the vertical and horizontal planes in Section 7.1. Varying degrees of asymmetry are also observed in the vertical plane, when considering reflection along the disk centreline, in the cases discussed. In Figure 7.1a (4Dx4D channel), the greatest symmetry is observed of all the cases investigated. This is no doubt due the equal distance of boundaries in both planes, and the disk placement being furthest from the channel boundary layer of all cases. In this case symmetry in the vertical plane is still observed at 20D downstream. A more asymmetric wake profile is observed in Figure 7.4a (3Dx3D channel). The centre of the wake is observed to be around 0.25D above the disk centreline at 5D downstream and by 13D downstream no symmetry is observed. As in the case above the boundary proximity is still equal in the vertical and horizontal planes, hence the results suggest that the effects of wake interaction with the boundary layer plays an important role in vertical wake migration. A more significant difference in wake asymmetry is observed in the more confined case in Figure 7.6a (1.75Dx1.75D channel). In this case the centre of the wake is observed to be around 0.3-0.4D above the disk centreline at 5D downstream. This implies that in more confined flows greater asymmetry in the vertical wake will be observed.

Changes in the cross-sectional geometry of the channel are also observed to affect the vertical wake migration. For example when comparing flows of the same vertical depth (and hence vertical channel boundary layer), i.e. Figure 7.6 with Figure 7.5, a reduction in the vertical wake migration is seen with increased lateral channel width. This demonstrates again that differences in lateral boundary position (and hence channel aspect ratio) can affect flow in the vertical plane. In less vertically constrained flows, i.e. comparing Figures 7.2a (3D x 13.7D channel) and 7.4a (3Dx3D channel), changes in lateral boundary position are still observed to have some affect on vertical asymmetry of the wake (e.g. at 1D downstream). However the differences seen are less extreme when compared to those of the 1.75D channel depth discussed above.

In the cases presented in this work the differences are seen to be more pronounced in the more greatly constrained flows. This is due to the increased forcing of fluid around the disk which, in the presence of a vertical boundary layer, causes a difference in the volume of flow above and below the disk. This difference results in a pressure imbalance in the bypass flow regions above and below the disk and hence causes vertical migration of the wake. Vertical wake migration is therefore expected to be a function of the boundary layer height, channel area blockage ratio and channel aspect ratio. Further work is needed in order to decouple the effects of each of these parameters. The importance of these observations of vertical wake migration are discussed in the next section.

7.4 Wake recovery in confined flows

Wake recovery is important when considering the placement of downstream devices within array deployments. This section discusses the differences in wake recovery in the different channel geometries already introduced in this Chapter. Figure 7.7a shows the velocity deficit measurements on the centreline behind a single porous disk operating in square cross section channels of different geometry.

In each channel geometry an initial increase in velocity deficit is observed followed by a reduction towards that of zero (ambient flow speed). A larger peak value of velocity deficit is seen in the channel of 3D depth channel in comparison to either the larger or smaller channel sizes investigated. Although a higher peak velocity deficit value is observed the recorded thrust coefficient for this channel is not the greatest recorded in the three cases. This indicates that thrust coefficient is not correlated with peak velocity deficit values within the wake of disk.

When considering the wake recovery, further downstream of the peak velocity deficit values, faster recovery is seen between the near and far wake regions (2-7D downstream) in the 3D channel case. This results in lower velocity deficit values than in the other cases between 5-13D downstream. Even though initially higher values are observed in this case the faster recovery results in much smaller difference in values further downstream between each of the cases investigated.

Figure 7.7b shows the maximum velocity deficit recorded behind a disk in the vertical plane at each downstream distance for each of the cases presented in Figure 7.7a. Changes observed between Figures 7.7a and 7.7b give an indication if the wake has moved off its centreline axis in the vertical plane. The greatest difference observed in the cases investigated is seen in the smallest channel case (1.75D depth). Higher velocity deficit values are observed in this case in Figure 7.7b between 3-11D downstream. This confirms the discussion in the previous section that disk wakes are more likely to migrate vertically in channel geometries that are more constrained.

This is an important finding in relation to the deployment of MCEC devices within arrays. The effects of shadowing were discussed in Section 2.4 where it was highlighted that operating within the wake of another device is detrimental to both power production and fatigue loading of downstream devices. When considering the results presented above in Figure 7.7b it is clear that the channel geometry could have a significant impact on the choice of downstream distance at which to deploy a second device. For example, a decision to deploy where there has been recovery of velocity deficit to at least 20% of the undisturbed flow could lead to a significant difference in downstream device separation. In the cases investigated here the 3D and 4D depth channels could utilise a separation of 7D to meet this criteria, however the 1.75D depth channel would require a downstream separation of 11D. It should be noted that these values will be sensitive

to the recovery of velocity deficit chosen; for example a 10% value of recovery would lead to a downstream distance requirement of between 10D and 13D for the cases under consideration. The need for larger downstream device spacing may have an impact on the number of turbines that may be installed at a development site (developers will have restrictions on sea bed deployment area that can be utilised) and hence the financial considerations of a development. This work therefore shows the need for developers to fully consider the channel geometry dependent wake-changes in order to fully consider the layout to minimise negative device interaction.

This work also highlights that centreline measurement directly behind devices is not always sufficient to understand the wake recovery of a device. It seems from the results presented in this work that smaller differences are expected in flows that are less constrained. It, hence, is in deployments within more constrained flows which developers must be careful to fully understand wake recovery not just on the centreline behind a device. This provides a dilemma for device developers at full-scale deployment sites where offshore flow measurement work is costly. The detailed measurements taken in this study are not practical in an offshore study and so the need for laboratory studies, to further understand wake development in constrained flows, is apparent.

The difference in rate of wake recovery observed in Figure 7.7 imply that there are differences in wake mixing which are dependent on channel geometry, as discussed in the previous sections. Figure 7.8 shows the normal stress values measured behind the cases presently discussed. Smaller values of normal stress are generally observed closer behind the disk upto 9D downstream in the least constrained case (4D depth channel) when compared with the other channel geometries. It is suggested that the closer proximity of boundaries to the disk creates a greater disparity in fluid velocity between the bypass and wake flows. This has the effect to cause greater levels of shear between the wake and the bypass flow regions which can alter the wake recovery through enhanced mixing. This explains the greater rate of wake recovery observed between 2-7D downstream in the 3D depth channel case. Larger normal stress values are also observed in the 1.75D case however faster wake recovery is not observed as a result. It is possible in this case that the extreme proximity of channel walls prevents the wake from expanding, leads to an extended region of high velocity deficit (7D downstream) and so downstream recovery rate is limited.

Figure 7.9a compares the velocity deficit values measured on the centreline behind the same disk operating in square channels and channels of similar depths but greater aspect ratio (i.e. wider channels). Maximum velocity deficit values for each downstream distance are also presented in Figure 7.9b. Only small differences are seen when comparing Figures Figure 7.9a and b in each case apart from the channel of 1.75D depth and 1.75D width (the differences of which are discussed earlier in this section). At distances greater than 11D downstream values of velocity deficit are greater in each of the rectangular channels investigated. The velocity deficit values in the rectangular channels also appear

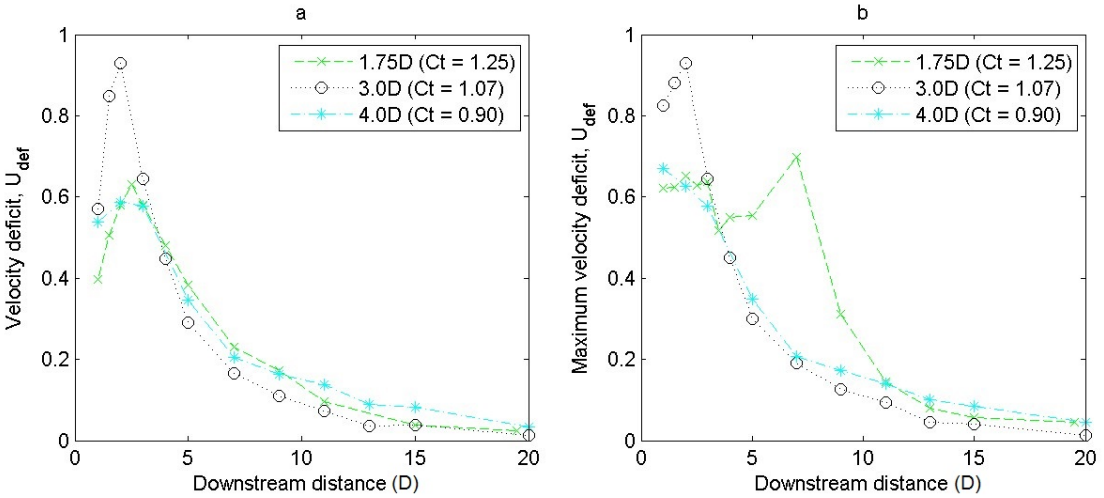

Figure 7.7: Velocity deficit measurements behind a single porous disk in channels of various square cross section (a) velocity deficit on centreline and (b) maximum velocity deficit in the vertical plane.

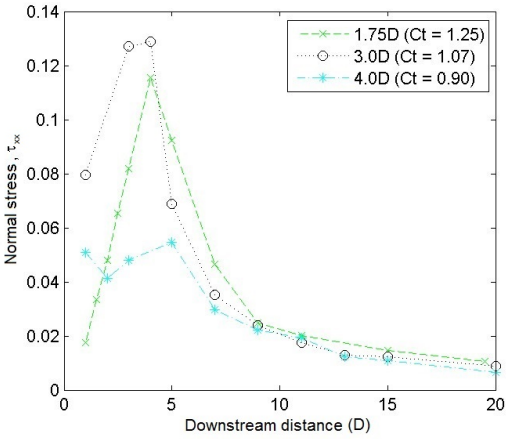

Figure 7.8: Normal stress measurements behind a single porous disk in channels of various square cross section.

to asymptote to a value greater than zero, indicating that full wake recovery is slower in channels of rectangular geometry. Results show that downstream wake recovery (beyond 11D downstream) is faster in channels of aspect ratio equal to one. This may be due to the more even mixing in lateral and horizontal planes (observed earlier in this Chapter) allowing a greater overall mixing of bypass and ambient flows. With mixing of bypass and ambient flows in both planes higher momentum fluid in the bypass regions can be transferred towards the centre of the lower momentum fluid contained in the wake more easily.

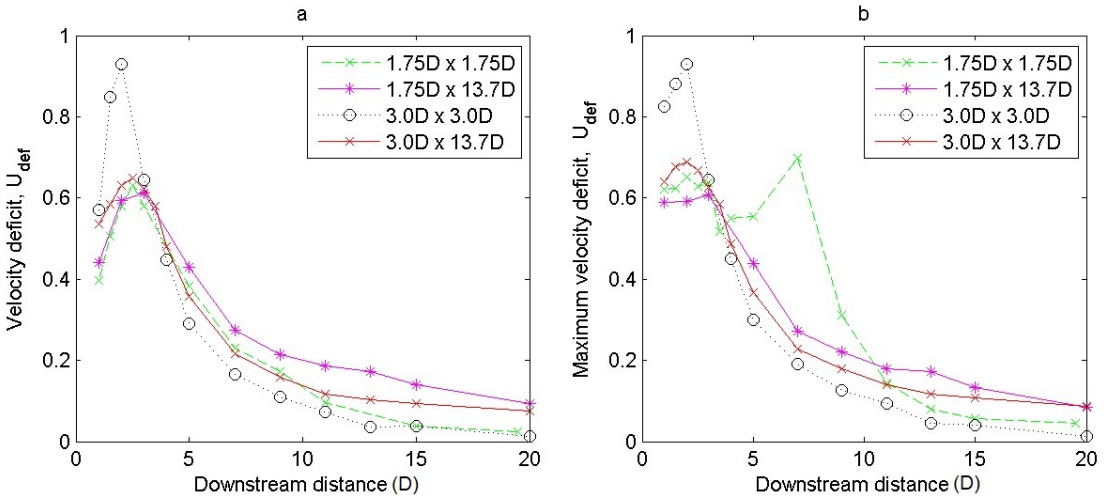

Figure 7.9: Velocity deficit measurements behind a single porous disk in channels of various square and rectangular cross section (a) velocity deficit on centreline and (b) maximum velocity deficit in the vertical plane.

7.5 Application to larger-scale and arrays

One limitation of the results presented is the use of a scaled model (porous disk). As discussed in Chapter 5 there will be differences in the turbulent wake structure of smaller scale devices to that of full scale, regardless of device type (i.e. porous disk or rotor model). Some findings presented in this chapter are expected to be universal with any device type and scale, e.g. vertical wake migration. The other general findings described (such as: the wake asymmetry, the link between lateral and vertical wake mixing and the effects of boundary proximity) are also expected to occur across all model scales/device types. However the effects of the mechanisms that result in wake change, e.g. changes in normal stress levels within disk wakes with boundary proximity, could produce differences in rate of wake recovery specific to device type and scale.

The results presented in this chapter are directly applicable to single devices operating in open channels. Such scenarios mainly include laboratory testing or deployments in man made channels such as the New York East River or Den Oever installations (discussed in Section 1.3.1). Some of the wider rectangular channel cases could also be representative of single device deployments at full-scale tidal sites (such as any of the devices detailed in Table 1.1 tested at the EMEC site) where lateral channel boundaries will not be located closely enough to have an effect on wake structure. One other application of the results presented in this chapter is to inform how devices may operate within arrays, where single devices are positioned alongside each other, in the same channel cross section. This could be the case in the EDF, Meygen and Scottish Power Renewables array developments detailed in Table 1.2. The results from changes in the proximity of solid walls could be indicative of wake behaviour that will occur with the changes in presence of other devices within arrays, i.e. device spacing within an array (as discussed in similar context

in Section 2.3.6. The use of solid walls allows the study of wake changes in constrained flow in a controlled manner, without introducing multiple devices within a channel.

When a device is surrounded by either solid walls or other devices it is suggested that the flow field the central device will see will be similar, due to each bounding element acting to constrain the flow around the central device. There will also be some similarity between the wake of a bounding device and the boundary layer of a solid wall as both represent a low pressure region characterised by slower moving and more turbulent flow. The main difference in the flows however will be that the boundary layer is continuously driven with shear downstream whereas any bounding wakes will be dissipating with downstream distance. This may indicate that the application of findings from a solid walled channel are more valid closer to the device, i.e. thrust and near wake measurements, with greater uncertainty in far wake dissipation findings. The effects of wake development and dissipation, with the presence of other devices, is investigated more in the next chapter.

7.6 Summary and further work

- Porous disk wakes have been shown to have different structures (transition point, normal stress production, wake width and wake expansion) in horizontal and vertical planes. Differences in wake structure are also observed with changes in boundary proximity in both the vertical and horizontal planes. A changes in the boundary proximity in a single plane (i.e. either the vertical or horizontal) is shown to alter the wake in both planes, indicating that the flow around a device in each plane is inter-dependant. The understanding of these wake changes in constrained flows is important to predict wake development and dissipation to negate MCEC interference or shadowing in future offshore arrays. Further work should look at isolating the effects of channel aspect ratio, area blockage ratio and Froude number on the wake properties discussed here. This characterisation of the changes in wake behaviour can lead to the more accurate use of simple wake models, in constrained flows, such as those described in Section 2.3.6.

- Porous disk wakes were observed to be asymmetric to varying degrees in the vertical plane when operating within channels of differing geometry. This effect was observed to be much greater in constrained flows and when compared to existing studies (such as Myers & Bahaj (2010*b*)) show that the areas of greatest velocity deficit within wakes can move either above or below the centreline directly behind the device hub. Measurements only on the centreline behind a device therefore may not be adequate to determine the dissipation of a turbine wake. This highlights how laboratory testing can provide important information for full-scale deployments and offshore measurement planning/interpretation.

- Far wake velocity recovery is shown to be similar in cases where channel aspect ratio is equal to one, however slower far wake recovery is observed in channels that are more rectangular in cross section (i.e. channel aspect ratio is greater than one). In cases where area blockage ratio are higher, greater high velocity deficit was observed to persist further downstream.

- Further experiments isolating the effects of vertical boundary layer on wake development and dissipation are required in order to inform how wakes may behave in any given channel geometry. For example fixing the boundary layer height/water depth ratio within experiments. Further experimental study investigating the differences between device wake structure in flows bounded by solid walls and those bounded by other devices is needed in order to understand how results presented here can be applied to array scenarios.

Chapter 8

Wake and thrust changes of devices operating within dual-device arrays

Results presented in this Chapter aim to answer Objective 4 outlined in Section 1.5 and are the result of the Investigation 4 experiments outlined in Section 4.6.

8.1 The effects of device spacing within a dual-device array

Results presented in this section are for a 3D depth channel with varying device spacing.

8.1.1 Wake changes with turbine proximity

Flow measurements were taken characterising the combined wake of the two disk arrangement, with particular emphasis placed on investigating the region of flow between the two disks. Figure 8.1a compares the velocity deficit at various downstream distances directly between the disks for each of the lateral disk separations between 0.5-1.5D. As was observed by Myers & Bahaj (2012) the smaller separations show an increased velocity deficit between the disks as the expanding wakes of each disk merge; the increase in velocity deficit is observed to be being more prominent in the most closely spaced case where velocity deficit values were observed to reach over 0.22 between the devices. As separation increases the wakes of each individual disk are more distinct, as if operating in isolation, with peak velocity deficit seen to be no more than 0.07 in the case of greatest separation.

When comparing with similar experiments conducted by Myers & Bahaj (2012) a new feature of the dual-disk flow field is captured. A small region of flow acceleration is

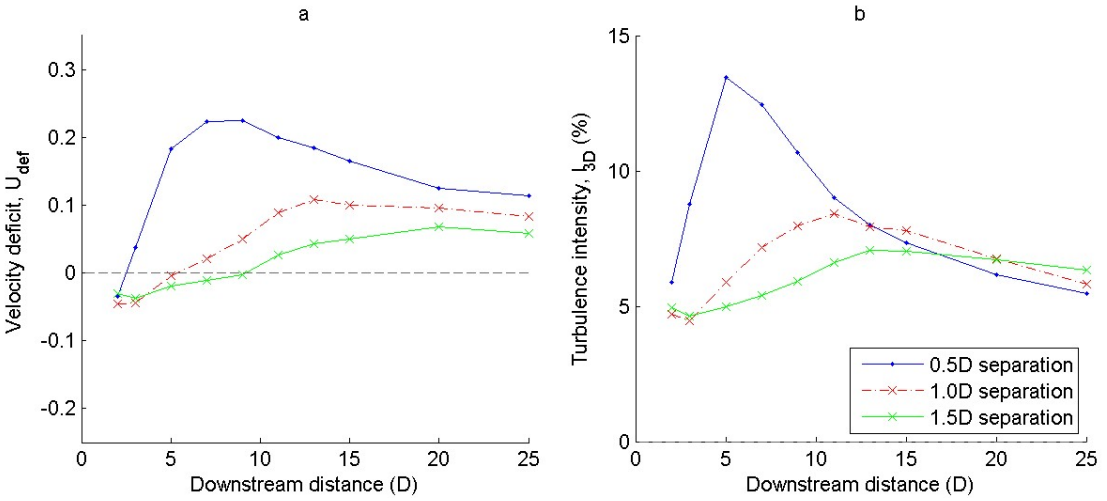

Figure 8.1: Comparison of data collected on the centreline between the devices for various disk separations: (a) velocity deficit and (b) 3D turbulence intensity.

observed between the devices at each of the spacings investigated (including the closest spacing) before the expanding wakes merge. This may have been observed in these experiments due to the turbulent characteristics of the undisturbed channel being lower in this experiment (3D turbulence intensities of 8% and 5% were recorded at hub depth by Myers & Bahaj (2012) and in these experiments respectively). One possible explanation is the smaller undisturbed channel turbulence intensity values result in differences in wake mixing. Differences in wake mixing could affect the the accelerated flow between the devices due to differences in wake expansion of the individual disks. Another explanation is that the Froude number in each experiment may have been different, resulting in different flow acceleration around the devices.

Turbulence intensity measurements between the disks can give an indication of the intensity of the merged wakes. Values above those of the undisturbed channel flow (5% in these experiments) give an indication that the wakes have merged to some degree. Figure 8.1b shows a plot of turbulence intensity change on the downstream centerline between the devices. The plot shows that turbulence intensity is similar to the ambient condition until further downstream when the expanding wakes of the two disks merge. With the wakes merging at closer distances downstream the more closely separated scenarios are seen to have a higher peak turbulence intensity (almost 3 times that of the undisturbed flow). The peaks are also observed to occur further upstream, closer to the disks, in the most closely position disk cases. The turbulence intensity values observed on the centreline between the devices are then seen to decay with increasing downstream distance, not returning to ambient conditions until distances greater than 25D downstream. In the 0.5D separation case the wakes merge at such a small downstream distance that only turbulence greater than ambient is observed at all until beyond 25D.

Figures 8.2a and 8.2b show velocity deficit and 3D turbulence intensity values respectively, on the centreline between the devices, for cases of greater disk separation. With increasing disk separation greater flow acceleration between the devices is observed with a maximum value of over -0.04 recorded at a disk separation of 2.0D. The region of accelerated flow is also observed to persist further downstream with greater disk separation. An increase in the downstream distance the accelerated flow region is observed to prevail increases from around 7D to 15D when comparing the 1.5D and 2.0D separation cases. At larger separations smaller peak velocity deficit values are observed. At a separation of 2.0D the maximum velocity deficit observed is 0.02. Further reduction in peak value would be expected as the devices begin to tend towards operating in isolation (i.e. not interacting) at greater spacing. A similar trend of reducing peak turbulence intensity value is observed in Figure 8.2b. At 2.0D separation turbulence intensity values above that of the undisturbed flow are only observed at distances greater than 15D downstream (at the same distance that the flow accelerated region ends), indicating that a merged wake of lower intensity forms in the cases of greater spacing.

The downstream intensity and propagation of the combined wake is important when considering that subsequent turbines may be positioned downstream of those investigated. Higher velocity deficit and turbulence intensity values recorded on the centreline between the two devices will take longer downstream distances to recover. Hence although it will be beneficial for array developers to space their devices closer in order to maximise the number of devices at a given development site, the close spacing could engender much longer wake recovery and therefore increase the downstream distance at which subsequent rows may be placed. Myers & Bahaj (2012) postulated that wider lateral device spacings, which show greater separation of wake structures, benefit from faster combined wake recovery due to the "increased surface area over which shear forces can act to dissipate the wake flow". It appears that if an array developer wishes to place a subsequent row of devices downstream then the upstream row spacing should be chosen carefully in order to ensure that wake dissipation of the upstream row occurs at a suitable distance downstream.

The extent of the region of accelerated fluid is also of interest due to the discussion outlined in Section 2.4. This relates to the placement of a subsequent downstream device between the two devices investigated in this immediate study. It has been postulated that the placement of a device within the region of faster moving fluid accelerated between two devices could result in a greater power output from the device. Based on the results discussed above in such a turbine array arrangement the lateral spacing between the two upstream devices would need to be greater, in order to take advantage of greater flow acceleration between the devices, with the downstream device perhaps 10D or less. This is investigated in further detail in the following section.

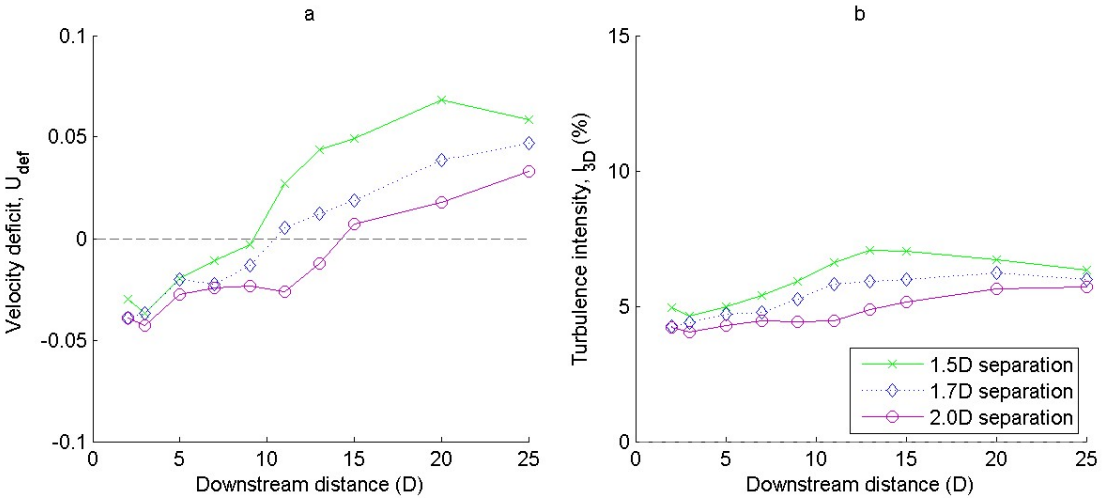

Figure 8.2: Comparison of data collected on the centreline between the devices for various larger disk separations: (a) velocity deficit and (b) 3D turbulence intensity.

8.1.2 Additional downstream devices

This section considers the possible introduction of a third device, located further downstream and between the dual-device layout already discussed. Further investigation of the central jet between two disks is essential to reduce any possible negative interaction and augmentation of power production. Clearly it is impractical (possible fatigue issues from higher turbulence intensity values in upstream device wakes) and counter-productive (smaller power output due to lower kinetic energy) to place a turbine in the central region between two devices with the close separations discussed in the previous section as optimal for a single row of turbines. As mentioned earlier the upstream row of a two row array would need a larger spacing to accommodate any devices placed downstream. Figure 8.2a shows the centreline plots for a number of larger lateral disk spacings. As lateral spacing is increased the length of the accelerated region also increases. At a separation of 2.0D an accelerated region is observed to persist over 10D downstream, almost double the length in comparison to 1.5D separation. The maximum velocity deficit observed is reduced with increased spacing.

Measurements were taken parallel to the centreline between the devices but offset by 0.5D in the lateral (y-direction) to characterise the width of the accelerated region into which a device may be placed. Results, seen in Figure 8.3a, show the potential of downstream disk placement is reduced heavily when considering the width of the jet. Over the three cases the edge of the accelerated region only propagates a little over half the distance downstream when compared to the centreline. In the 1.5D & 1.7D cases the accelerated region only propagates 3D & 4D downstream respectively, whilst with 2.0D separation the region extends to almost 8D downstream. For all the turbine separations investigated the flow acceleration was only observed for a maximum of 7D

downstream. This is the furthest downstream distance a third disk could potentially be located without incurring undesirable effects. Figure 8.4 illustrates how a third disk may be placed downstream from the two disk arrangements examined already in this work. The velocity deficit of the flow field is presented and shows how a similar diameter device potentially may be placed in the central jet 4D downstream without encountering negative flow acceleration effects.

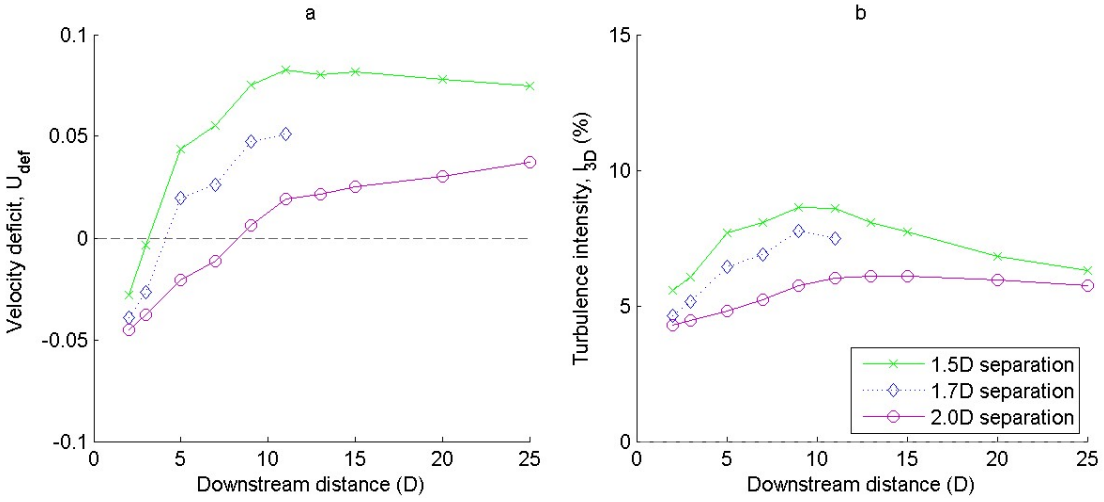

Figure 8.3: Comparison of data collected on the 0.5D offset centreline, between the devices, for various larger disk separations: (a) velocity deficit and (b) 3D turbulence intensity.

Figure 8.2b shows turbulence intensity on the centreline between the disks for the larger disk separations. The intensity and size of variation were seen to be much lower for the larger separation cases. Increases from ambient conditions are seen, with peak turbulence intensity of 7.1% for the 1.5D separation case at 13D downstream. In the largest case examined the peak turbulence intensity occurs further downstream at 20D, with a value of 5.7%. Again it is of course important to consider the entire width of the jet within which a downstream device may be located, therefore the turbulent intensity measurements of the +0.5D lateral offset must be considered which are shown in Figure 8.3b. Higher turbulence intensities are evident in the downstream lateral offset location shown with peak intensities reaching almost 9% and occurring further upstream. This supports the earlier argument that the edges of the expanding wakes from the disks are encroaching upon the central jet and implies negative interaction could be experienced if the upstream spacing of devices is insufficient. Although at first glance it may appear unimportant as these fluctuations are only acting on a small part of the rotor of a downstream device it is nonetheless a crucial area. In a conventional horizontal axis device (those which are planned for installation in the earliest arrays) fluctuations in flow in this region will be acting on the blade tips which would have the greatest impact upon blade root loading and potential fatigue failure. In Figure 8.4 a suggested layout for a three disk arrangement was presented with upstream separation of 1.7D. It was posed that the flow field produced by the two upstream disks provided no negative

flow acceleration effects in the region 4D downstream, where the third disk could be placed. However, the turbulence intensity results presented in Figure 8.3b suggest that in this downstream position an increase in turbulence intensity above that of the ambient conditions occurs at the extremity of the accelerated region into which the disk would be placed. Hence positive flow effects may be seen in terms of increased kinetic energy available to the device but negative effects due to operating in more turbulent flow are also observed. A layout using an upstream separation of 2.0D appears to provide both beneficial flow acceleration and no increased/negative turbulent interaction effects from the expanding wake up to 7D downstream. Placing a disk at the same 4D downstream location for the 2.0D separation case yields a conservative estimate of increased velocity and power available as around 3.5% and 11% respectively (assuming there is no change in inflow to the 3-device array).

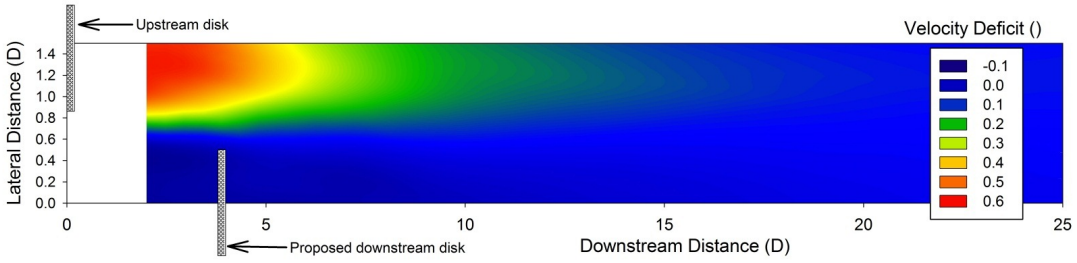

Figure 8.4: Horizontal plane velocity flow field around 1.7D laterally separated disks.

8.1.3 Loading changes with device proximity

Thrust measurements were recorded at various lateral disk separations in the 3D depth channel. Calculations of thrust coefficient are presented in Figure 8.5 and are compared to a thrust calculation from thrust measurements on a single device operating in isolation in the same channel. Values are seen to be dependent on the spacing between the two disks, whilst both lower and higher values are observed compared to those of the isolated device. When compared to an isolated device values +6% greater and -12% smaller are observed. This may be counter intuitive as it may be presumed that the increase in channel area blockage ratio (when inserting a second disk) would result only in greater values of thrust coefficient. However in light of results in Section 6.4, where it was shown that thrust coefficient is a function of both area blockage ratio and channel aspect ratio, the variation may be explained. The presence of a secondary device in a flow alongside another may behave in a similar way to the presence of a boundary within the flow field. Hence the effective shape of the channel in which each individual device is operating in a dual-disk array has been changed. As changes in channel shape have been shown to alter the thrust coefficient it is possible to see why variations such as those observed in the dual-disk array are possible.

The changes in thrust coefficient observed in Figure 8.5 appear to be linked to the flow profiles introduced earlier in this chapter. For example, when considering the separation of 0.5D, higher thrust coefficient values are observed. In Figure 8.1 it was observed at this separation that the wakes have merged to form a combined wake. It follows that the combined wake behind the devices results in a larger region of low pressure, which increases the loading and thrust coefficient on the disk. With spacings such as 1.0-1.5D a reduction of thrust coefficient is observed which is associated with the development of an accelerated flow region observed in Figure 8.1. With further increases in disk spacing coefficient of thrust values are seen to approach that of a single isolated disk by 2.0D separation. Measurements on the centreline between the disks at this separation (Figure 8.2) show the smallest differences to that of the ambient flow, indicating that the disks are operating in greater isolation to each other.

The results show that significant variation in thrust coefficient can occur with device spacing within a dual-device array. This is a significant finding for developers, showing that device spacing selected within an array development can have a significant impact on the loads which a device must be designed for. The results also suggest that it may be possible to design arrays in order to take advantage of the increase in loading (and potential power output) of particular device separations.

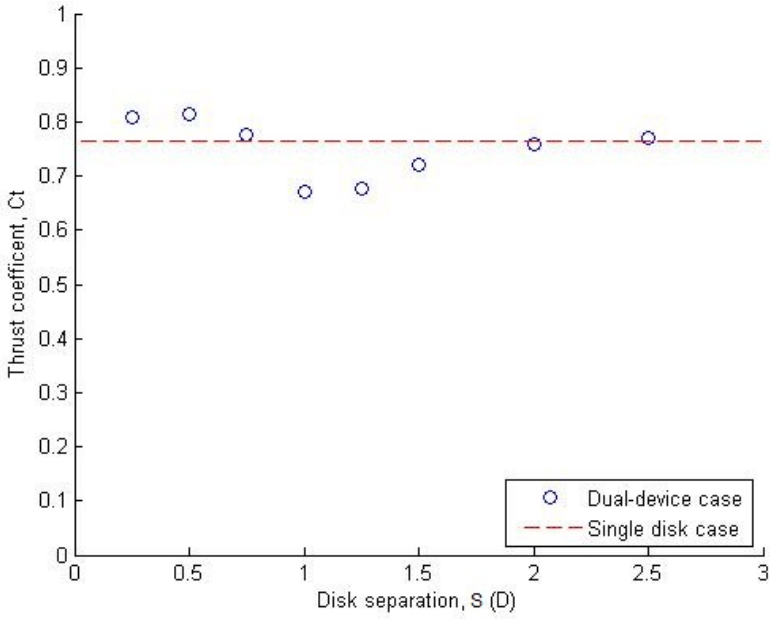

Figure 8.5: Thrust values for varying disk separation at 3D depth ($d/h = 0.33$).

8.2 Effects of device diameter/water depth ratio and spacing within a dual-device array

Figure 8.6 shows variation in thrust coefficient with changes in device spacing of a dual-device array within a 1.75D depth channel. Similar thrust coefficient values to those of a single device operating in isolation are observed at larger separations, such as 2.5D, in the dual-disk case. Increases in thrust coefficient are observed with reduction in device spacing within the array. The largest increase of 9% was observed at the closest separation of 0.25D. By comparison to Figure 8.5 the trend is much more simplistic, with a steady increase in thrust coefficient with reduction in spacing. No reduction in thrust coefficient is observed from the isolated disk value, as was the case in the 3D depth case. The differences in the shape of the trend are attributed to the close proximity of the vertical flow boundaries in the 1.75D depth case. At such close proximity there is limited flow above and below the disk, and hence much of the flow is directed/accelerated laterally around the disk (findings in Section 7.2). The introduction of a second disk acts in a similar way to the introduction of a solid boundary to constrain the flow laterally. In the more vertically constrained channel geometry fluid cannot be forced above and below the disk as easily due to the close proximity of the vertical boundaries, and hence is accelerated between the devices. This is confirmed in Figure 8.7 where more negative values (indicating acceleration of flow) are observed at 1.0D and 2.5D separation. The reason for the more complex trend in the 3D depth channel is that flow can be also forced above and below the disk with changes in lateral constraint (shown in Section 7.2), due to the reduced vertical constraint. Hence as the disk separation is reduced flow can be forced above and below the devices as well as between them. This leads to the more complex trend of varying thrust coefficient with changes in separation in the 3D depth case.

Figure 8.8 shows the variation in thrust coefficient with changes in device separation within a 2.25D depth channel. Variation is seen both above and below the value taken for an isolated device operating in the same channel. When compared to an isolated device values +4% greater and -3% smaller are observed. This is again attributed to the inter-dependency of vertical and lateral flow acceleration around each device. Smaller variations in value are seen when compared to the 3D depth case. Figure 8.9 shows the variation in velocity deficit on the centreline between the two devices.

Many individual experimental and numerical studies to date have investigated array spacing at fixed device diameter/water depth ratios. Such studies include those by Turnock et al. (2011), Myers & Bahaj (2012), Stallard et al. (2013), Hunter et al. (2013) and Schluntz et al. (2014). Some work has been completed on single devices operating in changing device diameter/water depth ratios (Giles et al. 2011) however no study has investigated this parameter in multiple device arrays.

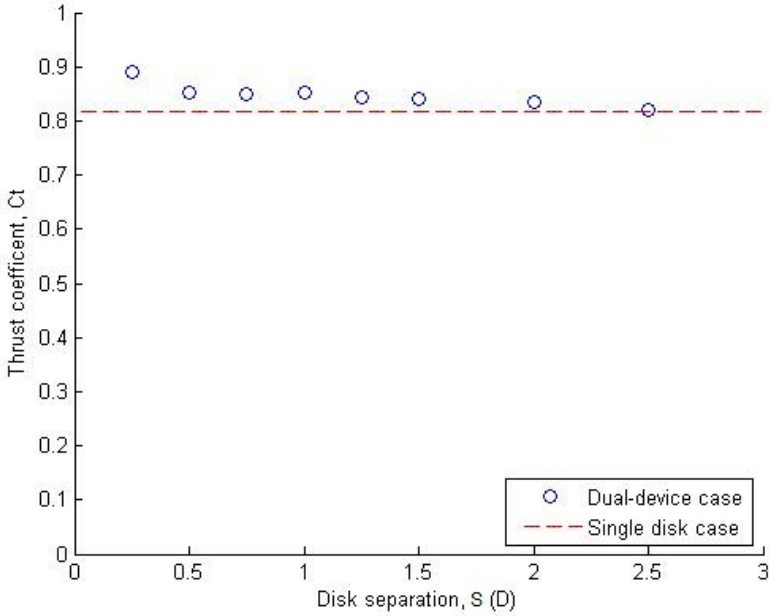

Figure 8.6: Thrust values for varying disk separation at 1.75D depth ($d/h = 0.57$).

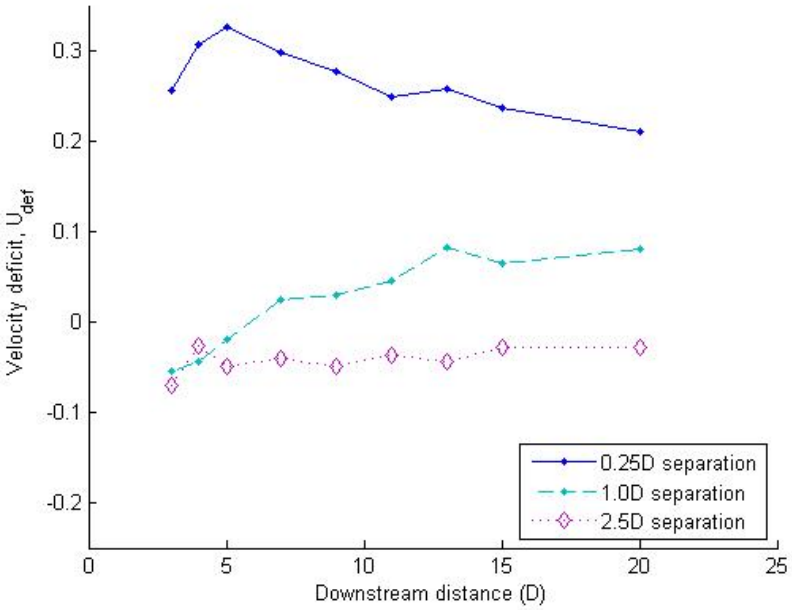

Figure 8.7: Comparison of centreline for varying disk separations at 1.75D depth ($d/h = 0.57$).

This section has highlighted the importance of device diameter/water depth ratio on both the device loading and wake development of a device operating within a dual-device array. Results presented build on the understanding introduced in previous chapters, of devices operating in confined flows, to highlight the differences that occur in the flow field around multiple devices when operating in differing degrees of spacing. It is shown

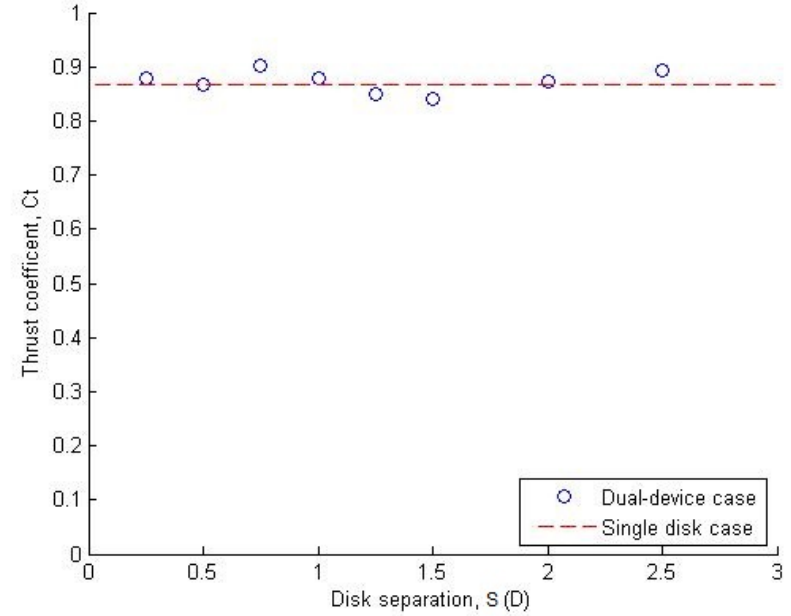

Figure 8.8: Thrust values for varying disk separation at 2.25D depth ($d/h = 0.44$).

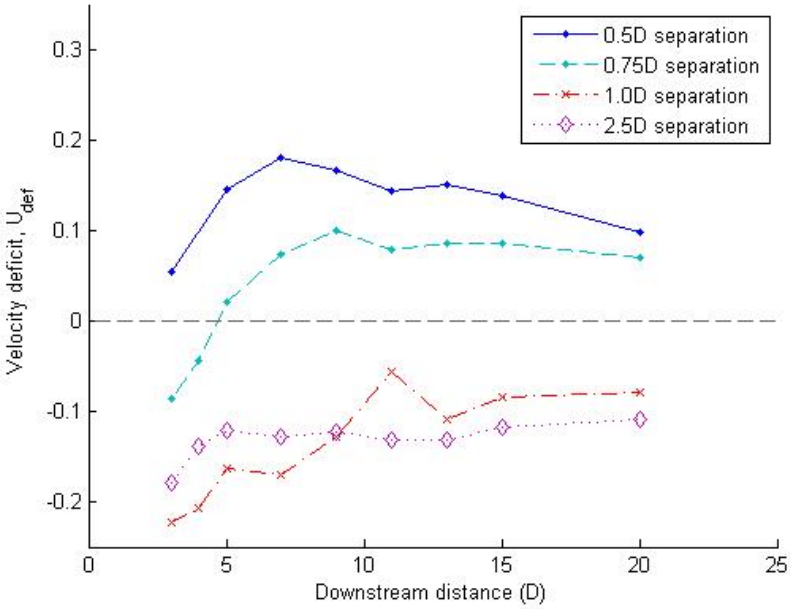

Figure 8.9: Comparison of centreline for varying disk separations at 2.25D depth ($d/h = 0.44$).

that the inter-dependency of vertical and lateral flow acceleration around each device, which differs due to flow geometry (i.e. device diameter/water depth ratio), can have significant effects on the loading and wake development of device within an array.

8.3 Application of findings to full-scale deployments

The first MCEC arrays could take many forms or arrangements, the designs of which are still being developed for each site. The main tools that array developers will be using in the site-specific designs will be three-dimensional CFD models. In the absence of full-scale array data such models will not be validated for full-scale sites. Hence findings such as those outlined in this chapter, which understand the differences in loading and wake development with changes in flow geometry, can be of importance to understand the ranges of conditions under which numerical models must perform. The findings could also be used to limit the number of numerical model cases which need to be run in order to optimise array layouts. In understanding the relationships between parameters such as device loading, device spacing and device diameter/water depth ratio it is possible to interpret model results from a limited number of cases. This offers the opportunity to save computational time and cost.

The dual-device cases investigated in this work are directly applicable to some full-scale array deployments discussed in Chapter 1. For example the dual-rotor array deployments planned by RWE power (Table 1.2), or the dual rotor floating devices of Sustainable Marine Energy Ltd described in Section 1.3.1. Although results from only dual-device arrays are presented in this work it may also be possible to infer the result of increasing array size by considering the discussion in Section 7.5. Due to the potential similarity between the proximity of solid wall boundaries and the proximity of other devices it is postulated that the introduction of additional devices on the same plane, of the two already investigated, could result in different loading and wake behaviour of the central devices. With additional devices present, at the same flow depth, it is postulated that the central two devices are less likely to see wake merging occurring at closer separations. This would be due to the additional lateral constraint present, with the additional devices, which would cause more fluid to be forced between the devices and hence prevent the merging of the wakes. As the different array wake structures have been linked to device loading earlier in this chapter it follows that different variation in device loading with device separation would be expected to occur. Therefore, for a single row multiple-device array different relationships between loading and device separation will be observed at each device diameter/water depth ratio to those presented in the dual-device array investigated in this work.

8.4 Summary and further work

- Experimental studies presented in this section have investigated in detail the effect of device spacing on performance and wake evolution within a dual-device array. It is shown that device wakes are likely to merge to form a larger region of increased

velocity deficit, which can propagate for a longer distance downstream, when devices are situated at closer lateral spacing. The nature of the downstream wake propagation is important for device developers who are looking to build arrays of devices which could be designed in different arrangements. Experimental results also show that for some of the possible device arrangements discussed in current literature (i.e. offset rows of arrays) wider spacing of upstream devices may be required due to the expanding wakes of upstream devices. Further experimental work is required in order to ascertain how the placement of a downstream device effects the upstream device performance, both in three-device arrays and larger offset row arrays. Tidal flows at real tidal sites are not necessarily bi-directional, hence further work is also needed to consider the effects of changes in flow direction on the wake propagation within arrays.

- Results have shown the importance of device diameter/water depth ratio on both the device loading and wake development of devices operating within a dual-device array. It is shown that the inter-dependency of vertical and lateral flow acceleration around each device, which differs due to flow geometry (i.e. device diameter/water depth ratio) and device spacing, can have significant effects on the loading and wake development of devices within an array. These findings are of significance to array designers as they can be used to aid in the planning of both upstream intra-row and downstream device spacing, in order to minimise negative device interaction (shadowing) within an array.

Chapter 9

Conclusions and engineering application

9.1 Conclusions

The need for greater amounts of generation from renewable sources of energy is increasing due to pressures over climate change and the need for security of supply. Generation of energy from the tides could provide a predictable and substantial resource. The tidal industry is still in it's early stages and is moving towards further offshore array deployments in order to demonstrate the industry is mature enough to provide secure investment opportunities. It is crucial that these early deployments are a success if sufficient funding is to be obtained to sustain the industry.

A literature review showed that, although tidal stream energy extraction devices will be placed into confined flows, there is only limited understanding of the effects of confined flows on device performance (thrust and power) and wake development. Similarly there is only limited data and understanding of device interaction (device performance and wake development) in confined flows, which is important within the context of array deployments. Linear momentum actuator disk theory (LMADT) models have been used to account for blockage: to re-calculate experimental model performance for comparison between testing facilities, and provide estimates of individual device performance when operating in isolation and in large arrays. However LMADT is only able to consider the area ratios of the flow field and, cannot take into account length ratios, hence cannot consider the aspect ratio of the flow field. Some extensions to the scope of the basic theory have been made (such as the incorporation of free surface modelling by Whelan et al. (2009)) but a comprehensive analysis of some of the key (additional) parameters has not been completed. In the absence of full-scale MCEC array data the validation of such models can only take place with smaller-scale laboratory data. The literature shows that

the limitations of smaller-scale laboratory data in informing full-scale predictive models are currently not fully understood.

A series of laboratory experiments were conducted with the aim to allow further understanding of these deficiencies in the literature. The following surmise the knowledge contribution of this work:

- **A comparative study of porous disk and turbine model wakes in open channels has shown little difference in the far wake development of each device type.** Experimental results comparing the wakes of turbine and porous disk models at differing experimental scale showed that device model type had little effect on the far-wake development in open channel MCEC environments. Results are presented in near and far wake regions in the vertical and horizontal planes, which provide greater understanding of the wake development of each device type than has been completed in previous studies. Small differences in velocity and turbulence intensity fields were observed beyond the transition region in each device type model wake. Although differences in both velocity deficit and turbulence intensity were seen in the near wake of the rotating model and porous disk models when compared (due to the different wake structures of each device), wake recovery appeared to be similar for each device type. This indicates that despite differences in near wake structure porous disks and rotating MCEC models may be used in laboratory scale testing to inform the far wake development of larger scale MCEC devices. Discussion also showed that differences in the near-wake velocity and turbulence field will occur with reduced model scale, not only with the difference in model type (i.e. porous disk or rotating model).

- **The thrust of a porous model operating in an open channel was shown to be a function of: Froude number, area blockage ratio and channel aspect ratio.** The variation in thrust coefficient of a porous model was measured within fixed area blockage ratio channels of varying geometry. Results showed that in constrained flows model thrust coefficient values are a function of Froude number, channel area blockage ratio and channel aspect ratio (a new non-dimensional parameter introduced in this work). For a disk operating in a relatively small fixed area blockage ratio (0.05) it was shown that variation in thrust coefficient of up to 28% can occur with variation in channel aspect ratio; this indicates significant variation in loading can occur with variation in this non-dimensional channel parameter. This result alone could indicate that existing one-dimensional LMADT models are limited in their accuracy for single device and array performance modelling, or when re-calculating experimental model performance for comparison between testing facilities in channels that have non-square cross section. However, further examination of the data showed that thrust coefficient was invariant with the product of channel aspect ratio and area blockage ratio. When simplified

this expression reduces to device diameter/water depth ratio, indicating that one-dimensional LMADT models are capable of accounting for changes in channel aspect ratio. In further porous fence experiments, at a fixed area blockage ratio, differences in thrust coefficient of up to 40% were shown to be a result of differences in channel Froude number. These results also showed the range of validity of bounded LMADT models to be less than that of traditional unbounded LMADT (axial induction factor < 0.5).

- **Wake expansion, wake width, transition point, vertical wake migration and wake dissipation of a porous disk are shown to be dependent on channel geometry.** This study has shown that differences in wake structure are observed when the same device operates in open channels of differing geometry. Differences are observed in the lateral and vertical planes of a wake in bounded flows indicating that wake mixing can vary in each plane. Changes in either lateral or vertical boundary proximity are shown to affect the flow around a device and wake structure in both planes. The links between these changes and the downstream wake development and dissipation are highlighted providing new data for array designers on device spacing within multi-row arrays. Far-wake dissipation was observed to be slower in channel geometries of greater aspect ratio. Vertical wake migration is shown to occur in more greatly constrained channels and is shown to be a function of both lateral and vertical boundary proximity. These findings indicate that the parameters used in semi-empirical wake models, which have been used in MCEC applications, can be calibrated from laboratory findings of devices operating in confined flows in order to provide more accurate wake modelling in bounded flow environments.

- **The thrust coefficient and wake propagation of a porous disk operating within an array is shown to be dependent on device spacing and device diameter/water depth ratio.** Thrust coefficient is shown to be dependent on device spacing at a fixed device diameter/water depth ratio. Variation in values of 18% were observed at a ratio of 0.33. The variation is shown to be linked with the merging of device wakes within a dual-device array. This study has also demonstrated that the merging of wakes and disk thrust coefficient within an array are dependent on changes in device diameter/water depth ratio; indicating that existing studies conducted at a single ratio are only capable of understanding the wake development and device loading of devices with varying lateral spacing to a limited degree.

  This study has shown in greater detail the effects of wake merging within a dual-disk array at a fixed water depth. Results showed that there is potential within the accelerated flow region between the disks for a third device to be placed without incurring negative effects from the upstream devices. Based on the increased

kinetic energy in the flow more than an additional 11% of power could be available for extraction by the device.

9.2 Engineering application of findings

It has been shown that the thrust of a porous model operating in an open channel is shown to be a function of: Froude number, area blockage ratio and aspect ratio. For a disk operating at a fixed area blockage ratio (0.05) it was shown that variation in thrust coefficient of up to 28% can occur with variation in channel aspect ratio. The channel conditions examined are comparable to the blockage within an offshore tidal array deployment. Hence the result provides evidence to array developers that small differences in array geometry layout within a tidal fence could have significant impact on the loadings which a device experiences. The results also showed that existing LMADT models, although inherently one-dimensional, are capable of accounting for channel aspect ratio. This increases confidence in the applicability of LMADT models in array performance modelling or when re-calculating experimental model performance for comparison between testing facilities in channels that have non-square cross section. The findings therefore provide evidence for potential increases in loading which can be designed for, or alternatively maximum loadings can be prevented by choosing appropriate intra-array blockages.

It has been shown in this study that the wake expansion, wake width, transition point, vertical wake migration and wake dissipation of a porous disk are dependent on channel geometry. Such results may be used to inform the wake changes in arrays of devices, where single devices are positioned alongside each other in the same channel cross section (which could be the case in the EDF, Meygen and Scottish Power Renewables array developments detailed in Table 1.2). Also the relationship between device spacing and device diameter/water depth ratio on device thrust coefficient and wake development has been presented for deployment scenarios which are currently planned offshore (see Section 1.3.1). The understanding of the wake changes that occur due to bounded flows is important to predict development and dissipation of device wakes. This is important when considering array deployments in order to negate interference such as shadowing (operating in the wake of an upstream device) which can result in increased fatigue loading and reduced power output. Hence the data and findings presented in this work allow array designers to better understand the limitations of their current models. By understanding the dependencies of the different parameters governing loading and wake development, and how they are related, array designers can understand more clearly which parameters have been accounted for in their models and the potential uncertainty surrounding other parameters which may not have been directly investigated in their own work. Ultimately this contribution in knowledge can reduce the chance of adverse loading

of devices operating in constrained flows as well as shadowing effects on downstream devices operating in arrays.

9.3 Further work

When utilising smaller-scale laboratory models it is not yet clear what the effects of near-wake merging will be on far-wake development in array investigations. Hence further work is required to understand the effects of the differences in near wake region interaction between small-scale devices. This will allow a greater understanding of the applicability of smaller-scale laboratory work to inform full-scale array model development.

Further study is required investigating the changes in wake structure with isolated changes in channel geometry and flow properties, i.e. varying either area blockage ratio, channel aspect ratio or Froude number and observing the effects on wake structure of that parameter. Measuring the effects of each parameter individually will allow the calibration of simple semi-empirical wake models. The effect of boundary layer with changing flow depth also needs to be isolated within any further study.

The differences in the bounding effects of solid boundaries and that of other devices will also need to be established in order to understand how the findings from this work can be applied to array models. Depending on these findings it may be possible to create a computationally efficient analytic/semi-empirical wake model which can be used to estimate array performance; a LMADT model used to predict device performance in constrained flow could be linked with a semi-empirical wake model, previously discussed, in order to predict subsequent device performances within a multi-row MCEC array.

References

Ainslie, J. F. (1988), 'Calculating the flowfield in the wake of wind turbines', *Journal of Wind Engineering and Industrial Aerodynamics* **27**, 213–224.

Atlantis Resources Ltd (2015), 'AR1000 series turbine'.
URL: *http://atlantisresourcesltd.com/turbines/ar-series/ar1000.html*

Aubrun, S., Loyer, S., Hancock, P. & Hayden, P. (2013), 'Wind turbine wake properties: Comparison between a non-rotating simplified wind turbine model and a rotating model', *Journal of Wind Engineering and Industrial Aerodynamics* **120**, 1–8.

Bahaj, A., Molland, A., Chaplin, J. & Batten, W. (2007), 'Power and thrust measurements of marine current turbines under various hydrodynamic flow conditions in a cavitation tunnel and a towing tank', *Renewable Energy* **32**(3), 407–426.

Bahaj, A. & Myers, L. (2013), 'Shaping array design of marine current energy converters through scaled experimental analysis', *Energy* **59**, 83–94.

Bahaj, A. S., Myers, L. E., Thomson, M. D. & Jorge, N. (2007), Characterising the wake of horizontal axis marine current turbines, *in* '7th European Wave and Tidal Energy Conference', Porto, Portugal.

Barnsley, M. & Wellicome, J. (1990), Final report on the 2nd phase of development and testing of a horizontal axis wind turbine test rig for the investigation of stall regulation aerodynamics, Technical report, Carried out under ETSU Agreement E.5A/CON5103/1746.

Barthelmie, R. J., Frandsen, S. T., Nielsen, M. N., Pryor, S., Rethore, P.-E. & Jorgensen, H. (2007), 'Modelling and Measurements of Power Losses and Turbulence Intensity in Wind Turbine Wakes at Middelgrunden Offshore Wind Farm', *Wind Energy* **10**, 517–528.

Barthelmie, R. J., Pryor, S. C., Frandsen, S. T., Hansen, K. S., Schepers, J. G., Rados, K., Schlez, W., Neubert, A., Jensen, L. E. & Neckelmann, S. (2010), 'Quantifying the Impact of Wind Turbine Wakes on Power Output at Offshore Wind Farms', *Journal of Atmospheric and Oceanic Technology* **27**(8), 1302–1317.

Betz, A. (1920), 'Das maximum der theoretisch möglichen ausnutzung des windes durch windmotoren.', *Gesamte Turbinenwesen* **17**, 307–309.

Black & Veatch Ltd (2005), Phase II, UK Tidal Stream Energy Assessment, Technical report.

Blackmore, T. (2013), Grid Generated Turbulence and Actuator Disc Representations of Tidal Turbines, PhD thesis, University of Southampton.

Blackmore, T., Batten, W. M. J., Mller, G. U. & Bahaj, A. S. (2014), 'Influence of turbulence on the drag of solid discs and turbine simulators in a water current', *Experiments in Fluids* **55**(1637).

BS ISO (2008), Hydrometry - Open channel flow measurement using thin-plate weirs, Technical report, 1438:2008.

Buckland, H. C., Masters, I., Orme, J. a. & Baker, T. (2013), 'Cavitation inception and simulation in blade element momentum theory for modelling tidal stream turbines', *Proceedings of the Institution of Mechanical Engineers, Part A: Journal of Power and Energy* **227**(4), 479–485.

Buhl, M. L. (2005), A New Empirical Relationship between Thrust Coefficient and Induction Factor for the Turbulent Windmill State A New Empirical Relationship between Thrust Coefficient and Induction Factor for the Turbulent Windmill State, Technical Report August, NREL, Report No. NREL/TP-500-36834.

Builtjes, P. (1978), The Interaction Of Windmill Wakes, *in* 'Second International Symposium on Wind Energy Systems', Amsterdam, Netherlands.

Burton, T., Sharpe, D., Jenkins, N. & Bossanyi, E. (2001), *Wind Energy Handbook*, John Wiley & Sons, Chichester, UK.

CBC News (2010), 'Turbine damage stalls Funday tidal power test'.
URL: *http://www.cbc.ca/news/canada/nova-scotia/turbine-damage-stalls-fundy-tidal-power-test-1.926011*

Cea, L., Puertas, J. & Pena, L. (2007), 'Velocity measurements on highly turbulent free surface flow using ADV', *Experiments in Fluids* **42**(3), 333–348.

Cleve, J., Greiner, M., Enevoldsen, P., Birkemose, B. & Jensen, L. (2009), 'Model-based Analysis of Wake-flow Data in the Nysted Offshore Wind Farm', *Wind Energy* **12**, 125–135.

Crammond, S., Caljouw, R., Jones, I., Wells, A., Hamill, I. & Petersen, O. (2011), MeyGen Tidal Energy Project : Numerical Modelling of Tidal Turbine Wake Interactions, *in* '9th European Wave and Tidal Energy Conference'.

Crespo, A., Hernández, J. & Frandsen, S. (1999), 'Survey of modelling methods for wind turbine wakes and wind farms', *Wind Energy* **2**(1), 1–24.

Cruise, J., Sherif, M. & Singh, V. (2007), *Elementry Hydraulics*, Thomson Canada Limited.

Daly, T., Myers, L. E. & Bahaj, A. S. (2011), Experimental investigation of the effects of the presence and operation of tidal turbine arrays in a split tidal channel, *in* 'World Renewable Energy Congress', Linköping, Sweden.

Darkoneko (2003), 'Moulin à marée de l'île de Bréhat'.
URL: *https://commons.wikimedia.org/wiki/File:Moulin_maree_brehat.jpg*

Department of Energy & Climate Change (2015), Digest of United Kingdom Energy Statistics, Technical report.

Department of Trade and Industry (2007), MEETING THE ENERGY CHALLENGE: A White Paper on Energy Meeting the Energy Challenge A White Paper on Energy May 2007, Technical Report May, HM Government.

Doman, D. a., Murray, R. E., Pegg, M. J., Gracie, K., Johnstone, C. M. & Nevalainen, T. (2015), 'Tow-tank testing of a 1/20th scale horizontal axis tidal turbine with uncertainty analysis', *International Journal of Marine Energy* **11**, 105–119.

Draper, S. & Nishino, T. (2013), 'Centred and staggered arrangements of tidal turbines', *Journal of Fluid Mechanics* **739**, 72–93.

España, G., Aubrun, S., Loyer, S. & Devinant, P. (2012), 'Wind tunnel study of the wake meandering downstream of a modelled wind turbine as an effect of large scale turbulent eddies', *Journal of Wind Engineering and Industrial Aerodynamics* **101**, 24–33.

European Commission (2012), 'Renewable Energy Targets by 2020'.
URL: *http://ec.europa.eu/energy/renewables/targets_en.htm*

European Parliament (2001), Directive 2001/80/EC of the European Parliament and of the Council of 23 October 2001 on the limitation of emissions of certain pollutants into the air from large combustion plants, Technical report.

Fraenkel, P. L. (2010), Development and testing of Marine Current Turbines SeaGen 1.2MW tidal stream turbine, *in* '3rd International Conference on Ocean Energy', Bilbao, Spain.

Galloway, P. W., Myers, L. E. & Bahaj, A. S. (2011), Experimental and numerical results of rotor power and thrust of a tidal turbine operating at yaw and in waves, *in* 'World Renewable Energy Congress', Linköping, Sweden.

Galloway, P. W., Myers, L. E. & Bahaj, A. S. (2014), 'Quantifying wave and yaw effects on a scale tidal stream turbine', *Renewable Energy* **63**, 297–307.

Garrad Hassan and Partners Ltd. (2009), GH WindFarmer: Theory Manual, Technical report.

Garrad Hassan and Partners Ltd. (2015), 'Tidal Farmer'.
URL: *https://www.dnvgl.com/services/tidalfarmer-3774*

Garrett, C. & Cummins, P. (2007), 'The efficiency of a turbine in a tidal channel', *Journal of Fluid Mechanics* **588**, 243–251.

Giles, J., Myers, L., Bahaj, A. S. & Shelmerdine, B. (2011), The downstream wake response of marine current energy converters operating in shallow tidal flows, *in* 'World Renewable Energy Congress', Linköping, Sweden.

Glauert, H. (1947), *The elements of aerofoil and airscrew theory*, 2nd edn, Cambridge University Press, Cambridge, UK.

González-Longatt, F., Wall, P. & Terzija, V. (2012), 'Wake effect in wind farm performance: Steady-state and dynamic behavior', *Renewable Energy* **39**(1), 329–338.

Harrison, M. E., Batten, W., Myers, L. & Bahaj (2010), 'Comparison between CFD simulations and experiments for predicting the far wake of horizontal axis tidal turbines', *IET Renewable Power Generation* **4**(6), 613–627.

Houlsby, G., Draper, S. & Oldfield, M. (2008), Application of Linear Momentum Actuator Disc Theory to Open Channel Flow, Technical report, University of Oxford, Report No. OUEL 2296/08.

Hunter, W., Nishino, T. & Willden, R. H. J. (2013), Investigation of Tidal Turbine Arrays using 3D Reynolds-Averaged Navier-Stokes Simulations, *in* '10th European Wave and Tidal Energy Conference', Aalborg, Denmark.

Ingram, D., Smith, G., Bittencourt-Ferreira, C. & Smith, H. (2011), Protocols for the Equitable Assessment of Marine Energy Converters, Technical report, EquiMar.

Jensen, N. (1983), A note on Wind Generator Interaction, Technical report.

Keogh, B., Myers, L. & Bahaj, A. (2014), Tidal stream turbine device performance with changes in channel size and geometry, *in* 'Grand Renewable Energy Congress Proceedings', Tokyo, Japan.

Koo, J. & James, D. (1973), 'Fluid flow around and through a screen', *Journal of Fluid Mechanics* **60**(3), 513–538.

Lin, T. (2014), 'A 'Rebel' Without a Ph.D.'.
URL: *http://www.simonsfoundation.org/quanta/20140326-a-rebel-without-a-ph-d/*

MacKay, D. (2009), *Sustainable energy without the hot air*, UIT, Cambridge, UK.

Maganga, F., Germain, G., King, J., Pinon, G. & Rivoalen, E. (2010), 'Experimental characterisation of flow effects on marine current turbine behaviour and on its wake properties', *IET Renewable Power Generation* **4**(6), 498–509.

Maskell, E. (1965), A theory of blocakge effects on bluff boddies and stalled wings in a closed wind tunnel, Technical report.

McAdam, R., Houlsby, G. & Oldfield, M. (2013), 'Experimental measurements of the hydrodynamic performance and structural loading of the Transverse Horizontal Axis Water Turbine: Part 1', *Renewable Energy* **59**, 105–114.

McTavish, S., Feszty, D. & Nitzsche, F. (2013), 'An experimental and computational assesment of blockage effects on wind turbine wake development', *Wind Energy* **17**(10), 1515–1529.

MeyGen (2015), 'MeyGen: The Tide of Change in Caithness'.
URL: *http://www.meygen.com/*

Milne, I. A., Sharma, R. N., Flay, R. G. J. & Bickerton, S. (2011), Characteristics of the Onset Flow Turbulence at a Tidal-Stream Power Site, *in* '9th European Wave and Tidal Energy Conference', Southampton, UK.

Milne, I. A., Sharma, R. N., Flay, R. G. J. & Bickerton, S. (2013), 'Characteristics of the turbulence in the flow at a tidal stream power site', *Philosophical transactions of the royal society A* **371**.

Morris, C., ODoherty, D., Mason-Jones, A. & ODoherty, T. (2015), 'Evaluation of the swirl characteristics of a tidal stream turbine wake', *International Journal of Marine Energy* .

Mortimer, A. (2010), Tidal Power with Hammerfest Strøm Technology : Towards Commercialisation, *in* 'International Conference on Offshore Mechanics and Arctic Engineering', Bilbao, Spain.

Munson, B., Young, D. & Okiiahi, T. (1998), *Fundamentals of fluid mechanics*, 3rd edn, John Wiley & Sons, UK.

Mycek, P., Gaurier, B., Germain, G., Pinon, G., Rivoalen, E. & Service, M. (2011), Numerical and Experimental Study of the Interaction Between Two Marine Current Turbines, *in* '9th European Wave and Tidal Energy Conference', Southampton, UK.

Myers, L. & Bahaj, A. (2010*a*), Design of 1st-generation marine current energy converter arrays, *in* 'World Renewable Energy Congress XI', Abu Dhabi, UAE.

Myers, L. & Bahaj, A. (2010*b*), 'Experimental analysis of the flow field around horizontal axis tidal turbines by use of scale mesh disk rotor simulators', *Ocean Engineering* **37**(2-3), 218–227.

Myers, L. & Bahaj, A. (2012), 'An experimental investigation simulating flow effects in first generation marine current energy converter arrays', *Renewable Energy* **37**(1), 28–36.

Myers, L. & Bahaj, A. S. (2009), Near wake properties of horizontal axis marine current turbines, *in* 'EWTEC', Uppsala, Sweeden, pp. 558–565.

Myers, L. E., Bahaj, A. S., Rawlinson-Smith, R. I. & Thomson, M. (2008), The Effect of Boundary Proximity Upon the Wake Structure of Horizontal Axis Marine Current Turbines, *in* 'International Conference on Offshore Mechanics and Arctic Engineering', Estoril, Portugal, pp. 709–719.

Myers, L. E., Keogh, B. & Bahaj, A. S. (2011*a*), Experimental investigation of inter-array wake properties in early tidal turbine arrays, *in* 'OCEANS 2011', Kona, Hawaii.

Myers, L. E., Keogh, B. & Bahaj, A. S. (2011*b*), Layout Optimisation of 1 st - Generation Tidal Energy Arrays, *in* '9th European Wave and Tidal Energy Conference', Southampton, UK.

Nishino, T. & Willden, R. H. (2012*a*), 'Effects of 3-D channel blockage and turbulent wake mixing on the limit of power extraction by tidal turbines', *International Journal of Heat and Fluid Flow* **37**, 123–135.

Nishino, T. & Willden, R. H. J. (2012*b*), 'The efficiency of an array of tidal turbines partially blocking a wide channel', *Journal of Fluid Mechanics* **708**, 596–606.

Nishino, T. & Willden, R. H. J. (2013), 'Two-scale dynamics of flow past a partial cross-stream array of tidal turbines', *Journal of Fluid Mechanics* **730**, 220–244.

Nortek AS (2014), 'Nortek products page'.
URL: *http://www.nortekusa.com/en/products/velocimeters/vectrino*

Nova Innovation Ltd (2015), 'Nova Innovation Ltd'.
URL: *http://www.novainnovation.co.uk/index.php*

OpenHydro (2015), 'OpenHydro: sea the future'.
URL: *http://www.openhydro.com/home.html*

Palm, M., Huijsmans, R. & Pourquie, M. (2011), The Applicability of Semi-Empirical Wake Models for Tidal Farms, *in* '9th European Wave and Tidal Energy Conference'.

Palm, M., Huijsmans, R., Pourquie, M. & Sijtstra, A. (2010), Simple wake models for tidal turbines in farm arrangement, *in* 'International Conference on Ocean, Offshore and Arctic Engineering', Shanghai, China, pp. 577–587.

Pope, S. (2000), *Turbulent flows*, Cambridge University Press, Cambridge, UK.

RenewableUK (2013*a*), 'Offshore Wind Energy Figures'.
URL: *http://www.renewableuk.com/en/renewable-energy/wind-energy/offshore-wind/index.cfm*

RenewableUK (2013*b*), Wave and Tidal Energy in the UK: Conquering Challenges , Generating Growth, Technical Report February.

Roberts, B. W. (1980), 'Drag and Pressure Distribution on a Family of Porous , Slotted Disks', *Journal of Aircraft* **17**(6), 393–401.

Royal Haskoning (2011), SeaGen Environmental Monitoring Programme: Final Report, Technical report, Edinburgh, UK.

Rusello, P. J., Lohrmann, A., Siegel, E. & Maddux, T. (2006), Improvements in acoustic doppler velocimetry, *in* '7th International Conference on Hydroscience and Engineering', Philadelphia, USA.

Schluntz, J., Vogel, C. R. & Willden, R. H. J. (2014), Blockage-enhanced performance of tidal turbine arrays, *in* 'Grand Renewable Energy Congress Proceedings', Tokyo, Japan.

Schluntz, J. & Willden, R. H. J. (2013), The Effect of Rotor Design on the Power Output of Closely Packed Tidal Turbines, *in* '10th European Wave and Tidal Energy Conference', Aalborg, Denmark.

Schottel Group (2015), 'Schottel Hydro'.
URL: *http://www.schottel.de/schottel-hydro/*

Sforza, P., Sheerin, P. & Smorto, M. (1981), 'Three dimensional wakes of simulated turbines', *AIAA Journal* **19**(9), 1101–1107.

Shives, M. R. (2011), Hydrodynamic Modeling , Optimization and Performance Assessment for Ducted and Non-ducted Tidal Turbines, Masters thesis, University of Victoria.

Stallard, T., Collings, R., Feng, T. & Whelan, J. (2013), 'Interactions between tidal turbine wakes : experimental study of a group of three-bladed rotors', *Philosophical transactions of the royal society A* **371**.

Stallard, T., Collings, R., Feng, T. & Whelan, J. I. (2011), Interactions Between Tidal Turbine Wakes : Experimental Study of a Group of 3-Bladed Rotors, *in* '9th European Wave and Tidal Energy Conference', Southampton, UK.

Sun, X., Chick, J. & Bryden, I. (2008), 'Laboratory-scale simulation of energy extraction from tidal currents', *Renewable Energy* **33**(6), 1267–1274.

Sustainable Marine Energy Ltd (2015), 'Sustainable Marine Energy Ltd'.
URL: *http://sustainablemarine.com/*

Taylor, G. (1963), *The scientific papers of Sir Geoffrey Ingram Taylor: Volume III*, Cambridge University Press, Cambridge, UK.

Tedds, S. C., de Jesus Henriques, T. A., Owen, I. & Poole, R. J. (2013), Near-wake characterisation of Horizontal Axis Tidal Stream Turbines in non-uniform steady flow, *in* '10th European Wave and Tidal Energy Conference', Aalborg, Denmark.

Thomson, J., Polagye, B., Durgesh, V. & Richmond, M. C. (2012), 'Measurements of Turbulence at Two Tidal Energy Sites in Puget Sound, WA', *IEEE Journal of Oceanic Engineering* **37**(3), 363–374.

Thomson, M. D., Whelan, J. I. & Gill, L. (2011), The Development of a Tool for the Design and Optimisation of Tidal Stream Turbine Arrays, *in* '9th European Wave and Tidal Energy Conference', Southampton, UK.

Tidal Testing Centre (2013), The Den Oever High Tidal Flow Site for Intermediate Scale Testing, Technical report.

Tswgb (2007), 'Aerial view of the tidal barrage on the Rance and of Saint Malo'.
URL: *https://commons.wikimedia.org/wiki/File:Barrage_de_la_Rance.jpg*

Turnock, S. R., Phillips, A. B., Banks, J. & Nicholls-Lee, R. (2011), 'Modelling tidal current turbine wakes using a coupled RANS-BEMT approach as a tool for analysing power capture of arrays of turbines', *Ocean Engineering* **38**(11-12), 1300–1307.

Vennell, R. (2010), 'Tuning turbines in a tidal channel', *Journal of Fluid Mechanics* **663**, 253–267.

Vennell, R. (2013), 'Exceeding the Betz limit with tidal turbines', *Renewable Energy* **55**, 277–285.

Vermeer, L., Sorensen, J. N. & Crespo, A. (2003), 'Wind turbine wake aerodynamics', *Progress in Aerospace Sciences* **39**(6-7), 467–510.

Walker, J. M., Flack, K. ., Lust, E. E., Schultz, M. P. & Luznik, L. (2014), 'Experimental and numerical studies of blade roughness and fouling on marine current turbine performance', *Renewable Energy* **66**, 257–267.

Whelan, J. I. (2010), A fluid dynamic study of free-surface proximity and inertia effects on tidal turbines, PhD thesis, Imperial College London.

Whelan, J. I., Graham, J. M. R. & Peiró, J. (2009), 'A free-surface and blockage correction for tidal turbines', *Journal of Fluid Mechanics* **624**, 281–291.

Whelan, J. I. & Stallard, T. (2011), Arguments for modifying the geometry of a scale model rotor, *in* '9th European Wave and Tidal Energy Conference', Southampton, UK.

Xiao, H., Duan, L., Sui, R. & Rosgen, T. (2013), Experimental investigations of turbulent wake nehind porous disks, *in* '1st Marine Energy Technology Symposium', Washington D.C.